

# **Error analysis for distributed fibre optic sensing technology based on Brillouin scattering**



**Ying Mei**

Department of Engineering  
University of Cambridge

This dissertation is submitted for the degree of  
*Doctor of Philosophy*

Lucy Cavendish College

August 2018



To my loving parents and brother



## **Declaration**

I hereby declare that except where specific reference is made to the work of others, the contents of this dissertation are original and have not been submitted in whole or in part for consideration for any other degree or qualification in this, or any other university. This dissertation is my own work and contains nothing which is the outcome of work done in collaboration with others, except as specified in the text and Acknowledgements. This dissertation contains fewer than 65,000 words including appendices, bibliography, footnotes, tables and equations and has fewer than 150 figures.

Ying Mei  
August 2018



## **Acknowledgements**

I would like to express my deepest thankfulness to my supervisor, Professor Kenichi Soga, who was so kind that he supervised and supported me throughout the course of my research. Without his persistent guidance this report would not have been written in its present state. I thank Professor Jize Yan, my co-supervisor who provided an insightful view of my work. I am fortunate to have Dr. Xiaomin Xu in the research team, whose vast expertise in Geotechnical engineering has led me to greater understanding of the operational method for BOTDR instruments. I would like to thank him for his contributions and initial guidance on Brillouin scattering and BOTDR raw data interpretation.

I would like to thank the CSIC members Mr. Peter Knott and Dr Cedric. K, who gave me much guidance during my research, and professional assistance with the lab experiments. They have led me to greater understanding of the distributed fibre optic technology as well as the calibration process. Nevertheless, I am grateful to Dr. Yue Ouyang for her initial guidance in mat-lab programming.

I would like to thank Dr. S. Gil-Lorenzo, Mr Matthew Wilcock, Mr Musa Mohammed, Dr Hyungjoon Seo, Dr. Nicky de Battista and Mrs Vanessa Di Murro for sharing the field sensing data. I am also grateful to Dr. Linqing Luo, Dr. Yifei Yu and Dr. Bo Li for their valuable feedback during the construction of the spontaneous Brillouin scattering model.

The research project presented in this thesis was funded by the Cambridge Centre for Smart Infrastructure and Construction (CSIC). The author's scholarships were sponsored by the Chinese Scholarship Council (CSC). I am therefore truly grateful for their financial supports. Worth acknowledging too are the travel grants awarded by the Engineering Department and Lucy Cavendish College. Last but not the least, I would like to thank my family: my parents and brother for supporting me spiritually writing this thesis and my life in general.



## **Abstract**

This dissertation describes the work conducted on error analysis for Brillouin Optical Time Domain Reflectometry (BOTDR), a distributed strain sensing technology used for monitoring the structural performance of infrastructures. Although BOTDR has been recently applied to many infrastructure monitoring applications, its measurement error has not yet been thoroughly investigated. The challenge to accurately monitor structures using BOTDR sensors lies in the fact that the measurement error is dependent on the noise and the spatial resolution of the sensor as well as the non-uniformity of the monitored infrastructure strain conditions. To improve the reliability of this technology, measurement errors (including precision error and systematic error) need to be carefully investigated through fundamental analysis, lab testing, numerical modelling, and real site monitoring verification.

The relationship between measurement error and sensor characteristics is firstly studied experimentally and theoretically. In the lab, different types of sensing cables are compared with regard to their measurement errors. Influences of factors including fibre diameters, polarization and cable jacket on measurement error are characterized. Based on experimental characterization results, an optics model is constructed to simulate the Brillouin back scattering process. The basic principle behind this model is the convolution between the injected pulse and the intrinsic Brillouin spectrum. Using this model, parametric studies are conducted to theoretically investigate the impacts of noise, frequency step and spectrum bandwidth on final strain measurement error.

The measurement precision and systematic error are then investigated numerically and experimentally. Measurement results of field sites with installed optical fibres displayed that a more complicated strain profile leads to a larger measurement error. Through extensive experimental and numerical verifications using a Brillouin Optical Time Domain Reflectometry (BOTDR), the dependence of precision error and systematic error on input strain were then characterized in the laboratory and the results indicated that a) the measurement precision error can be predicted using analyzer frequency resolution and the location determination error and b) the characteristics of the measurement systematic error can be described using the error to strain gradient curve. This is significant because for current data interpretation process, data quality is supposed to be constant along the fibre although the monitored strain

for most of the site cases is non-uniformly distributed, which is verified in this thesis leading to a varying data quality. A novel data quality quantification method is therefore proposed as a function of the measured strain shape.

Although BOTDR has been extensively applied in infrastructure monitoring in the past decade, their data interpretation has been proven to be nontrivial, due to the nature of field monitoring. Based on the measurement precision and systematic error characterization results, a novel data interpretation methodology is constructed using the regularization decomposing method, taking advantages of the measured data quality. Experimental results indicate that this algorithm can be applied to various strain shapes and levels, and the accuracy of the reconstructed strain can be greatly improved. The developed algorithm is finally applied to real site applications where BOTDR sensing cables were implemented in two load bearing piles to monitor the construction loading and ground heaving processes.

# Table of contents

<b>List of figures</b>	<b>xv</b>
<b>List of tables</b>	<b>xxv</b>
<b>Nomenclature</b>	<b>xxvii</b>
<b>1 Introduction</b>	<b>1</b>
1.1 Motivation . . . . .	3
1.2 Aims and objectives . . . . .	3
1.3 Report layout . . . . .	4
<b>2 Literature review</b>	<b>7</b>
2.1 Distributed fibre sensors . . . . .	7
2.1.1 Sensing principle . . . . .	8
2.1.2 Modelling spontaneous Brillouin scattering . . . . .	15
2.1.3 Sensing cable . . . . .	19
2.1.4 Sensing analyzer . . . . .	24
2.2 Measurement error . . . . .	26
2.2.1 Precision and accuracy issues in geotechnical monitoring applications	26
2.2.2 Measurement precision error . . . . .	29
2.2.3 Systematic error . . . . .	34
2.3 Data interpretation . . . . .	39
2.3.1 Conversional coefficients calibration . . . . .	40
2.3.2 De-noising . . . . .	40
2.3.3 Deconvolution . . . . .	42
2.3.4 Spectrum deconvolution . . . . .	45
2.4 Summary . . . . .	46

<b>3</b>	<b>Sensor Calibration</b>	<b>49</b>
3.1	Optical fibre characterization . . . . .	50
3.1.1	Fibre diameter effect characterization . . . . .	50
3.1.2	Polarization effect characterization . . . . .	56
3.1.3	Cable jacket effect characterization . . . . .	57
3.2	Strain calibration . . . . .	59
3.2.1	Strain calibration unit . . . . .	59
3.2.2	Strain tests . . . . .	63
3.3	Temperature calibration . . . . .	71
3.3.1	Temperature calibration unit . . . . .	71
3.3.2	Temperature tests . . . . .	72
3.4	Summary . . . . .	82
<b>4</b>	<b>Spontaneous Brillouin spectrum model</b>	<b>83</b>
4.1	Theoretical analysis . . . . .	83
4.1.1	Pulse simulation . . . . .	84
4.1.2	Brillouin scattering simulation . . . . .	86
4.1.3	Analyzer signal process simulation . . . . .	87
4.2	Simulation results . . . . .	89
4.2.1	STFT simulation . . . . .	90
4.2.2	Weighted average simulation . . . . .	92
4.3	Model verification . . . . .	98
4.3.1	Brillouin spectrum verification . . . . .	98
4.3.2	Strain measurement verification . . . . .	100
4.4	Parametric studies . . . . .	103
4.4.1	Cable parameters . . . . .	103
4.4.2	Analyser parameters . . . . .	105
4.5	Summary . . . . .	107
<b>5</b>	<b>Precision error</b>	<b>109</b>
5.1	Example of on site measurement precision error . . . . .	110
5.1.1	Newfoundland pile site . . . . .	110
5.1.2	National Grid tunnel site . . . . .	113
5.1.3	Precision error characteristics . . . . .	116
5.2	Precision error origin . . . . .	118
5.2.1	Frequency resolution . . . . .	120
5.2.2	Distance resolution . . . . .	121

---

5.3	Experimental verification . . . . .	123
5.3.1	Frequency resolution . . . . .	123
5.3.2	Distance resolution . . . . .	124
5.4	Precision error simulation . . . . .	125
5.4.1	Simulation methodology . . . . .	126
5.4.2	Experimental verification . . . . .	127
5.5	Precision error prediction . . . . .	130
5.5.1	Prediction methodology . . . . .	130
5.5.2	Experimental results . . . . .	131
5.5.3	Frequency resolution induced strain imprecision . . . . .	132
5.5.4	Distance resolution induced strain imprecision . . . . .	133
5.5.5	Precision error calculation . . . . .	135
5.6	Precision error correction . . . . .	135
5.6.1	Precision error correction method . . . . .	136
5.6.2	Test verification . . . . .	137
5.7	Summary . . . . .	141
<b>6</b>	<b>Systematic error</b>	<b>143</b>
6.1	Problem formulation . . . . .	144
6.2	Systematic error characterization . . . . .	145
6.2.1	Step strain change . . . . .	145
6.2.2	Slope strain change . . . . .	147
6.2.3	Systematic error-strain gradient curve . . . . .	148
6.3	Data interpretation . . . . .	150
6.3.1	Estimation of the spectrum power . . . . .	150
6.3.2	Data reliability . . . . .	152
6.3.3	Algorithm characterization . . . . .	154
6.4	Test case . . . . .	156
6.4.1	Strain reconstruction . . . . .	158
6.4.2	Strain increment calculation . . . . .	161
6.4.3	Systematic error compensation . . . . .	163
6.5	Summary . . . . .	166
<b>7</b>	<b>Case studies</b>	<b>167</b>
7.1	Data interpretation flow chart . . . . .	167
7.2	WOO case study . . . . .	170
7.2.1	Precision error prediction . . . . .	171

---

7.2.2	Data interpretation . . . . .	175
7.2.3	Raw strain increment . . . . .	175
7.2.4	Interpreted strain increment . . . . .	177
7.2.5	Data filtering . . . . .	180
7.3	Newfoundland case study . . . . .	182
7.3.1	Precision error prediction . . . . .	182
7.3.2	Data interpretation . . . . .	185
7.3.3	Raw strain increment . . . . .	186
7.3.4	Interpreted strain increment . . . . .	188
7.3.5	Data filtering . . . . .	189
7.4	Summary . . . . .	191
<b>8</b>	<b>Conclusions</b>	<b>193</b>
8.1	Summary of thesis and important findings . . . . .	193
8.1.1	Sensor calibration . . . . .	193
8.1.2	Spontaneous Brillouin optical model . . . . .	194
8.1.3	Error characterization . . . . .	195
8.1.4	Data interpretation methodology . . . . .	196
8.1.5	Field monitoring . . . . .	196
8.2	Future work . . . . .	196
8.2.1	Analyzer characterization . . . . .	197
8.2.2	Cable development . . . . .	197
8.2.3	Strain reconstruction algorithm . . . . .	197
	<b>References</b>	<b>199</b>

# List of figures

2.1	Principle of backscattered light in an optical fibre . . . . .	9
2.2	Raman scattering, Brillouin scattering and Rayleigh scattering . . . . .	9
2.3	The dependency of Brillouin gain spectrum on (a) strain and (b) temperature [94] . . . . .	13
2.4	Illustration of the Brillouin signal as an integration of the signal generated at different parts of the pulse [81] . . . . .	15
2.5	Dimension of a typical single mode fibre . . . . .	20
2.6	Illustration of the Fujikura reinforced strain sensing cable . . . . .	21
2.7	Illustration of the SMC3 strain sensing cable . . . . .	21
2.8	Illustration of the temperature sensing cable . . . . .	23
2.9	Illustration of the SMC2 simultaneous strain and temperature sensing cable	23
2.10	Data quality of the measured result along the sensing cable length [27] . . . . .	27
2.11	Cable deployment on concrete segments of a tunnel ring [14] . . . . .	28
2.12	The movements measured from the vibrating-wire strain gauges and the distributed optical fibre sensor at (a) superficial sections and (b) deeper sections [14] . . . . .	29
2.13	Strain measurement results of the distributed fibre optics sensor, vibrating-wire strain gauges and extensometers of the pile [79] . . . . .	30
2.14	Theoretical calculated and analyzer measured frequency resolution obtained at different numbers of averages for a 25 km length cable [78] . . . . .	33
2.15	(a) Frequency resolution curves for two orthogonal probe input state of polarizations (SOPs) measured over three days (b) Frequency resolution over distance (c) Frequency resolution curves for the scrambled probe input SOP measured over three days (d) Frequency resolution over distance [84] . . . . .	33
2.16	Illustration of double peaks in one received Brillouin spectrum [70] . . . . .	35

2.17	Diagram showing the borderline between single peak and two peaks regions (dashed curve), and the curve representing the induced strain as a function of the normalized section length (plain curve) [71] . . . . .	36
2.18	Strain reading obtained from the analyzer measurement and the weighted averaging calculation [38] . . . . .	37
2.19	The slippage of the cable inside the protection layer at different input strain levels [33] . . . . .	38
2.20	Data quality of the simultaneous strain and temperature measurement along the sensing cable length for the RCC Dam [27] . . . . .	39
2.21	Strain calibration beam [33] . . . . .	40
2.22	Picture of the water tank for temperature calibration [51] . . . . .	41
2.23	Illustration of wavelet decomposition [26] . . . . .	41
2.24	Raw data (left) and wavelet-denoised data (right) of the distributed force readings under different loadings [26] . . . . .	42
2.25	Raw strain measurement, real strain input and de-convoluted strain measurement along cable length [14] . . . . .	43
2.26	The reconstructed strain results with using data weight values (black lines) and without using data weight values (grey lines) for a point loaded plane [65]	44
2.27	Illustration of the Brillouin spectrum at strained and unstrained sections as well as analyzer measurement [91] . . . . .	45
2.28	Dependence of $RE$ (measurement relative error) on $r$ (ratio of strained length to spatial resolution) in different $\varepsilon_{NA}$ (normalized strain input) [91] . . . . .	46
3.1	Brillouin centre frequency measurement (with precision error shown as grey error bar) of fibre (a) which has $4.2 \mu m$ core and $125 \mu m$ cladding diameter	51
3.2	Brillouin centre frequency measurement (with precision error shown as grey error bar) of fibre (b) which has $6.4 \mu m$ core and $125 \mu m$ cladding diameter	51
3.3	Brillouin centre frequency measurement (with precision error shown as grey error bar) of fibre (c) which has $6.4 \mu m$ core and $85 \mu m$ cladding diameter .	52
3.4	Brillouin centre frequency measurement (with precision error shown as grey error bar) of fibre (d) which has $7.8 \mu m$ core and $125 \mu m$ cladding diameter	52
3.5	The histogram of strain precision error obtained along fibre (a) which has $4.2 \mu m$ core and $125 \mu m$ cladding diameter . . . . .	53
3.6	The histogram of strain precision error obtained along fibre (a) which has $6.4 \mu m$ core and $125 \mu m$ cladding diameter . . . . .	54
3.7	The histogram of strain precision error obtained along fibre (a) which has $6.4 \mu m$ core and $80 \mu m$ cladding diameter . . . . .	54

---

3.8	The histogram of strain precision error obtained along fibre (a) which has 7.8 $\mu m$ core and 125 $\mu m$ cladding diameter . . . . .	55
3.9	Strain measurements of a single mode fibre and a polarization maintaining fibre using analyzer (a) AQ8603 and (b) NBX5000 . . . . .	57
3.10	Brillouin centre frequency measurement of the strain sensing cable and the single mode fibre . . . . .	58
3.11	Measurement precision error of the strain sensing cable and the single mode fibre . . . . .	59
3.12	Picture of the strain calibration beam . . . . .	60
3.13	Simulated deflection of the clamp with 100 $N$ axial force applied . . . . .	61
3.14	Simulated stress of the clamp with 100 $N$ axial force applied . . . . .	61
3.15	Simulated deflection of the clamp with 500 $N$ force applied to one side of the clamp . . . . .	62
3.16	Simulated stress of the clamp with 500 $N$ force applied to one side of the clamp . . . . .	62
3.17	The analyzer measured strain of the Fujikura reinforced cable which was stretched for 1.5 $m$ at different strain levels . . . . .	65
3.18	The analyzer measured strain of the Brugg cable which was stretched for 1.5 $m$ at different strain levels . . . . .	65
3.19	The analyzer measured strain of the the Tight buffer telecomm which was stretched for 1.5 $m$ at different strain levels . . . . .	66
3.20	The analyzer measured strain of the Nanzee reinforced cable cable which was stretched for 1.5 $m$ at different strain levels . . . . .	66
3.21	The relationship between the analyzer measured strain and the input strain with measurement standard deviation as error bars for the Fujikura reinforced cable . . . . .	67
3.22	The relationship between the analyzer measured strain and the input strain with measurement standard deviation as error bars for the Brugg cable . . . . .	68
3.23	The relationship between the analyzer measured strain and the input strain with measurement standard deviation as error bars for the Tight buffer telecomm cable . . . . .	68
3.24	The relationship between the analyzer measured strain and the input strain with measurement standard deviation as error bars for the Nanzee reinforced cable . . . . .	69
3.25	Measurement residuals for the fitted linear curves of the analyzer measured strain and the input strain . . . . .	69

3.26	Standard deviation of measurements over the length of 1 m effective length with cables and readings made three times . . . . .	70
3.27	Temperature calibration bench of a water bath . . . . .	72
3.28	Repeated Brillouin centre frequency measurement in GHz for the temperature sensing cable . . . . .	74
3.29	Repeated Brillouin centre frequency measurement in GHz for the strain sensing cable . . . . .	74
3.30	The analyzer measured temperature readings of the temperature sensing cable during first the heating and then the cooling process in steps of 5 °C .	76
3.31	The analyzer measured temperature readings of the strain sensing cable during first the heating and then the cooling process in steps of 5 °C . . . . .	76
3.32	The linearity between analyzer measured temperature and input temperature for a) strain cable and b) temperature cable . . . . .	77
3.33	The linearity between measured temperature and input temperature for continuous three heating-cooling cycles . . . . .	79
3.34	Measurement error between the analyzer measured temperature and the real temperature during three heating and cooling cycles . . . . .	80
3.35	Measurement hysteresis test results for the temperature cable with jacket . .	81
3.36	Measurement hysteresis test results for the bare fibre . . . . .	81
4.1	Schematic diagram of the simulation process . . . . .	84
4.2	Graphically illustration of a squared pulse(black line) with rising/falling time of $\Delta\tau$ and a pulse width of $\tau$ . . . . .	85
4.3	Generation of a Brillouin spectrum from a pulsed light [59] . . . . .	86
4.4	Illustration of intrinsic Brillouin spectra for a step strain change . . . . .	88
4.5	Illustration of analyzer received Brillouin spectra for a step strain change . .	88
4.6	Comparison of the analyzer injected pulse and the modelled pulse . . . . .	90
4.7	Simulation result of a step change of 1000 $\mu\epsilon$ at different number of averages with 128 window size . . . . .	91
4.8	Simulation result of a step change of 1000 $\mu\epsilon$ at different number of averages with 512 window size . . . . .	91
4.9	Graphical illustration of the convolution between natural Brillouin spectrum and the weight function . . . . .	92
4.10	Simulated best fitting weight function for different strain input levels and the average fit line for the weight functions . . . . .	94
4.11	Repeated Brillouin spectrum measurements at one point of the free-strained cable . . . . .	95

---

4.12	Illustration of the peak and standard deviation of power measurements at all locations of the tested fibre . . . . .	95
4.13	Histogram of normalized power readings at a frequency level of $10.86\text{ GHz}$ . . . . .	96
4.14	The dependency of the repeated power measurements distribution bandwidth on power level . . . . .	97
4.15	The fitting between the analyzer measurements of the the tested strain cable with the previously characterized power fluctuation curve . . . . .	98
4.16	Comparison of the measured Brillouin gain spectrum and the simulated Brillouin gain spectrum . . . . .	99
4.17	Comparison of the analyzer measured repeated strain and the simulated repeated strain . . . . .	100
4.18	Comparison of the simulated results and the analyzer measured results at different strain input levels . . . . .	101
4.19	Comparison of the strain measurement obtained from analyzer and the simulated strain result at different strained section lengths . . . . .	102
4.20	The simulated strain fluctuation along the optical fibre of $20\text{ km}$ length . . . . .	104
4.21	The simulated strain precision along the optical fibre of $20\text{ km}$ length at different attenuation levels . . . . .	105
4.22	Comparison of the dependence of precision error on SNR in model simulation and equation calculation results . . . . .	106
4.23	Comparison of the dependence of precision error on scanning frequency step in model simulation and equation calculation results . . . . .	107
4.24	Comparison of the dependence of precision error on Brillouin linewidth in model simulation and equation calculation results . . . . .	108
5.1	Structural pile layout and fibre optic instrumentation in Newfoundland . . . . .	111
5.2	Variation of the measured Brillouin centre frequency over time for (a) temperature sensor and (b) strain sensor for Newfoundland pile . . . . .	112
5.3	Longitudinal temperature measurement at different stages of the concrete curing process in Newfoundland pile site[15] . . . . .	114
5.4	Analyzer measured strain, strain gradient and measurement precision error profile along the Newfoundland pile . . . . .	115
5.5	Schematic graph of the national grid tunnel segments and fibre optic cable instrumentation . . . . .	116
5.6	Strain variation over data collection period for both of (a) temperature sensor and (b) strain sensor in National Grid tunnel segments . . . . .	117

5.7	Profiles of strain, strain gradient and measurement precision error in National Grid tunnel segments . . . . .	118
5.8	Measurement fluctuation over distance for (a) temperature sensor and (b) strain sensor in National Grid tunnel segments . . . . .	119
5.9	Variation between strain gradient and measurement precision error . . . . .	120
5.10	The influence of frequency resolution on strain measurement precision for Brillouin optical time domain system . . . . .	121
5.11	The influence of distance error on strain measurement precision for Brillouin optical time domain system . . . . .	122
5.12	The comparison of Brillouin spectrum at a uniformly strained section, unstrained section and strain transit section . . . . .	124
5.13	Comparison of two repeated Brillouin spectrum measurements . . . . .	125
5.14	Comparison of two repeated Brillouin centre frequency measurements along the tested cable . . . . .	126
5.15	Comparison of the simulated Brillouin spectrum (upper figure) and the analyzer measured Brillouin spectrum (lower figure) . . . . .	128
5.16	Comparison of the simulated strain and the analyzer measured strain for a step strain change input . . . . .	129
5.17	Comparison of the simulated precision error and the analyzer measured precision error for a step strain change input . . . . .	129
5.18	The relationship between distance resolution and precision error . . . . .	131
5.19	Analyser measured strain, strain gradient, SNR and bandwidth of the measured Brillouin spectrum, and measurement precision of a step strain change . . . . .	132
5.20	Comparison of the predicted frequency resolution induced precision error and the analyzer measured precision error . . . . .	133
5.21	Comparison of the predicted distance resolution induced precision error and the analyzer measured precision error . . . . .	134
5.22	Comparison of the predicted precision error and the analyzer measured precision error at the strain change section . . . . .	135
5.23	Illustration of distance resolution induced precision error correction method . . . . .	137
5.24	Illustration of the bending beam test set up . . . . .	138
5.25	Illustration of three bending cases for the precision error correction method verification experiments . . . . .	139
5.26	Analyser measured strain and the corresponding precision error for three bending beam cases . . . . .	139
5.27	Illustration of precision error, strain gradient, spectrum bandwidth and gain . . . . .	140

---

5.28	Effects of the precision error compensation methods . . . . .	141
6.1	The weighted average process of the analyzer measured strain compared to the true strain [14] . . . . .	144
6.2	Comparison of the simulated strain results and the real strain inputs for step strain change . . . . .	145
6.3	Systematic error to strain gradient curve for a step strain input at three different strain input levels . . . . .	146
6.4	The strain results simulated with the calibrated weight function of the one metre spatial resolution analyzer . . . . .	147
6.5	Error to strain gradient curve for a slope strain input at different slope levels and lengths . . . . .	148
6.6	The normalized systematic error to strain gradient curve for sloping strain change . . . . .	149
6.7	Profile of a step strain followed by a polynomial strain change shape and the normalized data reliability index . . . . .	153
6.8	Illustration of the simulated reconstructed strain using the data interpretation algorithm a) considering data reliability and b) without considering data reliability . . . . .	154
6.9	The simulated accuracy of the data interpretation algorithm as a function of strained section length at three strain levels for step strain . . . . .	155
6.10	Diagram showing the borderline between good results and bad results regions, and the curve representing the normalized algorithm error as a function of the strained section length . . . . .	156
6.11	Graphical illustration of the test set up and expected strain change of the cable	157
6.12	Measured strain profile and its weight index profile . . . . .	158
6.13	Analyser measured Brillouin power in the lab test . . . . .	159
6.14	Back calculated Brillouin power in the lab test . . . . .	160
6.15	The analyzer measured Brillouin spectrum and back calculated decomposed spectrum . . . . .	160
6.16	Reconstructed strain using the back calculation method with a connected step shape input strain . . . . .	161
6.17	BOTDR measurements of the tested cable with a non-uniform pre-strain distribution . . . . .	162
6.18	Strain increment calculation along the tested cable . . . . .	163
6.19	Back calculated strain measurements using the reconstruction algorithm . .	164
6.20	Compensated strain increment along the tested cable . . . . .	165

7.1	The flow chart of the data interpretation methodology . . . . .	169
7.2	The analyzer measured result including strain, peak power and bandwidth of the Brillouin spectrum, strain gradient and precision error . . . . .	172
7.3	The comparison of the analyzer measured precision error and the frequency resolution induced error calculated from the SNR and bandwidth of the Brillouin spectrum . . . . .	172
7.4	The comparison of the analyzer measured precision error and the distance resolution induced error calculated from the calibrated timing error of the analyzer . . . . .	173
7.5	The comparison of the analyzer measured precision error and the predicted precision error which is the combining effect of distance error and frequency resolution . . . . .	174
7.6	The illustration of the agreement between the analyzer measured precision error and the simulated precision error . . . . .	174
7.7	Analysers measurement of the Fujikura strain sensing cable as well as the Brugg strain sensing cable for the WOO pile load test . . . . .	176
7.8	The raw strain increment results of the adjacently installed Fujikura and Brugg cables during the WOO pile loading test . . . . .	177
7.9	The illustration of the data interpretation section (shown as grey lines) which is determined by the data weight profile for the Newfoundland pile load test . . . . .	178
7.10	The interpreted strain increment results after horizontal shift treatment for the adjacently installed Fujikura and Brugg cables during the WOO pile loading test . . . . .	179
7.11	The interpreted strain increment results after horizontal shift and filtering interpretation processes for the adjacently installed Fujikura and Brugg cables during the WOO pile loading test . . . . .	181
7.12	Analysers measured strain, Brillouin peak power, strain gradient and measurement precision error profile along the pile . . . . .	183
7.13	Comparison of the predicted frequency resolution induced error obtained from analyzer measured Brillouin peak power information and the analyzer measured precision in Newfoundland pile site . . . . .	183
7.14	Comparison of the predicted distance resolution induced error and the analyzer measured precision at the Newfoundland pile site . . . . .	184
7.15	Comparison of the analyzer measured precision error and the predicted precision error at the Newfoundland pile site . . . . .	185

---

7.16	The linearity between the analyzer measured precision error versus the predicted precision error. . . . .	186
7.17	The Brillouin frequency shift measurements along the tested cable during the Newfoundland pile load test . . . . .	187
7.18	The raw strain increment results along the cable during the Newfoundland pile load test . . . . .	187
7.19	The illustration of the data interpretation section (shown as grey lines) which was determined by the data weight profile for the Newfoundland pile load test	188
7.20	The interpreted strain increment results along the cable after horizontal shift treatment during the Newfoundland pile load test . . . . .	189
7.21	The interpreted strain increment results along the cable after filtering treatment during the Newfoundland pile load test . . . . .	190



# List of tables

2.1	Comparison of different analyzers . . . . .	25
2.2	Influence of averaging times on measurement precision . . . . .	31
3.1	Core and cladding diameters of the tested single mode fibres . . . . .	50
3.2	The mean Brillouin centre frequency, frequency precision error, and equivalent strain error of the 100 repeated measurements for the four tested fibres .	55
3.3	Illustration of four strain sensing cables . . . . .	63
3.4	Comparison of different strain sensing cables . . . . .	71
3.5	Illustration of the tested cables for temperature tests . . . . .	73
3.6	Measurement precision at different temperature levels for strain and temperature sensing cable . . . . .	75
3.7	Measurement fluctuation over the tested cable length during the heating and cooling processes for the strain and temperature sensing cables . . . . .	78
3.8	Measurement accuracy during heating and cooling process for the strain and the temperature sensing cable . . . . .	78
4.1	Key parameters of the injected pulse characterized by NBX5000 analyzer .	90
4.2	Detailed description and graphically illustration of the analyzer parameters .	103
7.1	The construction process of the WOO site . . . . .	170
7.2	Comparison of strain increment fluctuations with or without using the horizontal shift interpretation method under different loading conditions for the Fujikura cable and the Brugg cable . . . . .	180
7.3	Comparison of the smoothing parameter effect on the filtered results . . . .	181
7.4	Comparison of strain increment fluctuations with or without using the horizontal shift interpretation method under different loading conditions for the Fujikura cable at the Newfoundland pile site . . . . .	190



# Nomenclature

## Greek Symbols

$\Delta\tau$  pulse rising and falling time

$\Gamma_1$  phonon damping rate

$\tau$  pulse length

$\varphi$  frequency scanning step

$\alpha$  fibre loss coefficient

$\varepsilon$  strain

$\lambda$  wavelength

## Other Symbols

$E$  wave amplitude

$I$  pulse intensity

$L_s$  spatial resolution

$P$  power

$w$  bandwidth

$C_\varepsilon$  strain coefficient

$C_T$  temperature coefficient

$\varepsilon$  strain

$T$  temperature

$c_0$	light velocity in vacuum
$n$	refractive index
$t$	time
$v_a$	sound velocity
$z$	distance
$\Delta\nu$	full linewidth at half maximum of the spectrum
$g_B$	Brillouin gain spectrum
$g_o$	Brillouin gain coefficient
$\nu$	frequency
$\nu_B$	Brillouin frequency shift

**Acronyms / Abbreviations**

ER	extinction ratio
STFT	short time Fourier transform
BEDS	Brillouin echo-distributed sensing
BGS	Brillouin gain spectrum
BOCDR	Brillouin Optical Correlation Domain Reflectometry
BOFDA	Brillouin Optical Frequency Domain Analysis
BOTDA	Brillouin Optical Time Domain Analyser
BOTDA	Brillouin Optical Time Domain Analyzer
BOTDR	Brillouin Optical Time Domain Reflectometry
BOTDR	Brillouin Optical Time Domain Reflectometry
CW	continuous wave
DFOS	distributed fibre optics sensor
EDFA	Erbium-doped Fibre Amplifiers

FWHM full width at half maximum

SNR signal to noise ratio

BSM bare single mode

PMF polarization maintaining fibre

SMF single mode fibre

TSM tight-buffered single mode

RCC roller compacted concrete

VWSG vibrating-wire strain gauges



# Chapter 1

## Introduction

Structural health monitoring (SHM) provides information about the status of civil engineering infrastructures and its long-term evolution by continuously or periodically measuring the structural response to loading and environmental changes such as stress, strain, and temperature. Using a proper infrastructure monitoring technology, anomalies in structural behaviour and performance can be detected. In this way, will the structural safety be enhanced and its service life be extended, eventually resulting in cost reductions.

Distributed fibre optic sensor (DFOS) based on Brillouin backscattering technology has many attractive properties such as small in size, good structural compatibility, lightweight, and immune to electromagnetic interference, etc. Traditional monitoring sensors, such as strain gauges, often require many cables to support them. The cable management cost limits the suitability of traditional sensor monitoring. However, the distributed fibre optic sensor is capable of measuring strain at every point along a standard optical cable, meaning that a suitably installed fibre can potentially replace many traditional point sensors. It has therefore received wide acceptance as a cost-effective sensing tool.

The distributed Brillouin fibre optics sensor has achieved wide acceptance in structural health monitoring. It offers distributed deformation measurements for large critical infrastructures such as bridges, tunnels, dams, and nuclear plants. It detects the development of cracks in structures by measuring highly localized strain. In addition to enhancing the safety of structures, fibre optic sensing technology can extend infrastructure life through proper system management and preventive maintenance. With fibre optic sensors embedded, performance-based design and maintenance for smart construction processes can come true.

The basic principle behind this novel distributed Brillouin optical fibre sensor is the interaction of the photon light wave with the characteristic density variation of the fibre itself, which is also called acoustic wave. The fibre acoustic wave is affected by the strain and temperature condition, shifting the centre frequency of the backscattered Brillouin light.

In other words, when the analyzer launches light into the fibre, the backscattered Brillouin light will have a centre frequency shift, extent of which is dependent on fibre strain and temperature. In this way, this Brillouin fibre optic sensor measures strain and temperature at any point along the cable.

The data analysis of the distributed strain/temperature data obtained in the field is sometimes not easy because of unavoidable measurement errors. It has been stated that the sensor measurement for a crack represents a considerable error in strain width and level determination [71]. Experimental results reveal that a beam with a small defect has a much more significant variation in strain profile readings over the whole beam compared to a non-damaged beam [7]. There are two sources for measurement uncertainty: one is systematic error due to the measurand, and the other is precision error introduced by the measuring system [56]. A better understanding of these measurement error is required to perform robust data interpretation.

The distributed Brillouin fibre optics sensor measurement precision error is the variation of the Brillouin peak frequency with time. It can be calculated as the standard deviation of the repeated measurement values. It is observed that the distributed Brillouin fibre optics sensor measurement has a larger precision error at points of cable fixation, splice connections, and at places with local losses [27]. Variables that influence precision error, such as Brillouin gain linewidth, frequency scanning step, and signal-to-noise ratio have been theoretically and experimentally investigated. A novel expression to predict measurement precision error has been derived [78]. In addition, Brillouin linewidth and peak frequency are varied with lightwave state of polarization due to the fact that fibre birefringence and sound velocity variation cause broadening and asymmetry of the Brillouin gain spectrum. This limits the sensing frequency resolution of the distributed fibre Brillouin sensor, and enlarges the precision error of the central frequency measurement [84].

The difference between the measured strain and real strain quantifies the systematic error. Due to the limit of pulse length, the measured Brillouin spectrum is a superposition of all spectrum components having different peak frequencies within the analyzer's pulse length [91]. The deviated fitting of the peak frequency of the deformed Brillouin spectrum leads to measurement systematic error. To characterize the superposition of the backscattered Brillouin spectrum, the sensing mechanism is simplified as a two dimensional convolution of the intrinsic Brillouin Lorentzian distribution and the launched pulse power with respect to time and frequency [49]. It is then obtained that a distributed Brillouin fibre optics sensor measured strain profile can be seen as a convolution product between the true strain profile and a weighting function of the analyzer [38]. Using that, the distributed strain measurement

could be corrected back to the original strain input, effectively minimizing the measurement systematic error [14].

Based on observations of the distributed temperature/strain data obtained from the field, this dissertation provides a detailed discussion on Brillouin precision and systematic error, and develops a novel data interpretation algorithm based on the characterized relationships between spatial variation in temperature/strain and Brillouin sensing error using a Brillouin Optical Time Domain Reflectometry (BOTDR). The Brillouin sensing error is first characterised using a novel calibration bench which is developed in the laboratory to accurately control the strain/temperature condition of the sensor. The systematic error and precision error of BOTDR are examined through an optics model which simulates the fundamental process of Brillouin scattering and experimental results of different shapes of strain input. A novel data interpretation algorithm which takes into consideration of the characteristics of Brillouin sensing error is finally developed and applied to field cases.

## 1.1 Motivation

Although BOTDR sensor has been recently applied to many infrastructure monitoring and infrastructure construction projects for strain and temperature monitoring, the reliability of sensor measurement results has not yet been thoroughly investigated. In most previous studies of structural monitoring using BOTDR, the structural conditions are directly evaluated from the acquired strain distributions, where unexpected data fluctuations are observed and the accuracy of strain and temperature measurement appears to degrade. The quality of the distributed Brillouin fibre optics sensor data values including systematic error and precision error needs to be investigated theoretically and experimentally.

Obtaining sensing error characteristics, the data analysis process has to be improved. Currently this process does not include much work towards error compensation. Without properly considering measurement error, engineers who use this technology will not be able to give a reliable interpretation of the infrastructure monitoring results. Therefore this research develops a novel data interpretation process that considers the reliability of the Brillouin fibre optics sensor measurement.

## 1.2 Aims and objectives

The following describes the aims of this research:

1. To construct a calibration bench characterizing analyzer and cable sensing measurement error to a high accuracy. This bench has a temperature constant circumstance for strain calibration, and a strain constant circumstance for temperature calibration.
2. To investigate the sensing efficiency of sensors. Sensitivity, accuracy, and precision of the existing analyzer and the newly developed analyzer are examined using the established calibration bench. Cable uniformity, level of strain transforming from the jacket to the core, slippage between cable different layers, and Brillouin conversional coefficient of cables are tested.
3. To establish an optics model for fundamentally simulating the Brillouin scattering process. The model is used to simulate the Brillouin 3D spectrum and to control measurement error by characterizing parameters that influence sensing precision through systematic use of the model. The relationship between sensor and sensing error is established.
4. To characterize Brillouin sensing measurement error. The precision error and systematic error of the measurement are investigated theoretically and experimentally. The origin, characteristics and compensation method of the error are established. The relationship between error and strain gradient is revealed, based on which an error prediction method is proposed.
5. To develop a novel data interpretation algorithm. The new algorithm reconstructs the strain considering the data uncertainty. Precision error and systematic error compensation methods are included to improve the reliability of the algorithm.

### **1.3 Report layout**

This thesis is composed of eight chapters. An overview of the following seven chapters is presented below:

*Chapter 2* is the literature review starting with the fundamentals of DFOS technology based on Brillouin backscattering. Currently available sensors are reviewed, including two analyzers, Brillouin optical time domain reflectometry (BOTDR) and Brillouin optical time domain analysis (BOTDA). Different types of sensing cables are compared with regard to their sensing accuracies. Methods to compensate errors are discussed. Some case studies are finally reviewed with a discussion of practical problems and issues.

**Chapter 3** introduces a novel calibration bench for strain and temperature controlling. This bench includes a water bath and an aluminum rig mounted with a linear stage to accurately change the temperature and strain condition of the tested cable sensor. The accuracy of both the water bath and aluminum rig is designed to be greater than  $10\mu\epsilon$  and  $0.5^{\circ}\text{C}$ . The calibration bench will be used to measure errors of the sensors in different strain/temperature conditions.

**Chapter 4** presents an optics model to simulate the backscattered Brillouin signal. The model exploits a weight function to simulate the convolution process of the analyzer and a characterized power fluctuation curve to represent the analyzer random noise. A cable with a step strain is tested and experimental results show that strain measurements at faster strain change sections have a larger precision error and systematic error. The characteristics of the measurement error and their dependency factors are investigated using the model.

**Chapter 5** investigates the characteristics of measurement precision error in non-uniformly distributed strain conditions using BOTDR sensor. The chapter describes the progress for precision error characterization. The precision error is investigated in two parts: analyzer frequency resolution, and distance resolution induced precision error. The origin and characteristics of the precision error are verified experimentally and theoretically. The relationships between precision error and strain gradient are revealed through laboratory results as well as field case measurements. A precision error compensation method using sectional shift is finally proposed.

**Chapter 6** discusses the measurement systematic error. A strain reconstruction algorithm is developed using the Brillouin spectrum back calculation method with consideration of the data reliability. The systematic error of the strain increment measurement is investigated and a compensation method is proposed. The reliability of the systematic error compensation method is verified through laboratory experiments.

**Chapter 7** analyses measurements obtained from two pile cases using the developed data interpretation algorithm. Strain measurement variation is minimized using the proposed algorithm, and the final results are interpreted considering the soil layers of the pile. Problems of the data analysis process are discussed based on the pile project.

**Chapter 8** summarizes the specific conclusions obtained so far.



# Chapter 2

## Literature review

Fibre optics sensing has long occupied a special role for structural health monitoring due to its advantages of lightweight, small in size, durable, easy to install and immune to electromagnetic interference. In comparison with conventional point-based sensors, fibre optics sensor provides distributed strain/temperature monitoring readings over large measurement ranges [57]. This chapter reviews the most general aspects of optical fibre sensing, including the basic principles of distributed optical fibre sensing technology, analytical mechanism of Brillouin scattering, a comparison of current available BOTDR sensing cables and analyzers, and measurement error analysis for BOTDR sensor. This chapter first looks at some fundamentals of optical fibre strain sensing technology including the basic physical principles of light and spontaneous Brillouin scattering model in optical fibres. The operating theory and some main parameters of Brillouin optical time domain analyzer are then reviewed. Some current available sensing cables and some established methods for sensor characterization are compared. The uncertainties of the measurement obtained by optical fibre instrumentation in geotechnical structures and their compensation methods are presented at the end of the chapter.

### 2.1 Distributed fibre sensors

Distributed fibre optic sensing (DFOS) has become a promising technology for large-scale strain and temperature monitoring in various engineering applications over the last decade, including oil and gas, and infrastructure industries [79][77][92]. Because of its sensitivity to local damage and unforeseen damage accumulation, DFOS has been installed in civil engineering structures to provide important information for structural maintenance and repair work. Unlike conventional sensors, such as strain gauges which measure point data and have to be installed in large numbers to exactly cover the damaged region, DFOS can monitor

strain all along the cable measuring points every  $0.05\text{ m}$  and over a length as long as several kilometres [4].

The merits of DFOS have led to the development of a suite of analyzer systems such as Brillouin Optical Time Domain Reflectometry (BOTDR) [37], Brillouin Optical Time Domain Analyser (BOTDA) [21], and Brillouin Optical Correlation Domain Reflectometry (BOCDR) [30]. The first spontaneous Brillouin optical time domain system was developed in Japan [29]. This was a single-ended system using a single laser to inject pulsed light into the fibre and to measure the backscattered Brillouin scattering light at the same end. The single-ended nature of this system and the distributed strain/temperature measurement made it attractive for many structural health monitoring applications [3][43][46]. However it was inevitable that the received signal is weak and the achievable spatial resolution and measurement accuracy is thus restricted. As the technology continuously developing, the highest measurement accuracy of an advanced system is now at the micro strain scale, and the highest spatial resolution can achieve  $0.01\text{ m}$  [47].

### 2.1.1 Sensing principle

The basic principle behind the distributed fibre sensor is that cable conditions such as a change of strain and temperature on the cable can influence the properties of the light signal travelling through an optics fibre [29]. Therefore, when light is launched into a sensing cable, the majority of the light travels through the cable, but a small fraction is backscattered and its properties are influenced by the fibre condition (Fig. 2.1). The backscattered light includes three types of scattering: Raman scattering, Brillouin scattering, and Rayleigh scattering (Fig. 2.2). Raman scattering comes from the interaction of light with the vibrational modes of the molecules in the scattering medium (optical phonons) [57]. Its intensity is temperature dependent and therefore can be used to monitor temperature. The interaction of light with the acoustic wave leads to Brillouin scattering [55]. The centre frequency of the backscattered Brillouin light is dependent on both temperature and strain. The scattering of light from material impurities results in Rayleigh scattering [41]. It does not induce frequency shift, and is the principle behind Optical Time Domain Reflectometry (OTDR).

The distributed fibre optics sensing technology discussed in this dissertation uses the phenomena of Brillouin backscattering to monitor strain and temperature. From the microscopic point of view, molecules in an optical fibre tend to stay at a stable separation distance from each other, as the intermolecular movement is a regular periodic fluctuation. This collective excitation of molecules generates acoustic wave. When light goes through an optical fibre, some of the acoustic phonon's energy is transferred and the backscattered light undergoes a frequency shift. The scattered light that lose energy corresponds to Stokes-type components,

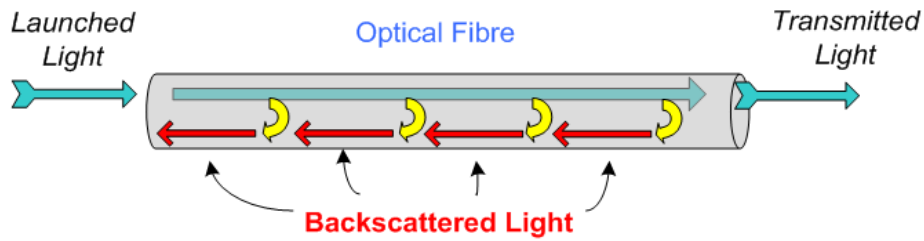


Fig. 2.1 Principle of backscattered light in an optical fibre

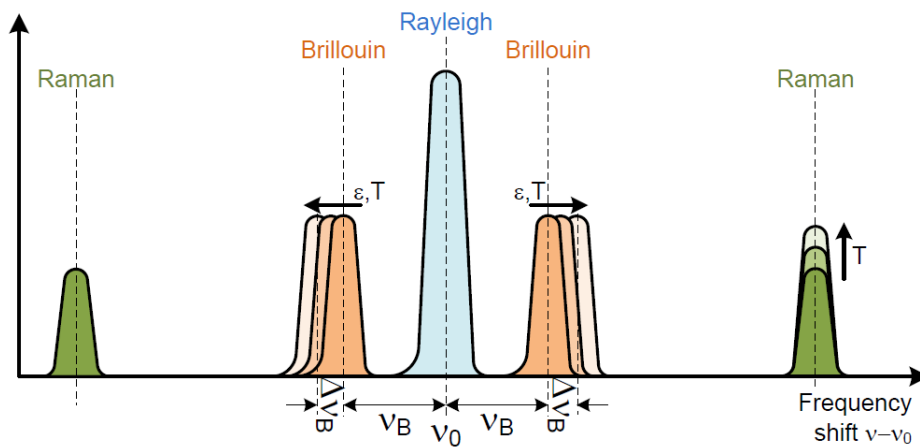


Fig. 2.2 Raman scattering, Brillouin scattering and Rayleigh scattering

and the frequency is down-shifted. On the other hand, anti-Stokes-type components imply a gain in scattered phonon energy with a corresponding up-shift in frequency [10].

The frequency shift of the Brillouin backscattered light is determined by the wave velocity of the acoustic phonon which is dependent on local pressure and the density of the fibre core [8]. The acoustic wave itself firstly induces a change to the local pressure and fibre density, leading to a frequency shift of the Brillouin backscattered light. Then the change of the strain and temperature condition further alters the fibre properties, thus causing an additional Brillouin frequency shift to the backscattered light [69]. Changes in strain and temperature can therefore be obtained by calculating the difference between the backscattered Brillouin frequency shift measured at different times.

The fibre's Brillouin frequency shift is proportional to the local velocity of the acoustic waves. For light with a wavelength  $r = 1.3 \mu m - 1.6 \mu m$  travelling through a standard single mode fibre, the frequency shift of the Brillouin backscattered light ( $v_B$ ) is in the range of  $9 GHz - 13 GHz$ , which is given by [4]:

$$v_B = \frac{2nv_a}{\lambda} \quad (2.1)$$

where  $n$  is the refractive index of the fibre core,  $v_a$  is the velocity of sound in glass and  $\lambda$  is the free-space wavelength.

Because the Brillouin frequency shift increases linearly with the strain and temperature of an optical fibre, Eq. 2.1 can be extended into the following form using the temperature and strain conversional coefficients ( $C_\varepsilon$  and  $C_T$ ).

$$v_B(z) = v_{B0}(z) + C_\varepsilon \varepsilon(z) + C_T T(z) \quad (2.2)$$

where  $v_B(z)$  is the Brillouin frequency shift at location  $z$ ,  $v_{B0}(z)$  is the original Brillouin frequency shift,  $\varepsilon(z)$  is the strain change, and  $T(z)$  is the temperature change.

The location  $z$  where Brillouin backscattering happens is determined as a function of time  $t$  with known light velocity  $c_0$  in a vacuum (Equation 2.3).

$$z = \frac{c_0 t}{2n} \quad (2.3)$$

The distributed strain profile of the fibre can then be reconstructed by resolving the Brillouin backscattered light in both the time and frequency domains. The precision of the location determination depends on the accuracy of the cable distance mapping and cable-lay loss of the fibre [67].

### Conversional coefficients

The frequency shift of the backscattered Brillouin spectrum is simultaneously sensitive to temperature and strain in the fibre. To distinguish them, a strain sensing cable and a temperature sensing cable are usually placed adjacent to each other for different measurements. The temperature cable consists of a loose buffered fibre to isolate strain effects, and the strain cable contains a tight buffered fibre to efficiently transfer external strain to the fibre inside.

$C_\varepsilon$  and  $C_T$  in Eq. 2.2 are parameters that depend on the properties of the sensing cable. They can be calibrated in the lab by precisely changing the strain and temperature conditions of the sensor and using Eq. 2.4- 2.5. Experimental results indicates that  $C_\varepsilon$  varies in a range of  $0.0483\text{MHz}/\mu\varepsilon - 0.058\text{MHz}/\mu\varepsilon$  and  $C_T$  in a range of  $1.17\text{MHz}/^\circ\text{C} - 1.59\text{MHz}/^\circ\text{C}$ , depending on the thermal expansion parameter of the fibre coating material [52].

$$C_\varepsilon = \frac{v_B(\varepsilon) - v_B(\varepsilon_0)}{\varepsilon - \varepsilon_0} \quad (2.4)$$

where  $v_B(\varepsilon_0)$  is the original Brillouin frequency shift,  $v_B(\varepsilon)$  is the Brillouin frequency shift after strain change,  $\varepsilon_0$  is the original strain condition of the cable and  $\varepsilon$  is the cable's final strain condition.

$$C_T = \frac{v_B(T) - v_B(T_0)}{T - T_0} \quad (2.5)$$

where  $v_B(T_0)$  is the original Brillouin frequency shift,  $v_B(T)$  is the Brillouin frequency shift after temperature change,  $T_0$  is the original temperature condition of the cable, and  $T$  is the cable's final temperature condition.

The conversional coefficients and their accuracies vary with temperature and strain levels. Previous experimental results indicates that  $C_T$  linearly decreases from  $1.113\text{MHz}/^\circ\text{C}$  to  $0.830\text{MHz}/^\circ\text{C}$  in the range of  $22^\circ\text{C} - 800^\circ\text{C}$  [6]. The measurement accuracy and precision are  $\pm 2.6^\circ\text{C}$  and  $\pm 5.5^\circ\text{C}$ , respectively.  $C_\varepsilon$  linearly decreases from  $0.054\text{MHz}/\mu\varepsilon$  to  $0.042\text{MHz}/\mu\varepsilon$  in the range of  $22^\circ\text{C} - 700^\circ\text{C}$  [6]. The measurement accuracy and precision are  $\pm 45\mu\varepsilon$  and  $\pm 76\mu\varepsilon$ , respectively. At  $800^\circ\text{C}$ , creep becomes significant, thus reducing the strain sensing precision. During the whole heating-cooling cycles or continuous heating processes, the sensors are stable up to  $800^\circ\text{C}$ .

### Brillouin spectrum

The frequency shift of the backscattered Brillouin light is in the order of  $10\text{ GHz}$  for silica at  $1550\text{ nm}$  and the gain spectrum ( $g_B(\nu)$ ) was shown to be Lorentzian-shaped [73]:

$$g_B(\nu) = \frac{g_0 \Delta\nu^2}{(\nu - \nu_B)^2 + \Delta\nu^2} \quad (2.6)$$

In the above equation,  $\nu_B$  is the central frequency (Brillouin frequency shift) of the fibre,  $\Delta\nu$  is the full width at half maximum which was theoretically and experimentally confirmed as  $30\text{ MHz}$  in [84],  $g_0$  is the Brillouin gain coefficient.

Once the experimental Brillouin curves are obtained, the parameters of the Lorentzian shape can be retrieved by a standard fit procedure. The central frequency  $\nu_B$  is inversely proportional to the pump wavelength, and is a relatively noise-immune value in the sense that it can be determined with high accuracy even from noisy measured data after Lorentzian fitting. However, the half-bandwidth  $\Delta\nu$  is crucially dependent on the quality of the measured spectrum so that it is not practical to just use bandwidth to represent the spectrum. It has to be noted that the frequency span encompassed has to be broad enough or the fit procedure may yield aberrant values. The dependency of  $\Delta\nu$  on pump wavelength was experimentally reported as a sway between  $\Delta\nu - \lambda^{-1.2}$  and  $\Delta\nu - \lambda^{-2.7}$  [22]. The Brillouin gain coefficient ( $g_0$ ) is reported to be approximately proportional to the temperature and inversely proportional to the strain.

Figure 2.3 illustrates the dependency of the Brillouin spectrum on strain and temperature [94]. Figure 2.3(a) represents the Brillouin gain spectrum measured at different elongations. When there is a longitudinal strain applied to a fibre, the fibre is elongated and its density changes. Since the sound velocity depends directly on the material density, this implies that a change in the sound velocity and eventually in the Brillouin frequency shift. It can be seen from the figure that the peak Brillouin gain coefficient is reduced with cable elongation, while linewidth is not strain dependent. As a result the received Brillouin signal should become weaker with strain.

The variation of the Brillouin spectrum with temperature is shown in Fig. 2.3 (b) where there are three Brillouin gain spectra of the fibre measured at  $-25\text{ }^\circ\text{C}$ ,  $30\text{ }^\circ\text{C}$  and  $90\text{ }^\circ\text{C}$ . On top of the drift of the central frequency, the narrowing of the curve is obtained as the temperature increases, as well as the concomitant increase in the peak value of the gain. It is therefore concluded that the peak gain coefficient increases with temperature while the bandwidth decreases.

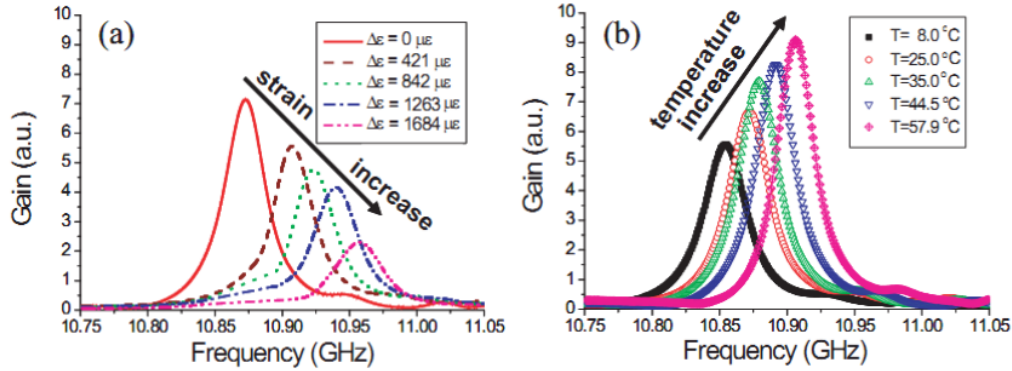


Fig. 2.3 The dependency of Brillouin gain spectrum on (a) strain and (b) temperature [94]

### Spatial resolution

The spatial resolution of the distributed sensing technology based on Brillouin scattering is governed by the minimum length over which the analyzer can discriminate between two adjacent locations having different temperature and/or strain. Since the received backscattered Brillouin signal is a convolution of the Brillouin spectrum with the input light pulse, the length of the light pulse determines the spatial resolution of the analyzer. The spatial resolution ( $L_s$ ) of BOTDR can be calculated as

$$L_s = \frac{c_0 \tau}{2n} \quad (2.7)$$

where  $\tau$  is the pulse width and  $c_0$  is the light velocity in vacuum. To improve the spatial resolution, a shorter pulse width can be used according to Eq. 2.7. However, it is important to notice that a shorter pulse width will lead to a broadened Brillouin gain spectrum and a weaker power of the backscattered light [4]. As result, the error of frequency shift decontamination will be enlarged and measurement accuracy will be affected.

Because of the above limit of accuracy, the minimum spatial resolution achievable is 1 m for the current available conventional analyzers [1]. In fibres, the damping time of a phonon wave is about 10 ns, corresponding to 30 MHz bandwidth of the backscattered spectrum. To limit the Brillouin spectrum width and maximize the signal strength, the length of the pulse width has to be longer than 10 ns (equivalent to 1 m spatial resolution) for the conventional BOTDR system, as below this value the Brillouin gain spectrum (BGS) linewidth steadily increases while power significantly drops [29].

The spatial resolution of BOTDR analyzer has been increasing with new technologies [12]. Brillouin Optical Time Domain Analyzer (BOTDA) uses a correlation-based-continuous-wave technique to stimulate the backscattered Brillouin signal [88]. In this way the distributed fibre Brillouin strain sensing achieves a spatial resolution of 0.01 m which is verified by

experimental results of a partly stretched fibre in the lab [31]. The new Brillouin echo-distributed sensing (BEDS), which uses a short  $\pi$ -phase pulse in addition to a long intensity pulse, is another successful case to improve the spatial resolution to as low as 0.01 m [45]. Compared to a BOTDR analyzer, BOTDA or BEDS generates stronger signal and thus better spatial resolution. However one limitation of BOTDA or BEDS is that they need connecting two ends of the cable for coupling two inter-propagating pulses. If the sensing cable is broken, the stimulated Brillouin analyzers will give no measurement results. However for BOTDR analyzer which connects to only one end of the cable, it will give some measurements all along the cable until the breakage point. Because cable breakage happens quite often on some construction sites (such as soil excavation process that may damage the embedded cable), it is necessary to use BOTDR in these sites and therefore methods to improve the BOTDR's spatial resolution are keeping under investigation.

For example, novel technologies such as de-convolution of the compound Brillouin spectrum have been investigated [90]. For a uniformly strained cable, the measured Brillouin power ( $P_c(\nu)$ ) is:

$$P_c(\nu) = P_u(\nu)(1 - r) + P_s(\nu)r \quad (2.8)$$

where  $P_u(\nu)$  is the Brillouin spectrum power distribution following a Lorentzian shape with a centre frequency the same as the free cable condition,  $P_s(\nu)$  is the Brillouin spectrum following a Lorentzian shape with a centre frequency the same as the uniformly strained cable condition,  $r$  is the ratio of the strained length to the spatial resolution, and the strained length can be obtained by spectrum width. The strained cable condition can therefore be decomposed by:

$$P_s(\nu) = \frac{P_c(\nu) - P_u(\nu)(1 - r)}{r} \quad (2.9)$$

Based on that, an iterative subdivision method is developed by iteratively extracting sub-Brillouin signal in fibre short segments to improve the spatial resolution of BOTDR to 0.1 m [81]. Assuming that the power of spontaneous Brillouin scattering is linearly proportional to the energy of the optical pulse, the measured Brillouin spectrum can be expressed as an integration of the signal generated from many short length segments. Figure 2.4(a) illustrates the measured Brillouin spectrum at position  $z'_0$ . When the pulse head moves from  $z'_0 + \frac{c\tau'}{2n}$  to  $z'_0 + \frac{c(\tau'+\tau)}{2n}$ , the pulse head generated Brillouin signal becomes backscattered and overlaps with the other part of the pulse generated signal (Fig. 2.4(b)). As a result, the detected Brillouin signal at  $z'_0 + \frac{c(\tau'+\tau)}{2n}$  will be an integration of the signal generated by a different part of the pulse within pulse length ( $\tau$ ). For a strain/temperature change event, the Brillouin spectrum before the heated/strained section can be easily obtained from the detected

Brillouin signal, and the sub Brillouin signal around the heated/strained section can therefore be decomposed iteratively based on the known Brillouin signal of the unstrained/unheated cable.

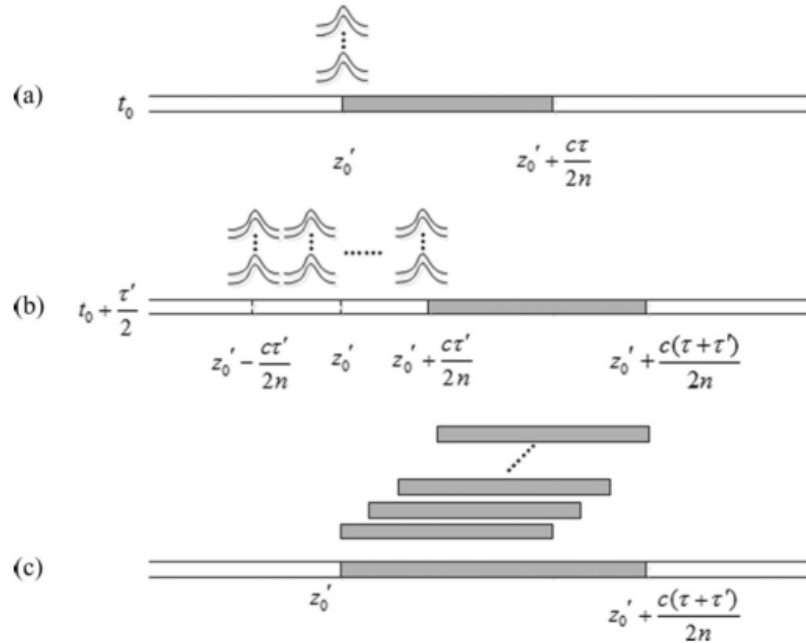


Fig. 2.4 Illustration of the Brillouin signal as an integration of the signal generated at different parts of the pulse [81]

Both of the above methods aim to improve the measurement spatial resolution of uniformly distributed strain/temperature changes, and they have been successfully verified by experimental tests [81][90]. However, in real strain monitoring cases, non-uniformly distributed strain is more often to be found which makes both methods impractical for real applications. New spatial resolution improving methods need to be developed for the BOTDR analyser under non-uniform strained conditions.

### 2.1.2 Modelling spontaneous Brillouin scattering

To compensate for measurement error and achieve more reliable interpretation of the measured strain profile, it is necessary to establish a model to connect analyzer measurements to real strain/temperature conditions based on Brillouin sensing mechanism. Fundamental models have been developed in the past to simulate the process of Brillouin scattering on the cable [9][64]. With some assumptions, such as expressing the measured Brillouin profile as a convolution of the injected pulse light and the intrinsic Lorentz shape distribution, the

model is further simplified [59][91]. Applying the Brillouin scattering model into the data interpretation, measurement error can be better controlled.

Brillouin scattering in an optical fibre uses the principle that the frequency shift of the backscattered Brillouin wave is proportional to the strain/temperature change, and the position can be estimated by the round-trip time of the light. In an optical fibre, the oscillations of the solid state matter excited by thermal fluctuation are called acoustic waves [61]. When the light propagating in the fibre core interacts with the acoustic waves, it will be scattered and its frequency shift will be proportional to the local velocity of the acoustic waves, which is dependent on the strain/temperature in each position of the fibre.

One approach to simulate the backscattered Brillouin power is to only consider the interaction between the pulsed light  $I_p$  and the backscattered Stokes wave  $I_s$ . If the fibre loss is neglected, which means the simulated fibre is not excessively long, the optical fibre of length  $z$  is modelled by two coupled partial differential equations under the steady state condition, as given below [36]:

$$\frac{dI_p}{dz} = -g_B I_p I_s \quad (2.10)$$

$$\frac{dI_s}{dz} = -g_B I_p I_s \quad (2.11)$$

The Brillouin gain coefficient  $g_B$  follows a Lorentzian profile as indicated in Eq. 2.6. The solution of the above partial differential equations is obtained as [36]:

$$\int_{I_s(z)}^{I_s(z+\Delta z)} \frac{dI_s(z', v)}{I_s(z, v)} = \int_z^{z+\Delta z} [-g_B(z', v) I_p(v)] dz' \quad (2.12)$$

If the fibre loss is considered, the coupled equations become [23]:

$$\frac{dI_p}{dz} = -g I_p I_s - \alpha I_p \quad (2.13)$$

$$\frac{dI_s}{dz} = -g I_p I_p + \alpha I_s \quad (2.14)$$

where  $\alpha$  is the fibre loss coefficient. Equation 2.13 calculates the pump power by integrating the pump power loss and the Brillouin gain, whereas the second equation calculates the Stokes power by integrating the pump depletion and the Stokes power loss.

The above partial differential equations can be solved using the perturbation method. In this approach, the boundary conditions have to be set up. Assuming that the initial pump pulse (which is at the beginning of the fibre) can be obtained as  $I_p(z=0) = I_{p0}$  and the initial Stokes wave is assumed to be  $I_s(z=0) = I_{s0}$ . Supposing that the Stokes wave is only subject to the fibre loss:

$$\frac{dI_s}{dz} = \alpha I_s \quad (2.15)$$

the Stokes intensity is therefore solved as:

$$I_s(z) = I_{s0} \exp(-\alpha z) \quad (2.16)$$

and the pump intensity can be written as:

$$I_p(z, \nu) = I_{p0} \exp\left(-\int (gI_s - \alpha) dz\right) = I_{p0} \exp\left(-\int (g(z, \nu) I_{s0} \exp(-\alpha z)) dz\right) \times \exp(\alpha z) \quad (2.17)$$

Substituting Eq. 2.17 into Eq. 2.14, and integrating over distance  $\Delta z$  which is the analyzer's spatial resolution, the Stokes wave intensity can be described as:

$$\int_{I_s(z)}^{I_s(z+\Delta z)} \frac{dI_s(z', \nu)}{I_s(z, \nu)} = \int_z^{z+\Delta z} [-g(z', \nu) I_p(z', \nu) + \alpha] dz' \quad (2.18)$$

$$\frac{I_s(z + \Delta z, \nu)}{I_s(z, \nu)} = \exp\left[\int_z^{z+\Delta z} [-g(z', \nu) I_p(z', \nu) + \alpha] dz'\right] \times \exp(\alpha \Delta z) \quad (2.19)$$

Equation 2.19 represents the propagation of the stokes wave along the fibre at frequency  $\nu$  generated by each components of the pump. To solve the stationary stokes spectrum for each section of the fibre, the stokes intensity at the start of the fibre has to be assumed. By minimizing the error between the simulated stokes intensity and the real stokes intensity at the end of the fibre, the initial stokes intensity can be determined. Therefore this simulation is only suitable when the stokes wave intensity is known at the end of the fibre.

The Brillouin backscattering model is further improved by considering the coupling of the three waves (the pump wave, Brillouin backscattered wave, and acoustic wave). The three partial differential equations are described as below, considering the linear optical attenuation

of the fibre [50][64]:

$$\left(\frac{\partial}{\partial z} + \frac{n}{c} \frac{\partial}{\partial t} + \alpha/2\right)E_p = -QE_s \quad (2.20)$$

$$\left(-\frac{\partial}{\partial z} + \frac{n}{c} \frac{\partial}{\partial t} + \alpha/2\right)E_s = Q^*E_p \quad (2.21)$$

$$\left(\frac{\partial}{\partial t} + \Gamma\right)Q = \frac{1}{2}\Gamma_1 g_B E_p E_s^* + R(z,t) \quad (2.22)$$

where  $E_p$ ,  $E_s$ , and  $Q$  are the complex amplitudes of the pump wave, the backscattered Brillouin wave, and the acoustic wave,  $c_0$  is the light velocity in vacuum,  $\alpha$  is the fibre loss coefficient,  $n$  is the linear refractive index of the fibre,  $\Gamma = \Gamma_1 + j\Delta$  where  $\Gamma_1 = 1/(2\tau)$  ( $\tau = 10\text{ns}$  is the phonon lifetime for silica fibres) is the damping rate and  $\Delta$  is the dependent detuning frequency, which is the Brillouin frequency shift at position  $z$ . Random force  $R(z,t)$  is a circular symmetric complex white noise in space and time.

For the BOTDR analyzer, the stimulated scattering term can be neglected, therefore, the equations can be simplified as:

$$\left(\frac{\partial}{\partial z} + \frac{n}{c} \frac{\partial}{\partial t}\right)E_p = 0 \quad (2.23)$$

$$\left(-\frac{\partial}{\partial z} + \frac{n}{c} \frac{\partial}{\partial t}\right)E_s = Q^*E_p \quad (2.24)$$

$$\left(\frac{\partial}{\partial t} + \Gamma\right)Q = R(z,t) \quad (2.25)$$

The boundary conditions of  $E_p(z,t)$  and  $E_s(z,t)$  are given by:

$$E_p(0,t) = \sqrt{\frac{P_p}{A_{eff}}} f(t) \quad (2.26)$$

$$E_s(z,t) = 0 \quad (2.27)$$

where  $P_p$  and  $f(t)$  are the power and shape functions of the pump pulse injected into an optical fibre, and  $A_{eff}$  is the effective core area of a fibre.

The analytical solution to the above BOTDR three wave equations can be found in [64]. For simplification, the spectrum measurement solution ( $EV(t, \nu)$ ) to the above equations is expressed as a two dimensional convolution of a time varying Lorentzian spectrum ( $L(t, \nu)$ ) and a point spread function ( $\Psi(t, \nu)$ ) with respect to  $t$  and  $\nu$

$$EV(t, \nu) = \gamma_R L(t, \nu) * \Psi(t, \nu) \quad (2.28)$$

where  $\gamma_R$  is a constant related to the optics property of the fibre, function  $L(t, \nu)$  is determined by the strain/temperature condition of the optical fibre, and  $\Psi(t, \nu)$  is dependent on the sensing mechanism of the BOTDR.

This result indicates that the analyzer measured backscattered spectrum can be expressed as a convolution of Brillouin spectrum with a spread function over time. This finding is used for later Brillouin model construction in Chapter 4.

### 2.1.3 Sensing cable

To successfully monitor temperature or strain, the BOTDR distributed fibre optic sensors need meet some special requirements. Since the sensing cables are installed under harsh conditions, they have to be designed to shield from any external influences, such as humidity, side pressure, crushing, and longitudinal strain applied to the cable. To keep the sensitivity of the system, strain sensing cable is mostly specially designed as the strain cable has to efficiently transfer strain from cable jacket to the fibre core. On the contrary, the temperature sensing cable has to isolate any strain effect and be made only sensitive to temperature.

For a Brillouin optical time domain system, both the strain and temperature sensing cable use single mode fibre. It enables only one mode of light to propagate in the fibre and therefore limits dispersion effects. A standard single mode fibre has low loss at the  $1550\text{nm}$  wavelength window which makes it suitable for long distance monitoring [44]. In addition, the optical signal characteristics are not affected in single mode fibre, and the spatial resolution is therefore maintained all along the sensing length [67].

A typical single-mode fibre, which is suitable for a Brillouin optical time domain analyzer, is illustrated in Fig. 2.5. It consists of a core surrounded by a transparent cladding layer. The core of the fibre is normally made from glass, which has a refractive index of 1.52. Cladding is a thin glass layer covering the core and has a relatively lower refractive index number, which helps protect the signal within the core region. Surrounding the core and cladding, a layer of buffer is used to protect the glass. The buffer is made of thermoplastic

elastomer material, ensuring the glass to have high tensile strength and protecting the glass from abrasion and excessive cable bending. The diameter of the core is set as small as  $8\ \mu\text{m}$  to limit the amount of dispersion.

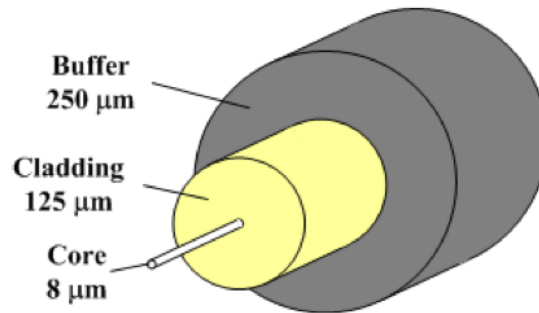


Fig. 2.5 Dimension of a typical single mode fibre

As mentioned previously, the frequency shift of the backscattered Brillouin spectrum is simultaneously sensitive to temperature and strain in the fibre. To distinguish them, the strain sensing cable and the temperature sensing cable are usually placed adjacent to each other for different measurements. The strain cable measures strain and temperature, while the temperature cable is only sensitive to temperature. The measurement of temperature cable is therefore used to compensate for the Brillouin frequency shift induced by temperature in strain cable measurement, leaving only strain induced Brillouin frequency shift in the result, and thus obtaining strain.

### Strain cable

The design and production of the strain sensing cable are critical elements for the success of any Brillouin distributed sensing projects. The strain cables should be able to efficiently transfer the strain applied on the jacket to the fibre core for accurate strain monitoring. The slippage between different layers of the cable has to be minimized, and this can be achieved by tight gripping of the protection layer of the cable. Creep deformation and the resulting stress relaxation of the cable jacket is found to be one important cause of strain decrease over time. To avoid this jacket effect on fibre strain, the jacket of tight buffered fibre should be made of elastic material which has good performance regarding creep deformation.

As well as tight buffering the fibre, all layers of the cable jacket have to be removable in order to splice the cable to a pigtail or another cable when necessary. In addition, fibre-optic strain cables have to be strong enough to withstand harsh installation conditions. Metal reinforced cable is one solution, but this kind of cable cannot be used to detect cracks since the plasticity of the metal under large strain conditions leads to unreliable measurements.

One of the reinforced strain sensing cables designed by the Fujikura Company is illustrated in Fig. 2.6. This cable has four single-mode optical fibres embedded in the middle of the cable and two steel wires on the sides to reinforce the cable (shown as strength member in the figure). Outside the fibres and steel wires is a nylon sheath, which is abrasion resistant, enabling the cable to survive in harsh environment.

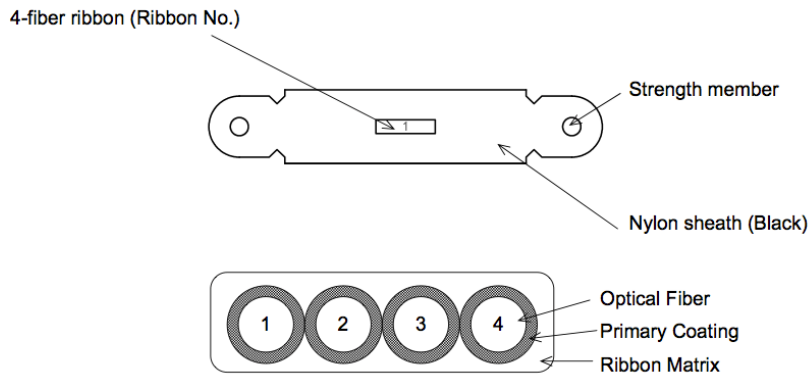


Fig. 2.6 Illustration of the Fujikura reinforced strain sensing cable

The SMC3 strain cable (Fig. 2.7) is a relatively more robust strain-sensing cable compared to the Fujikura reinforced strain cable. It consists of a single mode optical fibre surrounded by special high bonding coatings and a strain transfer layer. Outside the high bonding coatings and strain transfer layer there is a stainless steel metal tube, which hermetically seals the sensing fibre and enhances crush resistance. There is an additional stranded stainless steel wires integrated within the outer protective sheath. Stranded stainless steel wired armouring provides the cable with higher tensile strength and robustness.

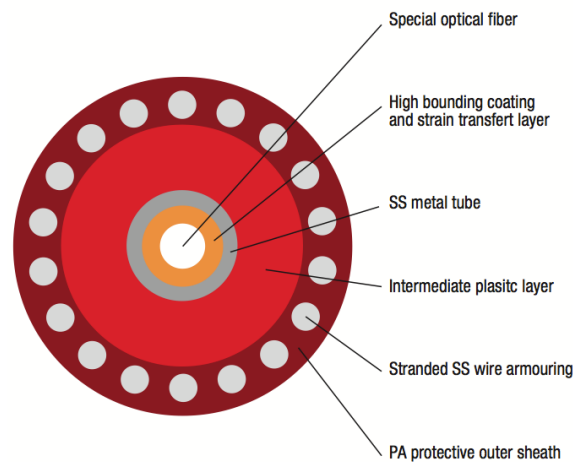


Fig. 2.7 Illustration of the SMC3 strain sensing cable

The SMC3 strain sensing cable is specially designed for DITEST strain sensing technology. This cable can accurately transfer strain from the outside to the inner fibre core. The mechanically reinforced cable design has very high tensile strength and abrasion resistance. The very robust design and the low loss characteristics make the SMC3 cable suitable for direct burial and long distance monitoring applications. However, one problem of this cable is that its jacket is too hard to remove manually, which makes it unsuitable for splicing on site.

### **Temperature cable**

Unlike the tight buffered strain sensing cable, temperature sensing cable is loose buffered in order to isolate the strain effects. In temperature cable, the coated fibre floats within a hard tube, which is filled with gel, and therefore much of the external strain placed on the tube will not be directly transferred to the fibre inside. However, because of ageing and creeping, the glue has a short life and its restricted durability prevents the cable from meeting practical installation requirements [93]. New types of packaging need be developed to improve the performance of the temperature cable.

Normally, telecommunication cable (Fig. 2.8) is loose buffered and suitable for temperature sensing for short term monitoring using BOTDR. Because telecommunication cable is well developed and has a large provision, it is cost-effective to use telecommunication cable as the temperature sensor. However, before largely using telecommunication cable for temperature compensation, some more tests need be done to characterize the optical performance of telecommunication fibre.

### **Strain and temperature cable**

Strain and temperature cable in a single package is developed to enhance the accuracy of temperature compensation process. For traditional methods where strain and temperature sensing cables installed in parallel, independent cable bending or twisting will induce a relative displacement between two sensing cables, making it difficult to align the locations of the measuring points of two cables. By manufacturing the two sensing cables into a single package, the aligning error between two sensing cable data sets is avoided.

The SMC2 cable (Fig. 2.9) embeds two sensing fibres together, one for strain sensing and the other for temperature sensing. The strain sensing fibre is a single-mode optical fibre surrounded by special high bonding coatings and a strain transfer layer. Outside the coatings and transfer layer is a stainless steel loose tube, which is the last protection layer for the strain fibre. Beside the strain sensing fibre is the temperature-sensing fibre. This element is a

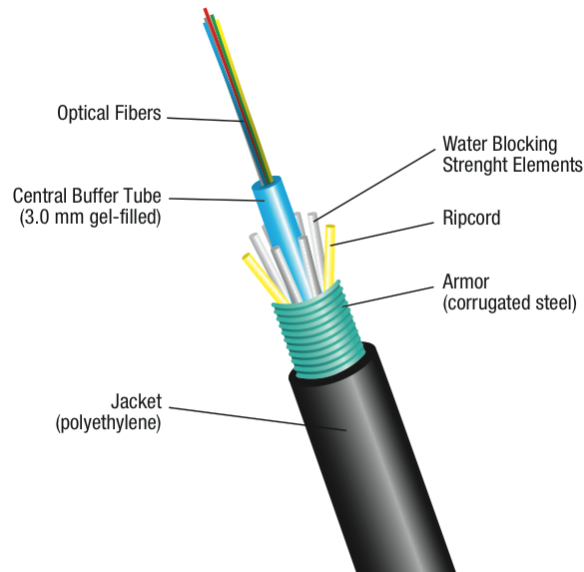


Fig. 2.8 Illustration of the temperature sensing cable

single mode fibre floated in a stainless steel loose tube. The fibre in the temperature-sensing element is laid with excessive length in order to make it free to move in the tube. The biggest advantage of SMC2 sensing cable is that it can simultaneously monitor strain and temperature in only one cable. It does not need to make use of any external temperature sensing cables for strain cable measurement compensation.

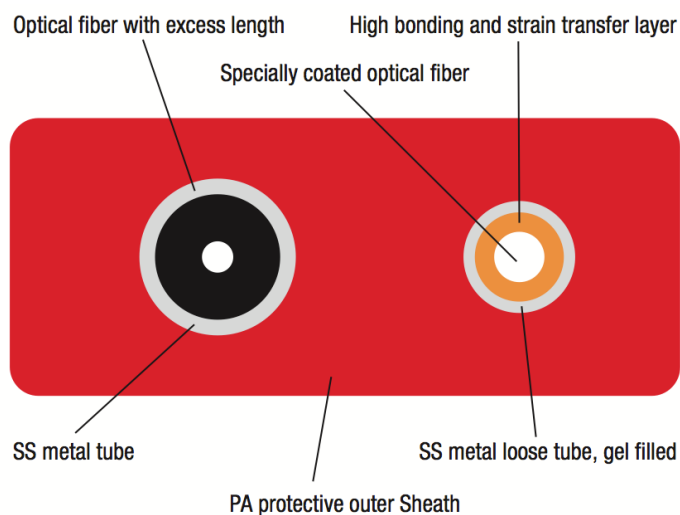


Fig. 2.9 Illustration of the SMC2 simultaneous strain and temperature sensing cable

### 2.1.4 Sensing analyzer

The distributed fibre optics sensor uses an analyzer to launch the pulse into the fibre and receive the backscattered light for later strain and temperature interpretation. The types of analyzer based on Brillouin scattering includes: Brillouin Optical Time Domain Reflectometry (BOTDR), Brillouin Optical Time Domain Analysis (BOTDA), Brillouin Optical Frequency Domain Analysis (BOFDA) and Brillouin Echo Distributed Sensing (BEDS). This section briefly reviews BOTDR and BOTDA based on some typical analyzers.

#### **BOTDR sensing system**

Brillouin optical time domain reflectometry (BOTDR) exploits spontaneous Brillouin backscattering light to measure strain and temperature. Connecting to one end of the sensing cable, a BOTDR analyzer launches a pulsed light within Stokes frequencies into the fibre and receives spontaneous Brillouin backscattered light through this end of the fibre. The received Brillouin wave will be at its peak power when the optical frequency of the launched light is same as that of the optical fibre. After frequency sweeping, Brillouin spectrum power at any frequency level is obtained. The location of the backscattered Brillouin spectrum is determined by transforming the received time to distance.

Spontaneous Brillouin backscattering does not happen in large quantities. For a BOTDR analyzer, the received signal of the Brillouin backscattering wave is very low compared to other stimulated Brillouin scattering analyzers. As a result, the BOTDR analyzer has a relatively lower accuracy and longer measurement time. AQ8603 BOTDR analyzer from Yokogawa Co. Ltd is claimed to have an accuracy of  $30 \mu\epsilon$ . NBX-5000 BOTDR analyzer from Neubrex Co. Ltd has a tested accuracy of  $15 \mu\epsilon$ , consistent with what the specification indicates.

#### **BOTDA sensing system**

Brillouin optical time domain analysis (BOTDA) uses two counter-propagating light waves to stimulate Brillouin scattering and thus achieves larger intensity of the backscattered Brillouin signal. This concept was first proposed in 1989 [28]. In a BOTDA sensing system, the analyzer is connected to the two ends of the optical fibre, where a short pumped pulse is launched into one end of the fibre and a continuous wave (CW) into the other end. The frequency of the CW light is set within the Stokes frequency of the cable, allowing CW light energy to be transferred to the Stokes wave and thus enlarging the Brillouin gain. Stimulation of the Brillouin scattering occurs when the frequency difference between two lasers corresponds to the Brillouin frequency of the optical fibre. By sweeping the frequency

of the CW light, the fibre's Brillouin frequency shift at peak power gain can be obtained. The location where the stimulated Brillouin scattering occurs is determined by the time dependence of the detected CW light.

Because a BOTDA analyzer stimulates the Brillouin backscattering process, a higher level of Brillouin backscattering signal can be received. Therefore a BOTDA analyzer has a relatively higher accuracy and better spatial resolution. DITEST BOTDA analyzer from Omnisens Co. Ltd can achieve an accuracy of  $2\mu\epsilon$  with a spatial resolution of  $0.02m$  using double-pulse configuration [73]. Similar results are found with NBX-6000 BOTDA analyzer from Neubrex Co. Ltd using pulse pre-pump technique [62]. However, due to the relatively higher signal power loss, a BOTDA analyzer has a limitation in sensing distance. The maximum distance for a BOTDA analyzer is normally limited to  $10km$ .

### BOTDA vs. BOTDR

The commonly used distributed fibre optics sensing analyzers based on Brillouin scattering includes AQ8603 BOTDR analyzer, DTSS BOTDR analyzer, NBX-5000 BOTDR analyzer, DITEST BOTDA analyzer and NBX-6000 BOTDA analyzer. A comparison of the analyzers is shown in Table 2.1. The strain/temperature accuracy is the measured accuracy on conditions of  $2^{16}$  averages and  $3MHz$  frequency sweep span. The spatial resolution represents the minimum length of strain/temperature change that can be discriminated by the analyzer. The read out resolution is the minimum distance between two measuring points of the analyzer.

Table 2.1 Comparison of different analyzers

Parameters	Analysers				
	AQ8603	DTSS	NBX-5000	DITEST	NBX-6000
Sensing type	BOTDR	BOTDR	BOTDR	BOTDA	BOTDA
Strain accuracy ( $\mu\epsilon$ )	30	20	15	7.5	2
Temperature accuracy ( $^{\circ}C$ )	1.5	1	0.75	0.37	0.1
Spatial resolution ( $m$ )	1	1	0.5	0.5	0.05
Read out resolution ( $m$ )	0.05	0.05	0.05	0.25	0.01
Sensing distance ( $km$ )	20	24	10	5	1

It can be seen that in general, the BOTDA analyzer has a better performance than the BOTDR analyzer in measurement accuracy ( $2\mu\epsilon$  for NBX-6000 BOTDA,  $15\mu\epsilon$  for NBX-5000 BOTDR) and measuring resolution ( $0.05m$  spatial resolution for NBX-6000 BOTDA,  $1m$  spatial resolution for NBX-6000 BOTDR). Due to the limit number of measuring points that can be achieved in the analyzer, the maximum measuring distance is therefore longer for BOTDA analyzer ( $24km$  for Sensornet BOTDR,  $10km$  for NBX-BOTDR analyzer).

Although a BOTDA analyzer is more accurate than a BOTDR analyzer, one limitation of a BOTDA analyzer is that it requires two laser lights to be injected into the cable from both ends. As a result, no signal will be obtained even if there is just one breakage on the cable. However, a BOTDR analyzer requires only one laser to launch light into the fibre. Therefore when the sensing cable is accidentally broken, the Brillouin backscattered wave from the laser injecting point to the breaking point can still be obtained. Because of harsh working environments on site, cable breakage happens quite often and it is mostly impossible to take out cable from structures to repair breakages. Therefore to make sure at least some information can be obtained, most of the strain monitoring site work is done with BOTDR analyzer.

## 2.2 Measurement error

The data analysis of the distributed strain/temperature measurements obtained in the field has been always non-trivial because of unavoidable measurement errors introduced by the complex input of the strain as well as the performance limits of the analyzer. It has been stated that the BOTDR measurement for a crack deflection represents a considerable error in strain width and level determination [32]. In addition, a beam with a small defect was observed to have a much more significant error in the strain profile read over the whole beam compared to a non-damaged beam [83]. Therefore it is crucial to characterize and improve the accuracy of the BOTDR measurement result.

There are two terms, precision and accuracy, that indicate measurement error. A precise measurement is one where the spread of data is 'small' relative to the average result. An accurate measurement is one in which the difference between the measurement and the real condition is within the 'accepted' range. This section will review some geotechnical applications of the distributed fibre optics sensors, focusing on the precision and accuracy of the measurement results. The fundamental origins and compensation methods of the two types of errors are then revised in detail.

### 2.2.1 Precision and accuracy issues in geotechnical monitoring applications

In the south of Brazil, a roller compacted concrete (RCC) dam was equipped with a distributed fibre optics sensor to monitor its impoundment process [27]. The dam is 43 m high with a crest length of 446 m. The major difference between RCC and a conventional mass concrete is that it contains less cement and essentially has no slumps, which makes RCC drier and

thus suitable to support heavy earth moving (dam) for its compaction. The strain and temperature sensing cable was installed along the reinforcement steel of the concrete to monitor deformation or potential cracks in the concrete dam during impoundment.

During the five days of impoundment, no significant changes of strain were observed by the distributed fibre optics sensor. The standard deviation of the repeated measurements at each measuring point was used to evaluate the data quality. Figure 2.10 illustrates the data quality before temperature compensation. In the first 500m, significantly low data quality (as much as 1500  $\mu\epsilon$  error) was found at points with some local sources of loss such as fixation and splice connections, otherwise the data quality was comparatively better and mostly kept at a low level of 70  $\mu\epsilon$ . Between block 11 and 15 the measurement uncertainty was at the minimum level of 10  $\mu\epsilon$ .

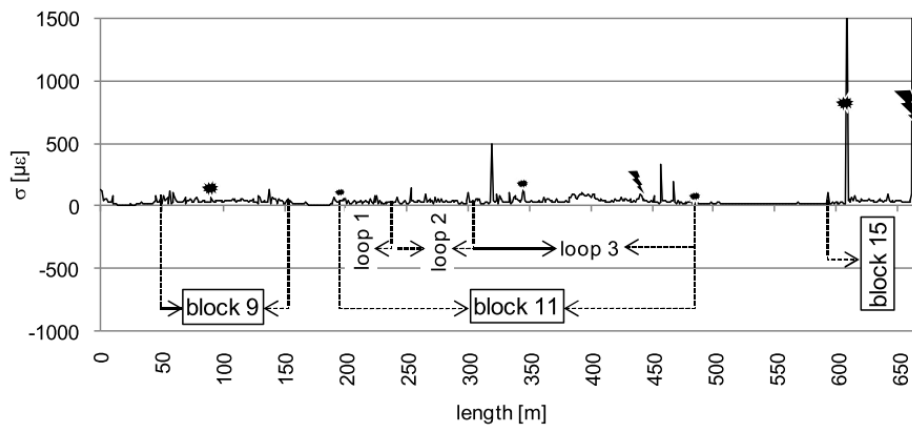


Fig. 2.10 Data quality of the measured result along the sensing cable length [27]

In an existing London underground tunnel, the distributed fibre optics sensor was installed to monitor the joint movements of concrete tunnel linings [14]. The tunnel ring was built with poor tolerance, leading to potential lining distortions. To monitor the joint movements in the concrete tunnel lining, the optical fibre was fixed to the lining by a 50mm diameter disc system (Fig. 2.11). During installation, the optical fibre was pre-tensioned and glued to the discs which were fixed to the concrete with screws and holes. As a result, the tested cable would show an increase in tensile strain when the joint opened at the inner surface of the lining, and a decrease in strain when the joint closed.

It has been reported that the strain distribution of BOTDR measurement is a weighted average result, leading to differences between the measured strain and the real strain, which thus deteriorates measurement accuracy. The weighted average process can be simulated as an integration of the local strain with a Gaussian distribution [14]. A least squares approach was then developed to decompose the real strain from the raw data measurement by minimizing

the difference between the measured strain and the calculated strain. Experimental results revealed that for different step strain values, the bandwidth( $w$ ) of the Gaussian distribution needs to adjust accordingly to provide best fit between the measured and the calculated strain [33]. It was suggested that the most suitable bandwidth of the Gaussian distribution is  $0.21\text{ m}$  for a step strain value of  $472\ \mu\epsilon$  and  $0.05\text{ m}$  for a step strain value of  $3550\ \mu\epsilon$  [33].

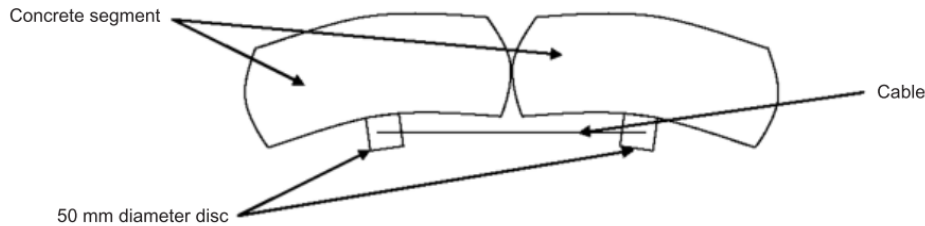


Fig. 2.11 Cable deployment on concrete segments of a tunnel ring [14]

The decomposed strain indicated that the joints opened by approximately  $25\ \mu\epsilon - 50\ \mu\epsilon$  over 16 weeks of monitoring time. The difference between the decomposed strain and the data measured by vibrating-wire strain gauges (VWSGs) was used to represent the accuracy of the deconvolution method. Figure 2.12 compares the movement measured by VWSGs and the movement calculated from the fibre optical sensor strain using different deconvolution bandwidth ( $w$ ). The results indicated that  $0.3\text{ m}$  bandwidth deconvolution was more accurate than deconvolution results using other bandwidth levels. However, even for a  $0.3\text{ m}$  bandwidth deconvolution process, the maximum error achieved as much as  $30\ \mu\epsilon$  on 7<sup>th</sup> of March 2008, which is about 50% of the measured strain in the first ring and 200% in the second ring. It was claimed that the bandwidth of the Gaussian distribution needs more investigation to improve the accuracy of this deconvolution method.

In a pile located in the Isle of Dogs, London, a distributed fibre optics sensor was installed to monitor the development of strain and/or temperature during the concrete curing process and pile loading test [79]. The pile was installed with a conventional monitoring system of vibrating wire strain gauges (VWSGs) and rod extensometers as references. During the O-cell load test, measurements taken by the distributed fibre optics sensor were compared with the conventional monitoring system data to investigate the accuracy of the fibre optics results.

Figure 2.13 illustrates the comparison between measurements from the fibre optics sensor, VWSGs, and extensometers, at the maximum load of  $30.9\text{ MN}$ . The general trends of the strain development along the pile for the fibre optics measurement were in reasonably good agreement with the conventional monitoring system results. However, the fibre optics strain profile showed more fluctuations than the VWSGs and extensometers did, especially at

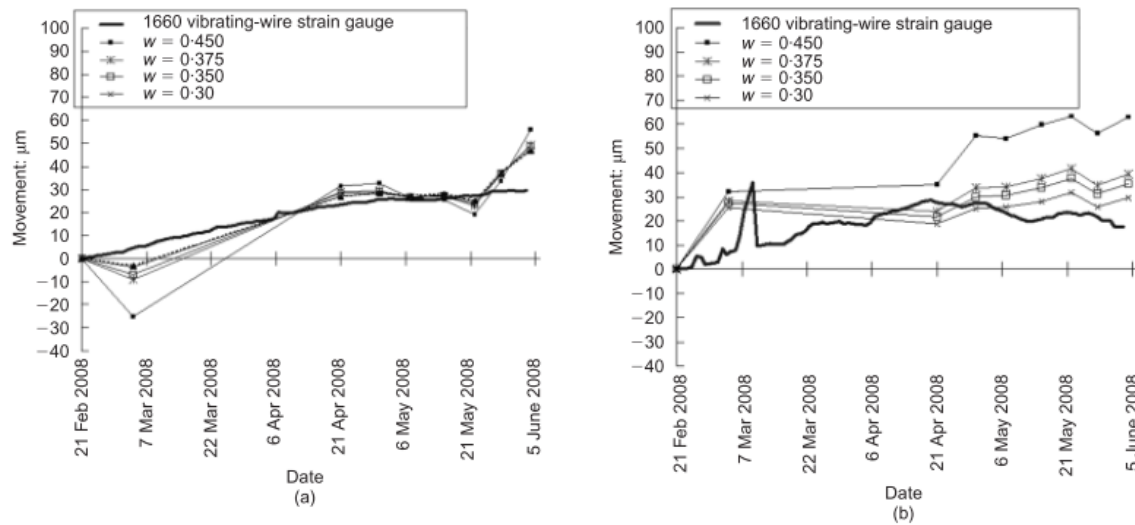


Fig. 2.12 The movements measured from the vibrating-wire strain gauges and the distributed optical fibre sensor at (a) superficial sections and (b) deeper sections [14]

deeper pile sections. The strain variations could be due to measurement error or real strain. It was suggested that because the waviness of the variation is longer than the spatial resolution of the analyzer, the strain variation was more likely to represent the real strain condition of the pile. More investigation needs to be done to characterize the fibre optics measurement error and its relationship to the measurement fluctuations. Only in that way can more reliable data interpretation be achieved.

### 2.2.2 Measurement precision error

BOTDR measurement precision error is the variation of the Brillouin peak frequency with time when there is no strain/temperature change happening on the tested cable. It can be quantified as the standard deviation of repeated measurement values. The precision error of BOTDR measurement is related to many aspects of the hardware design and implementation, as well as the measurement method used by the analyzer. For a typical BOTDR analyzer, its precision error follows a normal distribution with a standard deviation of  $15 \mu\epsilon$  [39].

It was found that the signal to noise ratio (SNR) primarily influences on BOTDR measurement precision. A  $20 \text{ dB}$  drop in SNR causes approximately a ten-fold increase in strain uncertainty [11]. The instability of the injected pulse, which is due to the thermal shift within electronic hardware components of the analyzer, is the most significant source of SNR. By calibrating the received BGS peak frequency with the reference fibre, the instability can be controlled as low as  $0.7 \text{ MHz}$  [85].

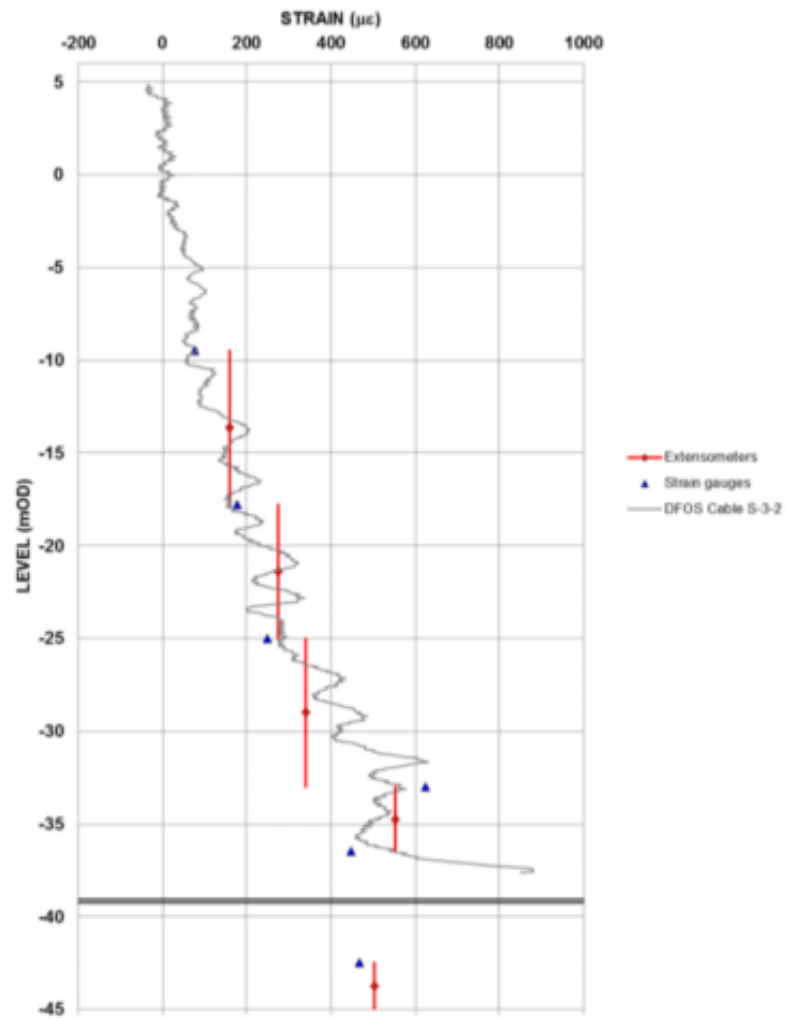


Fig. 2.13 Strain measurement results of the distributed fibre optics sensor, vibrating-wire strain gauges and extensometers of the pile [79]

Other analyzer setting parameters, such as frequency scanning step and the number of averages, also influence measurement precision. The set of those parameters and their corresponding measurement precision is summarized in Table 2.2. The result was calculated using a Neubrex PPP-BOTDA system [85]. As the number of averages increases from  $10^{13}$  to  $10^{15}$ , the measurement precision improves for about 25% at a frequency step of  $5\text{ MHz}$  (error reduces from  $\pm 50\ \mu\epsilon$  to  $\pm 36\ \mu\epsilon$ ).

Table 2.2 Influence of averaging times on measurement precision

No. of averages	Frequency step	precision
$10^{13}$	$5\text{ MHz}$	$\pm 2.5\text{ MHz}(\pm 50\ \mu\epsilon)$
$10^{14}$	$5\text{ MHz}$	$\pm 2.1\text{ MHz}(\pm 42\ \mu\epsilon)$
$10^{15}$	$5\text{ MHz}$	$\pm 1.8\text{ MHz}(\pm 36\ \mu\epsilon)$

The estimation of the precision error of the Brillouin frequency shift ( $\delta v_B$ ) was originally proposed as a function of the SNR and spectrum bandwidth ( $\Delta v$ ) [29]. The following numerical simulations reveal the contributions that linewidth broadening and reduced signal strength have on sensing precision [17]. The analyzer measurement precision error mainly comes from frequency resolution (which is the minimum frequency shift that an analyzer can detect). Assuming that the precision error equals to frequency resolution:

$$\delta v_B = \min(v - v_B) \quad (2.29)$$

where  $v_B$  is the central frequency (Brillouin frequency shift) of the fibre.

The Brillouin gain ( $g_B(v)$ ) at peak centre frequency can be rewritten as:

$$g_B(v_B) = N + \frac{g_0 \Delta v^2}{(\delta v_B)^2 + \Delta v^2} \quad (2.30)$$

where  $\Delta v$  is the half-linewidth,  $g_0$  is the central frequency gain coefficient, and  $N$  is the root mean square value of the noise.

Given that the maximum intensity of the spectrum is the signal ( $S = g_B(v_B) = g_0$ ), the SNR is therefore calculated as:  $SNR = \frac{S^2}{N^2}$ . Substituting SNR into Eq. 2.30 and assuming that the  $SNR \gg 1$ , the precision error is obtained as:

$$\delta v_B = \frac{\Delta v}{2[(SNR)^{1/2} - 1]^{1/2}} \approx \frac{\Delta v}{2(SNR)^{1/4}} \quad (2.31)$$

Another expression of the precision error was discussed considering not only the SNR, the Brillouin spectrum bandwidth, but also the property of the injected pulse [59]. Assuming that the Brillouin backscattered spectrum surrounding the peak-power frequency can be approximated by a quadratic function, the relationship between  $\delta v_B$ ,  $S$ , and  $N$  can be expressed as:

$$S - N = S[1 - p(\delta v_B/\Delta v)^2] \quad (2.32)$$

where the parameter  $p$  is a contrast value determined by the property of the pulse.

Because the electrical signal power is proportional to the square of the received optical signal power, the precision error  $\delta v_B$  is therefore expressed as:

$$\delta v_B = \Delta v / (\sqrt{p} SNR^{1/4}) \quad (2.33)$$

The investigation of the precision error has been further improved by other researchers [68][78]. The influence of the estimation methods (i.e. the type of curve fitting) or measurement conditions, such as the number of frequency points involved in the fitting (or equivalently the frequency sampling step) was verified [68]. Based on that, it was then revealed that the precision error is fundamentally dependent on the Brillouin gain linewidth, spatial resolution, frequency scanning step, number of averaging and SNR [78]. A simplified function (Eq. 2.34) of the measurement precision error was obtained as:

$$\delta v_B = \frac{1}{SNR(z)} \sqrt{\frac{3}{4} \varphi \cdot \Delta v_B} \quad (2.34)$$

where  $\varphi$  is the frequency scanning step.

For a BOTDR analyzer with an SNR of 20 dB, FWHM as 130 MHz, and  $\varphi$  as 3 MHz, the Brillouin frequency measurement precision error is calculated as 0.855 MHz (approximately 17  $\mu\epsilon$ ) using Eq. 2.34. Predictions of the long distance cable error and experimental results were then compared at different numbers of averages (Fig. 2.14). Both the experimental measured error and the predicted error obtained at 24.5 km distance showed that the frequency error with 10 times of averaging decreased up to 3.21 MHz from 0.75 MHz with 200 averages. This corresponds to an improvement factor of 4.28 on the Brillouin frequency precision, which is in good agreement with the equation factor of 4.47 ( $= \sqrt{200/10}$ ).

Besides analyser properties, the ubiquitous inhomogeneous of the optic fibre deteriorates the precision of the central frequency detection, as fundamentally limited by the use of a practical polarization scrambler with non-ideal polarization scrambling [19][84]. Experimental results (Fig. 2.15) indicated that the frequency resolution is scattered around 0.06 MHz over distance with an orthogonal probe input state of polarizations. By using practical polarization

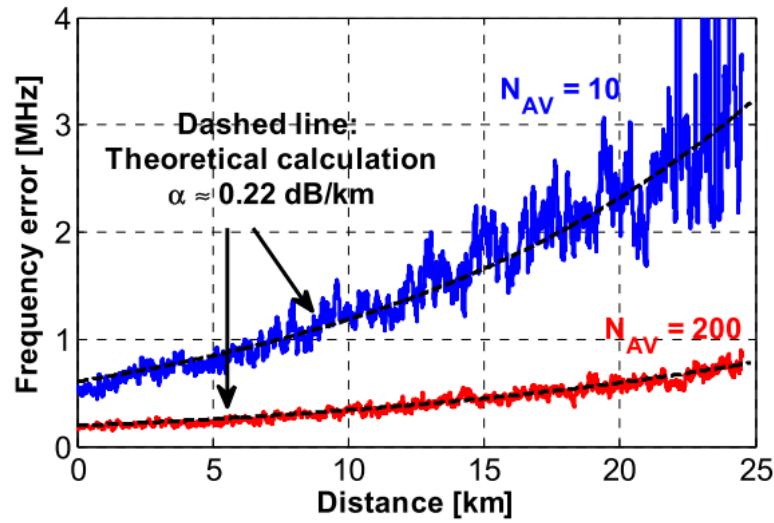


Fig. 2.14 Theoretical calculated and analyzer measured frequency resolution obtained at different numbers of averages for a 25 km length cable [78]

scrambling, the measurement precision error can be reduced to a very low level of 0.016 MHz.

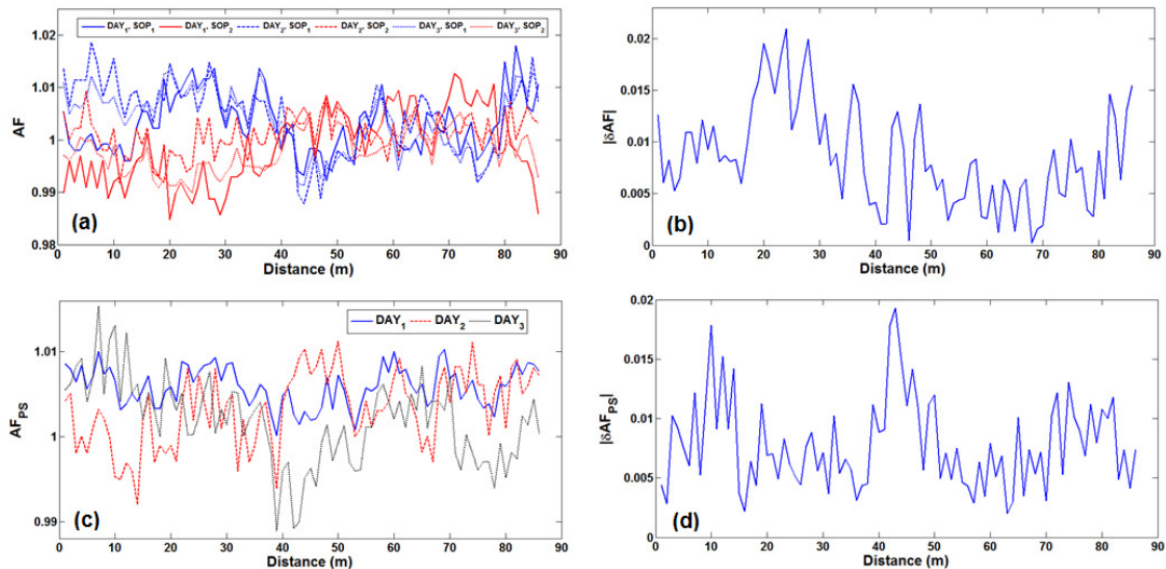


Fig. 2.15 (a) Frequency resolution curves for two orthogonal probe input state of polarizations (SOPs) measured over three days (b) Frequency resolution over distance (c) Frequency resolution curves for the scrambled probe input SOP measured over three days (d) Frequency resolution over distance [84]

Unfortunately, field measurements have shown that the actual precision error can be far more significant than the maximum simulated result of 0.855 MHz (approximately 17 με).

For example, as shown in the previous geotechnical application examples, the 5-day measurements of the RCC dam Fundao in Brazil revealed that the precision error was about  $70\mu\epsilon$ , and was up to  $500\mu\epsilon$  at some particular locations (e.g. cable fixation, splice connections, and places with local losses) [27]. It was also observed in the lab that for a fluctuating strain, the BOTDR measurement precision error was  $130\mu\epsilon$ , much higher than the nominal error of a BOTDR sensor, indicating that a fluctuating load will influence the stability of BOTDR [25]. In addition, for a cracked concrete beam, a maximum precision error of  $300\mu\epsilon$  under fluctuating loads was also reported from ten repeated measurements using BOTDR [25].

Therefore, the above precision prediction methods may not be practical on real site applications. The factors that have not been thoroughly discussed include the distribution of the strain profile. For example, the non-uniformly distributed strain leads to an asymmetric Brillouin gain spectrum, and thus a changing SNR and bandwidth of the received Brillouin spectrum, which in turn leads to a higher precision error. It was observed in the lab that an extra of  $5\mu\epsilon$  measurement precision error was found in non-uniformly distributed strain compared to a uniformly distributed strain [5].

The distance accuracy corresponds to the error of location determination of the readings from different sets of data. It comes from the accuracy of the analyzer's time acquisition, fibre refractive index, and fibre lay loss [63]. Because BOTDR sensor has an error in location determination, the strain non-uniformity can enlarge the effect of the distance error on measurement precision in the way that a more complicated measured strain leads to a larger measured strain error. Although the typical strain range for infrastructure monitoring is normally limited to several hundred micro-strain, this relatively higher precision error would become a critical problem for most applications. Therefore, a more comprehensive method needs to be constructed for future precision error prediction.

### 2.2.3 Systematic error

The measurement systematic error of Brillouin fibre optics sensor quantifies the difference between the measured strain and the true strain. This error comes from the fact that the BOTDR measurement output is a convolution of the intrinsic Brillouin spectrum with the injected pulse [20]. Due to the limit of the pulse length, the measured Brillouin spectrum can deform, which results in the difference. The length of the light pulse will determine the analyzer's spatial resolution, which can be calculated as  $L_s = \tau c/2$ , where  $\tau$  is the pulse duration and  $c$  is the group velocity of the pump pulse in the fibre. To generate a stronger signal and narrower spectrum, the pulse duration is mostly longer than  $10ns$  (the phonon lifetime in silica fibre). As a result, the minimum spatial resolution for a BOTDR analyzer is limited to  $1m$ , considering the trade-off between the Brillouin gain spectrum bandwidth

and Brillouin signal strength. If a local strain change occurs over a distance scale smaller than the sensor's spatial resolution, the measured result will be a relatively smaller value, sometimes too small for strain to be detected. Therefore, when the cable is strained in a way that the strain changes rather non-uniformly, few strain measurement results will match the real strain value, leading to a large measurement systematic error.

Besides the influence of the spatial resolution on systematic error, other sources that lead to measurement systematic error include the Brillouin frequency conversional coefficients error, fibre creep, and errors induced by temperature compensation process.

### Spatial resolution limitation

The received Brillouin spectrum power is proportional to the length and magnitude of the strain/temperature change event. If the event that happens within the analyzer's spatial resolution has comparable centre frequencies, the dominant peak will bury additional peaks and the convoluted Brillouin spectrum will show as one peak. On the other hand, the convoluted Brillouin spectrum may contain additional peaks (as shown in Fig. 2.16) [70].

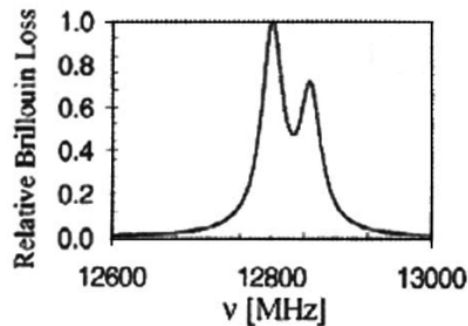


Fig. 2.16 Illustration of double peaks in one received Brillouin spectrum [70]

Figure 2.17 is the constructed length-strain diagram which represents the normalized relationship between the measured strain and the length of the strained section when the strain length is smaller than the spatial resolution [71]. The border separates the single and multiple peaks spectra, which are typical features of non-uniformly strained sections.

It was found that the difference between the calculated strain and the actual strain depends mainly on the strain value of the fibre and the strained length within the spatial resolution for the given distributed sensing system [91]. A backscattered Brillouin spectrum model was developed by Naruse [60] to quantify the BOTDR measurement systematic error and its dependence on strain status. In this model, the Brillouin backscattering power  $dP_B(z, \nu)$  in a

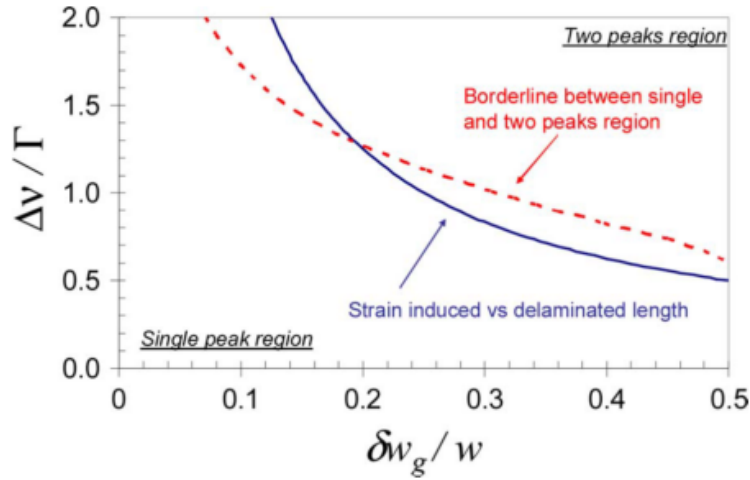


Fig. 2.17 Diagram showing the borderline between single peak and two peaks regions (dashed curve), and the curve representing the induced strain as a function of the normalized section length (plain curve) [71]

small section of the fibre is expressed as:

$$dP_B(z, \nu) = g_B(\nu, \nu_B) \left( \frac{c_0}{2n} \right) P(z) dx \times \exp(-2a_z z) \quad (2.35)$$

where  $P$  is the launched pulse power,  $c_0$  is the light velocity in vacuum,  $n$  is the fibre refractive index,  $a_z$  is the attenuation coefficient of the fibre,  $z$  is the scattering position defined by Eq. 2.3, and  $g_B(\nu, \nu_B)$  is the Brillouin gain spectrum with a Lorentzian shape defined by Eq. 2.6.  $\nu_B$  is the centre frequency at which  $g(\nu, \nu_B)$  has a peak power.

The frequency dependent factor of the Brillouin backscattered light produced by the pulsed light is simulated as:

$$H(\nu) = \int P_p(f, f_0) \frac{h(\omega/2)^2}{[v - (f - S_B)]^2 + (\omega/2)^2} df \quad (2.36)$$

Based on this, BOTDR sensor measurement was simplified as a weighted average value over its spatial resolution [38]. A weighting function follows the shape of Gaussian normal distribution, specified by the distance from the centre and the width of the weighting function was used. Figure 2.18 illustrates the comparison of the analyzer measured strain and the weighted average strain for a localized stretching. Good agreement between two measurements can be found, and the accuracy for this simulation was claimed as high as  $9.48 \mu\epsilon$ .

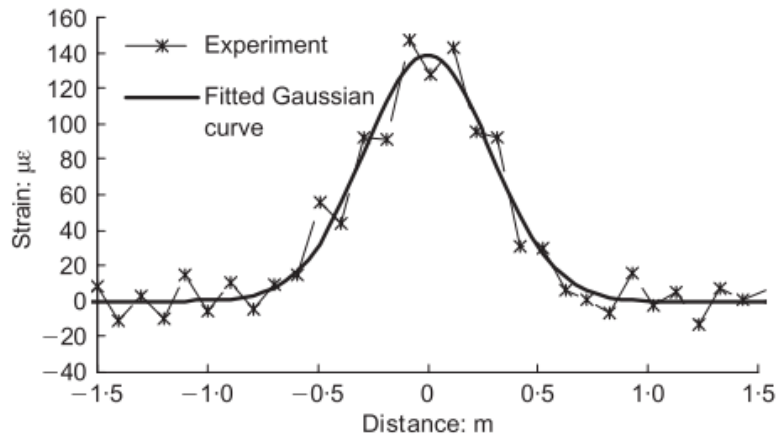


Fig. 2.18 Strain reading obtained from the analyzer measurement and the weighted averaging calculation [38]

### Brillouin conversional coefficients error

As previously reviewed, Brillouin frequency shift is proportional to the strain and temperature change of the cable. Both BOTDA and BOTDR use a conversional coefficient to convert the Brillouin frequency shift to strain/temperature measurement. However, for cables with different buffering methods, conversional coefficients are slightly different. For current available sensors, Brillouin conversional coefficients vary in a range of  $0.46 \text{ GHz}/\mu\epsilon$  –  $0.52 \text{ GHz}/\mu\epsilon$  [48]. In addition to cable property dependency, the conversional coefficients change with environmental conditions (such as temperature). Experimental results indicated that, the temperature conversional coefficient linearly decreases from  $1.113 \text{ MHz}/^\circ\text{C}$  to  $0.83 \text{ MHz}/^\circ\text{C}$  in temperature range of  $22^\circ\text{C}$  –  $800^\circ\text{C}$ , and the strain conversional coefficient linearly decreases from  $0.054 \text{ MHz}/\mu\epsilon$  to  $0.042 \text{ MHz}/\mu\epsilon$  in temperature range of  $22^\circ\text{C}$  –  $700^\circ\text{C}$  [6].

### Cable slippages

Cable slippage causes difference between the sensing fibre measured strain and the true strain of the tested structure. For example, at a fixation point, strain rapidly transfers from one cable layer to another, and the interfaces between cable layers will experience a large shear stress. When that large shear stress surpasses the maximum shear stress that can bond layers together, layers will glide against each other and slippage occurs [33]. In the same way occurs slippage between the sensing cable and the fixation devices.

A method to quantify slippage between cable layers was proposed [33]. The targeted measurements were the strain limit above which slippage occurs, and the slippage progression

along the cable. The applied optical measuring device was a Brillouin Echo Distributed Sensing (BEDS) analyzer, with a very accurate spatial resolution of  $0.01\text{ m}$ . The experimental results (Fig. 2.19) did show that there was slippage of the cable inside the protection layer. The larger the applied strain, the more significant slippage effects occurred at the fixation point of the cable. However, for most types of strain sensing cables, slippage propagates for no more than one metre. Therefore, a traditional BOTDA analyzer, which has a spatial resolution of  $1\text{ m}$ , will not be affected by slippage propagation along the cable.

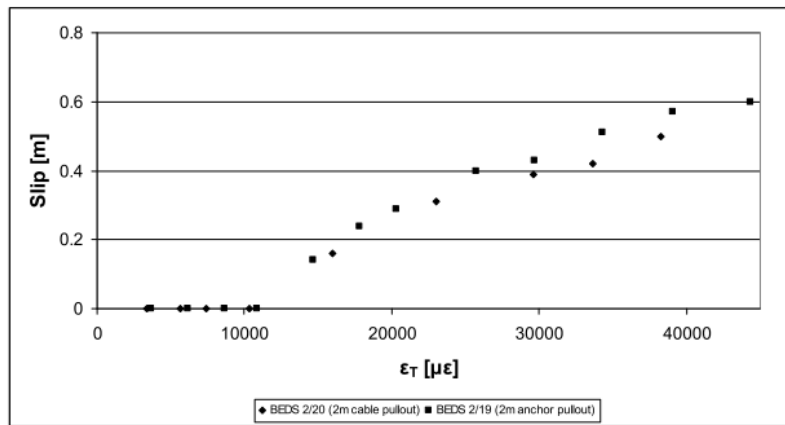


Fig. 2.19 The slippage of the cable inside the protection layer at different input strain levels [33]

### Temperature compensation process effects

Because the measured Brillouin frequency shift is a combined effect of strain and temperature change, there is a problem with distinguishing between strain and temperature, which makes it necessary to do temperature compensation during data interpretation. One solution is to use two sensing cables installed adjacent to each other: one being a normal strain sensing cable which measures the combined strain and temperature result and the other being a temperature cable isolated from strain effects. By subtracting the temperature cable measurement from the strain cable measurement, consolidated strain measurements can be obtained. However, because both the temperature cable and the strain cable have their own measurement errors (as previous site results showed), the alignment between the two cable measurement points and the subtraction process introduces more error to the temperature compensated strain result compared to the raw strain data.

Another temperature compensation method is using a separate Raman Optical Time Domain Reflectometry (ROTDR) analyzer to obtain the distributed temperature. Unlike Brillouin backscattering, which is dependent on both temperature and strain, Raman backscattering

is only dependent on temperature. Therefore, by using a cable embedded with temperature and strain sensors, strain results can be temperature compensated [42]. For a hybrid system, the measurement distance can achieve as long as 25 km, and in the mean time keep a high measurement resolution equivalent to 0.27 °C and 30  $\mu\epsilon$ .

The last method is the BOTDR-OTDR technique. This technique uses one polarization maintaining fibre to exploit both Brillouin frequency shift and Brillouin power gain information for simultaneous strain and temperature measurement. Experimental results revealed that both the Brillouin gain and centre frequency of an optical fibre are proportional to strain and temperature [35]. By solving two equations regarding the frequency shift and peak power change, it will be achievable to simultaneously measure strain and temperature along one single fibre.

However, in real geotechnical applications, this simultaneous strain and temperature monitoring method induces large error to the temperature compensated strain. For example, in the previously reviewed RCC dam site in Brazil, the data reliability of the raw strain data is at a level of 70  $\mu\epsilon$ , while after temperature compensation the calculated strain has a significant decrease in data reliability. As shown in Fig. 2.20, the measurement uncertainty grows to even more than 1000  $\mu\epsilon$  at the end of the cable [27]. The simultaneous strain and temperature monitoring method still needs more investigation on its reliability.

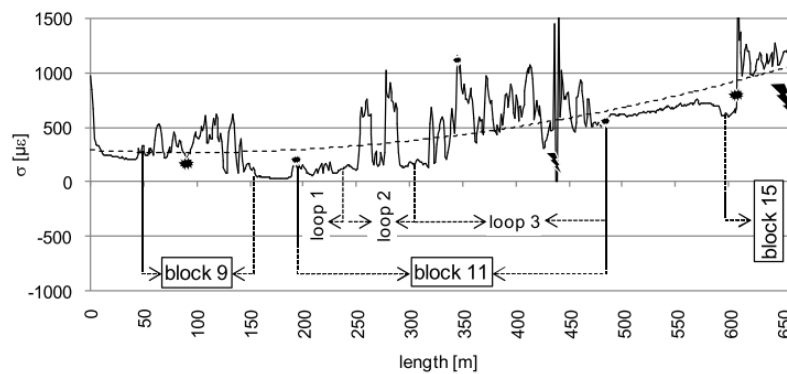


Fig. 2.20 Data quality of the simultaneous strain and temperature measurement along the sensing cable length for the RCC Dam [27]

## 2.3 Data interpretation

The Brillouin distributed fibre optics sensing measurement has various inevitable errors and it is unrealistic to evaluate structural conditions using data directly acquired from the distributed fibre optics sensor without considering measurement error. Data interpretation

algorithms have been developed to compensate for errors and reconstruct the strain profiles as much as possible using the analyzer measured strain and temperature information for site applications [39][54][53][16][24]. This section provides a detailed review of structural reconstruction methods through discussing the principle of algorithm reliability based on some real application results.

### 2.3.1 Conversional coefficients calibration

Although the Brillouin conversional coefficient for the single mode fibre is known, calibration is necessary for different types of sensing cables. The strain calibration process can be accomplished by mounting the sensor to a beam (Fig. 2.21) which is installed with a step motor to produce a known strain. The calibrated coefficient results were  $0.0507 \text{ MHz}/\mu\epsilon$ ,  $0.0500 \text{ MHz}/\mu\epsilon$ ,  $0.0455 \text{ MHz}/\mu\epsilon$  and  $0.0500 \text{ MHz}/\mu\epsilon$  for a bare single mode fibre (BSM), a tight-buffered single mode fibre (TSM), a single mode fibre protected by a polyamide layer (P07) and a Polyurethane protected strain cable (S08) [33].

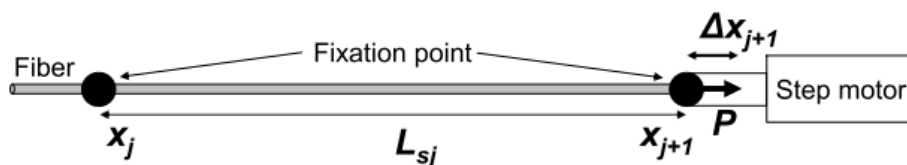


Fig. 2.21 Strain calibration beam [33]

Similar to the strain calibration process, temperature calibration exploits a temperature controlling system to change the temperature of the sensor (Fig. 2.22). The results indicated that a cable jacket significantly affects the sensitivity of the temperature sensor with a dependent relationship between the jacket thermal expansion coefficient and the sensor's temperature conversional coefficient [51]. In addition, experimental results showed that with temperature increase, thermal induced strain developed in some sections of the cable which needs further investigation.

### 2.3.2 De-noising

The wavelet de-noising method was proposed to filter noise from the measured raw data for the distributed fibre optics sensor based on Brillouin backscattering. This is an effective method developed from the Fourier transform, whose "multiscale" character enables it to comprehensively reflect the abnormality and the changes of signal at different scales. Figure 2.23 graphically illustrates the process of wavelet de-noising. If  $S$  is a section of raw signal, it

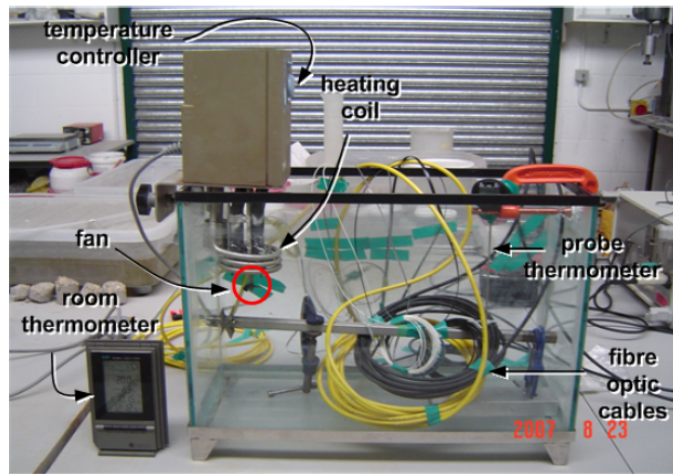


Fig. 2.22 Picture of the water tank for temperature calibration [51]

can be separated into a low frequency component (called approximation  $A_i$  in the figure) and a high frequency component (called detail  $D_i$  in the figure). The raw data can be decomposed in this way [26].

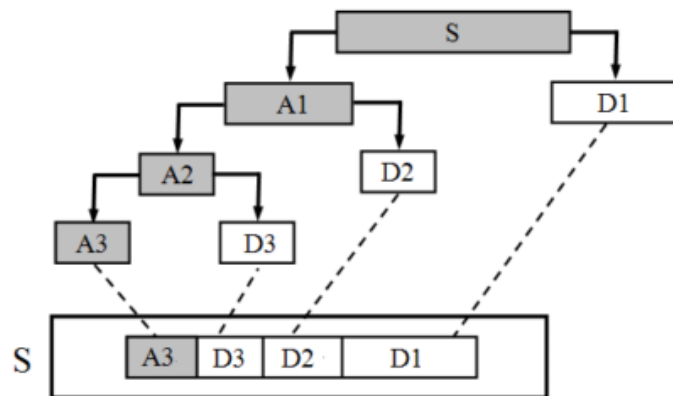


Fig. 2.23 Illustration of wavelet decomposition [26]

The raw signal of the distributed fibre sensor can be represented as:

$$s(k) = f(k) + \varepsilon \cdot e(k), k = 0, 1, 2, \dots, n - 1 \quad (2.37)$$

where  $s(k)$  is the raw data,  $f(k)$  is the desirable signal, and  $e(k)$  is the Gaussian noise signal. In the wavelet denoise process,  $e(k)$  and  $f(k)$  can be seen as  $D$  and  $A$  considering their frequency components. The filtering process mainly removes high-frequency noise  $D$  as much as possible and reconstructs the low-frequency  $A$  by using the principle that the Lipschitz index of noise is negative.

After applying the wavelet de-noising method, the measurement fluctuation due to noise can be minimized. The experimental measurement result (Fig. 2.24) indicated that with the wavelet de-noising technique, the fluctuation of the measured Brillouin frequency shift is largely reduced without affecting its accuracy in monitoring the real force.

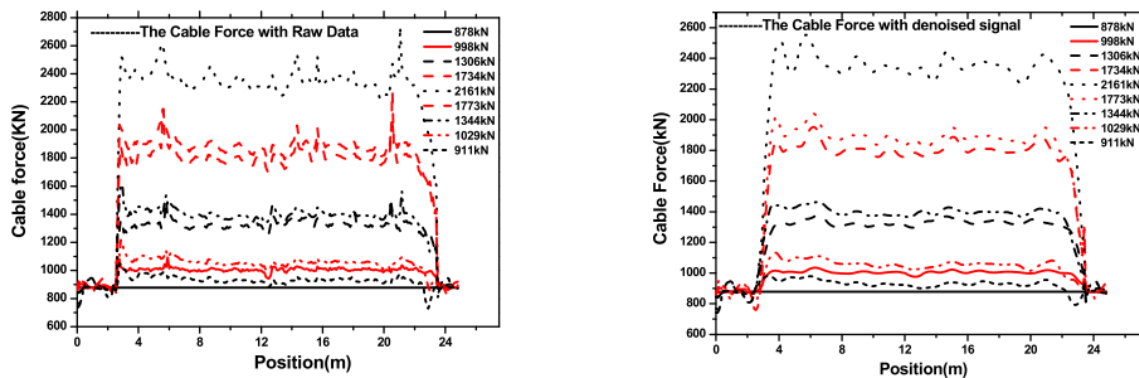


Fig. 2.24 Raw data (left) and wavelet-denoised data (right) of the distributed force readings under different loadings [26]

Another method to de-noise measurement results is rolling filtering. As the BOTDR analyzer measures a weighted average of strain over spatial resolution, a rolling filter (such as a Savitzky-Golay filter) was therefore proposed for noise reduction [77]. This method minimizes the least squares error in fitting a polynomial to each frame of the data. By adopting a rolling-frame approach, the heights and widths of the curves can be well preserved.

### 2.3.3 Deconvolution

The distributed fibre optics sensor measures a convoluted strain result, since its measured Brillouin spectrum is a convolution of the intrinsic Lorentz distribution with the injected pulse. The deconvolution process can be conducted on either the strain or spectrum profile. The spectrum deconvolution method is more fundamental and accurate, but it currently has some limitations such as it only being suitable for uniform strain distribution conditions, and takes a longer time in processing than the strain deconvolution method.

#### Strain deconvolution

Based on the assumption that BOTDR measured strain is a weighted average result, a least squares approach that minimizes the error between the measured strain ( $\epsilon_{Ai}^*$ ) and the calculated strain ( $\epsilon_{Ai}$ ) was proposed for strain deconvolution [14]. In this process, the weighted average function follows a Gaussian distribution with a characterized bandwidth of 0.3 m to 0.45 m.

The main principle of this algorithm is that the analyzer measured strain is the convolution of the real strain with the weight function. By inversely multiplying the weight function matrix with the analyzer measured strain, one real strain profile can be obtained. This strain matrix is then processed forwardly, that is to convolute it with the weight function and generates the calculated strain ( $\epsilon_{Ai}$ ). By minimising the difference between the calculated strain and the analyzer measured strain, the real strain profile can be finally reconstructed.

Figure 2.25 represents the measured strain and the deconvoluted strain. It can be found that gradual strain change was converted into step strain change due to this deconvolution method. This result agreed with the real condition of pre-tension in small sections for the monitored tunnel. The weight function needs more investigation into its reliability for different strain distribution shapes.

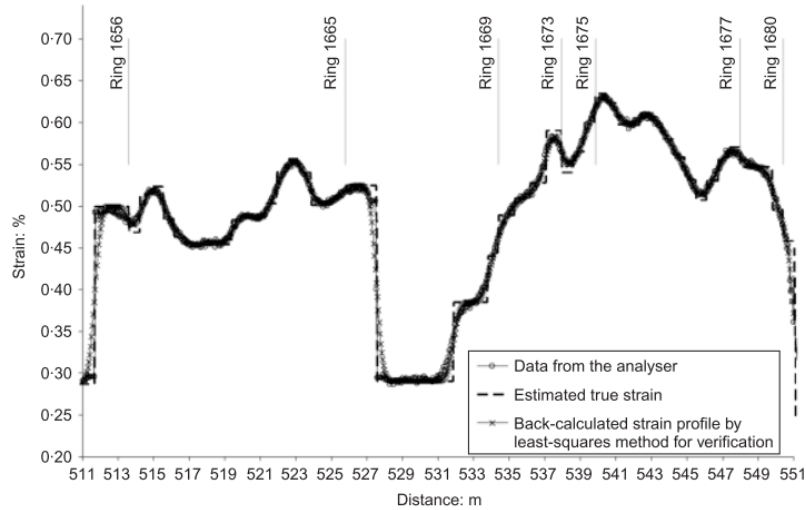


Fig. 2.25 Raw strain measurement, real strain input and de-convoluted strain measurement along cable length [14]

A finite element model was developed to reconstruct the structural conditions, not only exploiting the weight function assumption but also considering the reliability of the distributed strain data, which can be obtained from the characteristics of the Brillouin scattering based optical fibre sensor measurement [65]. The model was constructed consisting of  $N^N$  nodes and  $N^M$  elements. Based on this the strain is derived as:

$$\delta = [G^T W G]^{-1} G^T W d \quad (2.38)$$

in which  $G$  is the coordinate vector matrix,  $W$  is the weight matrix for each data point representing data reliability, and  $d$  is the matrix for the measured strain and in the form of:

$$[x_1 y_1 : : x_{ND} y_{ND}] \quad (2.39)$$

The algorithm was verified using experimental results which indicated that the strain construction accuracy was greatly improved by using weight values determined from the non-uniformity index of the strain distribution profile for each data point (Fig. 2.26). In this experiment, the load was applied to the plane around the corner  $(x, y) = (0, 500)$ . The black lines are the strain reconstruction results using data weight values and the grey lines do not use weight values during strain reconstruction process. The error between the reconstructed strain and the real strain is  $0.75 \text{ mm}$  for the black lines and  $0.97 \text{ mm}$  for the black lines. The accuracy of the reconstructed strain is improved by 20% using this strain deconvolution algorithm.

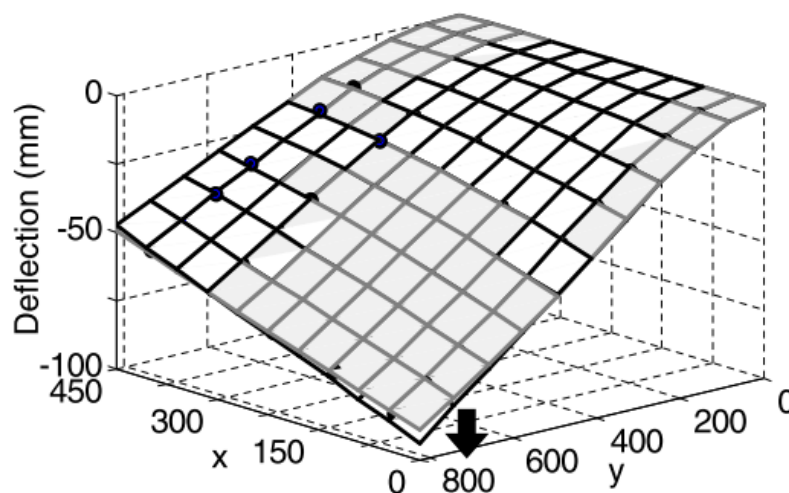


Fig. 2.26 The reconstructed strain results with using data weight values (black lines) and without using data weight values (grey lines) for a point loaded plane [65]

The remarkable point of this method is that using not only the raw strain data but also information regarding the non-uniformity of the strain distribution profiles, the algorithm considers the data reliability for accurate shape reconstructions. However, the strain shape dependent weight function makes this algorithm only suitable for simple strain distribution cases. The design process of structures commonly involves numerical analysis and the strain distribution of deformation modes has to be preliminarily figured out, further limiting the applicability of this algorithm.

### 2.3.4 Spectrum deconvolution

A more fundamental way to de-convolute the measured data is by solving the convolution function of the intrinsic Brillouin Lorentz shape spectrum and the injected pulse spectrum [91]. For a simplified uniform strain change case where the strain change length is less than spatial resolution (Fig. 2.27), the Brillouin spectrum can be given as:

$$G_i(\nu) = \int_{z_i-\Delta z/2}^{z_i-\Delta z/2+l} g\nu, \nu_B[\varepsilon(z)]dz + \int_{z_i-\Delta z/2}^{z_i-\Delta z/2+l} g\nu, \nu_B(0)dz \quad (2.40)$$

in which  $l$  is the length of the strained fibre and is in the range of 0 and  $\Delta z$ ,  $\nu_B\varepsilon(z)$  is the

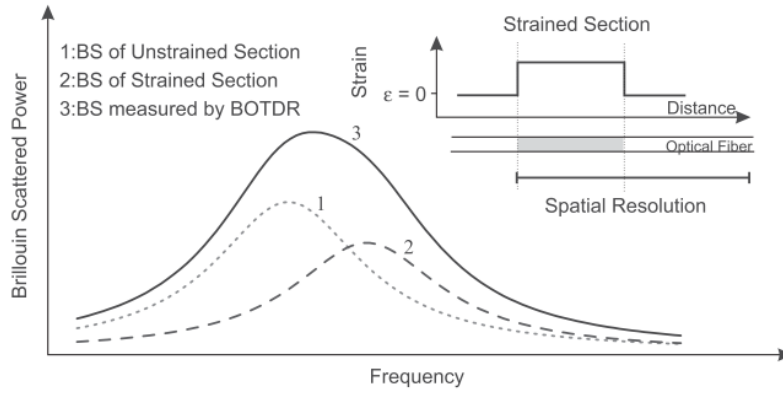


Fig. 2.27 Illustration of the Brillouin spectrum at strained and unstrained sections as well as analyzer measurement [91]

Brillouin frequency shift at the strained section, and  $\nu_B(0)$  is the Brillouin frequency shift with no strain change. Substituting Lorentz shape Brillouin gain distribution into Eq. 2.40, it is changed into:

$$G_i(\nu) = \frac{g_0(\Delta\nu_B/2)^2}{(\nu - \nu_g(0) - \Delta\nu(\varepsilon))^2 + (\Delta\nu_B/2)^2}l + \frac{g_0(\Delta\nu_B/2)^2}{(\nu - \nu_g(0))^2 + (\Delta\nu_B/2)^2}(\Delta z - l) \quad (2.41)$$

Equation 2.41 can be solved as a 5<sup>th</sup> order polynomial equation [91]. Based on this, the characteristics of the superposed Brillouin power spectrum, as well as the dependence of the calculated strain of BOTDR on the actual strain of the fibre, were investigated for the Brillouin power spectrum of a partially uniformly strained fibre within the spatial resolution.

Figure 2.28 illustrates the reliability of this spectrum deconvolution method by showing the relationship between the measurement relative error  $RE$  and  $r$  (which is the proportion of the strained section length to the spatial resolution) at different  $\varepsilon_{NA}$  (which is the normalized actual strain). If  $r$  is larger than 0.5, the relative error is close to zero (which means the

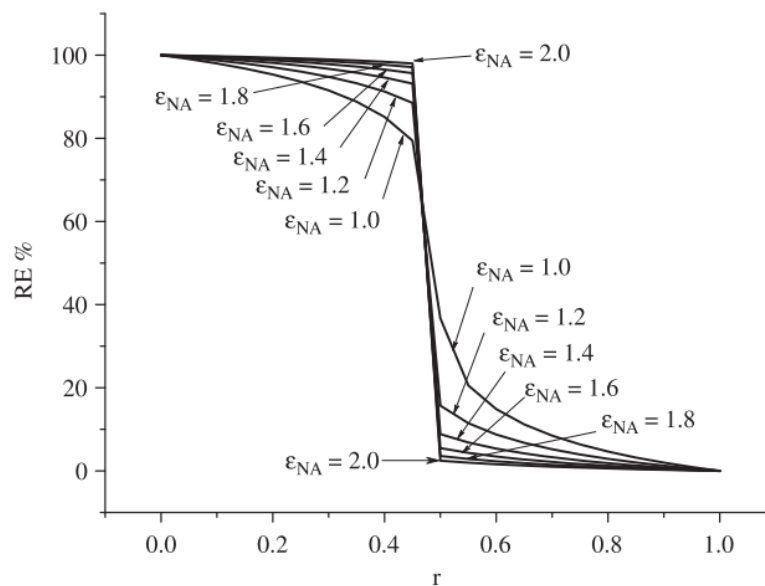


Fig. 2.28 Dependence of  $RE$  (measurement relative error) on  $r$  (ratio of strained length to spatial resolution) in different  $\epsilon_{NA}$  (normalized strain input) [91]

calculated strain is almost equal to the actual strain) with an increase of actual strain as well as  $r$ . In contrast, when  $r$  is less than 0.5, the relative error  $RE$  approaches 100% of the actual strain. In other words, the calculated strain is close to zero rather than the actual strain as the methodology automatically fits the peak of higher power within the Brillouin spectrum. As a result the calculated strain approaches 100% wrong in these cases.

However, this method is only useful for partially uniformly distributed strain and not applicable for complex strain conditions which are commonly found in real applications. Therefore, although spectrum deconvolution is a fundamental method for data interpretation, it still needs more investigation before using it for real applications.

## 2.4 Summary

Measurement of a distributed fibre optics sensor contains two types of error: systematic error and precision error. The characteristics of precision and systematic error are:

1. The precision error specifies the variation of the measurement. It is caused by the analyzer's random noise and can be minimized by averaging measurements. For a typical BOTDR analyzer, its precision error follows a normal distribution with a bandwidth of  $15 \mu\epsilon$ .

2. The precision error can be quantified by SNR, FWHM and frequency scanning step. The influence of the strain non-uniformity and distance precision on the precision error needs more thorough investigation.
3. The systematic error is the difference between the measurement and the real condition. For a Brillouin Optical Time Domain Reflectometry (BOTDR) analyzer, systematic error is mostly related to the spatial resolution of the analyzer, which is the minimum distance over which the sensor can indicate the value of the measurement within the specified uncertainty.
4. The systematic error is related to the pulse length of the analyzer as its measured spectrum is a convolution of the pulse width with a natural Brillouin gain distribution. The convolution process can be simulated as a weighted average process. However the weight function is dependent on the strain profile which limits the applicability of this simulation.



# Chapter 3

## Sensor Calibration

The key performance characteristics of a distributed fibre optics sensor can vary significantly using fibres with different cable tight buffering methods. There have been a number of calibration units reported in the past few years to evaluate sensor performance. For example, a robust strain calibration device was developed in Zurich to calibrate the strain sensing cable parameters including cable longitudinal stiffness, yield strain, Brillouin conversional coefficient and fibre slippage [33]. A simple water tank was designed to compare the temperature coefficients for different types of sensing cables [52] and a new ‘dissimilar-fibre-splicing’ method was proposed to calibrate the sensor spatial resolution [89]. Most previous calibration experiment results have verified that the sensing result varies with cables. It is therefore essential to calibrate the sensor and its measurement accuracy before applying it to real site cases.

Chapter 3 presents the experimental work conducted in the lab to calibrate the measurement performance and associated errors of different optical fibre sensors. Single mode fibres with different diameters and a polarization maintaining fibre were tested and compared to BOTDR measurement consistency over repeated readings. Several strain sensing cables, normally used for current infrastructure monitoring cases, were characterized according to measurement accuracy, hysteresis, and the linearity between the measured Brillouin scattered frequency shift and the input strain change. Experiments were conducted using a newly developed strain calibration platform, which consisted of an aluminium rig and a micrometer mounted onto it that automatically stretched the tested cable. Using a temperature calibration unit, which can control the embedded cable’s temperature accurately and precisely, the thermal characteristics of a temperature sensing cable, a strain sensing cable and a bare optical fibre were investigated with regard to potential errors in the temperature compensation process.

### 3.1 Optical fibre characterization

The characteristics of the optical fibres were first characterized under a constant strain and temperature condition. The tests investigated the effect of the sensing fibre core diameter, the variation of the polarization along the cable, and the effect of the buffered cable jacket on the BOTDR measurement error. A Neubrex NBX-5000 BOTDR analyzer was used to record the Brillouin centre frequency shift profile along the tested cables. The set up of the analyzer was: 1 m spatial resolution, 3 MHz frequency scanning step,  $2^{16}$  averages, and 5 cm sampling resolution, same for all the tests. The tested cables included: standard single mode fibre with different core diameters, polarization maintaining single mode fibre, and steel wire reinforced strain sensing cable.

#### 3.1.1 Fibre diameter effect characterization

The Brillouin centre frequency shift profile of four single mode fibres (SMF-28 from Corning Co. Ltd) with different core and cladding diameters were recorded repeatedly to investigate the influence of fibre diameter on the measurement precision error. The diameters of the tested fibres are listed in Table 3.1. One hundred repeated Brillouin centre frequency readings were taken for each tested fibre. At each measuring location, the measurement precision error was calculated as the standard deviation of the 100 repeated measurements .

Table 3.1 Core and cladding diameters of the tested single mode fibres

Fibres	Core diameters ( $\mu m$ )	Cladding diameters ( $\mu m$ )
Fibre (a)	4.2	125
Fibre (b)	6.4	125
Fibre (c)	6.4	80
Fibre (d)	7.8	125

Measurement results of the tested fibres in 10 m length were used to compare the sensing performance. Figure 3.1 to 3.4 illustrate the mean Brillouin centre frequency (red line) of the 100 repeated measurements along the fibre length with the precision error displayed as grey error bars for four tested fibres. The Brillouin centre frequency of the four tested fibres is different: 9.648 GHz – 9.649 GHz for fibre (a) and 10.3615 GHz – 10.3625 GHz for fibre (b)). The mean value of the Brillouin centre frequency measurements (the red line in the figures) varies over distance for the tested fibres, which is probably due to the strain induced by cabling process. However, the spatial variation of the Brillouin centre frequency is very

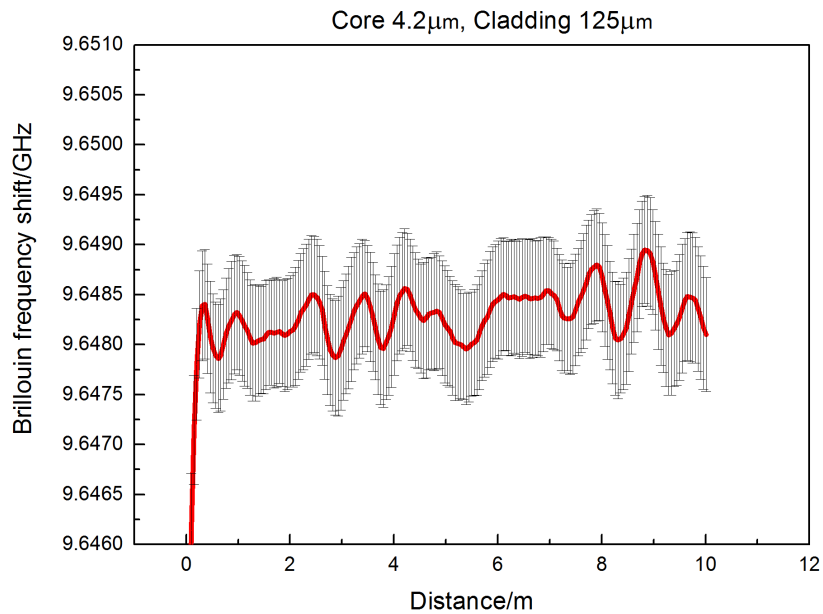


Fig. 3.1 Brillouin centre frequency measurement (with precision error shown as grey error bar) of fibre (a) which has 4.2  $\mu\text{m}$  core and 125  $\mu\text{m}$  cladding diameter

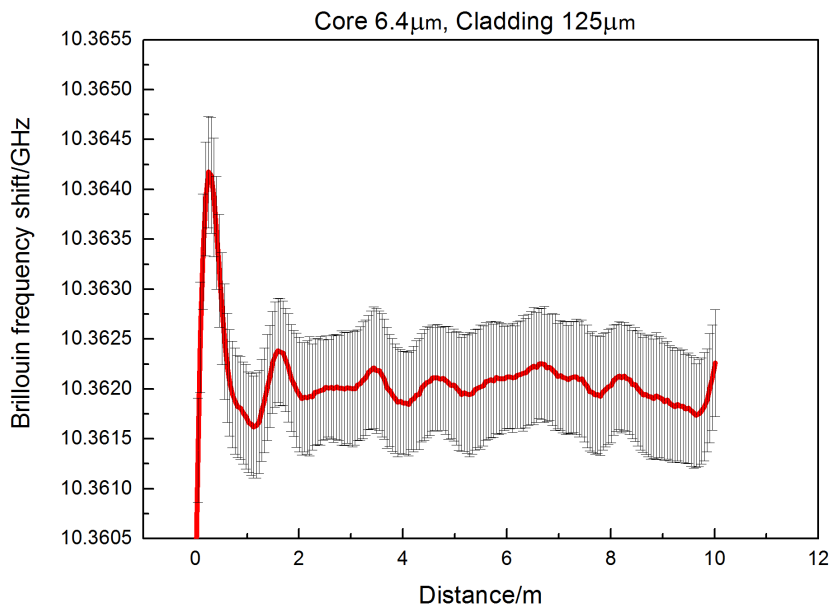


Fig. 3.2 Brillouin centre frequency measurement (with precision error shown as grey error bar) of fibre (b) which has 6.4  $\mu\text{m}$  core and 125  $\mu\text{m}$  cladding diameter

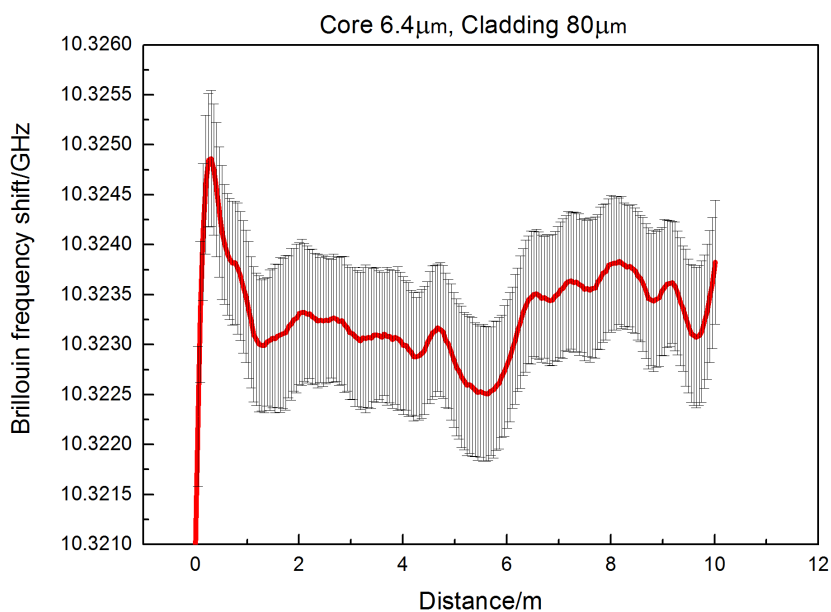


Fig. 3.3 Brillouin centre frequency measurement (with precision error shown as grey error bar) of fibre (c) which has 6.4  $\mu\text{m}$  core and 85  $\mu\text{m}$  cladding diameter

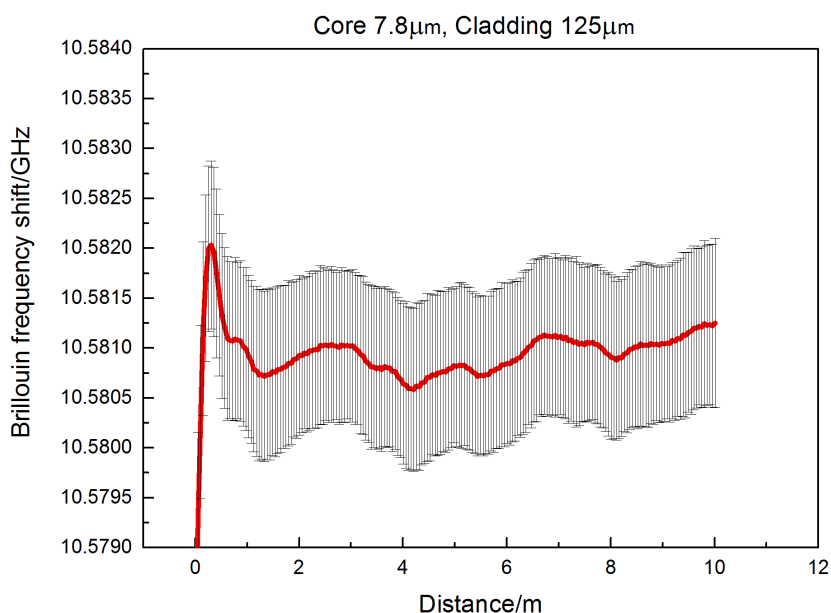


Fig. 3.4 Brillouin centre frequency measurement (with precision error shown as grey error bar) of fibre (d) which has 7.8  $\mu\text{m}$  core and 125  $\mu\text{m}$  cladding diameter

small and the precision error (grey error bar) seems not influenced by this, as the grey bar looks constant over distance.

The characteristics of strain precision error over fibre length is studied. Figure 3.5 to 3.8 show the histograms of strain precision error obtained over each tested fibre. As the histogram can be well fitted by a normal distribution curve (red lines in the figure) for the four tested fibre, the precision errors are characterized as normally distributed over distance. The peak value of the fitted curve is therefore used to represent the measurement precision of the fibres.

The precision error result for the tested fibres are  $11.2\ \mu\epsilon$ ,  $11.4\ \mu\epsilon$ ,  $14.8\ \mu\epsilon$  and  $16.2\ \mu\epsilon$  respectively as shown in Table 3.2). Fibres (a), (b) and (d) indicate that a bigger core tends to lead a larger measurement precision error. This phenomena is not significant for Fibre (a) and (b) as the difference in strain measurement is very small ( $0.2\ \mu\epsilon$ ). However the difference between fibre (b) and (d) is large enough to show this effect tend. Fibres (b) and (c) indicate that a smaller cladding diameter leads to a larger precision error. In general, a trend can be found from the test results, in which a bigger core and a smaller cladding of the sensing optical fibre can cause a larger measurement precision error for the distributed fibre topics sensor. An extra  $5\ \mu\epsilon$  precision error can be induced due to a bigger core and smaller cladding of the sensing fibre.

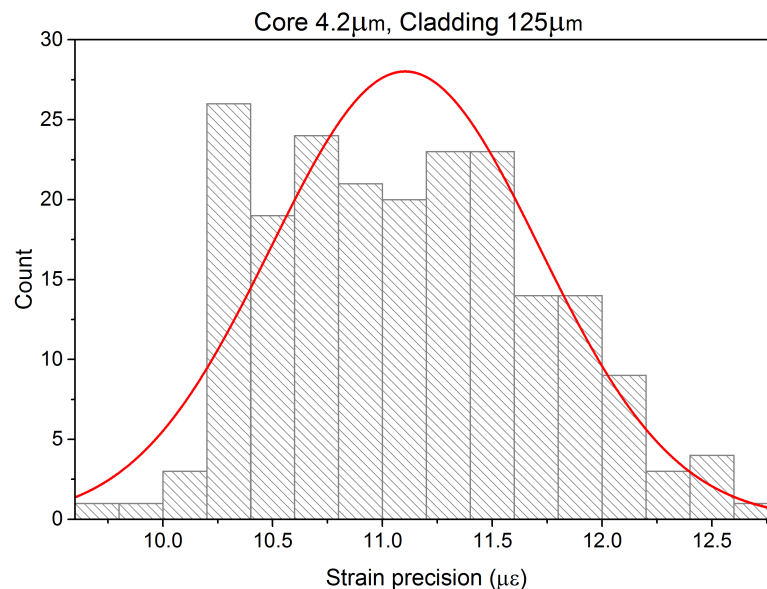


Fig. 3.5 The histogram of strain precision error obtained along fibre (a) which has  $4.2\ \mu\text{m}$  core and  $125\ \mu\text{m}$  cladding diameter

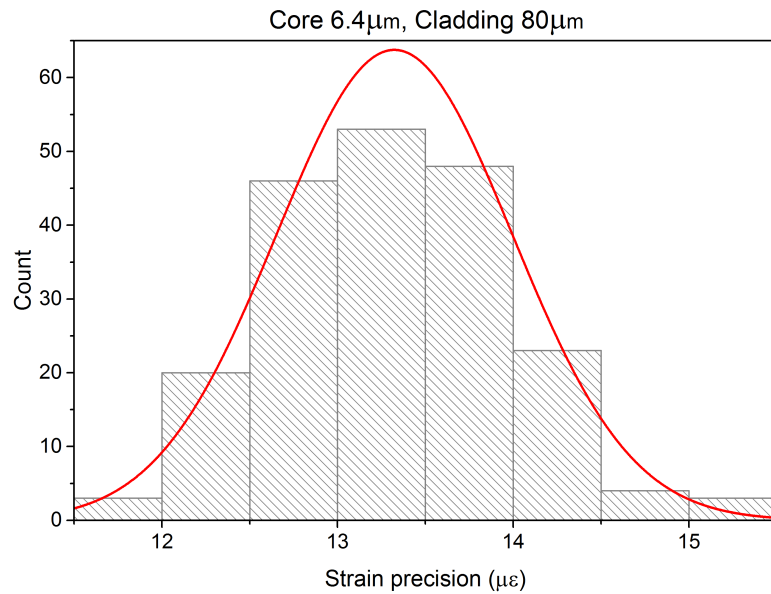


Fig. 3.6 The histogram of strain precision error obtained along fibre (a) which has 6.4  $\mu\text{m}$  core and 125  $\mu\text{m}$  cladding diameter

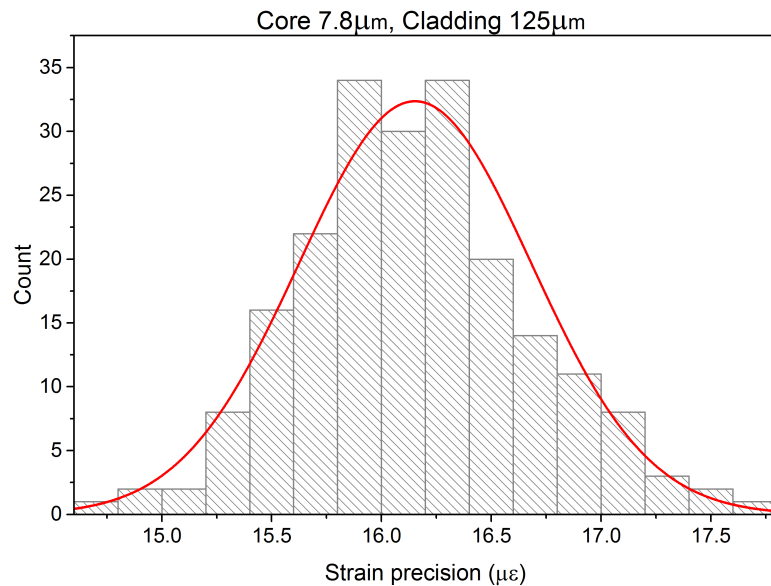


Fig. 3.7 The histogram of strain precision error obtained along fibre (a) which has 6.4  $\mu\text{m}$  core and 80  $\mu\text{m}$  cladding diameter

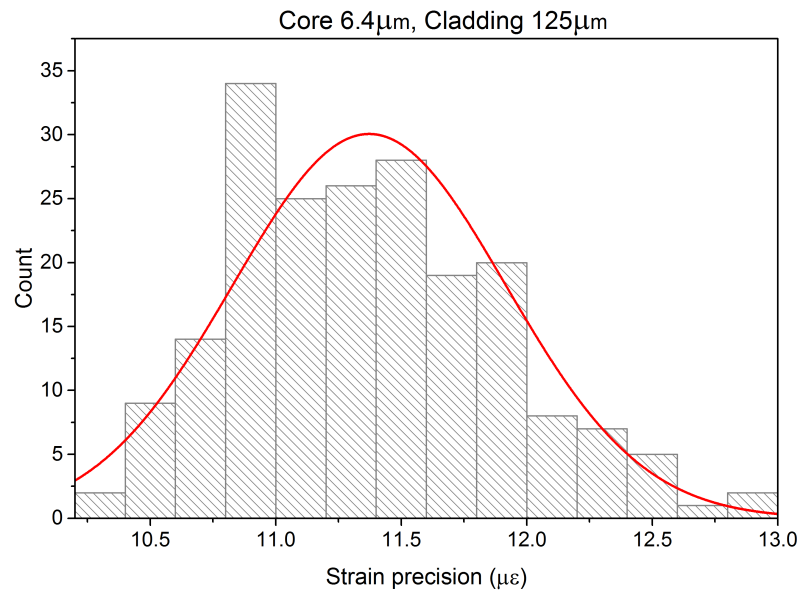


Fig. 3.8 The histogram of strain precision error obtained along fibre (a) which has 7.8  $\mu\text{m}$  core and 125  $\mu\text{m}$  cladding diameter

Table 3.2 The mean Brillouin centre frequency, frequency precision error, and equivalent strain error of the 100 repeated measurements for the four tested fibres

Fibres	Core diameters ( $\mu\text{m}$ )	Cladding diameters( $\mu\text{m}$ )	Strain precision ( $\mu\epsilon$ )
Fibre (a)	4.2	125	11.2
Fibre (b)	6.4	125	11.4
Fibre (c)	6.4	80	14.8
Fibre (d)	7.8	125	16.2

### 3.1.2 Polarization effect characterization

Polarization describes the oscillating direction of the light transferring through an optical fibre [66]. The speed of the propagating light in an optical fibre is determined by the fibre refractive index. When the fibre is absolutely symmetric, the oscillating direction of the injected pulse will not influence its propagating velocity since it 'sees' the same refractive indexes. However in real cases, the fibre is manufactured non-perfectly concentric due to external strain applied on the fiber during cabling process (e.g. bending and twisting) [34]. As a result, the optical wave velocity in the normal single mode fiber is affected by the polarization state of the input light.

A polarization maintaining fibre induces an excessive asymmetric refractive index profile to ensure only one polarization state of the injected pulse can be transferred through the fibre. For example, the Panda polarization maintaining fibre embedded two rods at the sides of the fibre to permanently stress the fibre core and makes the fibre geometrically asymmetric. In this way, the transferring velocity of the injected pulse becomes independent on the polarization.

To illustrate the influence of the fibre polarization on the measurement characteristics in BOTDR sensing systems, a comparison between two different fibre optic cables, namely Coning SMF-28 single mode fibre (SMF) and Panda polarization maintaining fibre (PMF) was made. The two cable types were compared using two different commercial BOTDR analyzers: Neubrex NBX-5000 BOTDR analyzer and Yokogawa AQ8603 BOTDR analyzer. Both the SMF and PMF cables were of the same length (100m), and were tested under no strain or temperature change condition. In total, 100 measurements were taken over a period of around 14 hours. A section of the interpreted strain data is presented in Fig. 3.9.

Statistical analysis on the 100 measurements indicated that the precision errors of the PMF and SMF cables were  $11.3 \mu\epsilon$  and  $14.7 \mu\epsilon$  for the NBX-5000, and  $27.7 \mu\epsilon$  and  $30.9 \mu\epsilon$  for the AQ8603, respectively. Note that both analyzers testing results suggested that the measurement precision error in PMF was about  $3 \mu\epsilon$  ( $0.15 \text{ MHz}$ ) lower than that of SMF. Because BOTDR measured result is a convolution of spectra over the analyzer's spatial resolution, the light velocity variance causes the broadening and asymmetry of the Brillouin gain spectrum (BGS) and thus contributes to the variation of the measured Brillouin centre frequency. Similar results were also reported in a fibre polarization characterization study [84]. These results implied that fibre polarization can induce  $0.15 \text{ MHz}$  (equivalent to  $3 \mu\epsilon$ ) error to the measurement result.

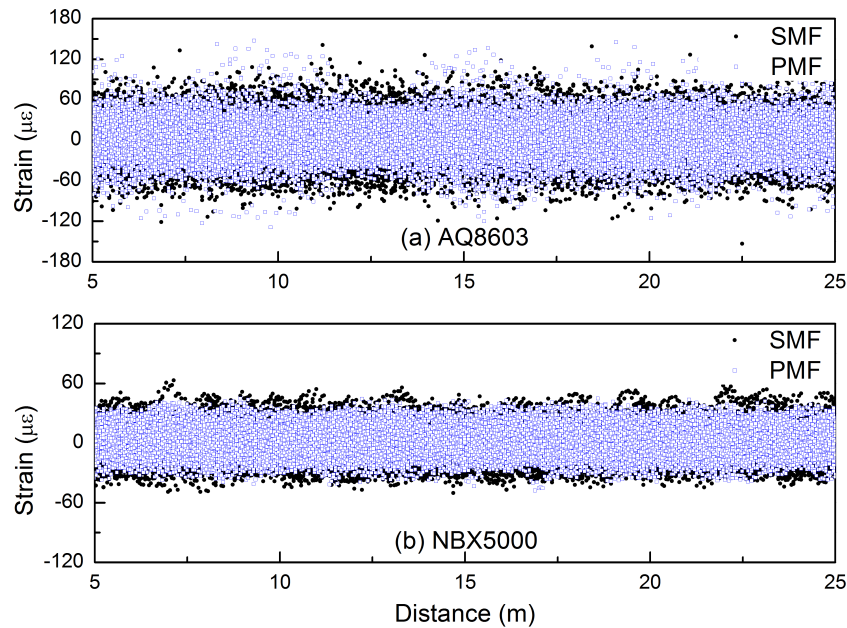


Fig. 3.9 Strain measurements of a single mode fibre and a polarization maintaining fibre using analyzer (a) AQ8603 and (b) NBX5000

### 3.1.3 Cable jacket effect characterization

The effect of strain sensing cable jacket (the tight buffered protection layer) on the BOTDR measurement precision error was characterized using 100m of the single mode fibre (Corning-28 SMF cable) and 100m of strain sensing cable (Fujikura reinforced strain cable). The SMF cable was bare fibre with no jacket protection. The reinforced strain cable has four embedded single mode fibres, wrapped with a layer of nylon jacket as a protection. The tested analyzer was NBX-5000 BOTDR analyzer. The tests were conducted at room temperature. The BOTDR analyzer settings were same as the previous set up.

Figure 3.10 represents the mean value of 100 repeated readings taken by the BOTDR analyzer. The strain cable result shows some periodic Brillouin centre frequency change which is the pre-strain of the cable. The base result of the strain cable is about 10.79 GHz and the pre-strained Brillouin centre frequency level is close to 10.81 GHz (equivalent to 1400 µε). Besides pre-strain, a higher frequency variation of the Brillouin frequency shift of the strain sensing cable is found in a range of 0.01 GHz along the cable, much larger than the bare fibre, which displayed a variation of less than 0.005 GHz. The possible reason for the higher frequency variation could be the non-perfect concentric inhomogeneity of the

optical fibre in manufacturing design, as well as external strain applied to the fibre cabling (e.g. bending and twisting) [66].

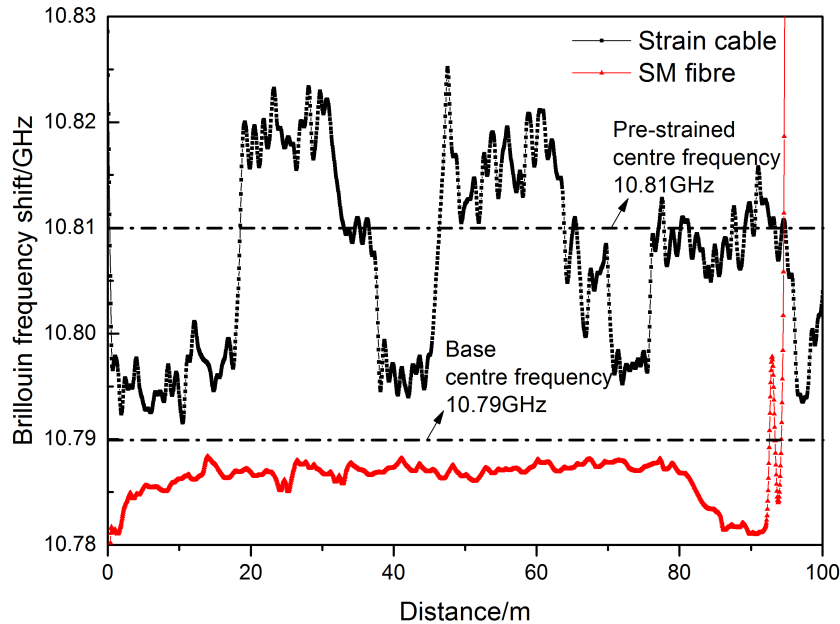


Fig. 3.10 Brillouin centre frequency measurement of the strain sensing cable and the single mode fibre

The precision error calculation results indicate that the cable jacket or the initial non-uniform strain measurement of the strain sensing cable affects the BOTDR measurement. Figure 3.11 compares the measurement precision error of the strain sensing cable and the single mode fibre. Strain variance is calculated as the standard deviation of the 100 repeated measurements recorded at each measuring point of the tested cable. It is found that, for both cables, the measurement precision error was scattered along the cable. However, the strain sensing cable which has non-uniform initial strain presents a mean precision error of  $15.9 \mu\epsilon$ , larger than the bare fibre results ( $14.2 \mu\epsilon$ ). The cable jacket (or initial strain induced by the cabling process) induces a measurement precision error of  $1.7 \mu\epsilon$  to the BOTDR sensing system in this experiment. The relationship between strain non-uniformity and the precision error will be discussed in more detail in Chapter 5.

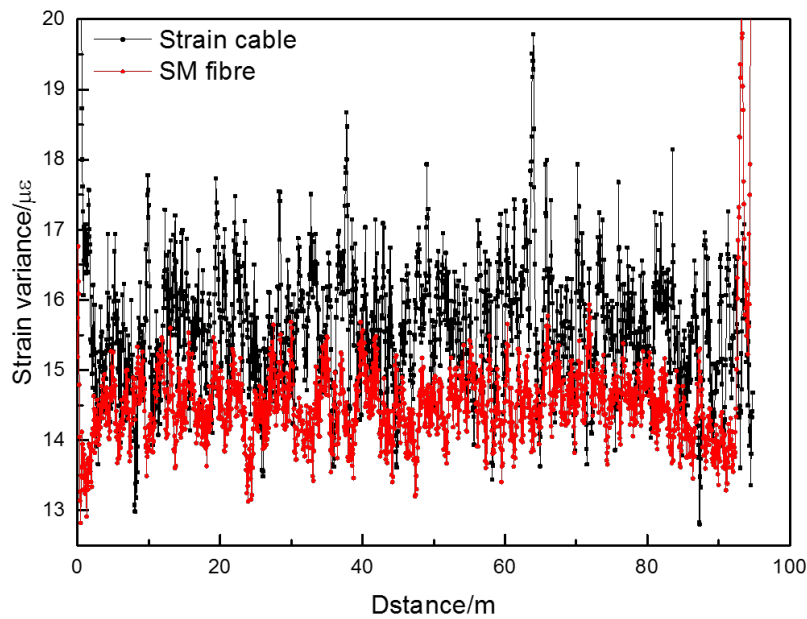


Fig. 3.11 Measurement precision error of the strain sensing cable and the single mode fibre

## 3.2 Strain calibration

To quantify the sensing characteristics of the fibre optics cables under different strain conditions, a calibration platform was established in the laboratory. This platform was made of an aluminium rig for strain calibration. The objective of this platform was to accurately change the strain condition of the tested cable while controlling the temperature of the cable in stable conditions.

### 3.2.1 Strain calibration unit

Figure 3.12 shows the strain calibration beam that was used to characterize the strain sensors. The strain calibration set up consisted of an electrical motorized linear stage to change the cable strain precisely and accurately, and an aluminium base structure to mount the micro-motor. At one end of the aluminium base was a mount for the optical fibre clamp. Another optical fibre clamp was placed upon the moving carriage of the traversing stage. Inside the clamp, there was an insert clamping bush design. This permitted the use of different cables, by using different bushes. The calibration bench was put in a temperature constant lab ( $20^{\circ}\text{C} \pm 0.5^{\circ}\text{C}$ ) to control the temperature effect on the Brillouin frequency shift readings. As

most of the strain calibration experiments were done in 1 hour (no longer than 2 hours), temperature was in quite stable condition during the short period of testing time.

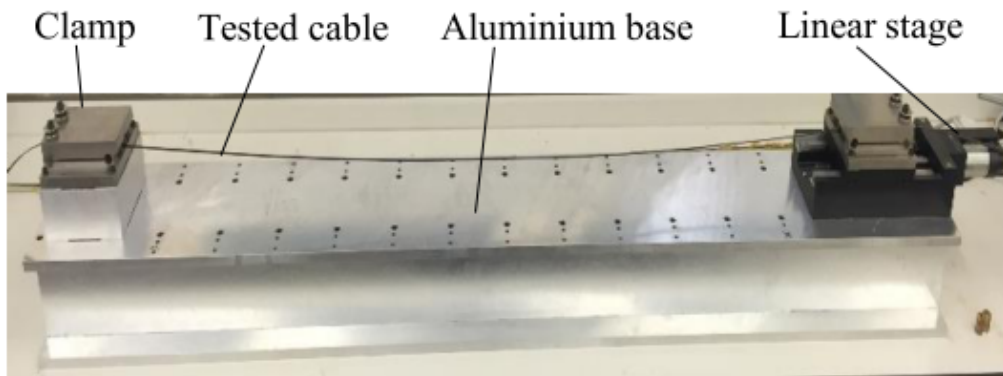


Fig. 3.12 Picture of the strain calibration beam

Previous site strain measurements showed that if the strain sensing cable's pre-strain is beyond  $3000 \mu\epsilon$ , the gel used to attach the cable to structures will start to degrade and the pre-strain will start to reduce. Therefore, the sensing cable for this strain calibration experiment was designed to be pre-strained by less than  $3000 \mu\epsilon$ . For the very robust strain sensing cable, such as steel wire reinforced cable, the force to stretch it for  $3000 \mu\epsilon$  was calculated as  $103.7 N$ .

The micro-motor for cable stretching was selected as a M414 ball-screw type precision linear stage from PI Company, considering its high performance in accurate motion control. The optical fibre could be strained by moving the linear stage in a motion resolution of less than  $0.11 \mu m$  and a positioning error specification of  $\pm 1 \mu m$ . The maximum force of the stage could achieve  $120 N$ , within the target range of the tests.

Finite element analysis of the testing rig was completed to check the positioning error of the whole mechanical structure. Figure 3.13 and 3.14 model the deflection and stress distribution of the clamp with  $100 N$  horizontal cable force applied to the bush of the clamp. The stress figure implied that the force was uniformly displayed on the clamp. Due to the fact that the clamp was mounted on the aluminium base with screws, the maximum movement of the clamp was close to  $670 \mu m$  at the upper side of the clamp and the base movement was less than  $5 \mu m$ . The base movement of the clamp indicated the positioning error of the mounted cable. Therefore, the statistical analysis results gave that when the fibre was stressed  $100 N$  horizontally, the positioning error of the structure was less than  $5 \mu m$ .

Figure 3.15 and 3.16 model the deflection and stress distribution of the clamp with  $500 N$  vertical force applied to one side of the clamp. This is to simulate the situation when the clamping force is not systematic. Because of the unbalanced force, the upper side of the

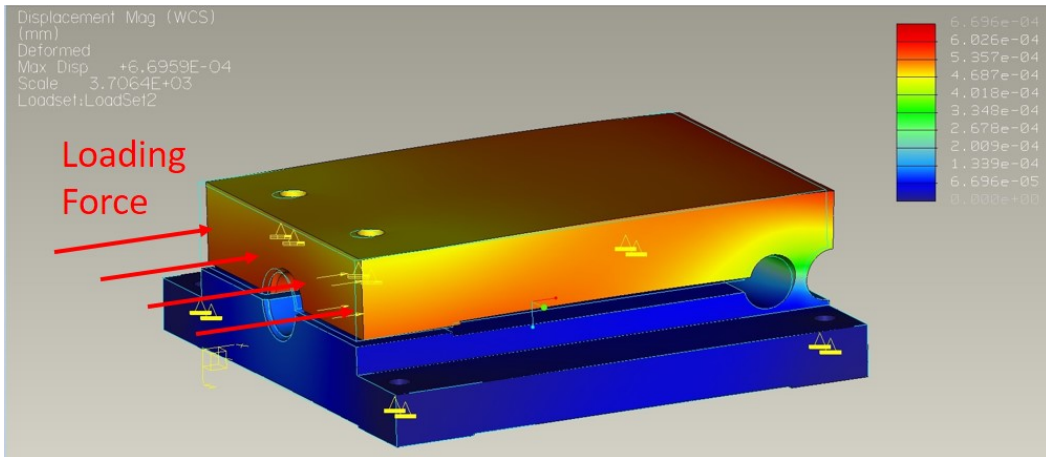


Fig. 3.13 Simulated deflection of the clamp with 100 N axial force applied

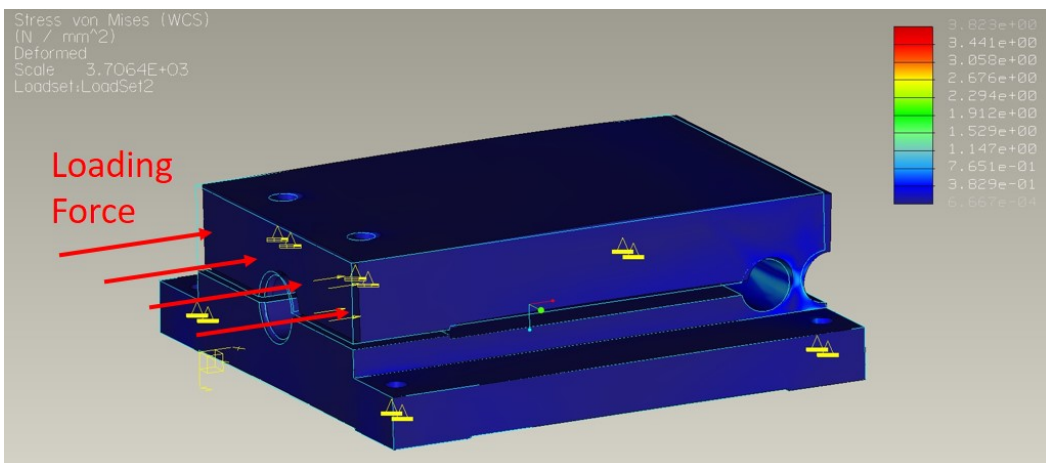


Fig. 3.14 Simulated stress of the clamp with 100 N axial force applied

clamp shows significant twist and the stress is displayed non-uniformly on the clamp section. However the displacement of the clamp base was close to  $1 \mu m$ , and therefore the precision and accuracy of the system was not influenced significantly in this case.

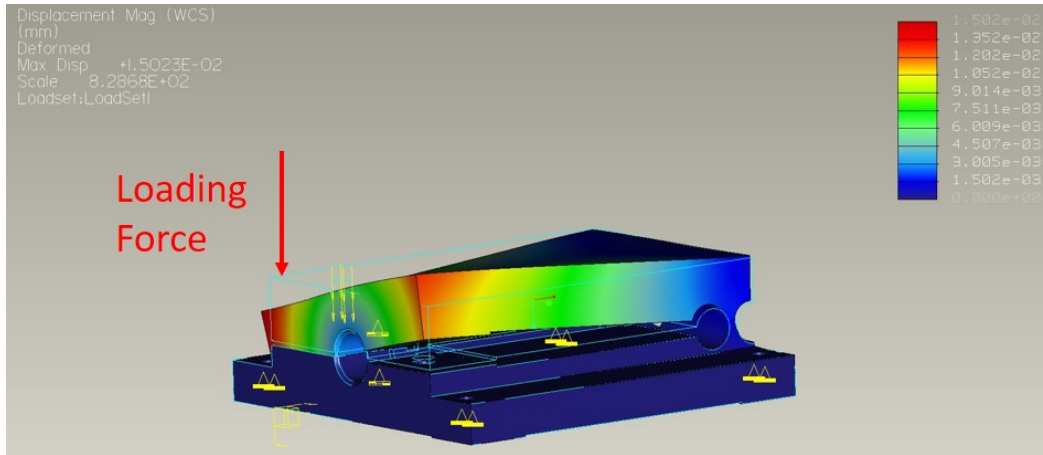


Fig. 3.15 Simulated deflection of the clamp with 500 N force applied to one side of the clamp

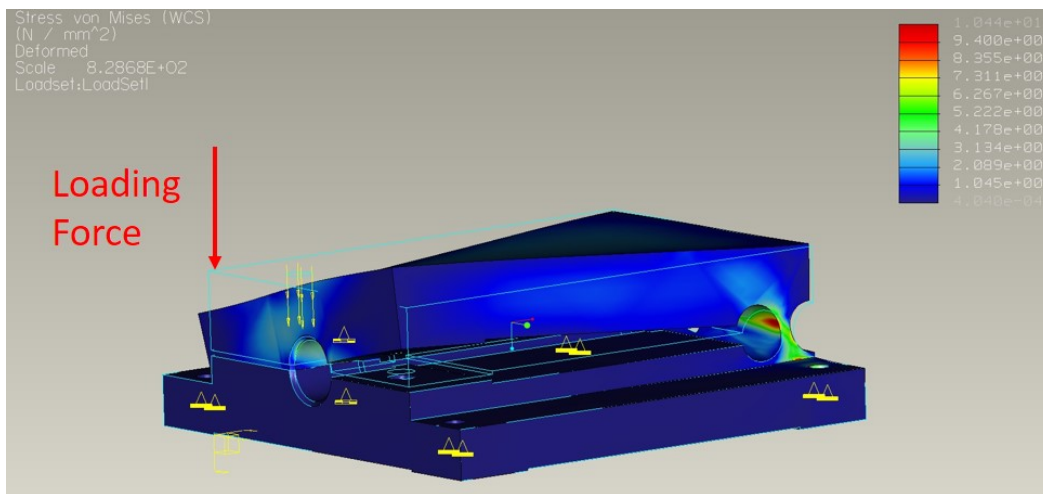


Fig. 3.16 Simulated stress of the clamp with 500 N force applied to one side of the clamp

In total, the analysis showed that there was no more than  $5 \mu m$  of mechanical compliance throughout the entire structure when the clamp was forced axially 100 N and perpendicularly 500 N. There was a further possible error of approximately  $5 \mu m$  from the linear stage. Therefore, the total positioning error was expected to be limited to  $10 \mu m$ , equivalent to  $6.67 \mu \epsilon$  considering the length of the calibration bench. The displacement resolution of the linear stage was  $0.1 \mu m$ , equivalent to  $0.067 \mu \epsilon$ . Generally, this strain calibration bench was expected to achieve stretching 1.5 m of the cable by a given displacement to a resolution of  $0.067 \mu \epsilon$  and to an accuracy of  $6.67 \mu \epsilon$ .

### 3.2.2 Strain tests

The strain calibration process generally involved: 1) holding a certain section of the cable, 2) changing its strain condition accurately and precisely, and 3) evaluating the input strain data recorded by the strain sensor with the frequency shift displayed on the analyzer. Four types of strain sensing cables were tested in the laboratory. The measurement hysteresis, accuracy, and linearity between input strain with regard to the analyzer measured strain were evaluated for each cable to quantify the cable’s sensing ability.

#### Tested cables

Table 3.3 lists the strain sensing cables that were tested in the laboratory. The Fujikura Ltd. designed strain sensing cable has four single-mode optical fibres embedded in the middle of the cable and two steel wires on the sides to reinforce the cable. The ribbon shape of the cable makes it easier to attach the cable to structures. The Brugg V1 Strain Cable has one single mode fibre tightly buffered in a round tube. The jacket of the Brugg V1 cable is robust enough so that no reinforcement is embedded in the cable. The tight buffer telecom cable from Sumitomo Ltd. has two fibres tightly buffered inside a squared protection layer. The NanZee Reinforced Strain Cable has four steel braids armouring the optics fibre. Outside the steel braids there is a protection tube which makes this cable the most robust one in the four tested strain cables. Due to the robust design, all tested sensing cables are ideal for harsh environment applications such as pipeline monitoring and burial in the soil.

Table 3.3 Illustration of four strain sensing cables

Cable	Fujikura reinforced Cable	Brugg Strain Cable	Tight buffer telecom cable	NanZee Reinforced Strain Cable
Details	Steel wire reinforced cable embedded with four single mode fibres	One up buffered optical fibre with robust outer sheath	Very compact tightly-jacketed cable	Tight buffered single mode fibre
Sketch	<p>Nylon sheath Steel wire Coated fibres</p>	<p>Plastic protection layer EPR Soft plastic buffer Coated fibre</p>	<p>PA protection layer Coated fibre Soft plastic buffer</p>	<p>Steel braids Jacket Coated fibre</p>
Picture				

## Test results

During strain calibration, the tested cables were pre-strained to  $1000\mu\epsilon$ . The Fujikura reinforced strain cable, the Brugg reinforced cable and the Nanzee reinforced cable were firstly loaded for  $1000\mu\epsilon$  in tension and released back to pre-strain condition in steps of  $100\mu\epsilon$  using the strain calibration rig.

To check the cable's sensing performance in higher strain range, the tested cables were then tensioned in larger range. The Fujikura reinforced strain cable, the tight buffer telecomm cable and the Nanzee reinforced cable were loaded and unloaded for  $2500\mu\epsilon$  in larger steps of  $250\mu\epsilon$ . The high stiffness of the tested cables limit the maximum strain ( $2500\mu\epsilon$ ) that can be applied to the cable, as the rig can not provide enough force to maintain the cable in large strain condition. Because the Brugg V1 strain cable is relatively softer, the maximum strain it can achieve is  $10000\mu\epsilon$ . Therefore, the Brugg cable was strained in steps of  $1000\mu\epsilon$  until  $10000\mu\epsilon$  for the larger strain range experiments.

During the experiment, three measurements were recorded at each strain condition, with a Neubrex (NBX-5000) BOTDR analyzer. The analyzer was set with  $0.5m$  spatial resolution and  $0.05m$  sampling resolution. Strain recorded at the cable pre-strained condition was used as a baseline reading.

Figure 3.17 to 3.20 show the results of tensile load tests on four strain sensing cables. Strain measurements at each loading/unloading level are plotted as colour lines. Step strain changes for about  $1.5m$  length of each tested cable can be clearly seen from the figure.

Comparing the strain measurement of the four tested cables, it can be found that after increasingly loading, the Tight buffer Telecom cable becomes unevenly strained (Fig. 3.19). Strain readings become non-uniformly distributed along the strained section of the cable. One explanation is that the cable experienced deformation at above  $1600\mu\epsilon$ . This is probably because the cable is twisted by large strain and can not go back to its original condition due to the elasticity of the cable jacket or stiffness of the steel wire. In future, this cable could improve its plasticity in order to perform more reclaimable strain monitoring.

Similar results can be found in Brugg V1 cable results. At smaller strains, the measurement is evenly distributed, as expected. However at above  $2000\mu\epsilon$ , spikes starts to appear in the measurement results at  $z = 4.3m$  where the cable is clamped to the mount. This result indicating that this cable has creeping effects at high strains when clamped to an object.

The measured strain along the holding sections of the four tested strain cables is averaged and plotted against the input strain change (Fig. 3.21 to 3.24). The averaging is made over 60 data points (i.e. averaged over the length of  $1m$  effective length with cables and readings made three times). The error bars at each strain level are calculated as the standard deviation of all 60 data points.

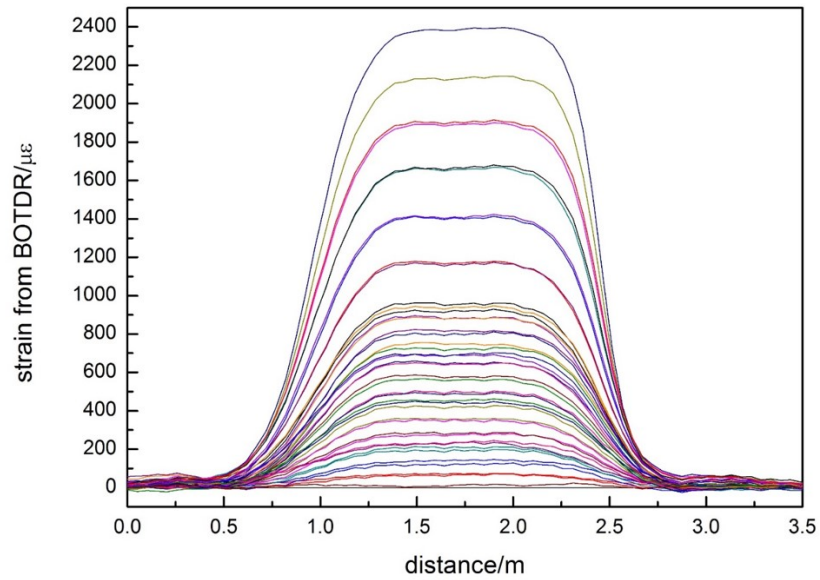


Fig. 3.17 The analyzer measured strain of the Fujikura reinforced cable which was stretched for 1.5 m at different strain levels

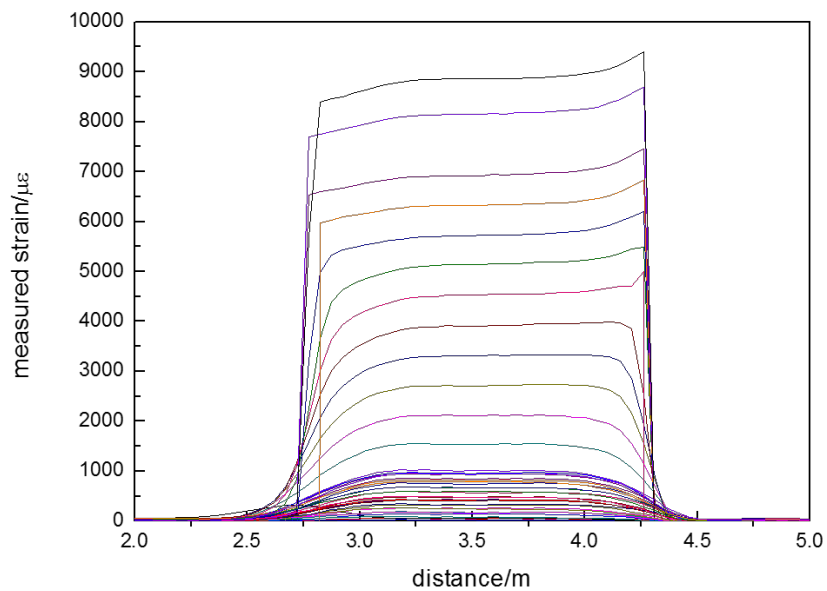


Fig. 3.18 The analyzer measured strain of the Brugg cable which was stretched for 1.5 m at different strain levels

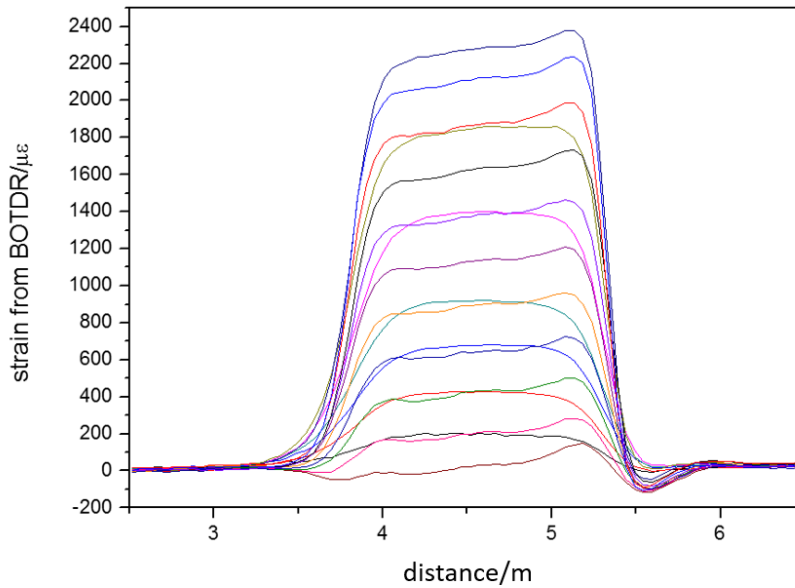


Fig. 3.19 The analyzer measured strain of the the Tight buffer telecomm which was stretched for 1.5 m at different strain levels

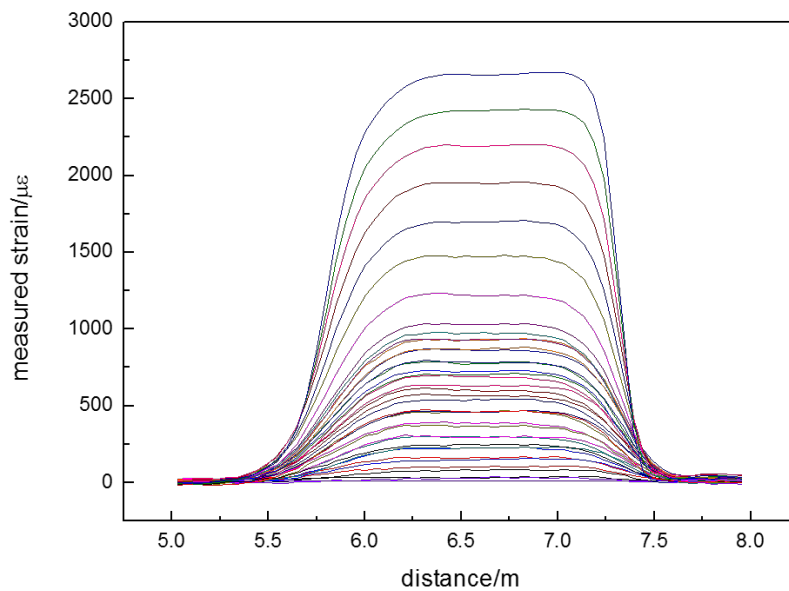


Fig. 3.20 The analyzer measured strain of the Nanzee reinforced cable cable which was stretched for 1.5 m at different strain levels

The analyzer measured strain readings are found to be linearly related to the input strain for all tested cables, but the linearity varies for four cables. The coefficient determination  $r^2$  is the regression of the fitting line, indicating the linearity between the analyzer measured results and the input results. The Fujikura reinforced strain cable, the Brugg cable and the Nanzee reinforced cable show better linearity ( $r^2 \geq 0.99$ ) than the Tight buffer telecomm cable ( $r^2 = 0.987$ ).

The standard deviations for measurements are relatively constant at each strain level for the tested cables. But the level of error vary significantly for different types of the tested cables. Again the Tight buffer telecomm cable indicates a much larger error compared to the other four cables at each strain level.

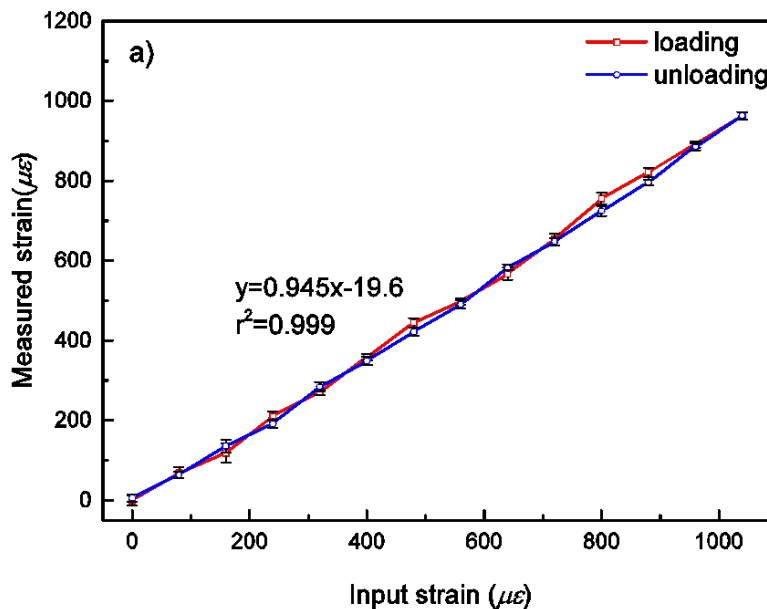


Fig. 3.21 The relationship between the analyzer measured strain and the input strain with measurement standard deviation as error bars for the Fujikura reinforced cable

The measurement residuals of the fitted lines for the tested fibres are illustrated in Fig. 3.25. It can be clearly seen that the Sumitomo Tight buffer telecomm cable has the largest residuals between the raw data and the fitted curve (more than  $120 \mu\epsilon$  at some strain level), indicating that this sensing fibre has a relatively larger error (as much as  $120 \mu\epsilon$ ) in strain measurement if using the linear Brillouin conversional coefficient to transfer Brillouin frequency shift into strain. For the other three sensing cables, the measurement residuals are mostly smaller than  $60 \mu\epsilon$ , indicating a relatively smaller error (generally in a range of  $10 \mu\epsilon - 40 \mu\epsilon$ ) in the measured strain result.

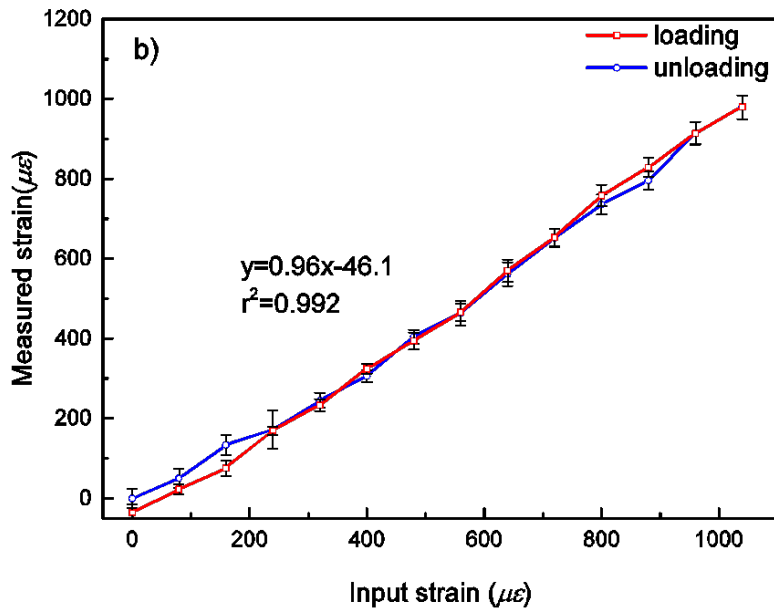


Fig. 3.22 The relationship between the analyzer measured strain and the input strain with measurement standard deviation as error bars for the Brugg cable

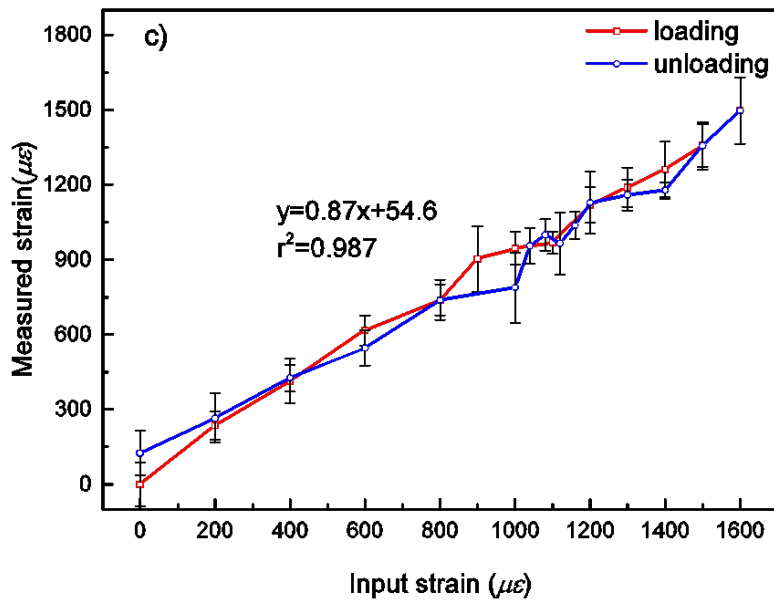


Fig. 3.23 The relationship between the analyzer measured strain and the input strain with measurement standard deviation as error bars for the Tight buffer telecomm cable

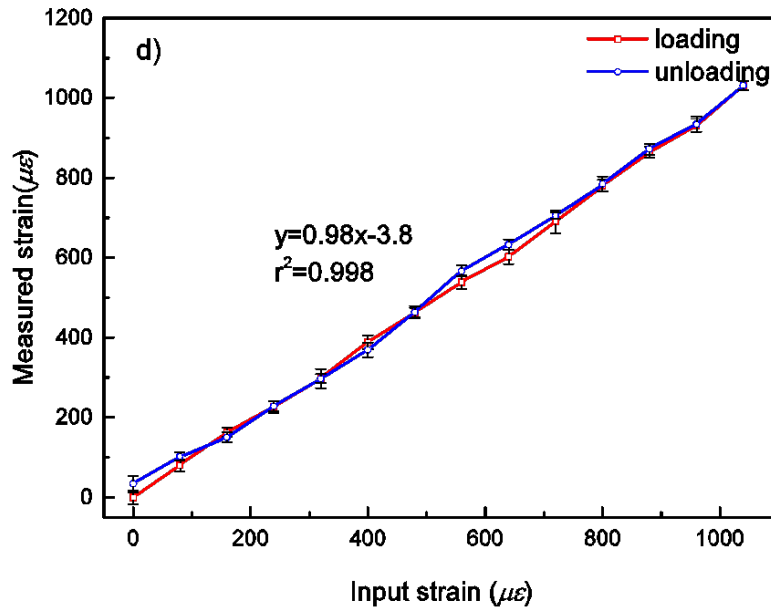


Fig. 3.24 The relationship between the analyzer measured strain and the input strain with measurement standard deviation as error bars for the Nanzee reinforced cable

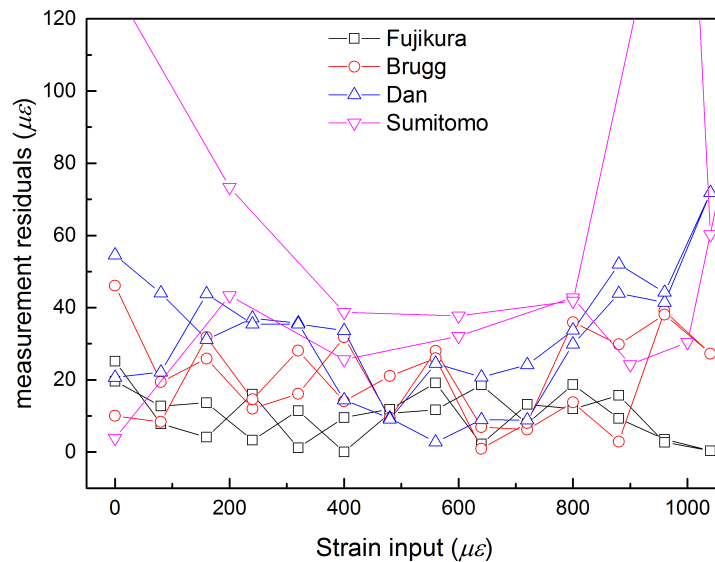


Fig. 3.25 Measurement residuals for the fitted linear curves of the analyzer measured strain and the input strain

The standard deviations of measurements over 1 m strained cable length and three repeated readings are shown in Fig. 3.26. The Sumitomo Tight buffer strain cable has the highest measurement error, about  $80 \mu\epsilon$ . In addition, the amount of error varies significantly with strain level, such as  $70 \mu\epsilon$  error at a strain level of  $600 \mu\epsilon$  and more than  $120 \mu\epsilon$  error at a strain level of  $1000 \mu\epsilon$ . The other three cables including Fujikura reinforced cable, Brugg V1 strain cable and Nanzee(Dan) reinforced cable show a relatively constant and lower measurement error ( $10 \mu\epsilon - 20 \mu\epsilon$ ). The Brugg V1 strain cable result shows a sharp increase in measurement error (from  $20 \mu\epsilon$  to  $60 \mu\epsilon$ ) at the strain level of  $200 \mu\epsilon$  during loading process, indicating a cable instability at this stage.

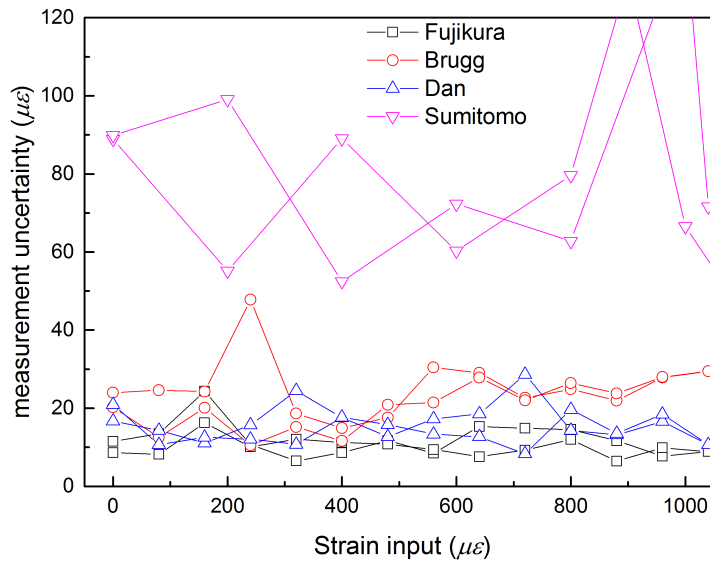


Fig. 3.26 Standard deviation of measurements over the length of 1 m effective length with cables and readings made three times

The qualities of the tested four strain cables were then evaluated with four sensing parameters:  $C_\epsilon$ ,  $r^2$ ,  $\sigma$  and  $\epsilon_d$ .  $C_\epsilon$  is the Brillouin frequency shift to strain conversional coefficient,  $r^2$  is the coefficient determination of the best fitted line between the measured strain and the input strain value,  $\sigma$  represents the measurement uncertainty which is the average of precision error calculated at different strain levels, and  $\epsilon_d$  indicates slippage which is calculated as the difference between analyzer measurement at pre-set cable condition and measurement after the cable is loaded and unloaded for one cycle.

Table 3.4 compares the quality of the tested strain cables in regard to their sensing parameters. It can be seen that  $C_\epsilon$  is in the range of  $0.0435 \text{ MHz}/\mu\epsilon - 0.049 \text{ MHz}/\mu\epsilon$  for four tested cables, which indicates that  $C_\epsilon$  can vary more than 13% for different types of strain

cable. The Brillouin conversional coefficient for Brugg V1 cable has been calibrated previously with four cycles of loading and unloading procedures, and the result is  $0.0476 \text{ MHz}/\mu\epsilon$  [40], in good agreement with this test result. Therefore the tested measurement result of one loading/unloading cycle is used to represent the cable's sensing characteristics. The table also illustrates that Fujikura reinforced cable and NanZee reinforced cable have relatively higher measurement accuracy and better measured linearity compared to that of Brugg and tight buffer telecomm cables. The reason for this is probably that the robust cable reinforcement holds the sensing fibre in a very stable condition during strain process. The small  $\epsilon_d$  of the Fujikura cable implies that this cable has little slippage effects which can be proved in various case studies [38]. In summary, the Fujikura Reinforced Strain Cable shows the best sensing performance during this strain calibration experiment.

Table 3.4 Comparison of different strain sensing cables

Parameters	Cables			
	Fujikura reinforced Cable	Brugg Cable	Tight buffer telecomm Cable	Nanzee reinforced Cable
$C_\epsilon (\text{MHz}/\mu\epsilon)$	0.047	0.048	0.044	0.049
$r^2$	0.999	0.992	0.987	0.998
$\sigma (\mu\epsilon)$	11.1	22.9	82.9	15.5
$\epsilon_d (\mu\epsilon)$	6	22	125	34

### 3.3 Temperature calibration

The temperature calibration tests were conducted to investigate the thermal characteristics of the sensing cables and the related errors in the temperature compensation process. The temperature sensing cable, the Fujikura reinforced strain cable and the Corning standard single mode optical fibre were calibrated with regard to their temperature hysteresis and associated errors.

#### 3.3.1 Temperature calibration unit

A water bath was used as a temperature calibration bench to allow a certain length of the fibre optic cable to be thermally isolated from the remainder of the cable, and maintained at a desired temperature. The temperature controlling system (Fig. 3.27) used in this test was a C1G cooling system and a T100-ST 18 water bath from Grant Instruments with dimensions of  $200 \text{ mm (h)} \times 540 \text{ mm (l)} \times 330 \text{ mm (w)}$ .



Fig. 3.27 Temperature calibration bench of a water bath

This set up can uniformly change the cable's temperature from 0 °C to 100 °C in a resolution of  $\pm 0.1$  °C with an accuracy of  $\pm 0.05$  °C. The cable section was freely immersed into the water bath in the form of many loops as shown in Fig. 3.27. There was a thermometer installed as well for temperature measurement reference.

### 3.3.2 Temperature tests

During temperature calibration tests, a section of the tested cable was immersed into the water bath to accurately and precisely change its temperature. One hundred Repeated measurements were taken by the NBX-5000 BOTDR analyzer at five different temperatures (15 °C, 20 °C, 25 °C, 30 °C, and 35 °C ) to look at the precision error characterization of the temperature sensor. Cycles of heating and cooling process were conducted for measurement accuracy and hysteresis investigation.

#### Tested cables

The tested cables include a single mode fibre SMF-28 from Corning.Ltd, a Fujikura reinforced strain sensing cable, and a temperature cable (loose tube LSOH black cable from Cables and Stuff company). Table 3.5 illustrates the detailed information of the tested cable. The normal loose buffered telecommunication cable has eight coated single mode fibres floating within a hard tube which is filled with glue. The glue makes it possible that the external strain placed on the tube is not directly transferred to the fibre and therefore isolates any strain effects. Because the strain cable is sensitive to both strain and temperature, its temperature sensing

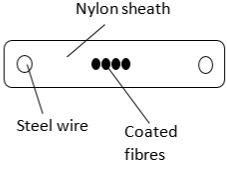
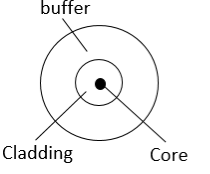
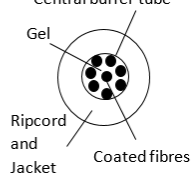
Cable	Fujikura reinforced cable	SMF-28	Loose buffer telecomm cable
Details	Steel wire reinforced cable embedded with four single mode fibres	Single mode fibre	loose tube cable
Sketch	 <p>Nylon sheath Steel wire Coated fibres</p>	 <p>buffer Cladding Core</p>	 <p>Central buffer tube Gel Ripcord and Jacket Coated fibres</p>
Picture			

Table 3.5 Illustration of the tested cables for temperature tests

characteristic is also tested in temperature calibration test. The Fujikura reinforced strain cable is the same as that used in the strain calibration test. The single mode fibre is a bare fibre with only one buffer layer as a protection. As this fibre is relatively fragile, it is not appropriate for site monitoring projects.

### Temperature precision characterization

The sensing errors of the temperature cable and the strain cable were firstly characterized at different temperatures. In the test, 100 repeated measurements of Brillouin frequency shift for the immersed cable section were recorded at  $T=15\text{ }^{\circ}\text{C}$ ,  $20\text{ }^{\circ}\text{C}$ ,  $25\text{ }^{\circ}\text{C}$ ,  $30\text{ }^{\circ}\text{C}$ , and  $35\text{ }^{\circ}\text{C}$  respectively. Figure 3.28 illustrates the repeated Brillouin centre frequency readings at one point of the temperature sensing cable, and Fig. 3.30 shows the other measuring point on the strain sensing cable. The relatively larger range of the Brillouin centre frequency change with temperature for the strain cable is due to the cable jacket thermal characteristics transferred to the optical fibre through tight buffering. As a result, the Brillouin centre frequency conversional coefficient was calculated as  $0.0024\text{ GHz}/^{\circ}\text{C}$  for the strain cable, larger than the temperature cable indicated ( $0.0012\text{ GHz}/^{\circ}\text{C}$ ).

The Brillouin centre frequency variations over time for the strain and the temperature cable are summarized in Table. 3.6. The results are calculated as the standard deviation of the repeated readings. It can be seen that for all tests conducted at different temperatures, the recorded Brillouin frequency shift oscillates in a range of  $0.0011\text{ GHz} - 0.0018\text{ GHz}$  (equivalent to  $0.92\text{ }^{\circ}\text{C} - 1.5\text{ }^{\circ}\text{C}$ ) for the temperature sensing cable, and  $0.0010\text{ GHz} - 0.0018\text{ GHz}$  (equivalent to  $0.44\text{ }^{\circ}\text{C} - 0.75\text{ }^{\circ}\text{C}$ ) for the strain sensing cable. In addition, the precision error does not show any dependency on temperature for either sensing cables. A general

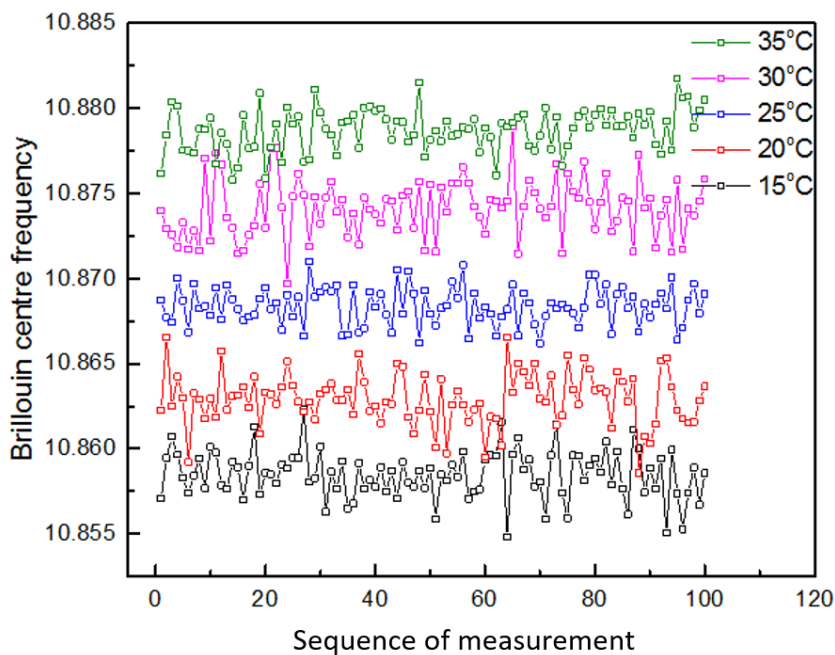


Fig. 3.28 Repeated Brillouin centre frequency measurement in GHz for the temperature sensing cable

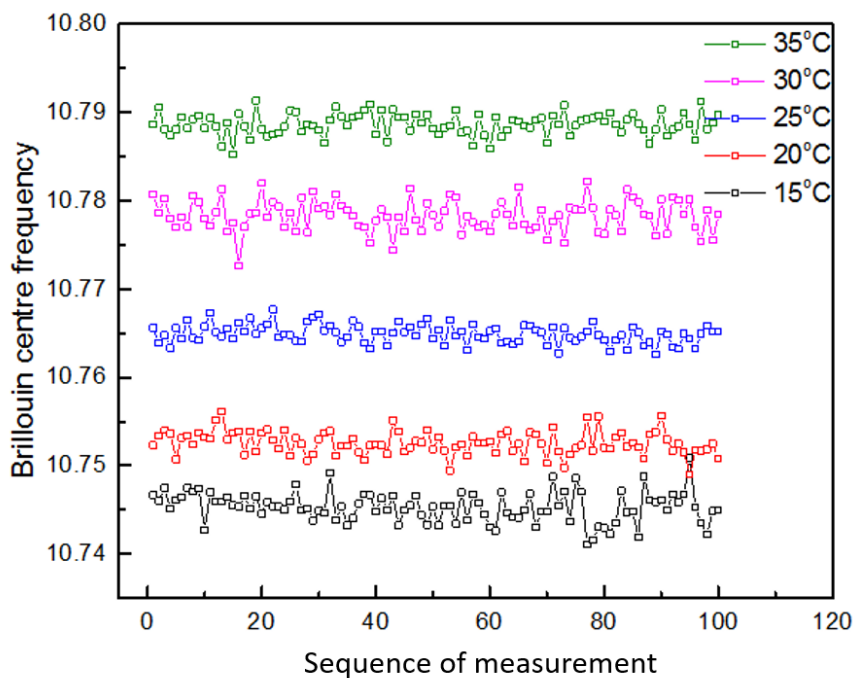


Fig. 3.29 Repeated Brillouin centre frequency measurement in GHz for the strain sensing cable

conclusion can therefore be obtained that the Brillouin optical fibre temperature sensor has a relatively larger precision error than the strain sensor does, but for both cables, the precision error does not have any dependency on temperature.

Table 3.6 Measurement precision at different temperature levels for strain and temperature sensing cable

Temperature	Brillouin CF variation( <i>GHz</i> )		Temperature variation( $^{\circ}\text{C}$ )	
	Temperature cable	Strain cable	Temperature cable	Strain cable
15 $^{\circ}\text{C}$	0.00142	0.00172	1.183	0.717
20 $^{\circ}\text{C}$	0.00154	0.00133	1.283	0.554
25 $^{\circ}\text{C}$	0.00111	0.00106	0.925	0.442
30 $^{\circ}\text{C}$	0.00172	0.00177	1.433	0.738
35 $^{\circ}\text{C}$	0.00124	0.00123	1.033	0.513

### Temperature accuracy characterization

The accuracy of the temperature reading and its dependence on temperature was investigated by heating and cooling the sensing cable in sequence, and comparing the Brillouin centre frequency readings during the two processes. In this test, 12 *m* of the temperature cable and 7 *m* of the strain cable were spliced together and immersed into the water bath in the form of many loops. Water taken from a tap was heated and cooled in a range of 20  $^{\circ}\text{C}$  – 45  $^{\circ}\text{C}$ , at 5  $^{\circ}\text{C}$  intervals. At each temperature level, three repeated measurements were taken using an NBX-5000 analyzer after the temperature was stabilized (mostly 5 minutes after the thermometer showed the temperature was stable in the water bath). The baseline reading was taken at 20  $^{\circ}\text{C}$ .

Figure 3.30 and 3.31 illustrate the temperature readings ( $T_m$ ) of the analyzer at every 5 *cm* along the temperature sensing cable and the strain sensing cable. The readings were calculated as an average of the three repeated measurements at each temperature level. During the heating and cooling process the strain cable readings stayed constant over the cable length, as expected, while the temperature cable reading developed fluctuations with the final temperature reading being rather different from the baseline reading after the whole heating and cooling process. It seemed that additional strain was induced to the temperature cable during the heating and cooling process.

The comparison between the measured temperature ( $T_{\mu}$ ) with regard to the input temperature ( $T$ ) for both the temperature and strain cable is shown in Fig. 3.32.  $T_{\mu}$  is calculated as the average result of  $T_m$ . The error bar is the standard deviation of  $T_m$ . It indicates the fluctuations

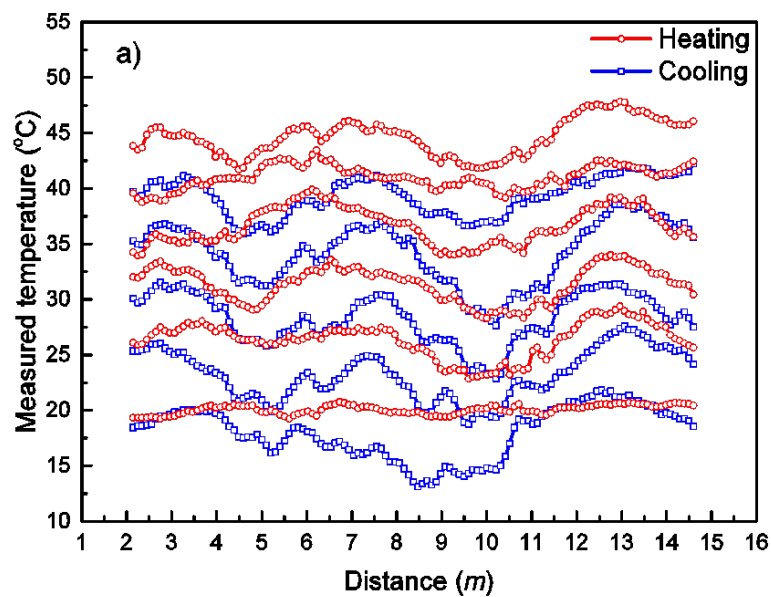


Fig. 3.30 The analyzer measured temperature readings of the temperature sensing cable during first the heating and then the cooling process in steps of 5 °C

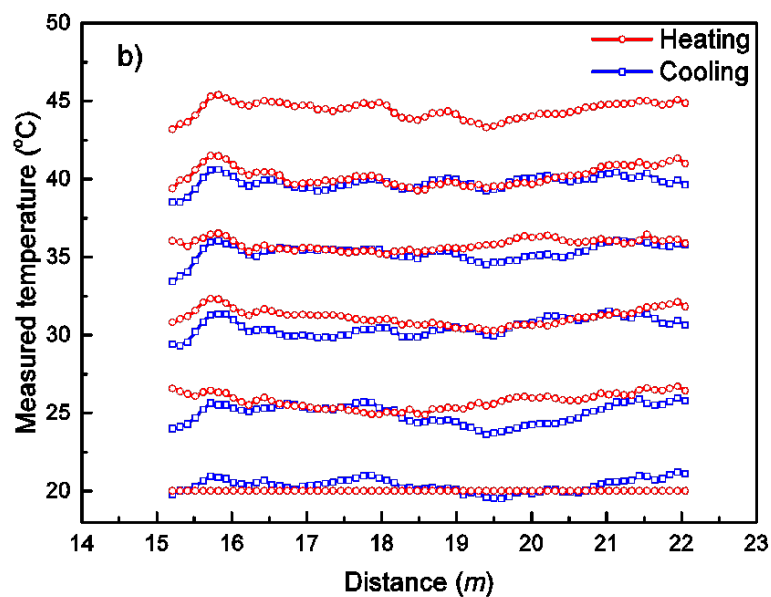


Fig. 3.31 The analyzer measured temperature readings of the strain sensing cable during first the heating and then the cooling process in steps of 5 °C

of the reading over distance. The strain cable shows good agreement between the analyzer measured temperature and the input temperature in both the heating and cooling processes. However, the temperature cable measurement shows a larger difference between the analyzer measurement and the real temperature with larger error bars, making the temperature reading unreliable.

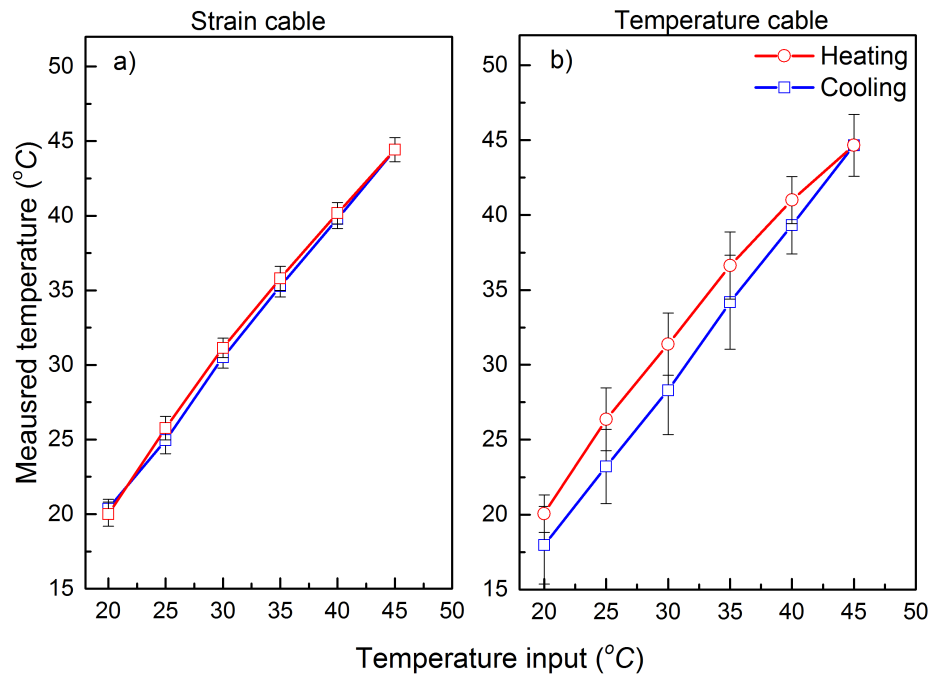


Fig. 3.32 The linearity between analyzer measured temperature and input temperature for a) strain cable and b) temperature cable

The fluctuations ( $\sigma_T$ ) of the temperature readings over distance are summarized in Table 3.7 where  $\sigma_T$  is the standard deviation of  $T_m$ . The temperature cable shows more fluctuations than the strain cable does, as  $\sigma_T$  for the temperature sensing cable is 2.22 °C on average, and for the strain sensing cable it is 0.75 °C. Even in the baseline condition,  $\sigma_T$  is calculated as 0.42 °C for the temperature cable and 0.19 °C for the strain cable. During the heating and cooling processes,  $\sigma_T$  does not change significantly and stays at around 0.49 °C for the strain cable. However, for the temperature cable,  $\sigma_T$  builds up during this heating and cooling process. It increases from 0.42 °C to about 2.35 °C after the whole experiment has finished.

Table 3.8 lists the accuracy of the Brillouin fibre optics sensing temperature measurement which is calculated as the difference between  $T_\mu$  and  $T$ . The average error of the test results in all temperature conditions is 0.443 °C for the temperature cable and 1.162 °C for the

Table 3.7 Measurement fluctuation over the tested cable length during the heating and cooling processes for the strain and temperature sensing cables

Temperature	$\sigma_T$ in heating process (°C)		$\sigma_T$ in cooling process (°C)	
	Temperature cable	Strain cable	Temperature cable	Strain cable
20°C	0.420	0.190	2.349	0.387
25°C	1.601	0.464	2.264	0.589
30°C	1.576	0.470	2.243	0.505
35°C	1.667	0.330	2.805	0.472
40°C	1.043	0.549	1.735	0.377
45°C	1.644	0.478	1.644	0.478

strain cable. The results do not present much error dependence on the temperature except for when the temperature cable is cooled. An increase in the measurement error (from 0.343 °C to 2.036 °C) is found in the temperature cable readings when the cable is cooled down from 45 °C to 20 °C. Temperature hysteresis is revealed during the cooling process for the temperature cable.

Table 3.8 Measurement accuracy during heating and cooling process for the strain and the temperature sensing cable

Temperature	Error in heating process (°C)		Error in cooling process (°C)	
	Temperature cable	Strain cable	Temperature cable	Strain cable
20°C	0.056	0.023	-2.036	0.356
25°C	1.367	0.762	-1.782	-0.039
30°C	1.379	1.147	-1.699	0.509
35°C	1.632	0.797	-0.810	0.294
40°C	1.005	0.177	-0.669	-0.213
45°C	-0.343	-0.572	-0.343	-0.572

### Temperature hysteresis characterization

To investigate the temperature hysteresis of the temperature cable more thoroughly, the cable is calibrated over a larger temperature range (5 °C – 85 °C) with more heating/cooling cycles. Figure 3.33 shows the analyzer measured temperature with regard to input temperature change for three continuous heating/cooling cycles. For all three cycles,  $\sigma_T$  is at a maximum in lower temperature ranges which again implies that external strain is induced to the sensing fibre when it is cooled. Hysteresis can be clearly seen in cycle 1, but almost disappears in

cycle 2 and cycle 3, indicating that after one cycle of heating/cooling, no further external strain is induced and the condition of the cable tends to get stable.

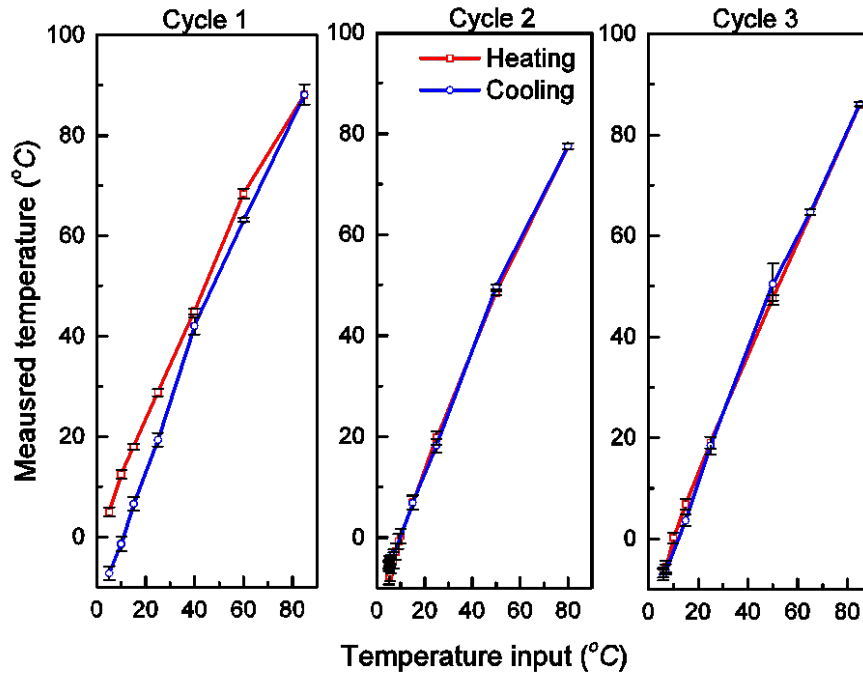


Fig. 3.33 The linearity between measured temperature and input temperature for continuous three heating-cooling cycles

Measurement errors between the analyzer measured temperature and the input temperature at different temperature levels are illustrated in Fig. 3.34. Initially, the measurement error is close to zero. However after the first cycle of heating process, the analyzer measured temperature increases to more than 8 °C at a temperature level of 60 °C. Afterwards, the trend of measurement error change is totally different with the 1<sup>st</sup> cycle heating result as the measurement error starts to decrease with temperature, and this trend is approximately the same for the 1<sup>st</sup> cycle cooling process and the rest two cycles. This again verifies that the tested temperature cable induces external error during cooling process and this error is not influenced by more heating and cooling processes. During the 2<sup>nd</sup> and the 3<sup>rd</sup> heating and cooling cycles, the measurement error keeps constant (0 °C-2.5 °C) at higher temperature conditions (T = 50 °C-85 °C) and decreases with temperature at lower temperature conditions (T = 0 °C-45 °C). The maximum error appears at 5 °C, where as much as 13 °C error is found between the analyzer measured temperature and the real temperature. This will induce more than 200  $\mu\epsilon$  error to the strain measurement during temperature compensation procedure.

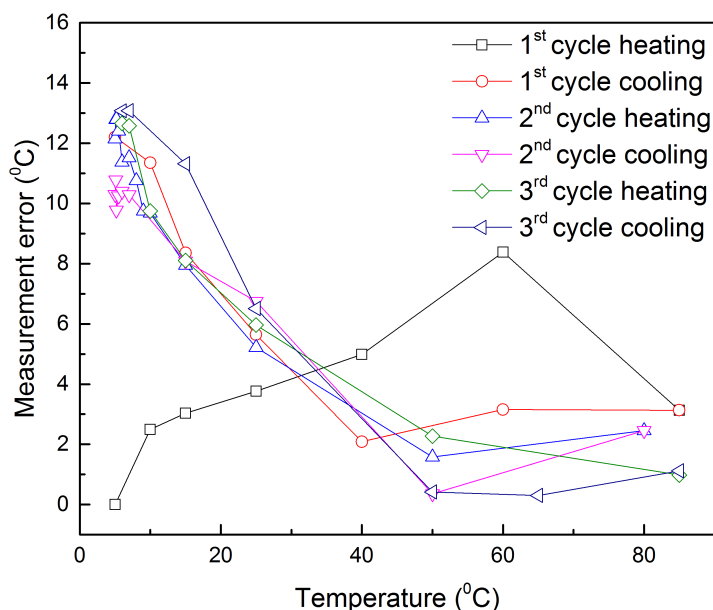


Fig. 3.34 Measurement error between the analyzer measured temperature and the real temperature during three heating and cooling cycles

The above experimental results indicates that the property of the temperature cable is unstable during cooling process and this effect only appears at the first time of cable cooling process. One explanation is that the gel inside the temperature cable induces external strain to the optical fibre during heating and cooling process. When the cable gel becomes hardened/softened with temperature change, it stores/releases strain. As a result, additional strain seems to build up during the heating and cooling test for the temperature cable as the gel inside the cable becomes unstable with the temperature change.

To investigate the influences of the temperature cable gel on the distributed fibre optics sensor measurement error, bare-fibre (cable that has no gel or jacket) was tested. The test was conducted after removing the jacket and gel of the telecommunication cable. The temperature was increased from 20 °C to 80 °C to resolution of 10 °C, and then decreased back to 20 °C to the same resolution. This time the averaged Brillouin frequency shift for two temperature-increasing-and-decreasing processes successfully matched each other, as shown in Fig. 3.35 and 3.36. It can therefore be concluded that temperature loop changes the value of the fibre Brillouin frequency shift due to the cable jacket and gel. New types of temperature cable with proper jackets should be designed and tested in the future.

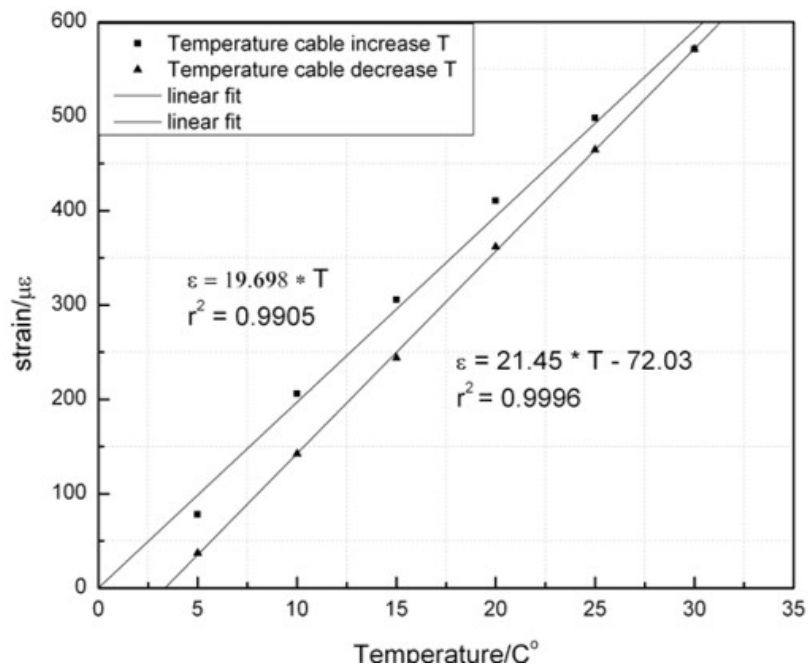


Fig. 3.35 Measurement hysteresis test results for the temperature cable with jacket

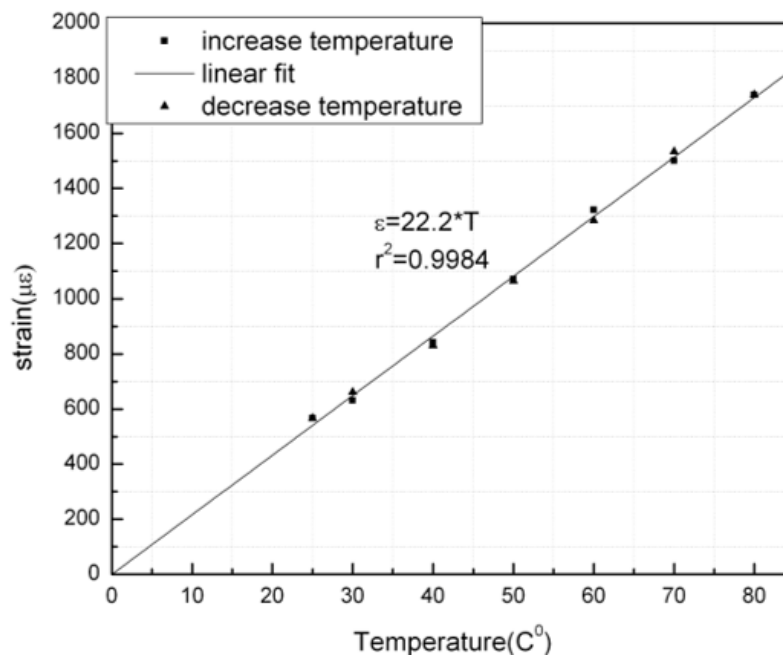


Fig. 3.36 Measurement hysteresis test results for the bare fibre

### 3.4 Summary

1. BOTDR analyzer measurement precision error was influenced by the diameter of the fibre, the fibre state of polarization and the cable tight buffering process. A larger core and smaller cladding lead to an extra precision error of more than  $5 \mu\epsilon$ . The fibre state of polarization induced  $3 \mu\epsilon$  precision error. The tight buffered strain cable had an extra precision error of  $1.7 \mu\epsilon$  compared to the standard single mode fibre.
2. Four types of tight buffered strain sensing cable were calibrated in the laboratory. The Brillouin conversional coefficients of the tested cables were in a range of  $0.044 \text{ GHz}/\mu\epsilon$  –  $0.049 \text{ GHz}/\mu\epsilon$  for the four tested cables. The measurement error varied significantly and achieved as much as  $83 \mu\epsilon$  for one of the tested strain cables.
3. The variation of the temperature readings over time was not dependent on temperature for both the temperature and strain cables. In general, the temperature cable variation proved to be twice that of the strain cable reading. The accuracy of the temperature cable measurement decreased when it was cooled, while the accuracy of the strain cable did not show that trend. Temperature hysteresis was found in the temperature cable, and the reason was verified as the external strain induced by the unstable property of the cable gel.

# Chapter 4

## Spontaneous Brillouin spectrum model

Spontaneous Brillouin scattering is the scattering of light from sound waves. It is one of the basic scattering mechanisms of the distributed sensing techniques which commonly occur in single mode optical fibres. In theory, spontaneous Brillouin scattering consists of the coupling between the injected pulsed wave and the vibration modes of the fibre itself, which are sound waves. The backscattered Brillouin wave has a different peak frequency than the injected pulse, and the frequency shift is dependent on the temperature and strain conditions of the cable. Based on this, the distributed fibre optics sensor measures the backscattered Brillouin gain spectrum as a function of the frequency shift to resolve the strain/temperature condition of the cable.

Chapter 4 develops a novel optical model to simulate the analyzer measured Brillouin spectrum. The reliability of this model was confirmed by comparing experimental measurements with simulation results. Parametric studies were conducted to investigate the impacts of different factors on the optical fibre sensor measurement error.

### 4.1 Theoretical analysis

Light travelling in an optical fibre can excite the fibre molecules from the ground to an excited vibrational state (which is called an acoustic wave), and the process of light scattering from acoustic wave is defined as Brillouin scattering [61]. In amorphous silica fibre, scattered lights that are shifted to lower frequencies are known as Stokes components, and those components that are shifted to higher frequencies are known as anti-Stokes components [74]. The frequency shift of the backscattered Brillouin wave is a function of the acoustic wave velocity, which is dependent on the optical fibre's thermodynamic variables such as density and temperature [8]. The distributed fibre optics sensor based on Brillouin scattering exploits the principle that the frequency shift of the Brillouin backscattered light is proportional to

the cable strain/temperature. By recording the frequency shift of the Brillouin backscattering light, strain and temperature conditions of the monitored structure can be obtained at any point of the fibre[75].

In a BOTDR system, a pulsed light is injected into one end of an optical fibre, and the backscattered Brillouin light produced in the fibre is received and processed at the same end of the fibre. The power of the Brillouin backscattered light  $P_B(z, \nu)$  which is produced in a small section of the fibre can be expressed using Eq. 2.35 [60].

The root cause of the frequency dependence is the finite life time of the acoustic phonons ( $10\text{ns}$ ), which is also the damping time ( $T_B$ ) of the acoustic wave. The limitation of the phonon life time leads to a small spectral width of the gain spectrum. As previously reported, the average  $\Delta\nu$  is equal to  $30\text{ MHz}$  [45].

The simulation steps of the backscattered Brillouin spectrum is shown in Fig. 4.1. In this process, the pulse injected to the optical fibre is firstly simulated. The Brillouin scattering process between the injected pulse and the fibre sensor is simulated and a raw measurement of 3D backscattered Brillouin spectrum result can be obtained. The raw Brillouin spectrum is finally processed to simulate the signal process inside the analyzer.

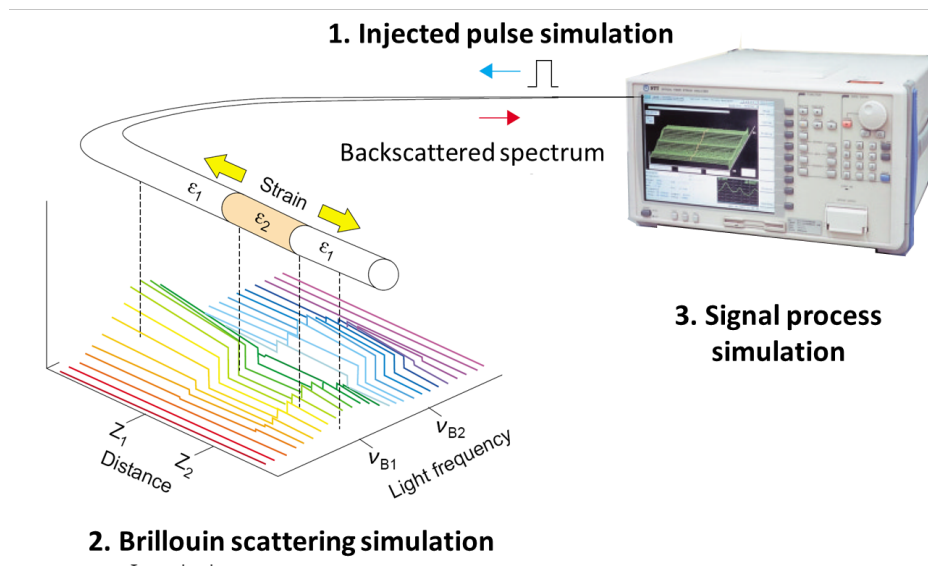


Fig. 4.1 Schematic diagram of the simulation process

#### 4.1.1 Pulse simulation

Assuming that the launched pulse is only amplitude-modulated and has a constant optical frequency in the frequency domain within the pulse duration, the input pulse is modelled as a

square pulse. Figure 4.2 schematically illustrates an injected pulse which starts at time  $t_0$ , with a duration of  $\tau$ , rising and falling time  $\Delta\tau$ .

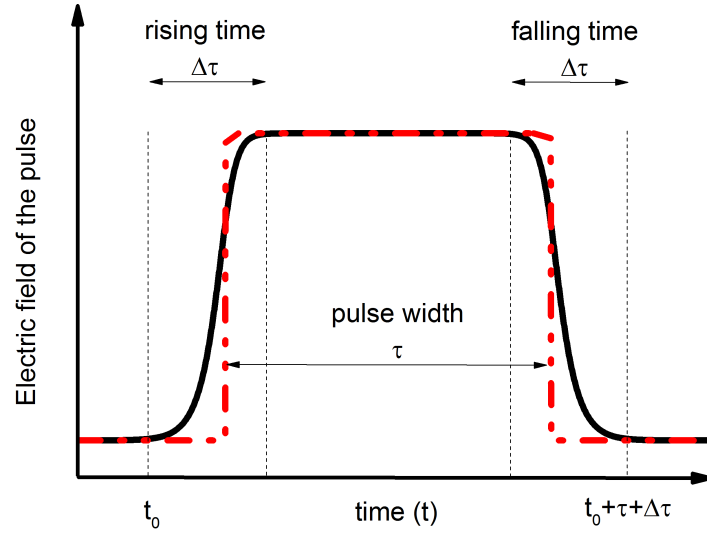


Fig. 4.2 Graphically illustration of a squared pulse(black line) with rising/falling time of  $\Delta\tau$  and a pulse width of  $\tau$

The power leakage of the pulse can be quantified by the extinction ratio which is the power ratio between the leak and the pulse power. With a known input peak power ( $P_P$ ) and an extinction ratio ( $ER$ ), the input leak power ( $L_P$ ) of the pulse can be calculated as  $P_P \times 10^{-ER/10}$ . The electric field  $E(t)$  of the launched pulse is then given by:

$$E(t) = (\sqrt{P_P} - \sqrt{L_P}) \times \sqrt{\left(\tanh\left(\frac{t-t_0}{0.45\Delta\tau}\right) - \tanh\left(\frac{t-t_0-\tau}{0.45\Delta\tau}\right)\right)/2 + \sqrt{L_P}} \quad (4.1)$$

where  $P_P$  is the input peak power of the pulse,  $L_P$  is the input leak power of the pulse calculated from the extinction ratio ( $ER$ ) of the pulse:  $L_P = P_P \times 10^{-ER/10}$ .

The pulsed light power spectrum in the frequency domain can be obtained by doing a Fourier transfer of the  $E(t)$ :

$$P_p(f) = FFT(E(t)) \quad (4.2)$$

### 4.1.2 Brillouin scattering simulation

The backscattered Brillouin spectrum is a convolution of the pulse and the intrinsic Lorentz distribution with key parameters dependent on the fibre strain/temperature condition. As shown in Fig. 4.3, for a launched pulse with a centre optical frequency of  $f_0$ , a small width  $df$  of the spectrum generates a Lorentzian shape backscattered Brillouin spectrum with a centre frequency of  $f - S_B$ . The Brillouin backscattered light power spectrum generated by the whole launched pulse is given by a Lorentzian profile with a peak power frequency of  $f - S_B$  and a full width at half-maximum of  $\Delta\nu$ .

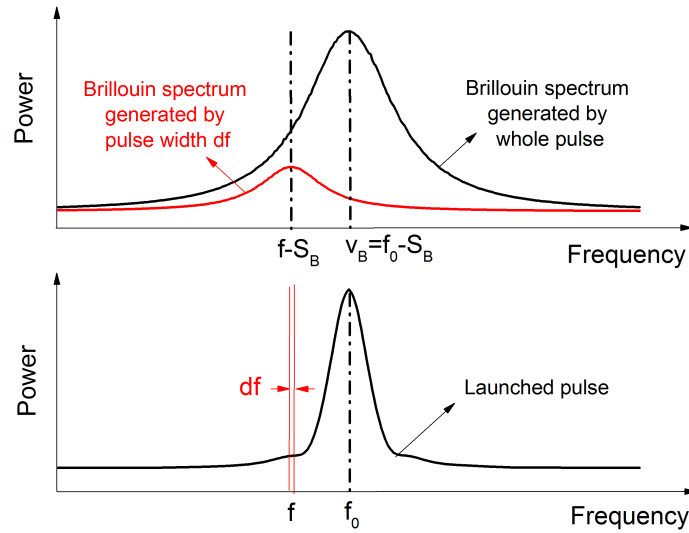


Fig. 4.3 Generation of a Brillouin spectrum from a pulsed light [59]

The frequency dependent factor  $H(\nu)$  of the Brillouin backscattered light on the launched pulse is therefore given by [59]:

$$H(z, \nu) = \int P_p(f, f_0) \frac{h(\Delta\nu/2)^2}{[\nu - (f - S_B(z))]^2 + (\Delta\nu/2)^2} df \quad (4.3)$$

where  $df$  is a small frequency width surrounding frequency  $f$  in the launched pulsed light with power spectrum  $P_p(f, f_0)$  and an optical centre frequency  $f_0$ . The parameter  $S_B(z)$  is the Brillouin frequency shift at location  $z$ , being the difference between the injected light optical frequency  $f_0$  and the centre frequency of the Brillouin spectrum  $\nu_B$ .

The simulated intrinsic Brillouin power spectrum can be expressed by Eq. 4.3, based on the assumptions that 1) there is negligible pump depletion and fibre loss so that in each

section the maximum gain is the same, and 2) the power of spontaneous Brillouin scattering is linearly proportional to the energy of the optical pulse.

During the Brillouin backscattering simulation process, the intensity of the local Brillouin response is measured and integrated as a function of time  $t$  for successive pump-probe frequency scanning processes. At each position, the local spectral distribution of the Brillouin gain spectrum (BGS) is reconstructed and the local peak gain frequency is then simulated through Lorentz fitting procedure. The location of Brillouin scattered light spectra  $z$  along the fibre can be calculated as a function of time  $t$  in the form of Eq. 2.3. A shorter pulse leads to an improved spatial resolution but also provides a broadened Brillouin gain spectrum and a weaker Brillouin signal, especially when it is shorter than the material's phonon life time (10 ns). As a result, the BOTDR input pulse width is limited to 10 ns and the spatial resolution to 1 m.

### 4.1.3 Analyzer signal process simulation

The final simulation procedure is adding noise to the obtained backscattered Brillouin spectrum and conducting the signal process. Figure 4.4 and 4.5 illustrates the effects of such signal process on Brillouin spectrum profile. In this case, a 1.5 m length of strain change occurred in the middle of the cable. It can be seen that due to the limitation of the analyzer (such as noise), the smooth intrinsic Brillouin spectrum (Fig. 4.4) is transferred into fluctuated spectrum (Fig. 4.5) and the sharp centre frequency change of the spectrum profile becomes spread. Two methods to simulate analyzer signal process are discussed here in detail.

#### Short-time-Fourier-transform Method

The first method includes phase noise simulation and a Short-time-Fourier-transform (STFT) signal process simulation which is suitable for the general BOTDR analyzer model [18]. Brillouin interaction is a phase-dependent process. Because light transfer ( $3 \times 10^8$  m/s) is much faster than an acoustic wave (2000 m/s), when a pulse passes through the fibre, the acoustic wave amplitude will grow up to the steady state only at correlation points, while remaining very small along the rest of the fibre. Thus, the change in probe power due to Brillouin gain will be given a strong interaction at a single point, and a background noise coming from the rest of the fibre. As a result, the electric fields of the Brillouin backscattered light produced at many scattering points in the fibre do not exhibit phase correlation, and the principle of super-position holds with respect to the backscattered light power.

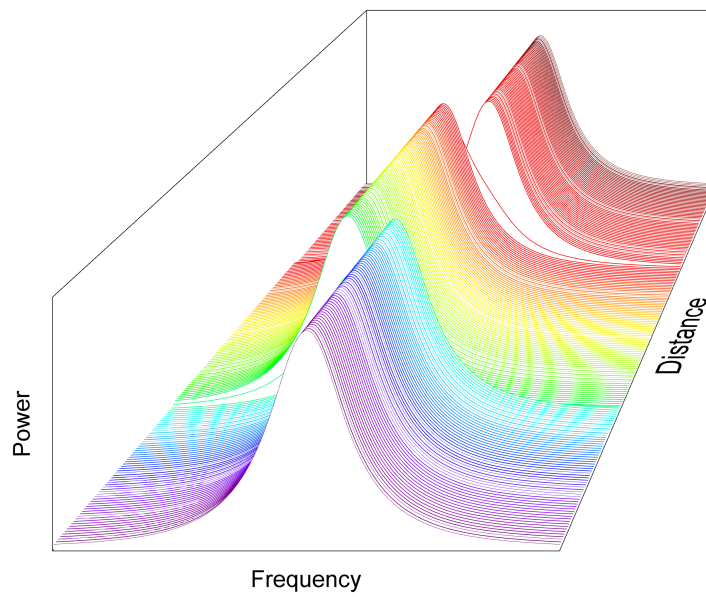


Fig. 4.4 Illustration of intrinsic Brillouin spectra for a step strain change

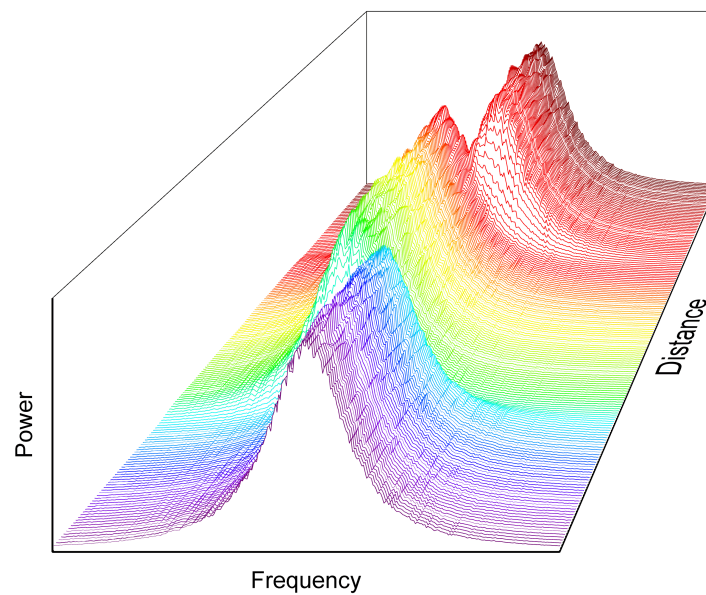


Fig. 4.5 Illustration of analyzer received Brillouin spectra for a step strain change

A random phase noise is therefore added to the model. With different times of averaging, random noise can be minimized. Obtaining the received Brillouin signal, STFT is performed to simulate the signal process happening inside the analyzer. The window size of the STFT program determines the spread function of the final output of the distributed strain. However, this simulation takes too long a time (a few hours) for one simulation of  $2^{10}$  number of averages with a cable length of 10 m. In reality, cable sensor length is to the scale of several thousand meters and measurement is taken in an average of  $2^{16}$  times to achieve necessary accuracy. As a result this model is impractical for real applications.

### Weighted average method

The second method is a simplified one made by characterizing some key parameters of the BOTDR analyzer. Considering the BOTDR analyzer as a black box, the output Brillouin spectrum is simulated as a weighted average spectrum over the analyzer's spatial resolution, which is an integration between the intrinsic spectrum and a weight function. The backscattered Brillouin spectrum profile  $H(x, \nu)$  is obtained through Eq. 4.3, and the measured Brillouin spectrum after analyzer processing can be expressed as:

$$P_{MB}(z, \nu) = \int_{z-L/2}^{z+L/2} H(x, \nu) W(x) \alpha(z) dx \quad (4.4)$$

in which  $W(x)$  is a weight function whose shape is dependent on the analyzer characteristics, and the fibre refractive index is  $\alpha(z)$ .

Rather than using phase noise as an input of the model, the power fluctuation of the analyzer measured spectrum after a certain number of averaging is characterized in the lab and then added to the simulation as a random error input. If the power fluctuation characteristic of the measured Brillouin spectrum is  $\delta P(z, \nu)$ , the simulated Brillouin spectrum can be finally obtained as:

$$P_B(z, \nu) = P_{MB}(z, \nu) + \delta P_{MB}(z, \nu) \quad (4.5)$$

in which  $\delta P_{MB}(z, \nu)$  is the random noise and its dependency on the power level needs characterizing with the BOTDR analyzer.

## 4.2 Simulation results

The simulation was conducted based on the characterization results of an NBX5000 BOTDR analyzer. Its injected pulse was measured by a spectrum analyzer. By fitting the measured pulse with Eq. 4.1, the key parameters of the pulse was obtained (Table. 4.1). Figure 4.6

compares the plots (in the time domain) of the simulated and the analyzer measured pulse. The error between the two is less than  $0.5\text{ mW}$  with an input pulse peak value of  $10\text{ mW}$ , indicating that this method to simulate a BOTDR analyzer input pulse has an accuracy of higher than 95%.

Table 4.1 Key parameters of the injected pulse characterized by NBX5000 analyzer

Pulse length	Rising time	Falling time	Power	Extinction ratio
10ns	3ns	8ns	10dBm	50dB

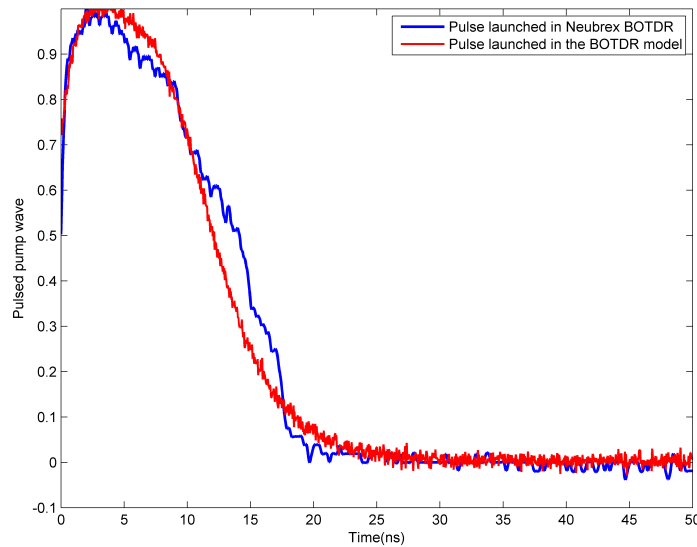


Fig. 4.6 Comparison of the analyzer injected pulse and the modelled pulse

The simulation of the received Brillouin spectrum with a step strain change was conducted using both STFT method and weighted averaging method.

#### 4.2.1 STFT simulation

The first simulation uses STFT method to investigate the impacts of averages and STFT window size on optical fibre sensor measurements. Figure 4.7 and 4.8 present the simulated strain results with different number averages of consecutive measurements for a step strain change case. The window size indicates the number of measurements that are processed within one STFT window. It can be clearly seen that a wider window size of STFT process in Fig. 4.8 leads to a longer spread length of the simulated strain result for this steep strain profile. For both signal processing window sizes, the simulated strain result is very noisy with

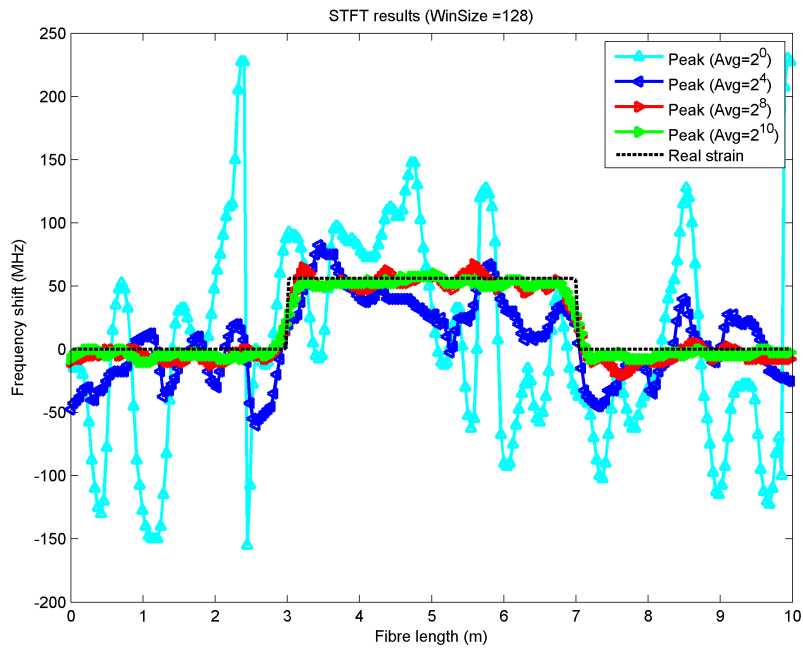


Fig. 4.7 Simulation result of a step change of  $1000 \mu\epsilon$  at different number of averages with 128 window size

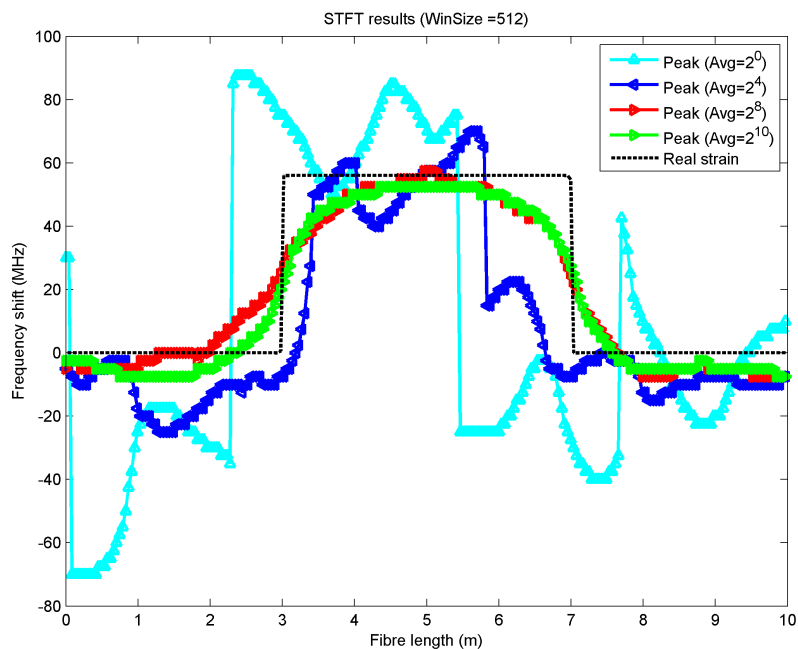


Fig. 4.8 Simulation result of a step change of  $1000 \mu\epsilon$  at different number of averages with 512 window size

an average of less than  $2^8$  measurements, making it difficult to reconstruct the input strain. When more than  $2^8$  measurements are averaged, a smoother strain shape can be obtained.

As STFT simulation method is time consuming and impractical, it is not used for subsequent analysis in this thesis.

### 4.2.2 Weighted average simulation

The second simulation uses weighted average method to model the analyzer measured Brillouin spectrum. The backscattered Brillouin spectrum ( $H(x, \nu)$ ) is simulated through the integration of the simulated pulse ( $P_p(f, f_0)$ ) and the intrinsic Brillouin spectrum information with Eq. 4.3. The intrinsic Brillouin centre frequency shift ( $S_B(z)$ ) is calculated from the input strain profile, and the bandwidth at half maximum ( $\Delta\nu$ ) is 30 MHz as previously reported.

The graphical illustration of the convolution between the backscattered Brillouin spectrum ( $H(x, \nu)$ ) and the weight function ( $W(x)$ ) for a step strain change is shown in Fig. 4.9. At a particular sampling point  $z$  and a particular frequency  $\nu$ , the measured Brillouin power  $P_{MB}(z, \nu)$  is an integration of  $H(x, \nu)$  with the weight function  $g(x)$  over spatial resolution  $L$ .

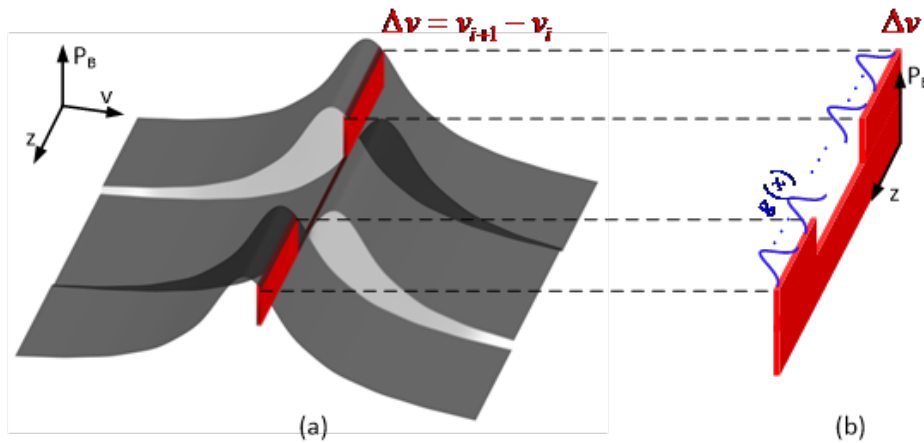


Fig. 4.9 Graphical illustration of the convolution between natural Brillouin spectrum and the weight function

Because of the weighted averaging process, the segregated Brillouin spectrum profile  $H(x, \nu)$  is converted into a continuous and distorted profile  $P_{MB}(z, \nu)$ . After fitting the processed spectrum  $P_{MB}(z, \nu)$  with a Lorentz shape function, the initial step centre frequency change will appear as a distributed centre frequency change, and the measured centre frequency result will be a relatively smaller value compared to the input centre frequency change.

### Weight function simulation

The weight function ( $W(x)$ ) of Neubrex NBX-5000 was first characterized through best fitting the simulation and the analyzer measured strain. In this experiment, the strain cable was stretched by two ends for  $1.5\text{ m}$  in the laboratory with seven different strain levels:  $250\ \mu\epsilon$ ,  $500\ \mu\epsilon$ ,  $750\ \mu\epsilon$ ,  $1250\ \mu\epsilon$ ,  $1750\ \mu\epsilon$ ,  $2250\ \mu\epsilon$  and  $2750\ \mu\epsilon$ , as most strain increment measurements in a typical field case in civil engineering are in a range of  $0 - 3000\ \mu\epsilon$ . The analyzer was set with a spatial resolution of  $1\text{ m}$ , sampling resolution of  $0.05\text{ m}$ , and measurement averages of  $2^{16}$ .

Four different shapes of weight function distribution (normal distribution, Weibull distribution, logistic distribution, and Beta distribution) were used to simulate the analyzer measurements, and it was found that a normal distribution gave the best fitting between the simulation and the analyzer measurement results. Therefore, the weight function takes the form of a Gaussian curve as described by the following equation:

$$W(x | z, \sigma) = \frac{1}{\sigma\sqrt{2\pi}} e^{-\frac{(x-z)^2}{2\sigma^2}} \quad (4.6)$$

The optimized weight function to fit the tested strain input levels with minimum standard variation has a  $\sigma$  of  $0.185\text{ m}$  as shown in Fig. 4.10. For the NBX-5000 BOTDR analyzer, the weight function  $W(x, v)$  takes the form of a Gaussian curve with a bandwidth of  $0.185\text{ m}$  and a length of  $1\text{ m}$ , when the pulse length of the analyzer is set as  $10\text{ ns}$ .

### Noise simulation

Measurement noise with  $2^{16}$  averages was characterized in regard of the power fluctuation along the cable distance as well as the power variation with time. The characterized noise was then applied to the model to replace the time consuming phase noise simulation process by STFT method.

The reason for power fluctuations with time is related to the stability of the analyzer hardware, that is the random noise of different analyzer components including the unstable pump and probe laser. Therefore, the amount of measurement fluctuation with time is analyzer dependent and needs be carefully characterized in the lab.

In this test, repeated Brillouin spectrum measurements of the sensing cable in the free strain condition were recorded and investigated for power fluctuation characterization. The tested cable was a single mode fibre (SMF-28) in  $200\text{ m}$  length. The characterized analyzer was an NBX-5000 BOTDR with averaging setting as  $2^{16}$ , frequency step as  $3\text{ MHz}$ , spatial resolution as  $1\text{ m}$ , and sampling resolution as  $0.05\text{ m}$ .

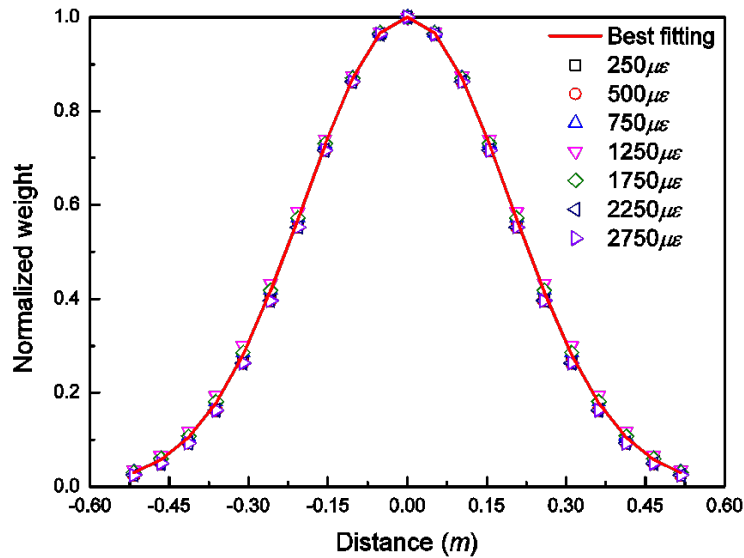


Fig. 4.10 Simulated best fitting weight function for different strain input levels and the average fit line for the weight functions

The analyzer power fluctuation with time is characterized with experimental results. Figure 4.11 illustrates the Brillouin spectrum measured repeatedly at one point of the tested cable ( $z = 40\text{ m}$ ). The figure shows that the tested sensor has a centre frequency of  $10.86\text{ GHz}$  and a bandwidth of  $150\text{ MHz}$ . Fluctuations in the power measurement with time can be clearly seen at different frequency levels in the figure. Because of random noise, the measured Brillouin spectrum slightly varies with time. Random power fluctuation can be clearly seen, especially at the peak power point.

The Power fluctuations at the peak power frequency ( $10.86\text{ GHz}$ ) is then investigated along the cable length. Figure 4.12 illustrates the peak Brillouin power distribution of the tested cable, with the standard deviation of the repeated peak power measurements as error bars. It can be clearly seen that the peak power value slightly reduces with fibre length, attributing to the fibre linear loss. The level of power fluctuation randomly distributes along the fibre in a range of  $4.1 \times 10^{15} - 4.9 \times 10^{15}$ . The repeated power measurement is then studied in detail at one point of the cable.

To investigate the distribution of repeated power measurement, the histogram of the repeated power readings at peak power frequency level  $10.86\text{ GHz}$  and at location of  $z = 50\text{ m}$  is plotted in Fig. 4.13. The x axis is the power reading which is normalized as the ratio of the measured power to the mean level of all measurements. The y axis is the counts of the power readings. The red line is the fitting result of the power reading histogram. It indicates that at

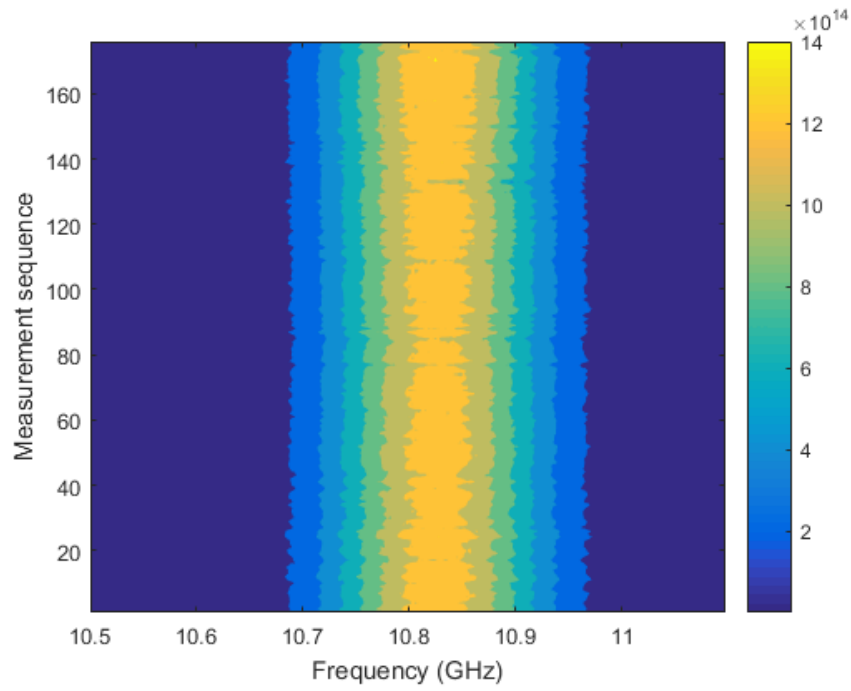


Fig. 4.11 Repeated Brillouin spectrum measurements at one point of the free-strained cable

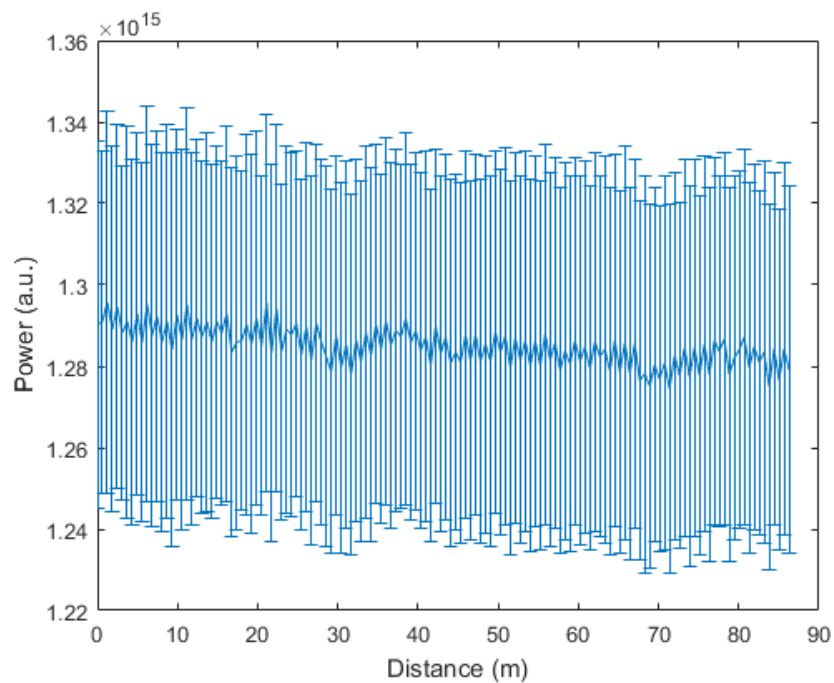


Fig. 4.12 Illustration of the peak and standard deviation of power measurements at all locations of the tested fibre

this particular frequency level, the power fluctuation in the time domain follows a normal distribution with a bandwidth of 0.0354.

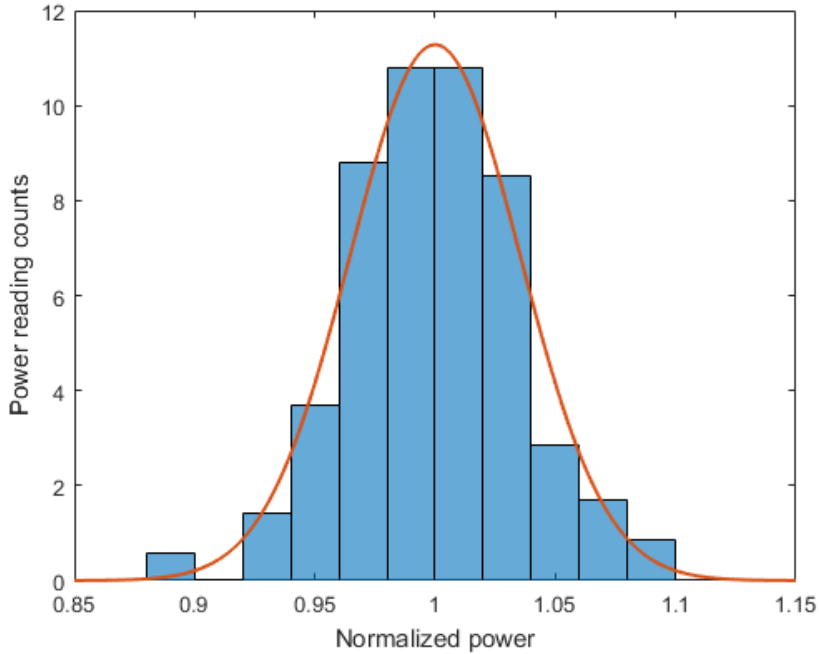


Fig. 4.13 Histogram of normalized power readings at a frequency level of 10.86 GHz

The dependency of the power fluctuation bandwidths on power level is finally obtained by characterizing the power fluctuation with time at different frequency. Figure 4.14 graphically illustrates the relationship between the bandwidth of power fluctuation and the power level. The blue dots in the figure are the characterized data measured by the analyzer and the red curve follows an exponential distribution. The analyzer measurements can be well approximated by the exponential distribution line which is:

$$N_{\delta P} = 9.325 \times 10^5 \times P_{MB}^{-0.5096} + 0.01684 \quad (4.7)$$

In this equation,  $P$  is the power reading, and  $N_{\delta P}$  is the fluctuating bandwidth of the repeated power readings.

A simplified model is therefore developed to simulate the analyzer measurement random noise based on the characterized power fluctuation curve. The relationship between the normalized power fluctuation ( $N_{\delta P}$ ) and the power level ( $P_{MB}$ ) can be described as:

$$N_{\delta P} = A \times (P_{MB})^B \quad (4.8)$$

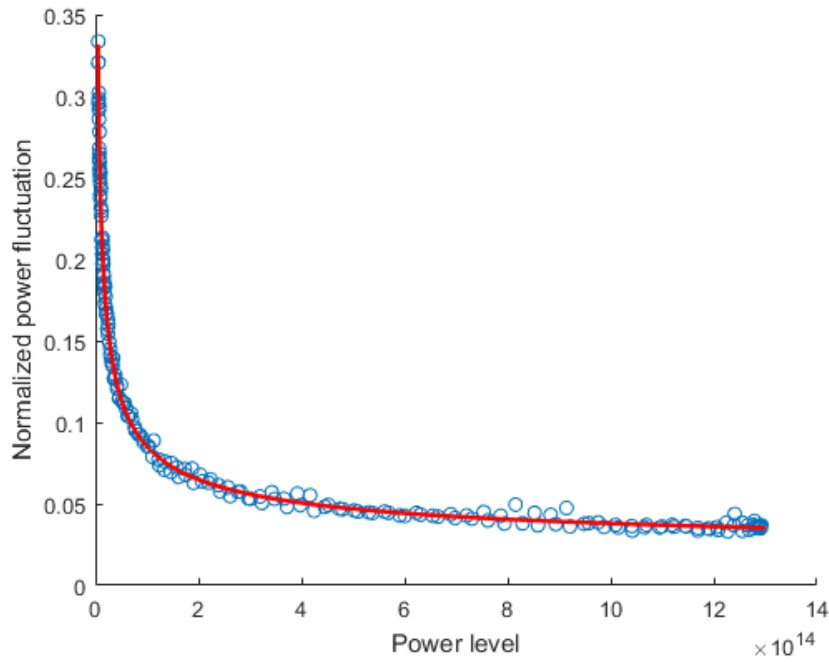


Fig. 4.14 The dependency of the repeated power measurements distribution bandwidth on power level

in which  $A$  and  $B$  are parameters that depend on the analyzer and its settings of measurement.

The absolute power fluctuation ( $\delta P_{MB}$ ) can be obtained by multiplying the normalized data  $N_{\delta P}$  with power level ( $P_{MB}$ ):

$$\delta P_{MB} = P_{MB} \times N_{\delta P} \quad (4.9)$$

Considering the power loss of the cable, the power fluctuation at distance  $z$  can be obtained. Equation 4.9 is therefore transferred into:

$$\delta P_{MB}(z) = P_{MB}(z=0) \exp(-2\alpha z) \times A \times (P_{MB}(z=0) \exp(-2\alpha z))^B \quad (4.10)$$

in which  $\alpha$  is the linear attenuation of the cable, and  $P_{MB}(z=0)$  is the power level at  $z=0$ .

The parameters  $A$  and  $B$  can be characterized in the lab using repeated Brillouin spectrum measurements. For the Neubrex analyzer used in this experiment,  $A = 1.11$ ,  $B = -0.4357$ . Therefore, the characterized relationship between the power fluctuation and the power level is  $\delta P_{MB}(z) = P_{MB}(z=0) \exp(-2\alpha z) \times 1.11 \times 10^5 \times P_{MB}(z=0) \exp(-2\alpha z)^{-0.4357}$ .

### 4.3 Model verification

The simulation results were compared with experimental measurements to verify the reliability of this model. The NBX-5000 analyzer was used with the same setting as before for Brillouin spectrum measurements. The Fujikura strain sensing cable was set in various conditions: free-strain status, or step strain at different strain levels/lengths.

#### 4.3.1 Brillouin spectrum verification

The characterized relationship between measurement fluctuation with power level is first verified by a strain sensing cable (Fujikura reinforced strain cable) in free strain condition. Figure 4.15 compares the previously characterized power fluctuation to power level curve and the analyzer measurement results at one point of the tested strain cable. The maximum measured power that the analyzer can achieve in this experiment is half of the previous characterized curve result, which is probably due to the power loss induced by the cabling process. However, a good agreement can be clearly found in the analyzer measured power range between the characterized curve and the analyzer measurements, indicating that the previously characterized curve is suitable for analyzer random noise simulation.

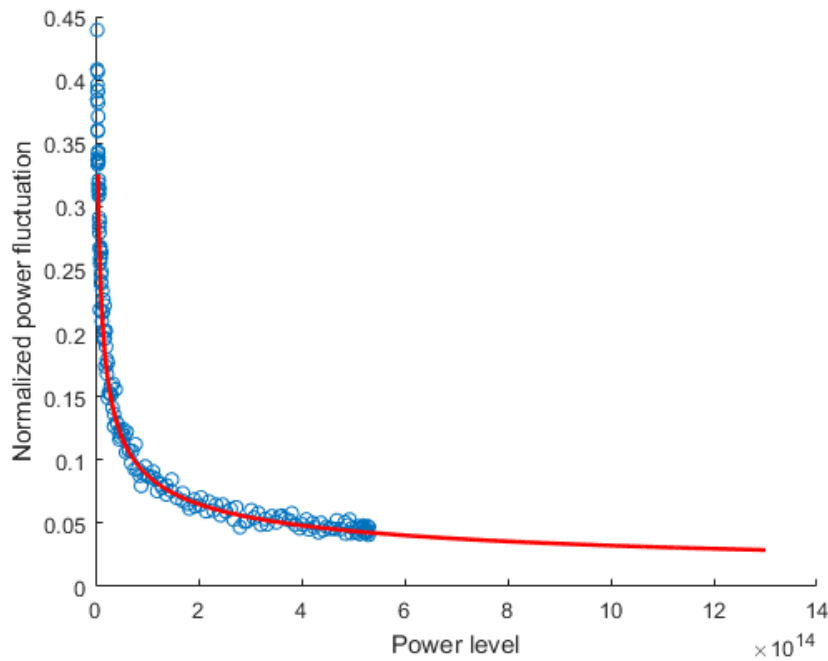


Fig. 4.15 The fitting between the analyzer measurements of the the tested strain cable with the previously characterized power fluctuation curve

The characterized curve is then used for measurement simulation all along the cable. The Brillouin spectrum is simulated as the weighted average process, and the noise is added by using the previously characterized power fluctuation curve and Eq. 4.10. The intrinsic Brillouin frequency shift input of the model is zero all along the cable. The final result of the analyzer measured Brillouin spectrum and the simulated spectrum result is compared in Fig. 4.16.

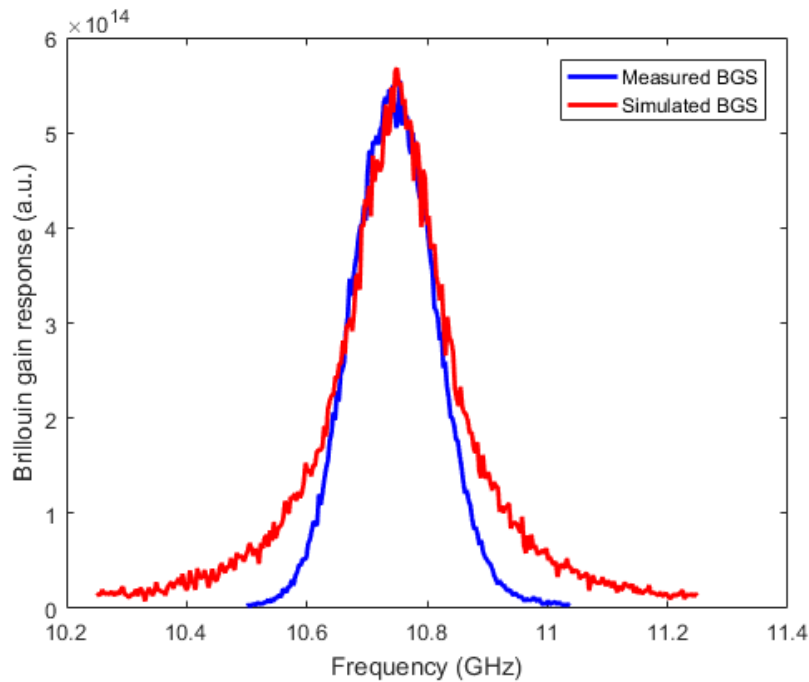


Fig. 4.16 Comparison of the measured Brillouin gain spectrum and the simulated Brillouin gain spectrum

The experimental Brillouin spectrum from the Neubrex analyzer is slightly different from the modelled result at the spectrum tailing sections because of Erbium-doped Fibre Amplifiers (EDFA) or some other optical components effects. Since the spectrum with half-bandwidth is used for peak centre frequency determination, the model is therefore within confidence of spectrum simulation.

The strain of the tested free strain cable is simulated with the developed model and the result is then compared with analyzer measurement. Because of the cabling process, measurement of the strain sensing cable has a pre-strain reading. To remove the effect of initial strain, the measurement of the strain cable is calculated as the difference between two repeated measurements along the cable. The simulated strain result is obtained by fitting the developed Brillouin 3D spectrum with a Lorentz shape to find the peak centre frequency and then transferred to strain using the Brillouin frequency to strain conversional coefficient.

The final measured and the simulated strain profiles are compared. The standard deviation of strain fluctuation with time is  $11.06 \mu\epsilon$  by analyzer measurements and  $10.46 \mu\epsilon$  by simulation results. At a particular point of the cable, the measured strain fluctuation with time is in agreement with the result of the simulated data, as shown in Fig. 4.17.

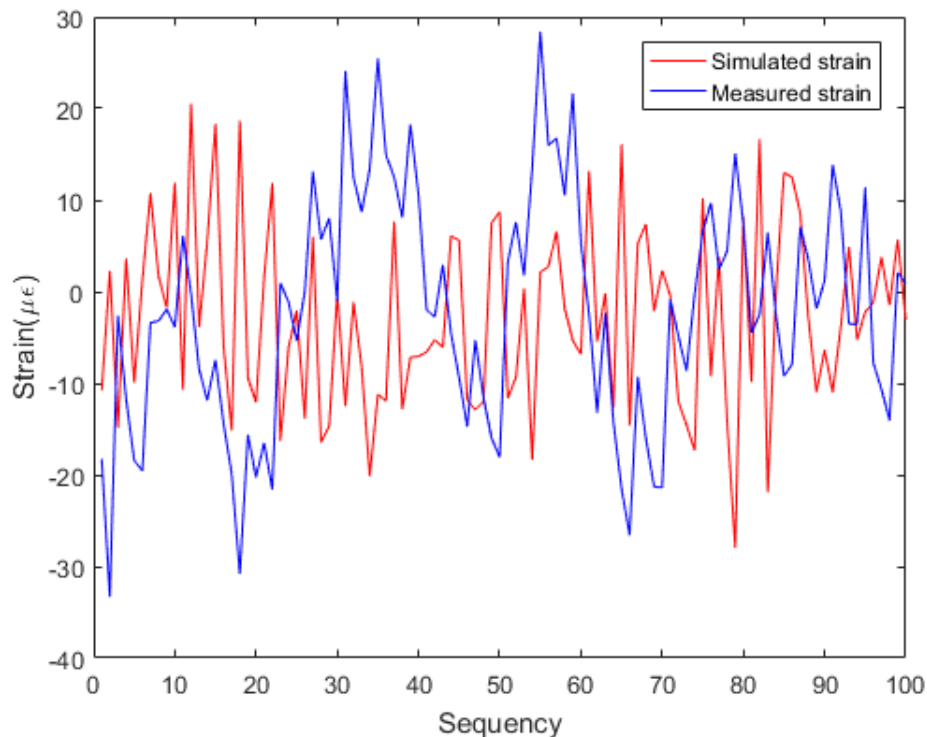


Fig. 4.17 Comparison of the analyzer measured repeated strain and the simulated repeated strain

The fluctuation of the simulated strain is suitable for simulating the analyzer measured strain fluctuation in time. The relatively higher strain variation measurement in cable length is due to the non-uniform strain distribution which is not considered in the model. The effect of cable strain conditions on measurement precision error will be discussed in detail in Chapter 5. In general, the good agreement between simulation and experimental results indicates that this Brillouin 3D model can effectively simulate the Brillouin spectrum with analyzer random noise.

### 4.3.2 Strain measurement verification

The reliability of the model in describing strain spread was then validated with laboratory tests where a section of  $1.5m$  reinforced strain sensing cable was fixed at one end and

stretched at the other end. Measurements were taken at three different strain levels (around  $1250 \mu\epsilon$ ,  $2000 \mu\epsilon$  and  $2800 \mu\epsilon$ ) by the Neubrex NBX-5000 BOTDR analyzer. The set up of this experiment was same as that used in Section 3.2.1.

Figure 4.18 shows the comparison of the laboratory local straining inputs, BOTDR measurement results and simulation results computed with the evaluated weight function which is given as  $0.185 m$ . A good agreement between the simulation and experimental values can be clearly seen in the figure. The correlations between the simulation and experimental values are above 99% for all three straining cases. The error between the experiment results and the simulated curve is  $11 \mu\epsilon$ . Therefore the theoretical error for such an operation is  $9.48 \mu\epsilon$ , which is in good agreement with the observed value.

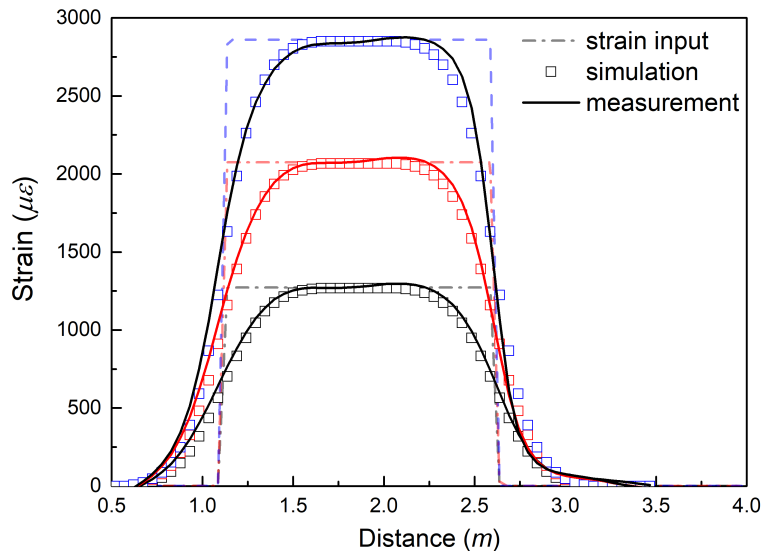


Fig. 4.18 Comparison of the simulated results and the analyzer measured results at different strain input levels

Figure 4.18 also implies that error is more significant at the strain change sections (distance =  $0.75 m - 1.25 m$  and  $2.25 m - 2.75 m$ ). For a BOTDR analyzer with a certain spatial resolution  $L_s$  (one metre in this case), a non-uniformly distributed strain over  $L_s$  will distort the received Brillouin spectrum or induce additional peaks to the spectrum. As a result, strain measurement will have a larger error at points where strain changes rapidly (i.e. a step function in this case). This will be discussed later in Chapter 5 and 6.

The reliability of the optics model in describing strain in a length shorter than the analyzer's spatial resolution was then validated. The strain sensing cable was tensioned at

$1200\mu\epsilon$  in three sections, with the tension length of  $0.5\text{ m}$ ,  $1\text{ m}$ , and  $1.5\text{ m}$ . The spatial resolution of the analyzer was set as  $1\text{ m}$ .

As shown in Fig. 4.19, good agreement between the simulation results and the analyzer readings was found, and the correlation coefficient was better than 99%. In addition, both the analyzer measured and the simulated strain shows rather unreliable measurement at sections one and two: comparing to the input strain ( $1200\mu\epsilon$ ), a maximum measurement of  $900\mu\epsilon$  and  $1100\mu\epsilon$  are found for sections one and two in the figure. The relatively smaller strain measurement is due to the analyzer's spatial resolution, over which the measured strain is a convoluted result. Therefore, when the strained length of the cable is less than or around the analyzer's spatial resolution, analyzer readings is far smaller than true strain, leading to measurement systematic error.

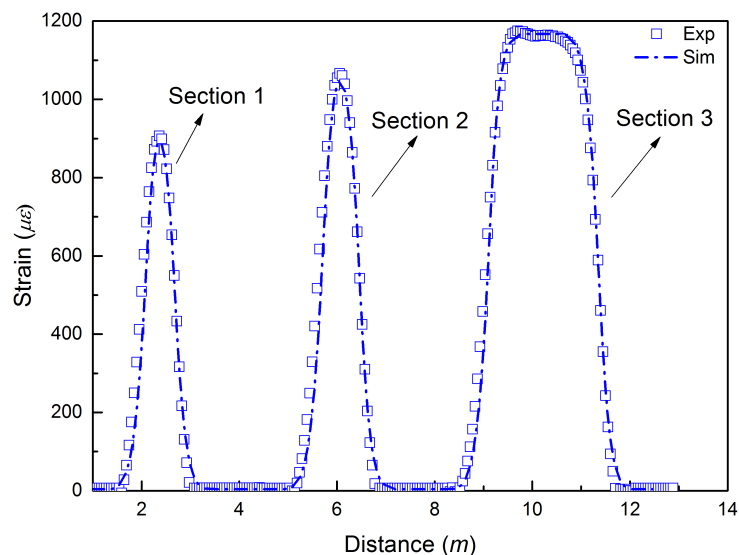


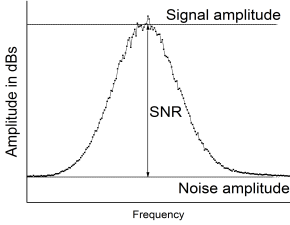
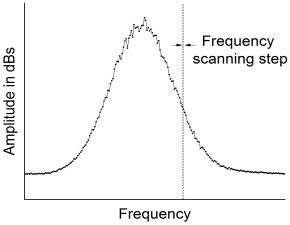
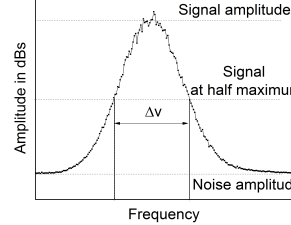
Fig. 4.19 Comparison of the strain measurement obtained from analyzer and the simulated strain result at different strained section lengths

In general, the above examples show good agreement between the modelled results and the analyzer measurements when there is a sharp strain change. It is therefore verified that this weight function can be used to simulate the signal process inside the analyzer. The measured strain can later be back calculated using this model to reconstruct the strain from analyzer measurements with higher accuracy.

## 4.4 Parametric studies

The constructed model was used to simulate the effects of different factors, including cable parameters (fibre loss and cable length) and analyzer specifications (SNR, frequency scanning step, and spectrum bandwidth, etc.) on the distributed sensor measurement precision error. The detailed description and graphically illustration of the analyzer parameters are summarized in Table. 4.2.

Table 4.2 Detailed description and graphically illustration of the analyzer parameters

Parameters	SNR	$\varphi$	$\Delta\nu$
Details	signal to noise ratio $SNR = P_{signal}/P_{noise}$	frequency step between two points	bandwidth at half maximum power
Sketch			

The relationship between precision error and measurement parameters can be characterized as below[78]:

$$\sigma_v(z) = \frac{1}{SNR(z)} \sqrt{3/4\varphi \cdot \Delta\nu} \quad (4.11)$$

in which SNR is the signal to noise ratio,  $\Delta\nu$  is the half bandwidth of the measured spectrum, and  $\varphi$  is the frequency scanning step.

For a typical BOTDR analyzer with an SNR of 20 dB, FWHM of 130 MHz, and  $\varphi$  of 3 MHz, the measurement precision error is calculated as 0.855 MHz (approximately 17 $\mu\epsilon$ ) using Equation 4.11.

### 4.4.1 Cable parameters

Cable length and attenuation factor are two parameters that affect the simulation results of the optics model. When light travels through a sensing cable, its power will keep loss through the cable length and thus reduce the SNR of the received measurement. As a result, the measurement precision error, which is proportionally related to the SNR, is affected by the power attenuation factor of the sensing cable. The influence of the fibre power loss as well as the cable length on the measurement precision error are therefore investigated. To conduct a

parametric study on cable effects, the analyzer inputs are set as constant. For this simulation, the same inputs (pulse shape, power fluctuation characteristics, 3 MHz frequency step and 30 MHz FWHM) as previously characterized in the lab are used.

The simulated strain measurement of a cable in the free strain condition, with 20 km length and attenuation factor of 0.02 dB/km is shown in Fig. 4.20. It can be clearly seen that the range of strain fluctuation increases from nearly  $\pm 10 \mu\epsilon$  (equivalent to  $\pm 0.5$  MHz) to  $\pm 40 \mu\epsilon$  (equivalent to  $\pm 2$  MHz) along the 20 km cable. This result is in agreement with previous reported experimental measurement [63]. The exact inverse relationship between the measurement fluctuation and SNR is evident in the figure when considering the growth of the strain fluctuation with distance, due to the one-way fibre attenuation.

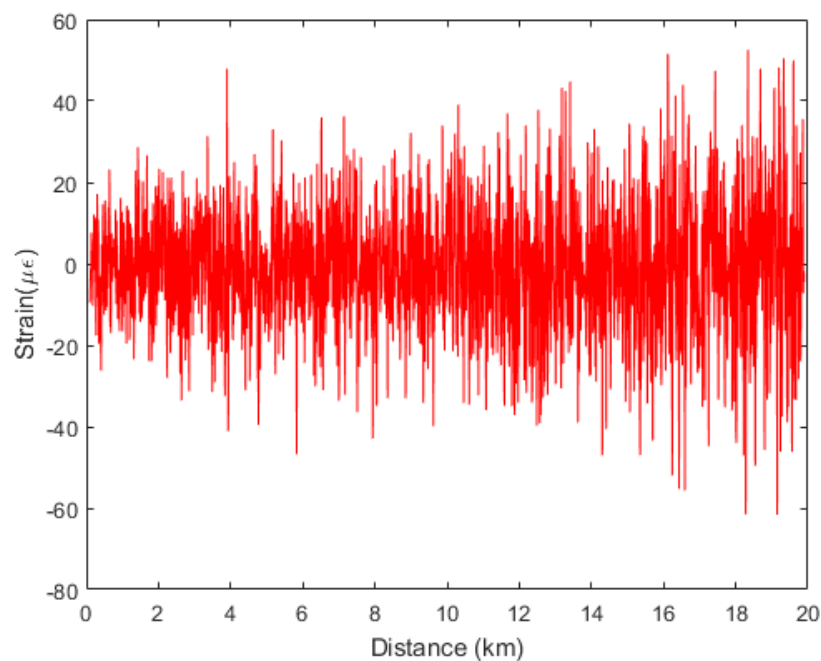


Fig. 4.20 The simulated strain fluctuation along the optical fibre of 20 km length

The simulation is then done repeatedly with fibre linear loss of 0.25 dB and 0.23 dB. Figure. 4.21 compares the measurement precision error as a function of distance at different fibre attenuation levels. The scattered measurement error is calculated as the standard deviation of the simulated strain obtained in a 200 m cable section. The lines in the figure represent the respective strain error calculated using Eq. 4.11, based on the simulated SNR and bandwidth information.

The impact of the fibre attenuation coefficient can be clearly observed in the above figure. When the cable length is shorter than 2 km, the fibre attenuation factor does not have a significant impact on the precision error. It stays close to  $10 \mu\epsilon$  for all three cases. As the

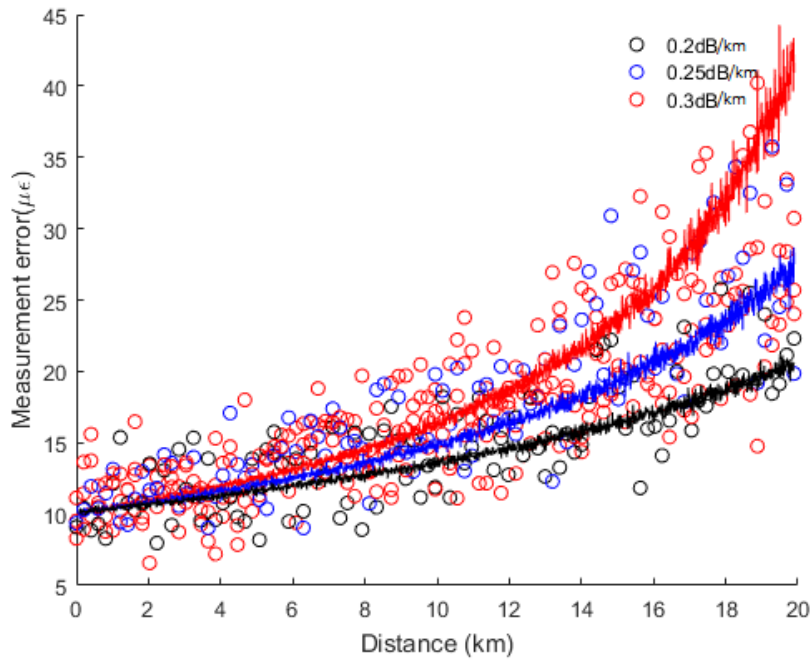


Fig. 4.21 The simulated strain precision along the optical fibre of 20 km length at different attenuation levels

location of the measurement gets longer, the precision error starts to increase with distance. The gradient of the increase is dependent on the attenuation factor, that is, a larger fibre attenuation factor causes a faster precision error increment along the fibre. The precision error obtains at 20 km distance with 0.3 dB/km loss is 44.3  $\mu\epsilon$ , which is improved down to 21.1  $\mu\epsilon$  with 0.2 dB/km loss. This corresponds to an improvement factor of 2.1 on the measurement precision error by improving fibre loss in 0.1 dB/km for 20 km length of cable.

#### 4.4.2 Analyser parameters

The analyzer parameters that influence the optics model simulation results are investigated upon a short length of cable to remove any cable effects. The essential discrepancy of the model simulation with the formerly published precision error equation is checked. The analyzer input parameters includes scanning frequency, SNR, and Brillouin full width at half maximum (FWHM). By changing one parameter and fixing the others, the simulated precision error dependency on analyzer parameters is obtained and then compared with the equation relations.

The inverse dependency of SNR on precision error is first investigated. The pulse extinction ratio input of the optics model is used to change the SNR of the received Brillouin

signal. Based on typical BOTDR settings, the frequency step is fixed at 3 MHz and the final convoluted Brillouin spectrum FWHM is fixed at 130 MHz. Figure 4.22 illustrates the simulated and calculated results of the precision error with a changing SNR. An inverse linear relationship between SNR and the random error is obtained from the model, correlating well with the published Eq. 4.11.

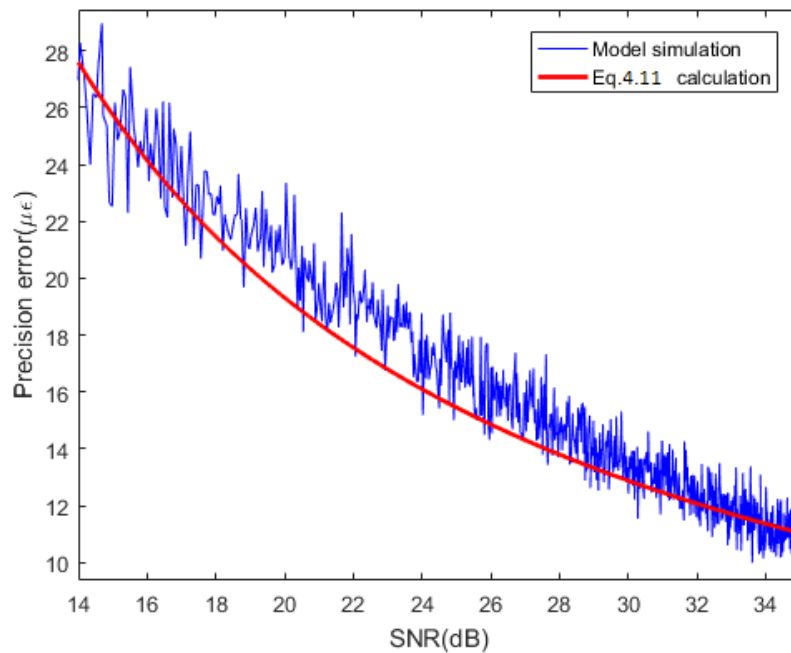


Fig. 4.22 Comparison of the dependence of precision error on SNR in model simulation and equation calculation results

The dependence of the precision error on the frequency scan increment is investigated by fixing the SNR and full width at half maximum, and changing the frequency step in the model. Figure 4.23 shows the simulated precision error as a function of the frequency scanning step when using 30 MHz FWHM and 32 dB SNR. It can be observed that a small frequency step (i.e. when more data points are involved in the fitting of the gain spectrum) leads, as expected, to more accurate frequency measurements. Therefore, as shown in Fig. 4.23, if the frequency increment is larger, the frequency error grows with a factor proportional to  $\varphi$ , in full agreement with Eq. 4.11.

Finally, the impact of the Brillouin linewidth on the frequency error is analyzed, as shown in Fig. 4.24. Here, the Brillouin linewidth is simply changed using different pump pulse widths (between 10 ns and 50 ns). However, it is important to take into account that when the spatial resolution varies, the local Brillouin gain will change, affecting the SNR of the traces accordingly. To evaluate the impact of the Brillouin spectral width only, the peak pump

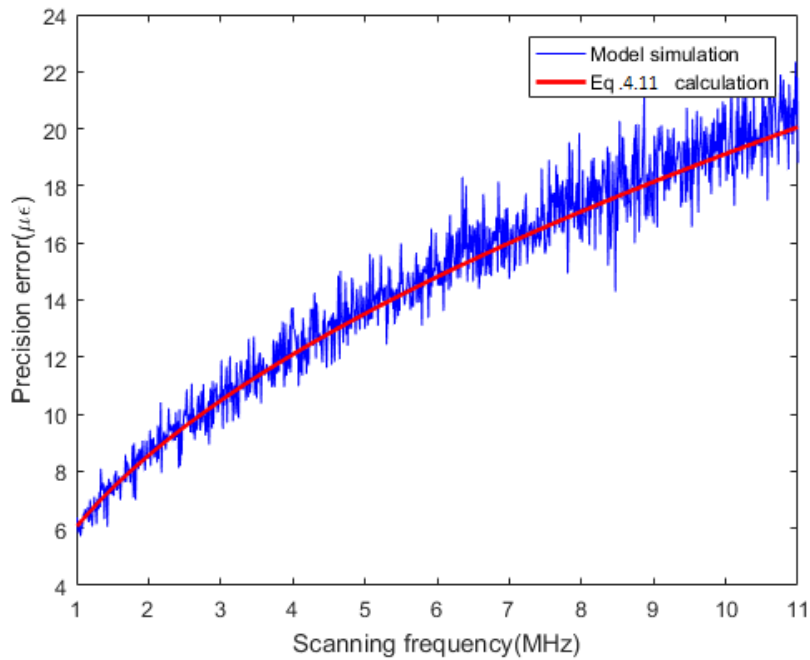


Fig. 4.23 Comparison of the dependence of precision error on scanning frequency step in model simulation and equation calculation results

power is adjusted in order to keep a constant Brillouin gain between measurements. This way, the SNR on the analyzer traces at the peak frequency is the same for all measurements (SNR = 32 dB as in the previous case), making a reliable comparison possible between different Brillouin linewidth conditions.

## 4.5 Summary

1. A novel and applicable spontaneous Brillouin backscattering spectrum model was developed. The model includes the injected pulse simulation, the received Brillouin spectrum simulation through a 3D weighted averaging process, and the spectrum noise simulation.
2. It was revealed that there is a dependent relationship between the analyzer measured Brillouin spectrum power fluctuation and the power level.
3. The model is experimentally verified to suit for the monitoring cable strained in different lengths and levels.

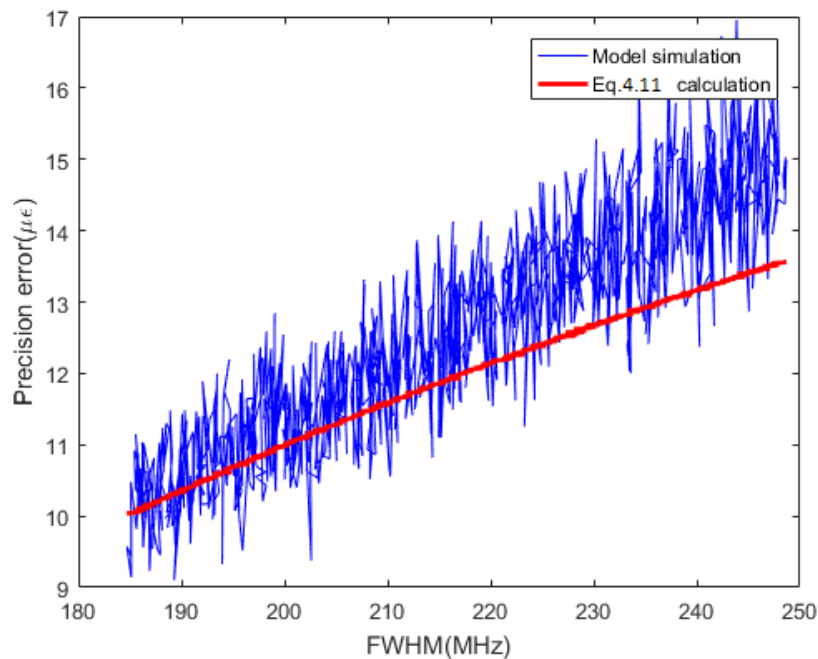


Fig. 4.24 Comparison of the dependence of precision error on Brillouin linewidth in model simulation and equation calculation results

4. The impact of the fibre attenuation factor on the precision error started to occur when the fibre length was longer than 2 km. There was an improvement factor of 2.1 on the measurement precision error by improving fibre loss by 0.1 dB/km for 20 km length of cable.
5. The precision error decreased from 28  $\mu\epsilon$  to 11  $\mu\epsilon$  when the SNR increased from 14 dB to 35 dB. The precision error increased from 6  $\mu\epsilon$  to 20  $\mu\epsilon$  when the scanning frequency step increased from 1 MHz to 11 MHz. The precision error increased from 10  $\mu\epsilon$  to 14  $\mu\epsilon$  when the full width at half maximum increased from 185 MHz to 250 MHz.

# Chapter 5

## Precision error

Distributed Brillouin fibre optic sensing has been widely used for large-scale strain and temperature monitoring in infrastructure monitoring applications. Being a new technology, one of its key measurement parameter is sensing repeatability, which is characterized by precision error using the standard deviation of a number of consecutive measurements [13]. Theoretical and experimental studies have shown that the precision error of Brillouin distributed fibre optics sensing measurement is fundamentally dependent on the Brillouin gain linewidth, spatial resolution, frequency scanning step, number of averaging times, and signal to noise ratio (SNR) [58][87]. For a typical Brillouin Optical Time Domain Reflectometry (BOTDR) analyzer, its precision error follows a normal distribution with a standard deviation of around  $15 \mu\epsilon$  [52].

Unfortunately, real site monitoring results have shown that the measured precision error can be far more significant, resulting in a nontrivial data interpretation for the field sensing data. In some field applications, unexpected data fluctuations have been observed and the accuracy of strain and temperature measurement appears to degrade. For example, the 5-day measurements on the roller compacted concrete (RCC) dam Fundão in Brazil revealed that the precision error was mostly about  $70 \mu\epsilon$  along the cable, and up to  $500 \mu\epsilon$  at some particular locations (e.g. cable fixation, splice connections and places with local losses) [27]. For a cracked concrete beam, a maximum precision error of  $300 \mu\epsilon$  under fluctuating loads was also reported from ten repeated measurements using BOTDR [25]. The significant data precision error obtained on site makes it important to investigate the characteristics of the precision error and its impacts on the reliability of the interpreted strain profile.

Chapter 5 explores the mechanism and characteristics of the dependent relationship between strain non-uniformity (using strain gradient as an index) and measurement precision error, through both numerical simulations and lab experiments with a BOTDR sensing system and field sensing data from two typical civil engineering site applications. The precision

error in this chapter is characterized as frequency error and distance error. The former is the random error in the frequency domain, closely related to the signal to noise ratio, while the latter is dependent on the timing error of the analyzer's acquisition system. A theoretical estimation method is proposed to quantify the BOTDR frequency and distance resolution induced precision errors using the measured 3D Brillouin gain spectrum. To illustrate the reliability of this precision error prediction method, comparisons between the experimental measured error and the predicted error are performed. A dependent relationship between the measured strain gradient and measurement error was revealed by both experimental and predictive results. A precision error compensation method was finally developed and evaluated with experimental sensing data sets.

## 5.1 Example of on site measurement precision error

Field continuous sensing data sets from two typical Civil Engineering applications, Newfoundland (NFL) piling and National Grid (NG) tunneling sites, were used to examine the characteristics of measurement precision error.

### 5.1.1 Newfoundland pile site

The Newfoundland construction site is located at No. 1 Park Place, Canary Wharf, London. In this project, fibre optic cables were installed in a 1.5 *m*-diameter pile, to monitor the development of strain and/or temperature during the concrete curing process. The used strain sensing cable was as Fujikura reinforced cable, and a loose buffered temperature sensing cable was installed adjacent to the strain cable for temperature compensation. Both fibre cables were attached along the reinforcement cage. The schematic layout of the test pile is shown in Fig. 5.1. Detailed description of the field work is given in the pile test reports [15] [79].

After the cage was installed inside the borehole, concrete was cast in the borehole to create a pile. This was carried out on 31<sup>st</sup> January 2014. The concrete was left to cure for more than 10 days. During that time, BOTDR measurements were taken every 7 minutes until 14<sup>th</sup> February, 2014. By 13<sup>th</sup> February 2014, the hydration was expected to be complete. On 14<sup>th</sup> February when the hydration was complete, 40 repeated FO data readings were collected continuously with a Neubrex BOTDR analyzer (NBX-5000). The relatively stable variation of the data sets over time for both of the temperature cable and strain cable can be seen in Fig. 5.2. During the data collection period, the temperature variation along the fibre was within 1°C (equivalent to  $\pm 10 \mu\epsilon$  variation in strain cable result), smaller than the

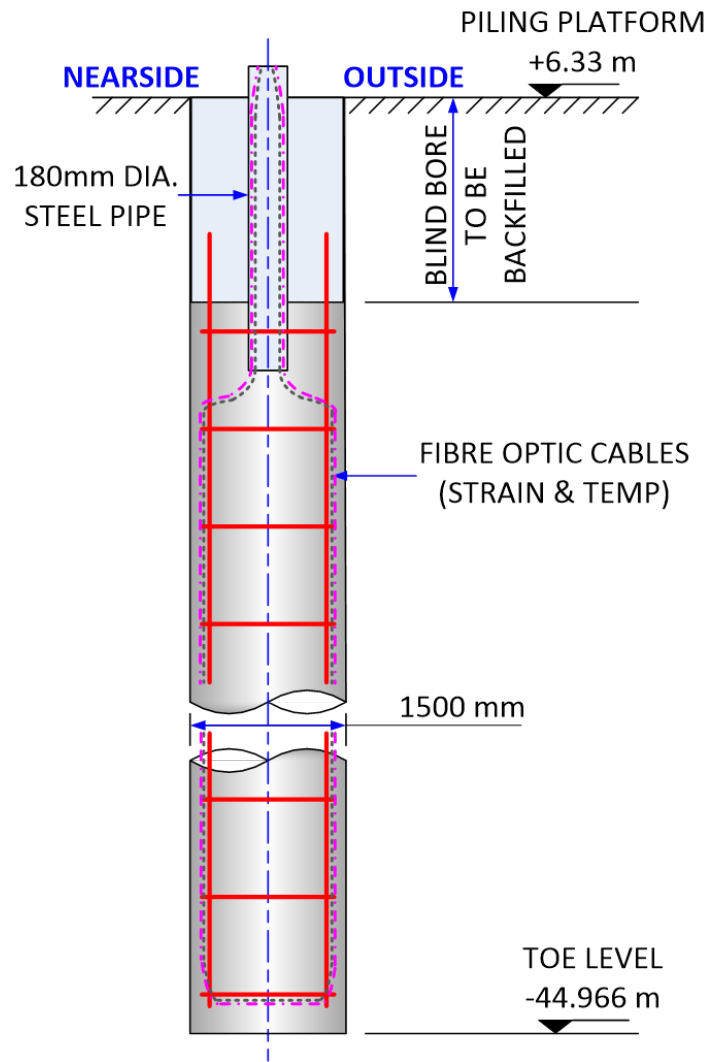
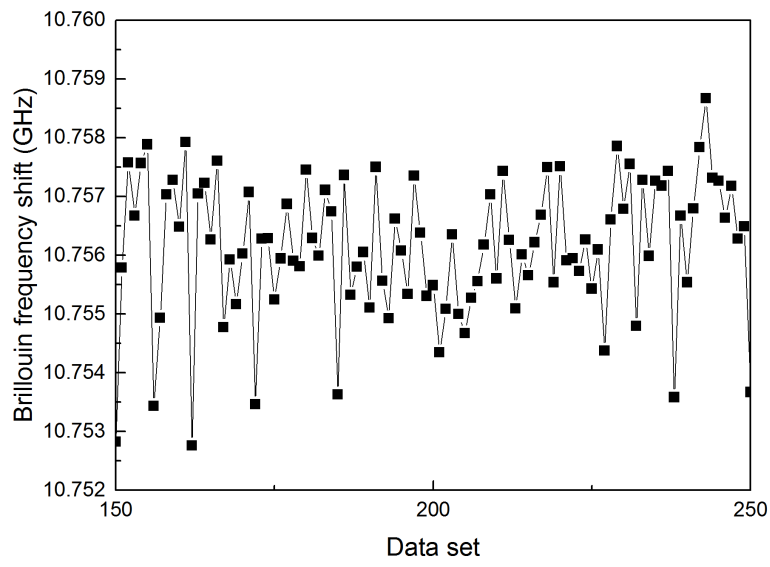
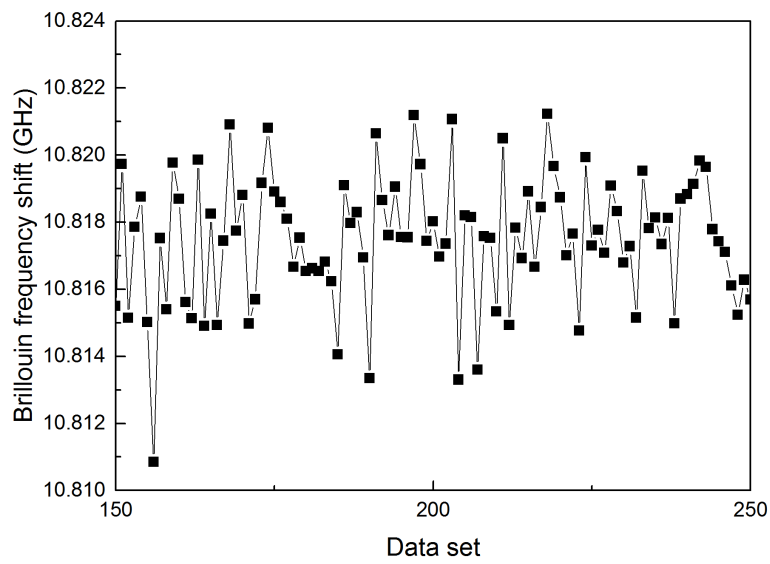


Fig. 5.1 Structural pile layout and fibre optic instrumentation in Newfoundland



(a)



(b)

Fig. 5.2 Variation of the measured Brillouin centre frequency over time for (a) temperature sensor and (b) strain sensor for Newfoundland pile

characterized strain measurement error in the lab ( $\pm 15.9 \mu\epsilon$  in chapter 3), the temperature variation is therefore neglected. It was found that the measurement variation over time for the Brillouin centre frequency result was randomly distributed with a standard deviation of maximum 2 MHz ( $40 \mu\epsilon$ ) for the strain cable and 1 MHz ( $2^\circ\text{C}$ ) for the temperature result.

Figure 5.3 illustrates the longitudinal temperature measurement at different stages of the concrete curing process [15]. Originally, the fluctuation of the temperature cable measurement over distance was about  $1^\circ\text{C}$  (within the analyzer's random noise range). When the concrete started to cure, the temperature of the sensor tended to vary more significantly (as large as  $3^\circ\text{C}$ ). Over the last day of monitoring when the concrete hydration was complete, the measurement fluctuation of the sensor returned to its original condition, less than  $1^\circ\text{C}$ .

In addition to temperature fluctuation, strains developed due to shrinkage of the concrete during the hydration process. This created an inhomogeneous strain profile within the pile. This can be verified in Fig. 5.4 which plots the interpreted strain  $\epsilon$ , strain gradient  $\epsilon'$ , and measurement precision error  $\Delta\epsilon$  along the pile over the last day of monitoring. During the data collection period, it was noticed that the temperature variation along the fibre was negligible, only within  $1^\circ\text{C}$ . The strain was converted from the measured Brillouin frequency shift using their linear relationship, and the precision error was calculated as the standard deviation of the 40 measurement data sets. It is clear from Fig. 5.4(a) that the strain profile along the fibre was rather non-uniform. This was most likely induced by the interactions between the cables and concrete aggregates. It was also possible that the concrete hydration during the curing process have contributed to the uneven strain profile. The measurement precision error, as shown in Fig. 5.4(c), displays a varying precision error along the cable length, with a baseline and peak values of about  $25 \mu\epsilon$  and  $40 \mu\epsilon$ , respectively. This is much larger than that of the free cable, where a uniform precision error of  $15 \mu\epsilon$  was reported, attributed to analyzer random noise [52]. It is very interesting to note that there is a close link between the precision error and strain gradient, as indicated in Fig. 5.4(b). The larger the absolute value of strain gradient is, the higher the precision error appears.

### 5.1.2 National Grid tunnel site

At a National Grid site in London, a DFOS sensor was installed inside the concrete tunnel lining in order to measure the structural performance of the tunnel during and after construction.

Figure 5.5 (a) shows the schematic graph of the tunnel. The blue highlighted section is one particular tunnel ring, which has a width of  $1.3\text{ m}$  and comprises 6 segments. Thirty-six concrete segments (with dimensions of  $1.5\text{ m} \times 1\text{ m} \times 0.75\text{ m}$ ) were installed with Fujikura strain sensing cable adjacent to a loose buffered temperature sensing cable. The cage structure

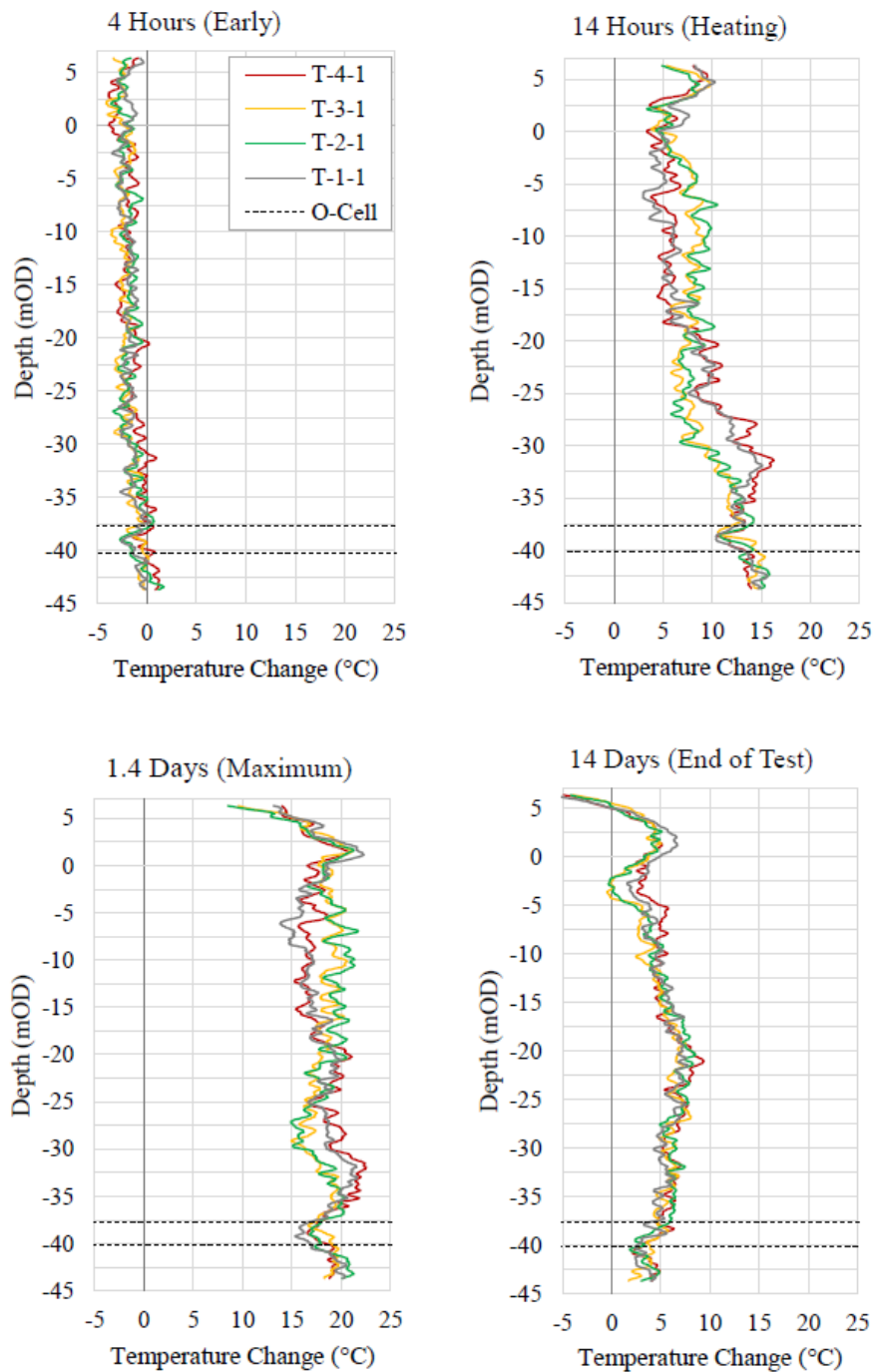


Fig. 5.3 Longitudinal temperature measurement at different stages of the concrete curing process in Newfoundland pile site[15]

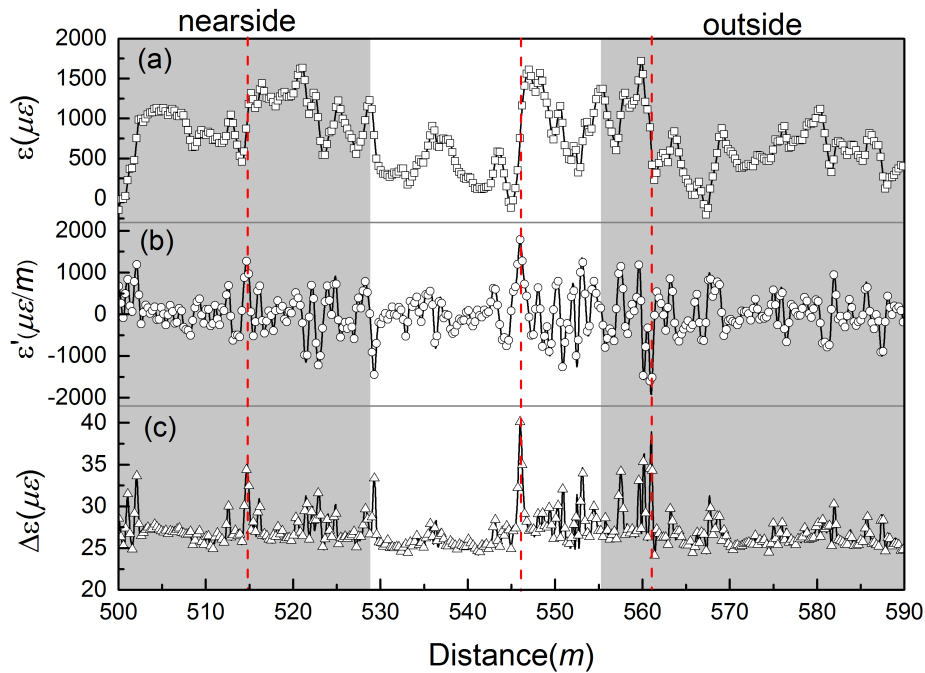


Fig. 5.4 Analyzer measured strain, strain gradient and measurement precision error profile along the Newfoundland pile

with the fibre optic cable attached was placed inside the mould, and concrete was poured to create a tunnel segment. Figure 5.5 (b) shows the attachment of the fibre to the mould in a route from A to S. Unlike the Newfoundland site,  $1000 \mu\epsilon$  pre-straining was applied to the cable by clamping a section of the cable over  $1 m$  and stretching the cable by  $1 mm$ . Three particular pre-strained sections (from F to G, J to K and N to P) are highlighted as pink in Fig. 5.5(b). Strain measurements were taken using a Yokogawa BOTDR analyzer (AQ8603). Further details of the tunnel test can be found in an ECSMGE paper [79] [82].

After the segments were installed inside the excavated tunnel, forty repeated measurements were taken every three hours over five days. It was noted that during the time, the loading within the tunnel segments should be constant and the longitudinal loading should be same as the pre-strain.

Figure 5.6 presents the measurement variation over the data collection period for both the strain and temperature sensor at one point of the cable. It indicates that measurement variation is random for both the strain and temperature cables.

However, after comparing the bandwidth of the measurement variation at each point of the cable, it was found that the strain repeatability changed along the cable ( $30 \mu\epsilon$  maximally) while the temperature variation was more consistent along the cable, at about

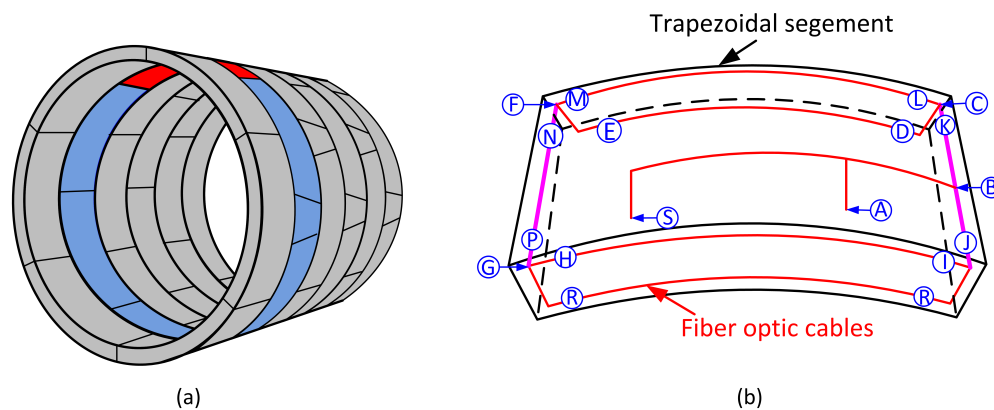


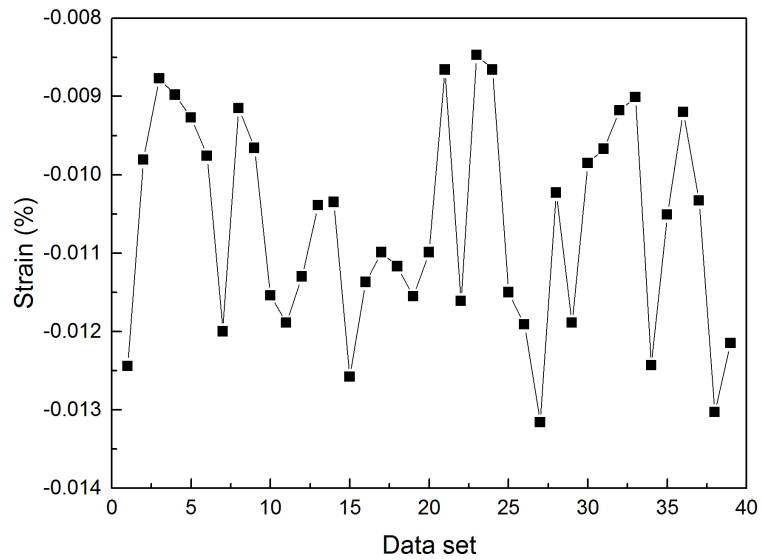
Fig. 5.5 Schematic graph of the national grid tunnel segments and fibre optic cable instrumentation

1.5°C. Figure 5.7 presents the measured strain, strain gradient and measurement repeatability along the fibre. The strains were large at the sections containing pre-straining instrumentation (gray zones). The baseline and peak values of the measurement precision error were around  $14 \mu\epsilon$  and  $35 \mu\epsilon$ , as highlighted in the three pre-strained sections (from F to G, J to K and N to P). Interestingly, the calculated precision error became larger at the peaks and troughs of the strain gradient profile, similar to the results from Newfoundland site.

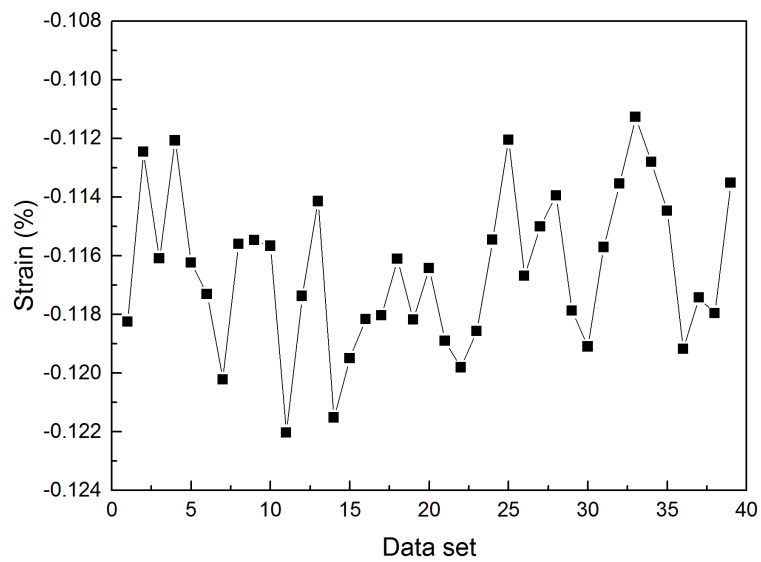
Measurement fluctuation over distance was also investigated. The longitudinal differential strain and temperature (which is calculated as the difference between two measurements) is presented in Fig. 5.8. Both the cable measurements fluctuated in an approximately random way over the cable length. The temperature fluctuation along the distance was about 1.5°C and the strain variation was about  $100 \mu\epsilon$ .

### 5.1.3 Precision error characteristics

The relatively higher precision error is most likely due to the ubiquitous inhomogeneous nature of the real strain field. On one hand, non-uniformly distributed strain will lead to an asymmetric Brillouin gain spectrum, and thus a lower SNR and broader bandwidth of the received Brillouin spectrum frequency resolution, which is directly related to the frequency resolution of the sensing system. On the other hand, strain non-uniformity can enlarge the distance error in the analyzer acquisition system, affecting the measurement repeatability as a faster strain change rate can result in a larger variation range of strain measurements at a typical distance resolution. Although the strain range for infrastructure monitoring is commonly limited to several hundred micro-strain, this relatively high precision error caused by the non-uniformity of the strain would become a critical problem for most applications.



(a)



(b)

Fig. 5.6 Strain variation over data collection period for both of (a) temperature sensor and (b) strain sensor in National Grid tunnel segments

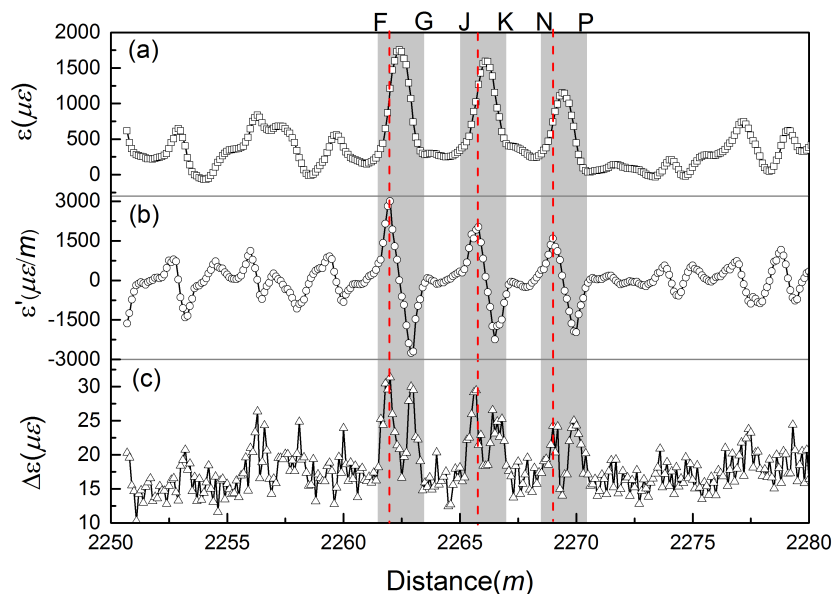
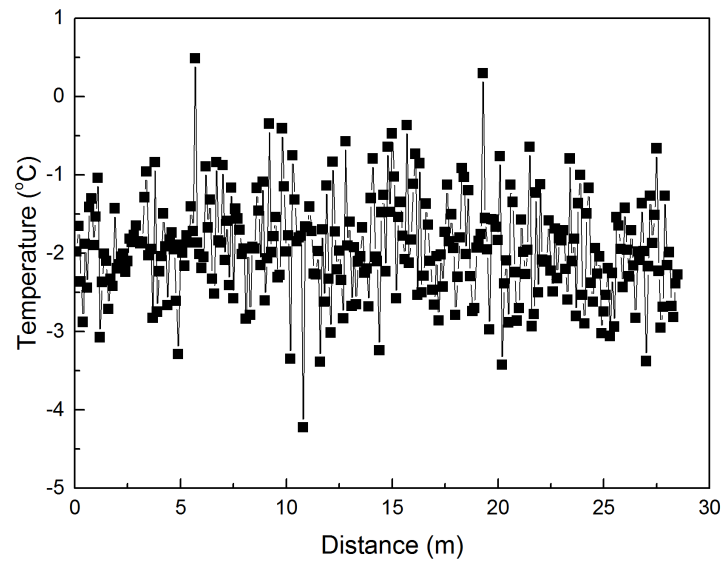


Fig. 5.7 Profiles of strain, strain gradient and measurement precision error in National Grid tunnel segments

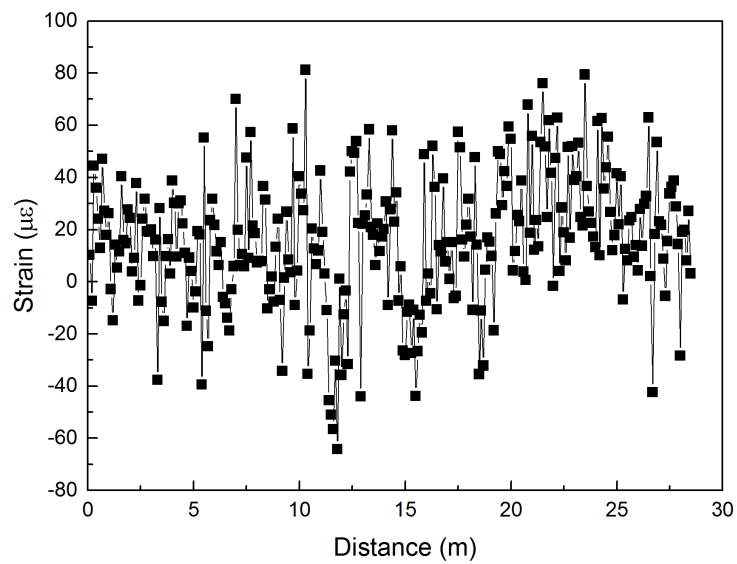
As shown in Fig. 5.3 and Fig. 5.7, both the Newfoundland site and National Grid site measurement indicated that there is an dependency between the measured strain gradient and the measurement precision error. Figure 5.9 shows the dependency of the measurement precision error on the strain gradient for both sites. It can be seen that the precision error is closely related to the strain gradient, including a baseline region and an approximately linear growth phase. The former was within a strain gradient range of around  $\pm 1000 \mu\epsilon/m$ , and the baseline values of  $\Delta\epsilon$  are  $25 \mu\epsilon$  and  $14 \mu\epsilon$  for Newfoundland and National Grid sites, respectively. For the linear growth phase, the slope of the  $\Delta\epsilon - \epsilon'$  relationship at the Newfoundland site was much steeper than that of the National Grid site. The relatively higher values of both the  $\Delta\epsilon$  baseline and  $\Delta\epsilon - \epsilon'$  slope at the Newfoundland site are mostly likely due to the more inhomogeneous strain distribution, and this will be further investigated in the following sections.

## 5.2 Precision error origin

The measured strain/temperature magnitude as well as its location are subject to measurement repeatability error. Hardware design and implementation factors that influence the precision of the measurements for a typical Neubrescope PPP-BOTDA system can be found in paper



(a)



(b)

Fig. 5.8 Measurement fluctuation over distance for (a) temperature sensor and (b) strain sensor in National Grid tunnel segments

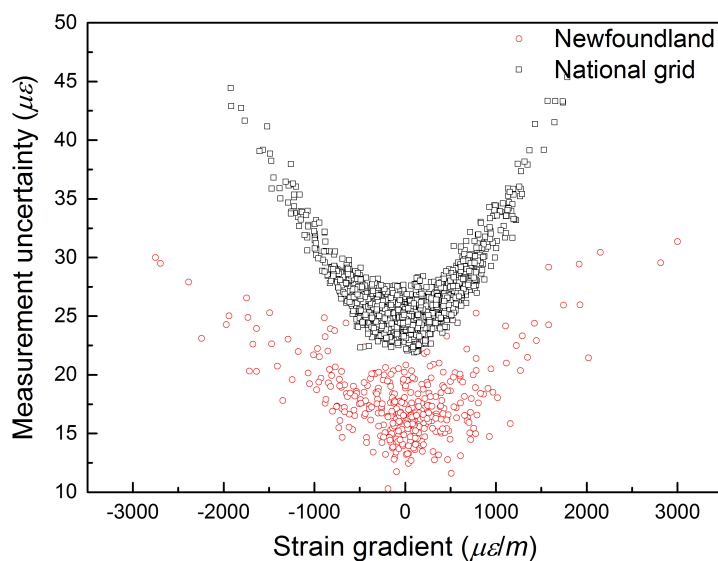


Fig. 5.9 Variation between strain gradient and measurement precision error

[85]. It was claimed that hardware related instability of the pump and probe laser strongly influence on the measurement accuracy and repeatability, the Brillouin gain spectrum properties including SNR, FWHM and frequency scanning step directly influence on the measurement accuracy and repeatability, and the influence of fitting function for the Brillouin spectrum on measurement error is slight [85].

The precision error in the BOTDR case is mainly induced by two factors: frequency resolution and analyzer location determination error.

### 5.2.1 Frequency resolution

Frequency resolution is directly related to the signal noise of the analyzer. As shown in Fig. 5.10, the measured Brillouin spectrum presents power fluctuations which make it imprecise to determine the centre frequency at power peak. As a result, the analyzer measured centre frequency output locates in the range of two dotted lines, leading to precision error.

Frequency resolution is on one hand affected by the optical power. The optical power losses that accumulate along the fibre configuration are going to reduce significantly the signal to noise ratio in the detection stage inside the measuring equipment. On the other hand, it is dependent on the Brillouin spectrum bandwidth. It was claimed that frequency resolution is dependent on the SNR and FWHM of the received Brillouin spectrum [44]. Previous experimental results verified that the dependency of the Brillouin frequency resolution on

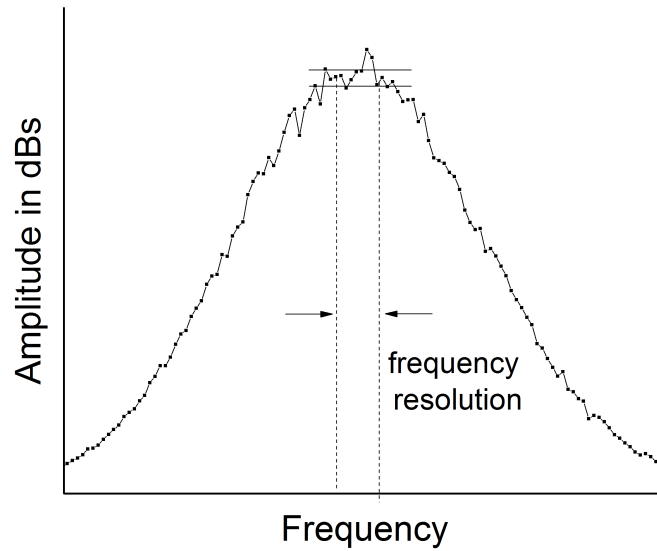


Fig. 5.10 The influence of frequency resolution on strain measurement precision for Brillouin optical time domain system

measurement parameters can be approximated as [78]:

$$\delta v_f = \frac{1}{SNR(z)} \sqrt{\frac{3}{4} \varphi \cdot \Delta v_B} \quad (5.1)$$

where SNR is the ratio between peak power and noise, FWHM is the full width at half maximum of the Brillouin gain spectrum, and  $\varphi$  is the frequency step. The equation suggests that the measurement precision error is proportional to the square root of the FWHM and inversely proportional to the SNR.

In a strain change condition, the measured Brillouin spectrum turns wider as it is a convolution of the intrinsic Brillouin spectra with different peaks over the analyzer's spatial resolution. In this way, the signal noise induced frequency resolution is enlarged, and thus leads to a worse strain precision. Therefore, when the cable is non-uniformly strained, the broadening and the asymmetry generated in the Brillouin gain curve is going to alter the frequency resolution of the analyzer.

### 5.2.2 Distance resolution

Distance resolution corresponds to the precision of the spatial location of a measured point. Distance resolution induced measurement imprecision is the variance of Brillouin frequency

shift due to the uncertainty of the cable location determination inside the analyzer [85]. In optical time-domain based systems, the acquisition scheme, i.e. the sampling rate of the detection system, sets the number points along the distance (sampling interval) that corresponds to the localization precision of a measured point with respect to its geographical position.

Distance resolution induced BOTDR measurement imprecision is graphically illustrated in Fig. 5.11 where three Brillouin spectra represent one measuring point result but have different fibre locations where back scattering occur due to distance error. When the injected pulse transfer through the fibre, the analyzer measured Brillouin spectrum is the convolution of fibre intrinsic spectrum over the pulse length (analyzer spatial resolution) because of limit of injected pulse length. In this figure, the convoluted spectrum represents analyzer measured result, and spectrum 1 and 2 represent the intrinsic Brillouin spectra of the fibre over the spatial resolution of the analyzer. It can be seen from the figure that the intrinsic Brillouin spectrum over spatial resolution slightly change with three sub-figures as the location of the pulse change. As a result, the convoluted Brillouin spectrum result deform and the centre frequencies at peak vary for three measurements which leads to precision error.

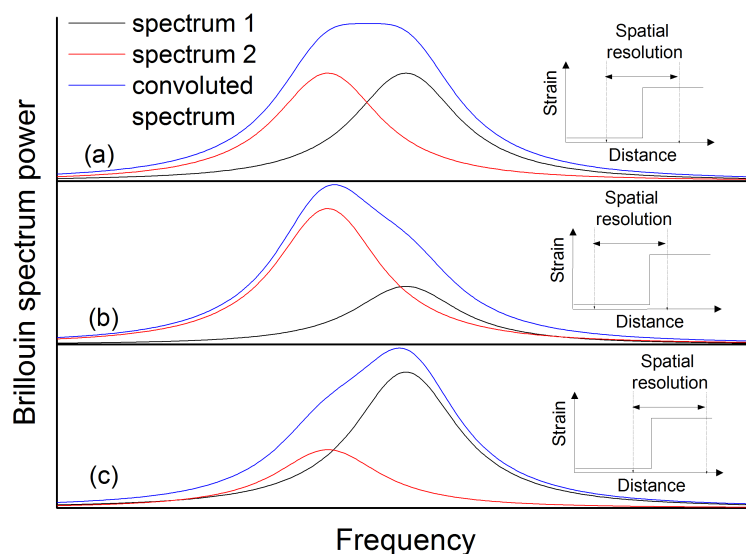


Fig. 5.11 The influence of distance error on strain measurement precision for Brillouin optical time domain system

The amount of distance error induced precision is dependent on the analyzer distance resolution as well as the strain change rate. When the fibre is under no external strain, the distance resolution will not affect the strain readings. However, when the fibre experiences

a rapid strain change, a small error in location determination will lead to a large difference in the measured strain. As a result, this should lead to a growth of the precision error in the strain/temperature determination at rapid strain change sections.

## 5.3 Experimental verification

To clearly visualize the frequency and distance resolution induced measurement imprecision, a sharp strain change was generated by splicing two optics fibres together with a centre frequency difference of  $500\text{MHz}$  (equivalent to 1% strain). The tested cable was put in free condition and repeated measurements were recorded using an NBX-5000 BOTDR analyzer. The measured Brillouin centre frequency profile was expected to have a step change at the splicing point of the two fibres with different centre frequencies. The analyzer was set as  $1\text{m}$  spatial resolution and  $0.05\text{m}$  sampling resolution. The averaging time was  $2^{16}$ . The recorded Brillouin centre frequency profiles were used for later frequency resolution and distance resolution investigation.

### 5.3.1 Frequency resolution

Based on the experimental results, the Brillouin spectrum of the measurement at different strain section locations was investigated, as shown in Fig. 5.12. Since the BOTDR sensor measures a convoluted result over the spatial resolution, the measured Brillouin spectrum at a strain change section contains two peaks, one representing the spectrum at the strained section and the other representing the spectrum at the unstrained section. In this sharp strain change case, the centre frequency difference between the strained and un-strained condition is so significant that the double peaks can be clearly seen.

In the above figure, at the strain transit section, the obtained BGS becomes distorted compared to that of the uniformly strained section or unstrained section. Because of the sharp frequency change of  $500\text{MHz}$  (red dotted line as the measured Brillouin gain spectrum at the strained section and black dotted line as the measured Brillouin gain spectrum at the unstrained section in Fig. 5.12), the measured Brillouin spectrum at the strain change sections shows visible double peaks (blue dotted lines). As a result, the SNR is reduced with a lower peak power (assuming the noise level is constant along the cable) and FWHM is contrarily increased for the Brillouin gain spectrum at the strain transit section.

According to Eq. 5.1, a lower SNR and broader FWHM leads to a larger precision error. At rapid strain change sections, FWHM is enlarged and SNR is reduced due to the convolution of Brillouin spectra in different peak frequency profiles. This should result in

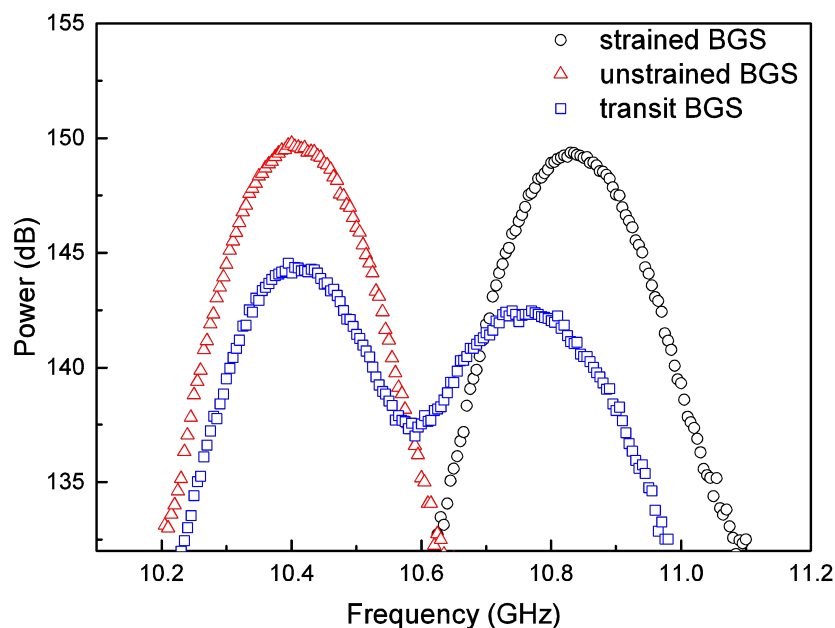


Fig. 5.12 The comparison of Brillouin spectrum at a uniformly strained section, unstrained section and strain transit section

a growth of the precision error in the analyzer measurement frequency domain. Therefore, frequency resolution induced precision error can be related to the non-uniformity of the measured strain profile. It is expected that at strain change sections, the frequency resolution is larger than the free cable condition, and the increase of the precision error is quantitatively related to the measured gradient of the Brillouin centre frequency shift (corresponding to the measured strain gradient).

### 5.3.2 Distance resolution

To investigate distance resolution induced precision error, two repeated Brillouin spectrum measurements at the splicing point of the tested cable is compared (Fig. 5.13). The power ratio between two peaks varies with this two measurements: the ratio of peak power at  $10.77\text{ GHz}$  to peak power at  $10.42\text{ GHz}$  is 1.005 for the first measurement, and 0.998 for the second measurement in Fig. 5.13. It has been stated that the spectrum peak power is roughly proportional to the length of the event because the measured spectrum is a convolution of the intrinsic Brillouin spectrum over the analyzer's spatial resolution [91]. Therefore the peak with relatively higher power means that the measuring point is closer to that peak section.

The first measurement has higher a power in the strained section, indicating its location is closer to the strained section and the second measurement is the opposite, implying that there is a distance error in measuring point between the two repeated measurements.

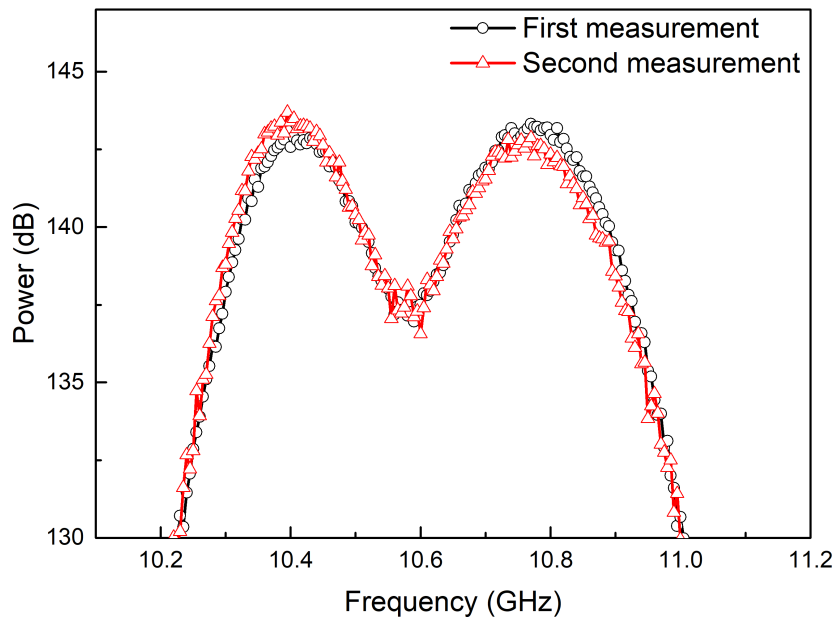


Fig. 5.13 Comparison of two repeated Brillouin spectrum measurements

Figure 5.14 presents the longitudinal Brillouin centre frequencies of the two repeated measurements. The final measured centre frequency is  $10.77\text{ GHz}$  for the first time and  $10.42\text{ GHz}$  for the second time. A horizontal shift of the centre frequency can be clearly seen, which will lead to a larger precision error at the strain change section, as expected.

## 5.4 Precision error simulation

The precision error and its dependency on the strain gradient was investigated through simulation. The Brillouin spectrum of a changing strain was simulated using the established model described in Chapter 4. The power fluctuation was generated using the previous characterized power error curve. The final precision error was determined by creating a repeated Lorentzian spectrum and extracting the Brillouin peak frequency through fitting of the spectrum.

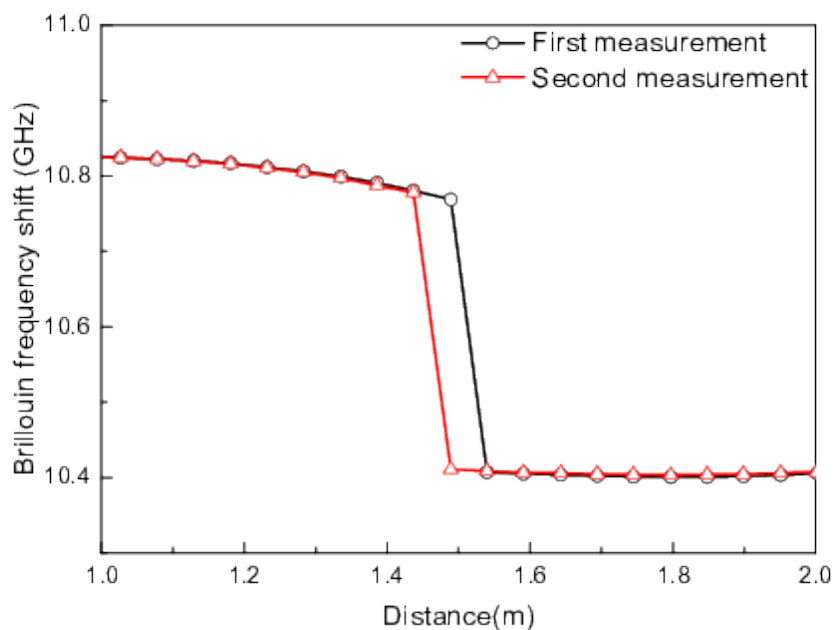


Fig. 5.14 Comparison of two repeated Brillouin centre frequency measurements along the tested cable

### 5.4.1 Simulation methodology

In this simulation, the Brillouin power spectrum at point  $z$  ( $P_B(z, \nu)$ ) is given as:

$$P_B(z, \nu) = P_{MB}(z + \Delta z, \nu) + \delta P(z + \Delta z, \nu) \quad (5.2)$$

$$P_{MB}(z, \nu) = \int_{z-L_s/2}^{z+L_s/2} H(x, \nu) g(x) \exp(-2\alpha x) dx \quad (5.3)$$

$$\delta P(z, \nu) = A \times (P_{MB}(z, \nu))^B \times P_{MB}(z, \nu) \quad (5.4)$$

where  $P_{MB}(z, \nu)$  is the Brillouin power spectrum calculated as a convolution of the intrinsic Brillouin spectrum ( $H(z, \nu)$ ) and a weight function ( $g(x)$ ),  $\delta P$  is the power fluctuation which is dependent on the power level, the parameters  $A$  and  $B$  are dependent on the analyzer,  $L_s$  is the spatial resolution, and  $\alpha$  is the fibre linear loss. Variable  $\Delta z$  is the analyzer timing error induced distance resolution. Because of this distance resolution, the corresponding measured frequency shift is therefore calculated as  $\Delta \nu_B(\varepsilon(z + \Delta z))$ .

The intrinsic Brillouin spectrum ( $H(z, \nu)$ ) is an integration of a Lorentzian shape distribution with the input pulse:

$$H(z, \nu) = \int P_p(f, f_0) \frac{h(\Delta\nu/2)^2}{[\nu - (f - \nu_B(z))]^2 + (\Delta\nu/2)^2} df \quad (5.5)$$

where  $P_p$  is the pulse power with a centre frequency of  $f_0$ ,  $\nu_B(z)$  is the Brillouin frequency shift of the fibre, which is linearly proportional to the strain,  $\Delta\nu$  is the half bandwidth of the Brillouin spectrum, and  $h$  is the peak power of the Brillouin spectrum.

The weight function follows a normal distribution and its bandwidth ( $\sigma$ ) is dependent on the analyzer:

$$g(x | z, \sigma) = \frac{1}{\sigma\sqrt{2\pi}} e^{-\frac{(x-z)^2}{2\sigma^2}} \quad (5.6)$$

### 5.4.2 Experimental verification

The measurement precision error of a step strain was simulated with the model and compared with the analyzer measurement result. Experimental work was performed using an NBX-5000 analyzer. The strain-sensing cable was a reinforced-ribbon cable manufactured by Fujikura Ltd. It consists of four single-mode optical fibres that are reinforced with a pair of steel wires. The cores are tightly bonded to the protective nylon sheath for effective mechanical strain transmission. In the test, a section of 1.5 m length Fujikura reinforced cable ( $z = 1.1\text{ m} - 2.6\text{ m}$ ) was strained to  $2075\ \mu\epsilon$  whilst the other sections were under the free condition. The cable was fixed and strained using the calibration unit developed in Section 3.2.1. In total, 100 consecutive measurements were recorded.

At each measuring point, the repeated Brillouin spectra were simulated using Eq. 5.2 based on the input strain condition. The weight function used in the model ( $g(x)$ ) followed a normal distribution with a bandwidth of  $0.195\text{ m}$ , and the parameters for the power fluctuation curve were  $A = 4.465 \times 10^5$ ,  $B = -0.469$  as previously characterized in the lab. The timing error was used as  $9.4\text{ ps}$  for the currently used BOTDR analyzer. The comparison of the simulated 3D Brillouin spectrum and the measured 3D Brillouin spectrum is shown in Fig. 5.15.

It can be seen that the simulated Brillouin spectrum is in good agreement with the analyzer measured one in Fig. 5.15. A gradual spectrum shift in the frequency domain for both the simulated and analyzer measured Brillouin spectra can be clearly seen at  $z = 1\text{ m} - 1.5\text{ m}$  and  $z = 2.5\text{ m} - 3\text{ m}$ . Random power fluctuation with distance can be found in the two sub-figures and the amount of fluctuation looks to be in good agreement. However, the full width of the simulated Brillouin spectrum looks larger than the analyzer measured one, which is the

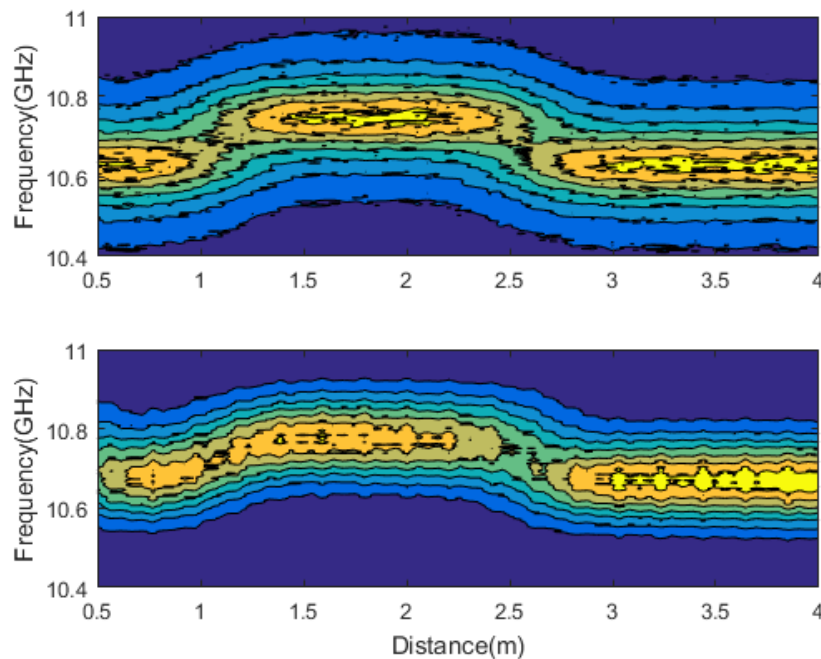


Fig. 5.15 Comparison of the simulated Brillouin spectrum (upper figure) and the analyzer measured Brillouin spectrum (lower figure)

limitation of this model as shown in Fig. 4.16 in the previous chapter. Although the tailing of the Brillouin spectrum does not fit well, the spectrum over the half bandwidth is in good agreement between the analyzer measured and the simulated spectrum. Therefore, the fitted Brillouin centre frequency should not be affected. The comparison of the analyzer measured strain and simulated strain at the strain drop section is indicated in Fig. 5.16. It can be seen that the step strain change input is properly spread over the simulation process. The correlation between the simulation and experimental values was above 99% for this strain cases.

To model precision error, the above Brillouin spectrum simulation process was conducted 100 times, and the Brillouin peak centre frequency was calculated through fitting the simulated Brillouin spectrum with a Lorentzian shape at each measuring point. The simulated precision error and the analyzer measured precision error are compared in Fig. 5.17. At  $x = 2.5\text{ m} - 2.7\text{ m}$  where the strain drops relatively faster, both the simulated and analyzer measured precision error are enlarged as expected. On average, the difference between the simulated error and the analyzer measured error was less than 8% of the measured error for the tested analyzer.

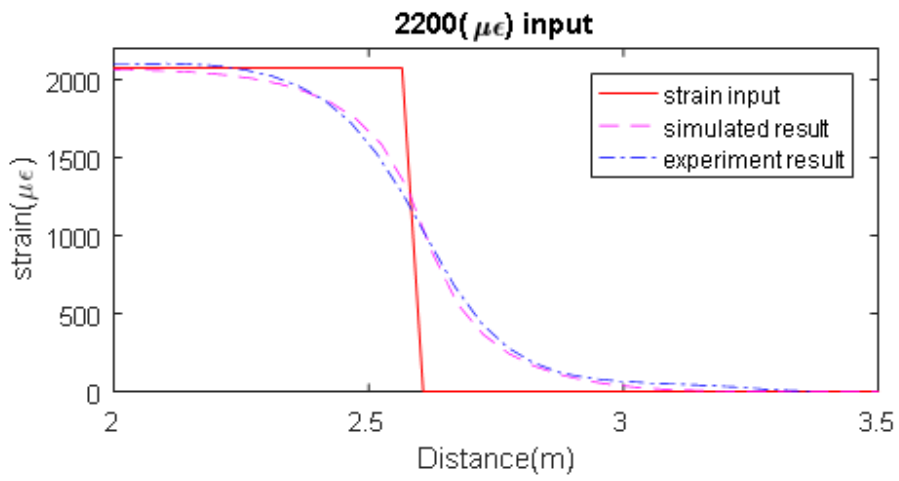


Fig. 5.16 Comparison of the simulated strain and the analyzer measured strain for a step strain change input

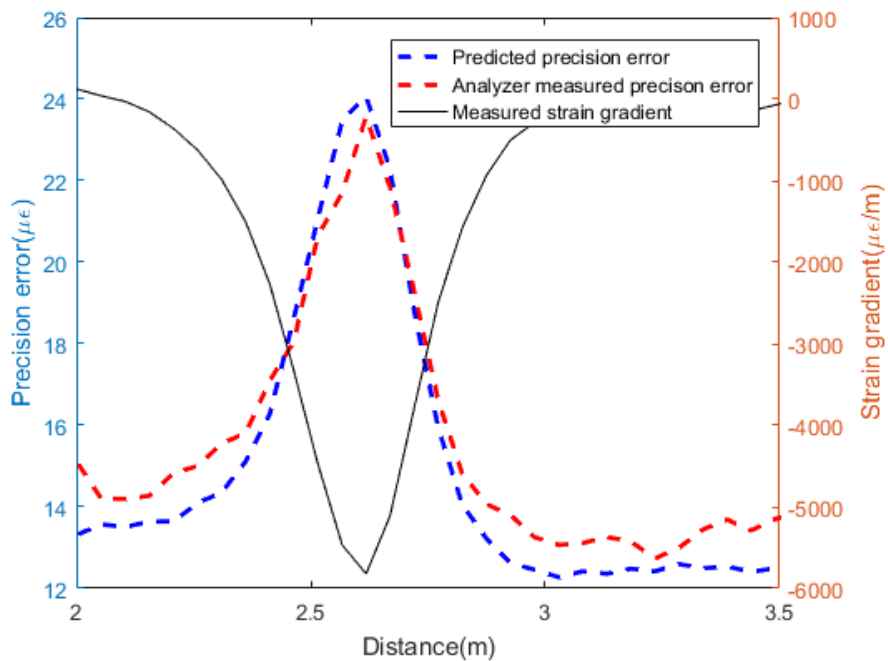


Fig. 5.17 Comparison of the simulated precision error and the analyzer measured precision error for a step strain change input

## 5.5 Precision error prediction

In this section, a method was developed to predict the measurement repeatability error based on one analyzer measurement. The prediction process was separated into two parts: the frequency resolution, and the distance resolution induced precision error.

### 5.5.1 Prediction methodology

Brillouin measurement frequency resolution ( $\delta v_f$ ) can be well approximated by Eq. 5.1 as experimental and simulation results indicated [78]. The frequency resolution is dependent on the characteristics of the spectrum and parameter settings of the analyzer. For a typical BOTDR analyzer with an SNR of 20dB, FWHM of 130MHz, and frequency scanning step of 3MHz, the measurement precision error is calculated as 0.8553MHz using the equation.

To predict the distance resolution induced measurement precision error, the analyzer timing error ( $\Delta t$ ) first needs to be calibrated in the lab. Figure 5.18 illustrates the relationship between the analyzer measured precision error ( $\delta v$ ) and the distance resolution ( $\Delta z$ ). By subtracting frequency resolution from the analyzer measured precision error, the distance resolution induced precision error can be obtained:

$$\delta v_d = \sqrt{\delta v^2 - \delta v_f^2} \quad (5.7)$$

In a short length section, the Brillouin centre frequency distribution can be regarded as linearly distributed. If the frequency shift gradient at point  $z$  is given as  $\Delta v'_B(\epsilon(z))$ , the distance resolution induced precision can be then transferred into distance resolution:

$$\Delta z = \delta v_d / \Delta v'_B(\epsilon(z)) \quad (5.8)$$

The corresponded timing error of the analyzer is therefore calculated as:

$$\Delta t = \frac{\Delta z \times n}{c_0} \quad (5.9)$$

At strain change sections where there is a fast strain change rate, the distance resolution induced measurement precision error will be enlarged, as indicated by Eq. 5.8. Therefore, the analyzer timing error should result in a larger precision error at strain change sections, similar to the previous frequency resolution effect.

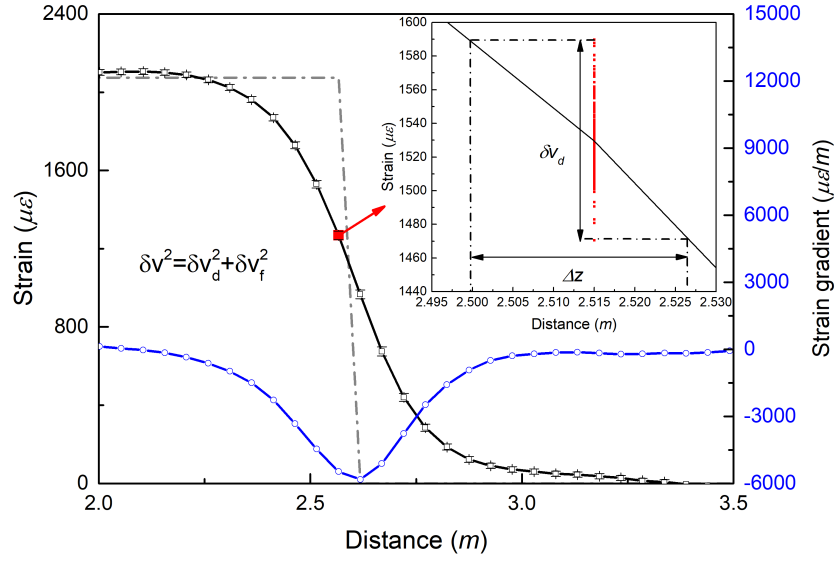


Fig. 5.18 The relationship between distance resolution and precision error

Given the analyzer dependent timing error ( $\Delta t$ ), the distance resolution induced precision error can be predicted as:

$$\delta v_d = \Delta v'_B(\varepsilon(z)) \times \frac{\Delta t \times c_0}{n} \quad (5.10)$$

The final predicted precision error can therefore be obtained by combining the frequency and distance resolution induced measurement precision error together:

$$\delta v = \sqrt{\delta v_f^2 + \delta v_d^2} \quad (5.11)$$

### 5.5.2 Experimental results

The prediction of the frequency and the distance resolution induced strain measurement imprecision was then verified using one Brillouin spectrum measurement obtained from the previous lab experiment with a step strain change. Figure 5.19 plots the strain measurement, SNR, and bandwidth of the measured Brillouin spectrum. The strain gradient was calculated from the measured strain and measurement precision error evaluated from 100 repeated strain measurements recorded by the NBX-5000 BOTDR analyzer. The SNR of the received signal varied around 16 dB at uniformly strained cable sections, and slightly reduced by 21 dB at strain change sections (at around  $z = 1\text{ m}$  and  $z = 2.6\text{ m}$ ). In the meantime, the measured Brillouin spectrum bandwidth increases was measured as 160 MHz generally, and enlarged

to  $250\text{MHz}$  at strain change sections. The measurement precision error increased from  $14\mu\epsilon$  to  $24\mu\epsilon$  again at cable sections with a faster strain change rate. In total, there was a dependent relationship between the SNR, the bandwidth of the measured spectrum and the measurement precision error with the measured strain gradient. The measured Brillouin spectrum information will be used for later frequency resolution and distance resolution predictions.

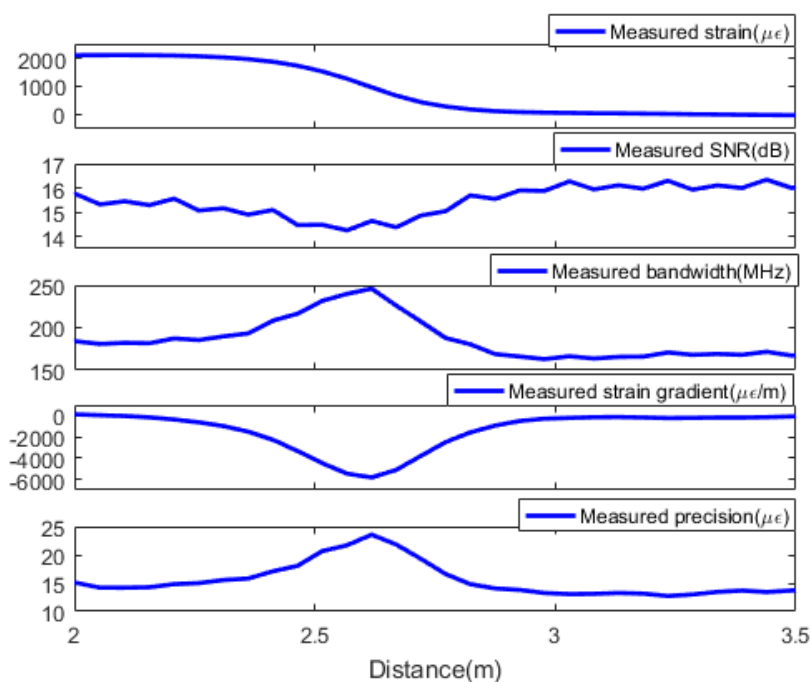


Fig. 5.19 Analyser measured strain, strain gradient, SNR and bandwidth of the measured Brillouin spectrum, and measurement precision of a step strain change

After obtaining one measurement of the Brillouin spectrum, the frequency and distance resolution induced measurement imprecision can be predicted using Eq. 5.1 and 5.10. The detailed process and prediction result will be discussed in the next two sections.

### 5.5.3 Frequency resolution induced strain imprecision

Using the SNR and FWHM information obtained from the BOTDR analyzer as plotted in Fig. 5.19, the frequency resolution induced precision error was calculated using Eq. 5.1. Figure 5.20 illustrates the result of the predicted frequency resolution induced precision error at  $z = 2\text{m} - 3.5\text{m}$ .

It can be seen that the maximum predicted frequency resolution is approximately  $17\mu\epsilon$  at distance around  $2.6\text{m}$  where there is a fast strain change. This verifies again that frequency

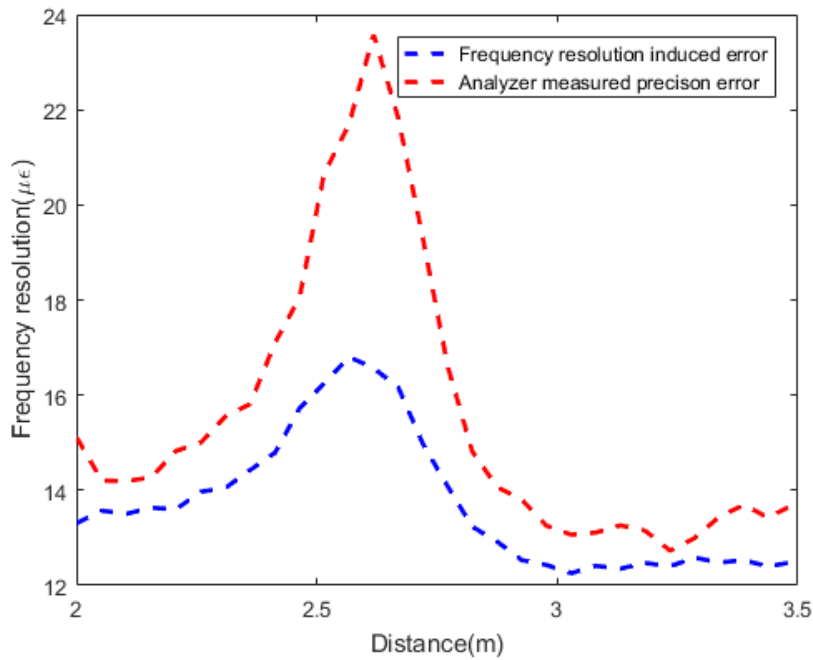


Fig. 5.20 Comparison of the predicted frequency resolution induced precision error and the analyzer measured precision error

resolution increases with strain gradient. Similar trend can be found by the analyzer measured precision error but with a larger value of maximum error of about  $24\mu\epsilon$ . This indicates that at rapid strain change sections, the frequency resolution is not enough to describe the increase of the measurement precision error as the calculated frequency resolution presents  $8.5\mu\epsilon$  smaller value than the measured error at around  $z = 2.6m$ .

At distance around  $z = 3m - 3.5m$  and  $z = 2m$ , where the cable is in unstrained or uniformly strained condition, both the calculated frequency error and the analyzer measured error stay around  $14\mu\epsilon$ . This verifies that the calculated frequency resolution induced error can efficiently characterize the precision error in the unstrained section and uniformly strained section ( $14\mu\epsilon$  for both the frequency resolution and measured precision error).

#### 5.5.4 Distance resolution induced strain imprecision

The analyzer timing error was characterized using Eq. 5.10 and Eq. 5.9 in the lab. The result shows that  $\Delta t$  follows a normal distribution with a bandwidth of  $9.4ps$  for the tested BOTDR analyzer.

With the characterized timing error, the distance resolution induced measurement precision error was predicted using Eq. 5.10. Figure 5.21 compares the predicted distance resolution induced strain imprecision and the analyzer measured precision error.

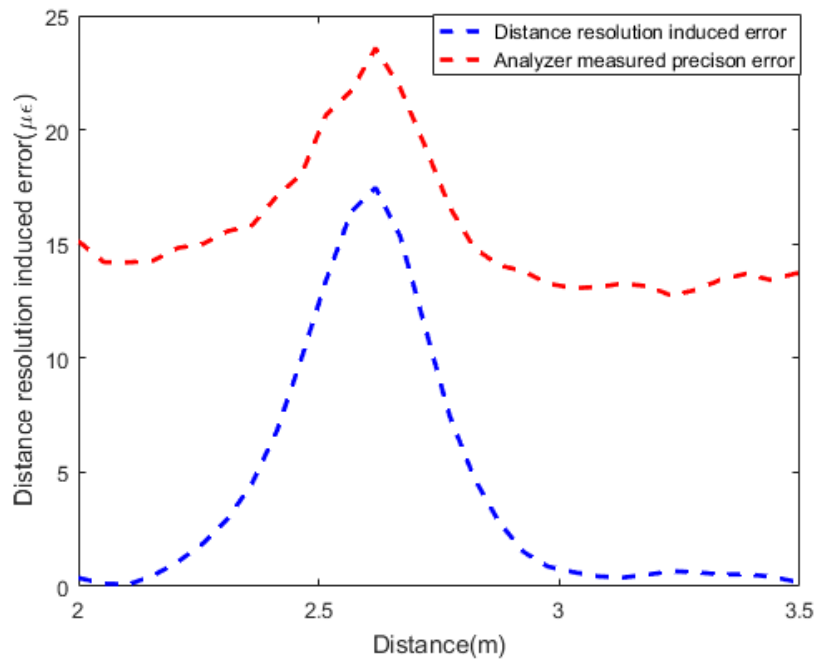


Fig. 5.21 Comparison of the predicted distance resolution induced precision error and the analyzer measured precision error

At the rapid strain change section (around  $z = 2.6\text{ m}$ ), the distance resolution induced error largely increases, verifying the previous conclusion that distance resolution induced error is dependent on strain change rate. Similar with the calculated frequency resolution result, the maximum calculated distance resolution induced error is close to  $17\ \mu\epsilon$ , smaller than the analyzer measured results ( $24\ \mu\epsilon$ ). Therefore only distance resolution induced error is not enough to predict the precision error at large strain change rate condition.

It can be seen that at uniformly strained and unstrained sections ( $z = 2\text{ m}$  and  $z = 3\text{ m} - 3.5\text{ m}$ ), the distance resolution induced error stays around zero and the analyzer measured error stays around  $14\ \mu\epsilon$ . This indicates that distance resolution effect less on precision error at unstrained and uniformly strain conditions. It can not be used to represent precision error at uniformly strained or unstrained condition.

### 5.5.5 Precision error calculation

The strain precision error was finally calculated by combining the predicted frequency resolution induced precision error ( $\delta v_f$ ) and the timing error induced precision error ( $\delta v_d$ ) together using Eq. 5.11.

The final result of the predicted precision error is indicated in Fig. 5.22. At  $z = 2.5\text{ m} - 2.7\text{ m}$  where the strain rapidly drops, both the predicted and the analyzer measured precision error enlarged as expected. The difference between the simulated error and the analyzer measured error was less than 8% of the measured error for the BOTDR analyzer. This finding is consistent with the previously published lab observations, where an extra repeatability error of  $5\ \mu\epsilon$  was reported in a non-uniformly compressed beam where a load was applied to the middle of the beam [5].

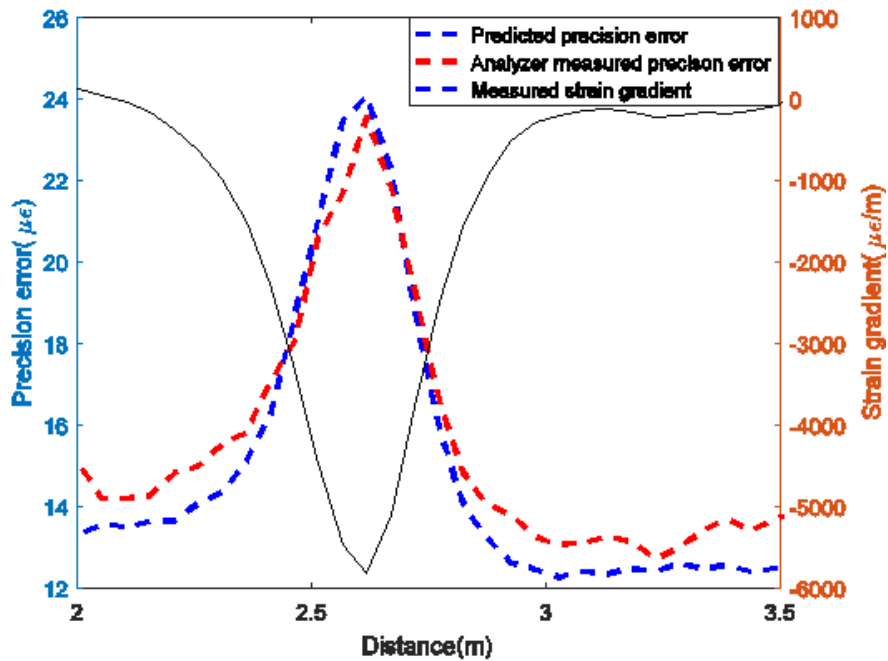


Fig. 5.22 Comparison of the predicted precision error and the analyzer measured precision error at the strain change section

## 5.6 Precision error correction

Previous experimental measurements and site monitoring results indicated that at faster strain change sections, the distance error contributes more significantly than the frequency resolution toward the measurement imprecision. The most direct way to minimize precision

error is by averaging. However, it is unrealistic to do an average for too a long time, especially on site where the temperature/strain condition varies unexpectedly with time. This section develops a distance error correction method using a sectional horizontal shift algorithm. This process can greatly improve the measurement precision for non-uniformly distributed strain cases. The reliability of the method was finally verified using measurements taken by a BOTDR system.

### 5.6.1 Precision error correction method

As previously discussed, the BOTDR measurement precision error is a combination effect of frequency resolution and distance resolution. The frequency resolution is directly related to the properties of the analyzer, and can be minimized by optimising the analyzer parameters such as increasing the number of averages, improving signal power, etc. Distance resolution is caused by the unstable localization scheme of the analyzer, and its effect can be enlarged by the non uniformity of the strain distribution. When the number of averages is determined, it is applicable to compensate for distance resolution induced error during data interpretation process.

To correct for distance error, a shift of strain measurement in the horizontal direction method is proposed considering the localization determination error of the analyzer. For example there are two repeated measurements ( $\epsilon_r$  and  $\epsilon$  in Fig. 5.23). During precision error correction procedure, the emphasis is on strain change sections as the precision error is verified to be larger at those sections.  $\epsilon_r$  is first estimated as the reference strain and separated into different sections based on its strain change information. The other strain data ( $\epsilon$ ) is then corrected back by horizontally shifting  $\epsilon$  with distance of  $\Delta z$  to minimise the sum of the absolute strain differences  $\Delta\epsilon$  over each sections.

Two ways of horizontal shift are introduced here: global shift and sectional shift. Sectional shift means that measurements are separated into different sections based on strain gradient information (sections 1 2 and 3 in Fig. 5.23) and horizontally shifted separately to minimize the absolute sum difference between ( $\epsilon$  and ( $\epsilon_r$ ) in each section. Global shift means that measurements all along the cable are shifted together to minimize the absolute sum difference between  $\epsilon$  and ( $\epsilon_r$ ) for the whole cable. The comparison of these two shifting ways is achieved by experimental results in Section 5.6.2.

The easiest way to determine the horizontal shift is to quantify by how many units the repeated measurement has moved to the reference, the absolute sum difference between two sets of data is minimum. To improve the accuracy of the horizontal shift, interpolation

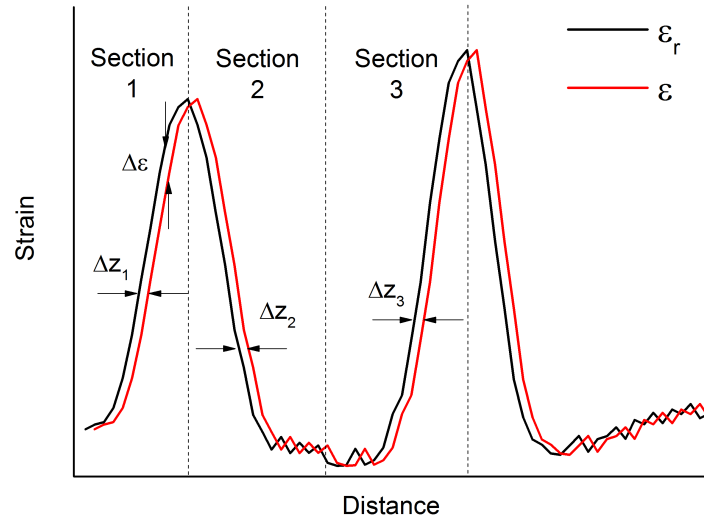


Fig. 5.23 Illustration of distance resolution induced precision error correction method

between measured points is used. The horizontal shift process can be expressed as:

$$\Delta z = \min \sum |\varepsilon(z_0 + \Delta z) - \varepsilon_r(z_0)| \quad (5.12)$$

where  $\Delta z$  is the horizontal shift,  $z_0$  is the original location of the measuring point,  $\varepsilon$  is the strain value of the target data set, and  $\varepsilon_r$  is the strain reading of the reference data set.

The measurement distance error due to imprecise localization determination is randomly distributed along the cable length. Therefore, the distance error compensation method to horizontally shift the measurement should be done locally. The strain profile therefore can be separated into different strain change sections for measurement precision error minimisation.

### 5.6.2 Test verification

The sectional horizontal shift method to minimize repeated measurement precision error was verified by lab experiments. Figure 5.24 illustrates the experimental set up where an optical fibre was glued all along the groove of a Glass Fibre Reinforced Polymer (GFRP) beam considering the fact that the Young's modulus of the beam is similar to that of concrete and is thus appropriate to imitate the optical fibre sensing condition on site. The structure was installed with five fixing points to place and deflect the beam. In that way changed the strain condition of the glued fibre sensor. The cross-sectional areas of the tested cable and

the beam were  $1.3\text{ mm} \times 5\text{ mm}$  and  $7\text{ mm} \times 40\text{ mm}$  respectively. The cable was pre-strained inside the beam for both tension and compression measurement.



Fig. 5.24 Illustration of the bending beam test set up

In the experiment, the beam was bent in three cases: Case 1) symmetric bending, Case 2) asymmetric bending and Case 3) even more asymmetric bending condition (Fig. 5.25). For each bending case, 100 repeated measurements were recorded by an NBX-5000 BOTDR analyzer for calculation of precision error. The experiment was conducted in a temperature controlled room, so temperature compensation was not necessary. The measurements and the sectional/global horizontal shift of the measurements were obtained to verify the reliability of this precision error correction method.

The average strain as well as the precision error for the three cases were shown in Fig. 5.26. It can be seen that Case 3 has the most non-uniform strain distribution, and its measurement precision error is the largest of the three cases. For both Case 2 and Case 3, the precision error is enlarged at strain change sections, as expected. However, Case 1 does not show obvious precision error enlargement at the strain change sections since its strain change rate is so small that the distance error is buried in analyzer random noise. Efforts toward precision error correction were then focused on Case 3 since its relatively larger precision error has more impacts on later data interpretation.

The characteristic of precision error and its dependency on Brillouin spectrum gain and bandwidth as well as strain gradient is shown in Fig. 5.27. The precision error of the tested beam mostly keeps at around  $25\ \mu\epsilon$ . At around  $z = 2.6\text{ m}$  and  $z = 3.3\text{ m}$  where strain changes relatively faster, two peaks of the precision error (as much as  $120\ \mu\epsilon$ ) can be clearly seen in the figure. In addition, at those places, the corresponded Brillouin gain decreases from 0.3 to 0.2 and the Brillouin width increases from  $100\text{ MHz}$  to nearly  $200\text{ MHz}$ . The clear dependent relationship between the precision error and the strain gradient as well as the Brillouin spectrum information again verifies that the frequency resolution of the backscattered Brillouin spectrum and the distance resolution of the analyzer are the two important sources of the measurement precision error for BOTDR analyzer.

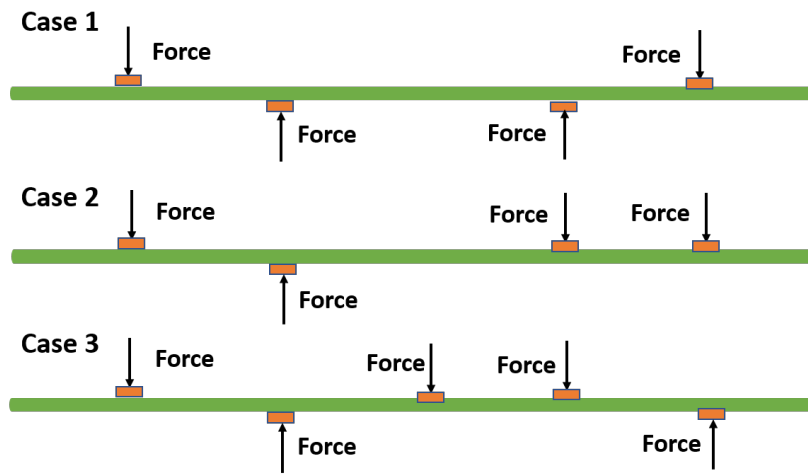


Fig. 5.25 Illustration of three bending cases for the precision error correction method verification experiments

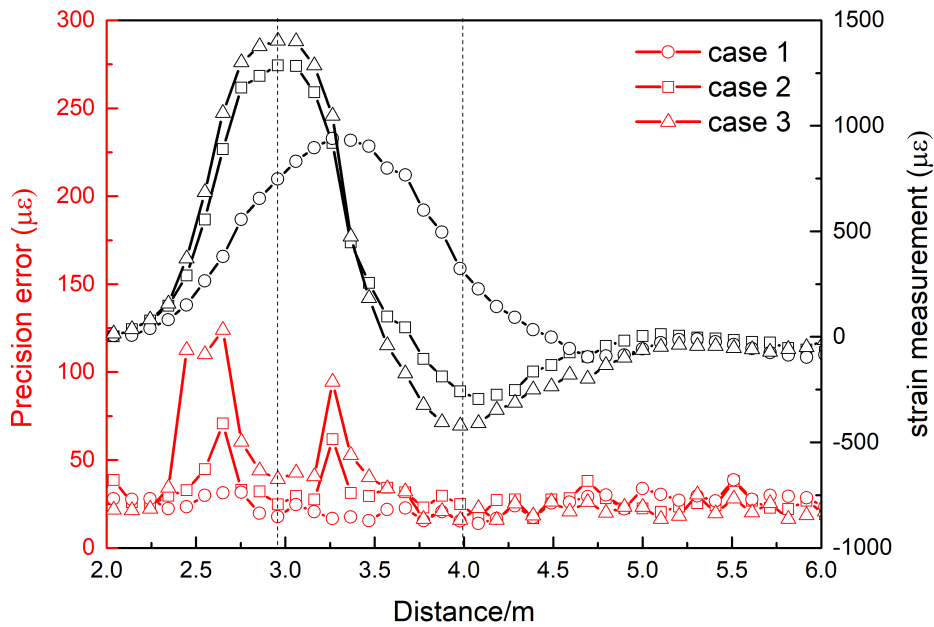


Fig. 5.26 Analyser measured strain and the corresponding precision error for three bending beam cases

Based on the obtained measurement strain gradient and Brillouin spectrum information, the strain reading profile is separated into three sections (separated by the dashed lines in the Fig. 5.27). This can be used for later sectional precision error correction.

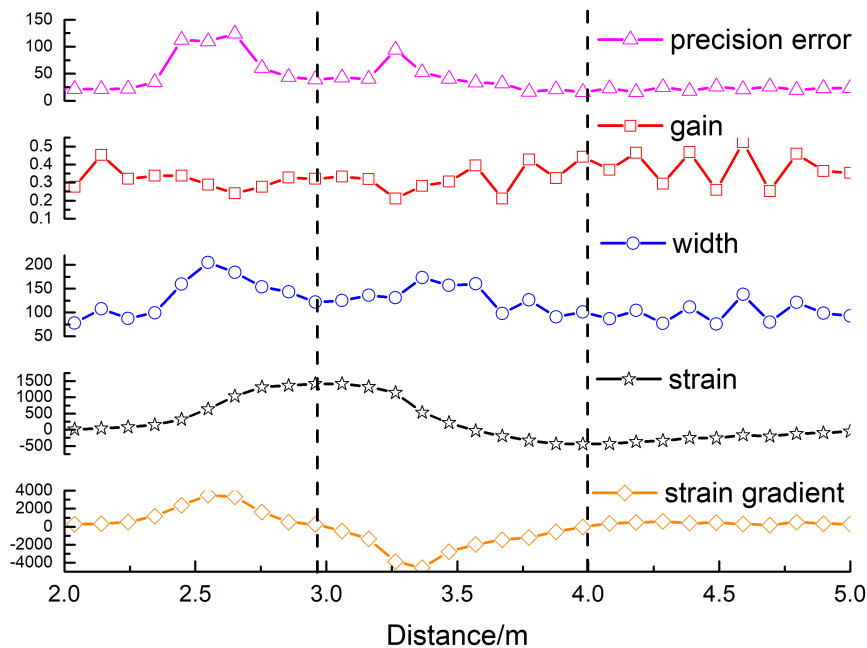


Fig. 5.27 Illustration of precision error, strain gradient, spectrum bandwidth and gain

The precision error correction is then completed in two different ways: horizontally shifting the strain data as a whole (interpolation 1) or horizontally shifting the strain data into different strain sections (interpolation 2). Interpolation 1 method is to shift the repeated strain measurements all over the tested sections ( $z = 0 - 5m$ ) so as to minimise the sum difference between the repeated measurements to the baseline reading. Interpolation 2 method is to shift the repeated strain measurements in three sections separately ( $z = 0 - 2.9m$ ,  $z = 2.9m - 4m$  and  $z = 4m - 5m$ ) for minimising the sum difference between the repeated measurements and the baseline reading at each section.

Figure 5.28 compares the measurement precision error result without any corrections, and with two correction processes. Globally horizontal shift (interpolation 1) reduces the measurement precision error from  $120 \mu\epsilon$  to  $80 \mu\epsilon$  at around  $x = 2.6m$ . However, at  $x = 3.5m - 4.5m$ , the measurement precision error increased from  $20 \mu\epsilon$  to  $80 \mu\epsilon$  after applying method interpolation 1. Sectionally horizontal shift reduced the measurement precision error all along the cable, and the maximum error reduction reached as large as

$70\mu\epsilon$  (at  $x = 2.5\text{ m}$ ). It can be concluded that using a partially horizontal shifting method can reduce the overall measurement precision error at most to 50% of its original level.

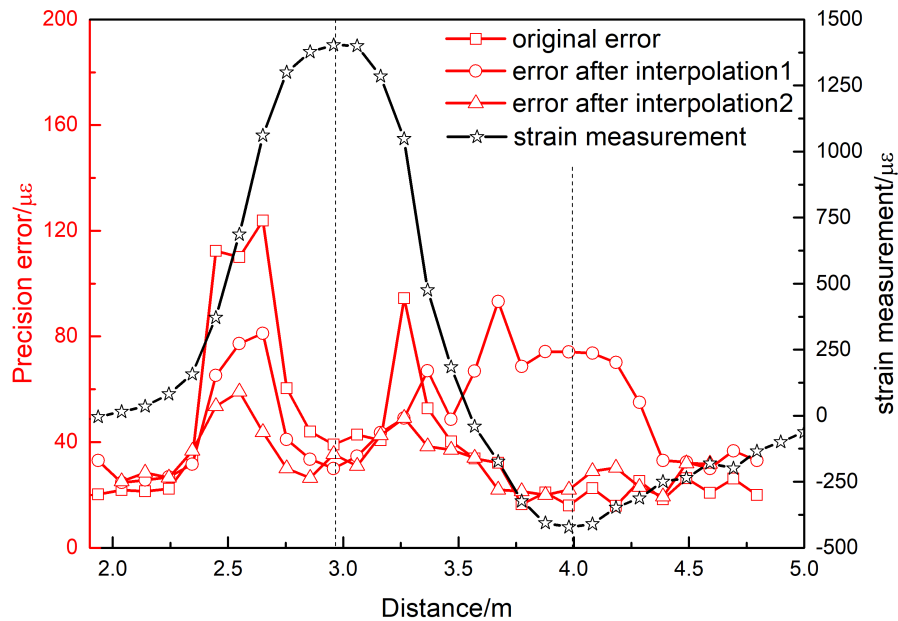


Fig. 5.28 Effects of the precision error compensation methods

## 5.7 Summary

1. The dependency of the precision error on the strain gradient profile was revealed, consisting of a baseline region which and an approximately linear growth phase. A faster strain change rate generally leads to a larger precision error.
2. Both experimental and simulation results verified that frequency and distance resolution contribute to the measurement precision error, and that error can be effectively characterized by the combined effect of the frequency resolution as well as the distance resolution induced error.
3. Analyzer measurement precision error can be predicted using one reading of 3D Brillouin spectrum along the monitored cable.

4. The precision error can be compensated by horizontally shifting the measurement in sections. In this way, the error was reduced from  $120 \mu\epsilon$  to  $60 \mu\epsilon$ , almost half of the original error.
5. It is therefore necessary to consider the reliability of the DFOS sensing data, by taking the strain non-uniformity characteristics into account. In practice, the quality of the sensing data can be quantified using the strain gradient information, and this is currently under investigation to achieve a more robust data interpretation framework for DFOS.

# Chapter 6

## Systematic error

The systematic error of the Brillouin optical time domain reflectometry (BOTDR) measurement quantifies the difference between the measured strain and the real strain. It is related to the sensor's spatial resolution as the measured spectral distribution is a convolution of the natural Brillouin gain distribution with the pulse spectrum [80]. Due to the limit of the pulse length (longer than  $10\text{ ns}$  considering the trade-off between the Brillouin gain spectrum width and Brillouin signal strength), the measured Brillouin spectrum can deform, which results in the difference. As a result, if a local strain change occurs at a distance scale smaller than the sensor's spatial resolution, the measured result will be a relatively smaller value, sometimes so small that no strain change presents in the result.

Attempts have been made to characterize BOTDR systematic error. It is stated that the measured Brillouin spectrum is a superposition of all spectrum components with different peak frequencies within the analyzer's spatial resolution [91]. To characterize the superposition of the spectrum, the Brillouin backscattered spectrum detected at the analyzer is expressed as a convolution of a Lorentzian distribution function with the launched pulse power [59]. Using this, BOTDR measurement is simplified as a weighted average strain value over its spatial resolution [38][33]. The weight function follows a normal distribution shape and its width is strain level dependent [33]. Real strain can then be reconstructed by de-convoluting the measured strain. To improve the accuracy of this strain reconstruction method, consideration of the data reliability due to strain non-uniformity was investigated [65]. However, the established algorithm is not general enough as long as the weight function is limited by the strain shape. More estimation and numerical analysis has to be done to optimize the weight function.

In this chapter, a 3D spectrum decomposition approach is used to develop a general data interpretation algorithm that is free from strain shape influence. An optics model that fits BOTDR strain measurements at different strain levels with one particular weight function is

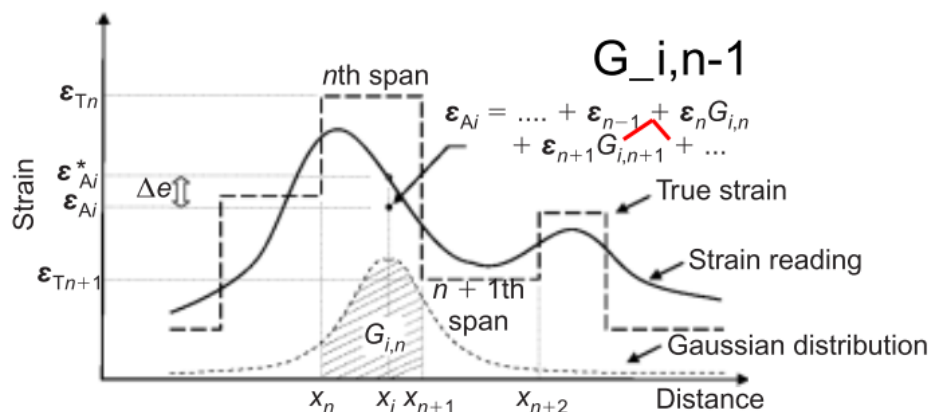


Fig. 6.1 The weighted average process of the analyzer measured strain compared to the true strain [14]

established. Using this model, the relationship between the measurement systematic error and the strain gradient is revealed. An inverse analysis algorithm is finally constructed by decomposing the Brillouin power data for strain interpretation. It uses a regularization decomposing method, taking advantage of the characteristic of the distributed strain gradient information.

## 6.1 Problem formulation

The frequency shift of the Brillouin backscattering signal is related to the localized acoustic wave, and is thus dependent on the strain and temperature along the fibre [76]. The spatial resolution of the BOTDR system is governed by the minimum length over which the analyzer can discriminate between two adjacent locations having different temperature and/or strain. Since the received backscattered Brillouin signal is a convolution of the linewidth of the Brillouin spectrum with the input light pulse, the length of the light pulse will determine the analyzer's spatial resolution, which can be calculated as  $L_s = \tau v_g / 2$ , where  $\tau$  is the pulse width and  $v_g$  is the group velocity of the pump pulse.

The BOTDR sensor measures a weighted average value over its spatial resolution. As shown in Fig. 6.1, if a local strain change occurs over a distance scale smaller than the sensor's spatial resolution, the measured strain level will be smaller than the true value and will appear as a spread profile. Given the difference between measured strain and true strain, the measured strain length and its magnitude are subject to measurement systematic error.

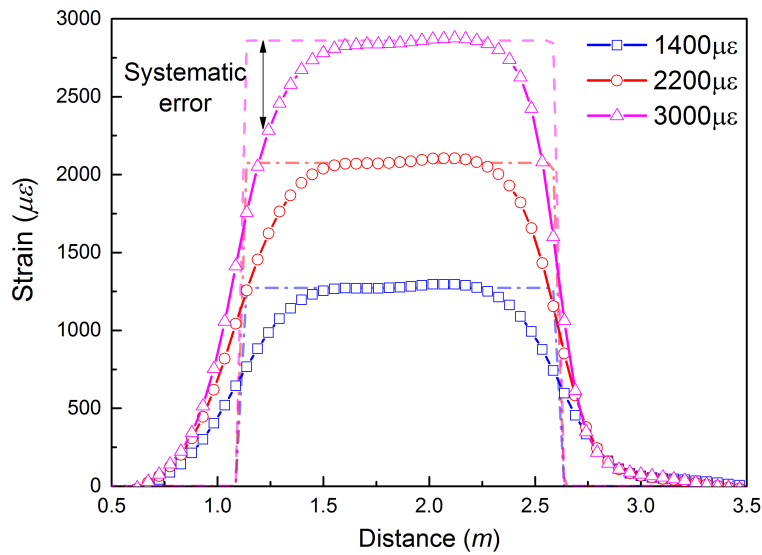


Fig. 6.2 Comparison of the simulated strain results and the real strain inputs for step strain change

## 6.2 Systematic error characterization

Measurement systematic error is related to the spatial resolution of the analyzer. With varying strain shapes, the amount of systematic error will be different. By using the optics model developed in Chapter 4, a parametric study is completed by producing strain data in different sloping shapes: step strain change case and gradually varying strain case. During this process, simulations are conducted to characterize the dependency of systematic error on strain characteristics and the characterization of measurement systematic with regard to strain distribution parameters such as strain gradient is achieved. A systematic error to strain gradient curve is finally obtained.

### 6.2.1 Step strain change

The systematic error of step strain is characterized with regard to the local strain gradient. Fig. 6.2 compares the simulated measurements (dash lines) of step strain change and real strain inputs (dotted lines). The difference between the two types of lines is regarded as measurement systematic error. It can be clearly seen that systematic error is larger at strain change sections (distance around 1.1 m and 2.6 m).

Figure 6.3 shows the relationship between the systematic error (colourful dots) and the strain gradient of the step strain change input for rising strain section. The difference between the simulated strain and the strain input value is computed as systematic error. The localized strain change rate of the measured strain is computed as the strain gradient. The falling strain section is not shown in this figure as its result is similar with the rising strain section. The black curves are the fitted lines representing the relationship between the systematic error and the strain gradient.

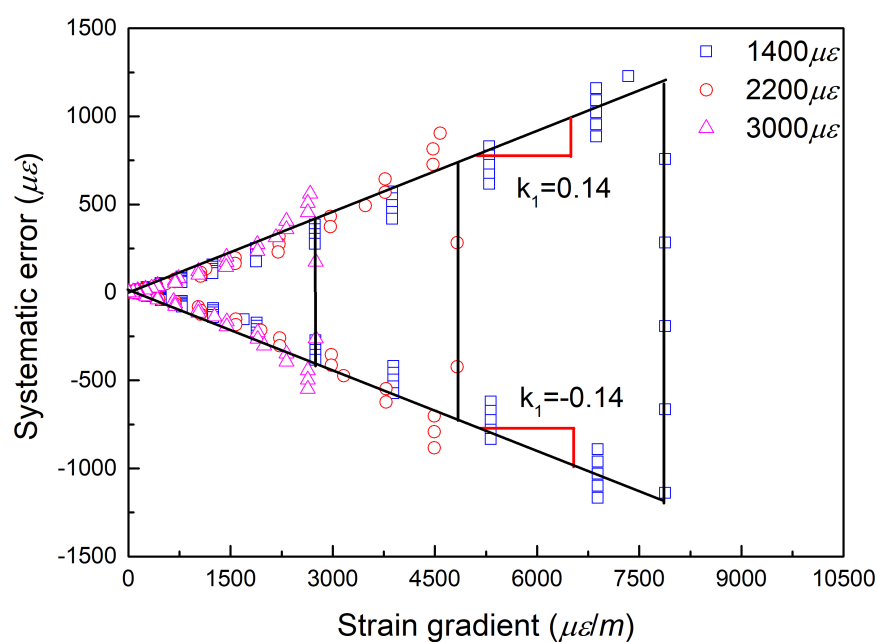


Fig. 6.3 Systematic error to strain gradient curve for a step strain input at three different strain input levels

The above figure indicates that the systematic error is approximately linearly related to the strain gradient. The curve of the error-strain gradient is symmetrical between the positive and negative error ranges. Taking the positive error range as an example, the linear coefficients ( $k_l$ ) for all three strain levels are close to  $0.14 \mu\epsilon / (\mu\epsilon \times m^{-1})$  indicating that  $k_l$  is independent of the input strain level. It can be concluded that there is a linear relationship between measurement systematic error and strain gradient, and the linear coefficient is independent on strain level.

### 6.2.2 Slope strain change

In practice, a gradually varying strain rather than a step strain change is more often found (such as Fig. 2.25 reviewed in Chapter 2). Therefore, to characterize a generalized systematic error to strain gradient curve, sloping strain measurement is characterized. The slope of the strain inputs are  $1000 \mu\epsilon/m$ ,  $2000 \mu\epsilon/m$ , and  $4000 \mu\epsilon/m$  and each of them is set over different rising lengths ( $l$ ) to achieve a maximum strain level ( $\epsilon_{max}$ ) of  $1400 \mu\epsilon$ ,  $2200 \mu\epsilon$ , and  $3000 \mu\epsilon$  (Fig. 6.4).

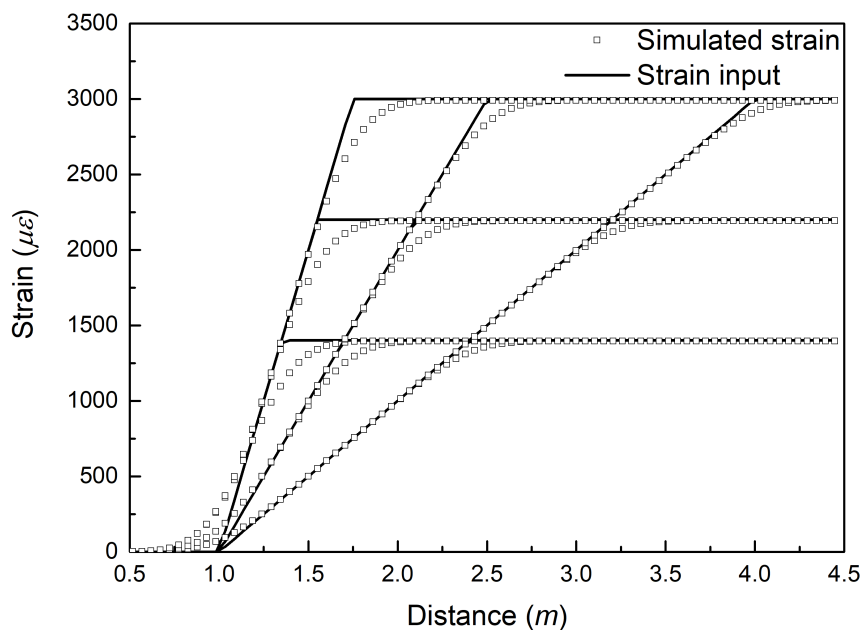


Fig. 6.4 The strain results simulated with the calibrated weight function of the one metre spatial resolution analyzer

Figure 6.5 presents the error-strain gradient curve in slope strain condition. A linear relationship between the error and the strain gradient is obtained again, but drops in the systematic error occur at high strain gradient locations. This happens because the gradually rising measurement intersects with the slope strain input, leading to very accurate strain measurement at some high strain gradient points. As a result, systematic error linearly increases with strain gradient at smaller strain gradient condition and decreases with strain gradient afterwards. However for both cases, linearly relationship between systematic error and strain gradient can be found.

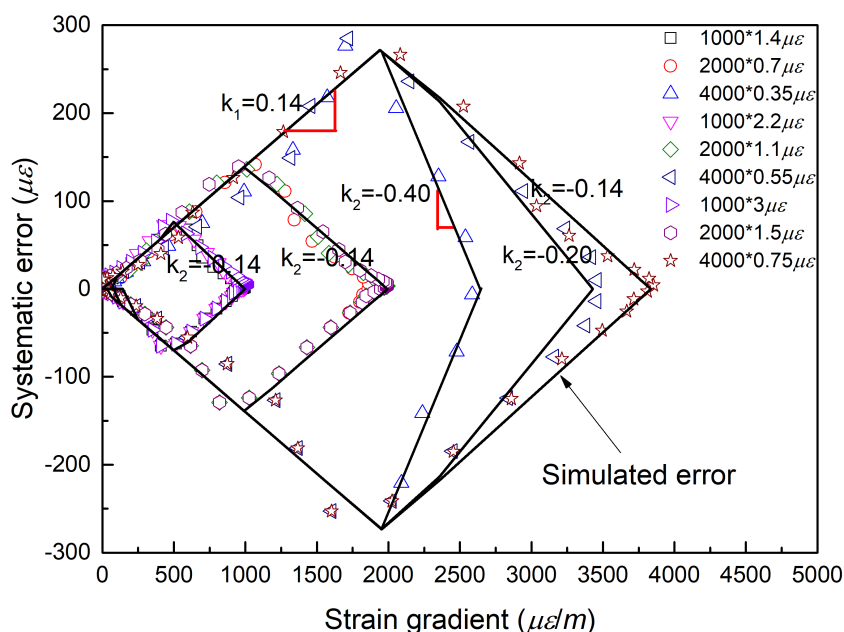


Fig. 6.5 Error to strain gradient curve for a slope strain input at different slope levels and lengths

For the slope strain case,  $k_1$  is again derived as  $0.14 \mu\text{E}/(\mu\text{E} \times m^{-1})$ , same as that obtained from the step strain experiments. The point where  $k_1$  starts to become a different level  $k_2$ , is dependent on the slope of the real strain change. For the slope length ( $l$ ) longer than  $0.7 m$ ,  $k_2$  is the same as  $k_1$  but has a negative value. In other cases, a shorter  $l$  leads to a sharper  $k_2$  until  $k_2$  reaches infinity which is the step strain change case where  $k_2$  does not exist. This results also indicates that if the maximum strain level is less than  $3000 \mu\text{E}$ ,  $l$  can be assumed to be  $l_M - l_s$ , in which  $l_M$  is the rising length of analyzer measurement and  $l_s$  is the pre-set spatial resolution.

### 6.2.3 Systematic error-strain gradient curve

The normalized plot of the systematic error versus strain gradient is given in Fig. 6.6. A linear relationship between the normalized error (the error divided by the input strain level) and the normalized strain gradient (the measured strain divided by the maximum strain gradient) is obtained. This linear relationship implies that the strain gradient can be used for data reliability quantification in the later spectrum decomposition algorithm.

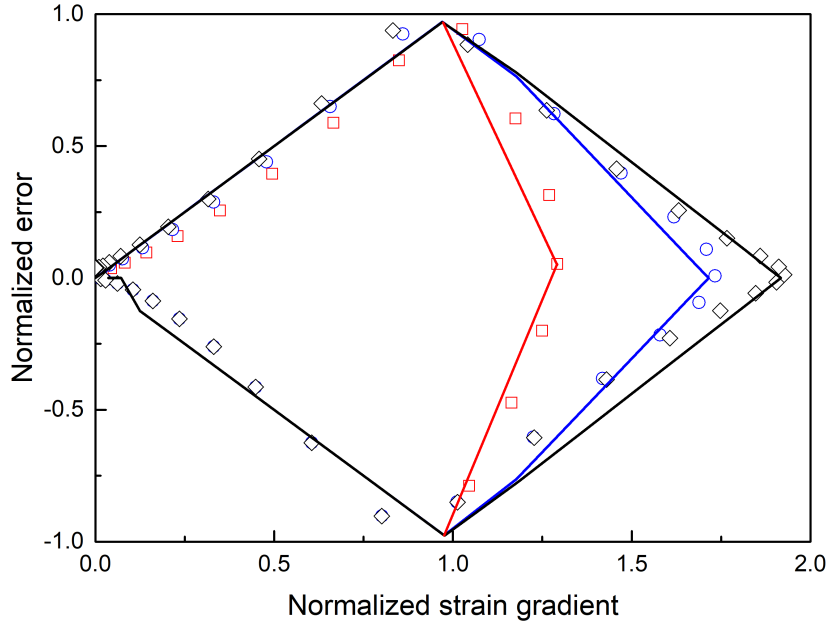


Fig. 6.6 The normalized systematic error to strain gradient curve for sloping strain change

It can be concluded that there is an approximately linearly relationship between the systematic error and the strain gradient. The linear coefficient ( $k_1$ ) is constant for different strain inputs when the systematic error increases with the strain gradient. The level of strain change slope ( $\Delta s$ ) determines the point where  $k_1$  changes to  $k_2$ , and the level of  $k_2$  is  $l$  dependent. The systematic error is therefore described as:

$$\Delta \varepsilon(\varepsilon', \Delta s, l) = \begin{cases} k_1 \times \varepsilon' & \varepsilon' \leq t_{\Delta s} \\ k_2(l) \times \varepsilon' + C & \varepsilon' > t_{\Delta s} \end{cases} \quad (6.1)$$

where  $k_1$  is the increasing linear coefficient between systematic error and strain gradient,  $k_2$  is the decreasing linear coefficient between systematic error and strain gradient,  $\Delta \varepsilon$  is systematic error,  $\varepsilon'$  is strain gradient,  $\Delta s$  is the strain slope,  $l$  is the strain rising/falling length, and  $t_{\Delta s}$  is the level of strain gradient when there is maximum systematic error in the measurement result.

For both step and sloping strain cases,  $k_1$  is a constant number ( $0.14 \mu \varepsilon / ((\mu \varepsilon \times m^{-1}))$ ) regardless of  $\Delta s$ ,  $l$  or strain input level.  $k_2$  only occurs at sloping strain case. It is equal to  $k_1$  when  $l$  is longer than  $0.7 m$  otherwise  $k_2$  is a parameter dependent on  $l$ , which is the half of the slope:  $t_{\Delta s} = \Delta s \times 0.5$ .

The error at  $t_{\Delta s}$  is then calculated as  $\Delta\epsilon(t_{\Delta s}) = k_1 t_{\Delta s} = 0.14 \times 0.5 \times \Delta s = 0.07 \times \Delta s$ . Applying the above equations to the strain measurements, the systematic error can finally be simulated with regard to the strain gradient (black line in Fig. 6.3 and Fig. 6.5).

In summary, the systematic error of BOTDR measurement originates from the limit of the analyzer's spatial resolution. As shown by the field data presented earlier, a rapid strain change will appear as a gradually distributed strain profile in the BOTDR measurement result. Simulation result shows that systematic error follows an error to strain gradient curve in which a faster strain change rate leads to a larger systematic error.

## 6.3 Data interpretation

Given the relationship between the measurement systematic error and strain gradient, a novel data interpretation method is developed in this study to reconstruct the strain using not only raw strain data but also Brillouin spectrum information (e.g. width and power level) with considering the data systematic error. In the main flow of the data interpretation algorithm, the 3D Brillouin spectrum is decomposed using the regularization method. This algorithm eliminates lower qualified Brillouin spectrum data through data reliability calculation and obtains the peak frequency of the Brillouin spectrum by statistically decomposing the rest of the Brillouin spectrum data. During this process, the strain measurement gradient is used to calculate the data reliability.

### 6.3.1 Estimation of the spectrum power

Chapter 4 has already verified that the received Brillouin spectrum can be calculated as the integration of the local Brillouin spectrum data with a weight function over the analyzer's spatial resolution at each frequency level. Therefore, the main objective of this back analysis algorithm is to decompose the received Brillouin power with the weight function along the cable distance at each frequency level.

In the forward process, the measured Brillouin power can be calculated as the product of the weight function ( $\mathbf{H}$ ) and the real local Brillouin power ( $\mathbf{x}$ ). They are given as

$$\mathbf{y} = \mathbf{H} \cdot \mathbf{x} \quad (6.2)$$

$$\mathbf{H} = \begin{bmatrix} g_1 & g_2 & \dots & g_n & 0 & \dots & 0 & 0 & 0 & 0 \\ 0 & g_1 & g_2 & \dots & g_n & 0 & \dots & 0 & 0 & 0 \\ 0 & 0 & g_1 & g_2 & \dots & g_n & 0 & \dots & 0 & 0 \\ 0 & 0 & 0 & g_1 & g_2 & \dots & g_n & 0 & \dots & 0 \\ \dots & & & & & & & & & \\ 0 & 0 & 0 & 0 & 0 & \dots & g_1 & g_2 & \dots & g_n \end{bmatrix} \quad (6.3)$$

$$\mathbf{y} = \begin{bmatrix} P_{MB}(1) & P_{MB}(2) & \dots & P_{MB}(N-n) \end{bmatrix} \quad (6.4)$$

$$\mathbf{x} = \begin{bmatrix} P_B(1) & P_B(2) & \dots & P_B(N) \end{bmatrix} \quad (6.5)$$

In the back analysis process, it is necessary to solve  $\mathbf{x}$  with known  $\mathbf{H}$  and  $\mathbf{y}$ . Due to  $\mathbf{H}$  being singular, the problem is regularized. A common approach to this equation is to minimize the weighted sum of the ‘energy’ of vector  $\mathbf{x}$  as well as the energy of the error (Tikhonov regularization) [72]:

$$\mathbf{J} = \min\{\|\mathbf{H}\mathbf{x}-\mathbf{y}\|_2^2 + \lambda\|\mathbf{x}\|_2^2\} \quad (6.6)$$

Taking the derivative of this objective function obtains

$$\frac{\partial}{\partial \mathbf{x}} J(x) = 2\mathbf{H}^T(\mathbf{H}\mathbf{x} - \mathbf{y}) + 2\lambda\mathbf{I}\mathbf{x} \quad (6.7)$$

Setting the derivative to zero:

$$\frac{\partial}{\partial \mathbf{x}} J(x) = 0 \Rightarrow \mathbf{H}^T\mathbf{H}\mathbf{x} + \lambda\mathbf{I}\mathbf{x} = \mathbf{H}^T\mathbf{y} \quad (6.8)$$

$$\Rightarrow (\mathbf{H}^T\mathbf{H} + \lambda\mathbf{I})\mathbf{x} = \mathbf{H}^T\mathbf{y} \quad (6.9)$$

where  $\mathbf{I}$  is an identity matrix, and  $\lambda$  is a parameter that depends on the noise level of  $\mathbf{H}$ . In this least squares function, minimizing  $\|\mathbf{H}\mathbf{x}-\mathbf{y}\|_2^2$  forces  $\mathbf{x}$  to be consistent with the output  $\mathbf{y}$ . Minimizing  $\|\mathbf{x}\|_2^2$  forces  $\mathbf{x}$  to have low energy. To improve the simulation result in the presence of noise, the energy of the derivative of  $\mathbf{x}$  instead can be minimized. Minimizing the sum forces  $\mathbf{x}$  to be consistent with  $\mathbf{y}$  and to have smoother  $\mathbf{x}$  (as far as possible, and depending on  $\lambda$ ). For noisy data  $\mathbf{y}$ , a larger  $\lambda$  is needed so as to attenuate the noise. But if  $\lambda$  is too large, then the estimate of the input signal is distorted. To achieve the best simulation

result,  $\lambda$  needs to be optimized. With the derivative matrix  $\mathbf{D}$ , the new solution is:

$$\mathbf{x} = (\mathbf{H}^T \mathbf{H} + \lambda \mathbf{D}^T \mathbf{D})^{-1} \mathbf{H}^T \mathbf{y} \quad (6.10)$$

$$\mathbf{D} = \begin{bmatrix} 1 & -1 \end{bmatrix} \quad (6.11)$$

### 6.3.2 Data reliability

The measurement systematic error is linearly proportional to the measurement strain gradient. This causes differences in data reliability among the data points obtained from the same optical fibre, depending on the measured gradient of the strain distribution profile. Therefore, it is not appropriate to treat all data points equally in the inverse analysis. The objective function is then changed to:

$$\min\{\|\mathbf{W}^{\frac{1}{2}}(\mathbf{H}\mathbf{x} - \mathbf{y})\|_2^2 + \lambda \|\mathbf{A}\mathbf{x}\|_2^2\} \quad (6.12)$$

where  $\mathbf{W}$  is the matrix that quantifies data reliability and  $\mathbf{A} = \mathbf{D} \times \mathbf{W}$ .

Taking the derivative of this objective function obtains:

$$\frac{\partial}{\partial \mathbf{x}} J(x) = 2\mathbf{H}^T(\mathbf{W}\mathbf{H}\mathbf{x} - \mathbf{W}\mathbf{y}) + 2\lambda \mathbf{A}^T \mathbf{A}\mathbf{x} \quad (6.13)$$

Setting the derivative to zero:

$$\frac{\partial}{\partial \mathbf{x}} J(x) = 0 \Rightarrow \mathbf{H}^T \mathbf{W}\mathbf{H}\mathbf{x} + \lambda \mathbf{A}^T \mathbf{A}\mathbf{x} = \mathbf{H}^T \mathbf{W}\mathbf{y} \quad (6.14)$$

$$\Rightarrow (\mathbf{H}^T \mathbf{W}\mathbf{H} + \lambda \mathbf{A}^T \mathbf{A})\mathbf{x} = \mathbf{H}^T \mathbf{W}\mathbf{y} \quad (6.15)$$

So the solution is given by:

$$\mathbf{x} = (\mathbf{H}^T \mathbf{W}\mathbf{H} + \lambda \mathbf{A}^T \mathbf{A})^{-1} \mathbf{H}^T \mathbf{W}\mathbf{y} \quad (6.16)$$

Since the data reliability is linearly related to the measured strain gradient, the data reliability index of the distributed strain data can be normalized by the strain gradient:

$$\mathbf{W} = \max(\sigma'_i) - \left\| \frac{\sigma'_i - \text{mean}(\sigma'_i)}{\text{std}(\sigma'_i)} \right\| \quad (6.17)$$

Figure 6.7 shows an example of  $\mathbf{W}$  distribution for step strain change in addition to a polynomial strain change, both at a maximum of  $2000 \mu\epsilon$ . In this figure, the measurements where the data distribution profile become discontinuous need to be considered with low weight during the back analysis process because the  $\mathbf{W}$  of these data points indicate low data reliability values. Moreover, the  $\mathbf{W}$  values of the polynomial strain data are relatively larger than those of step strain data, depending on the non-uniformity of the data distribution. From this verification,  $\mathbf{W}$ , which can be obtained by a simple normalized process, can be considered appropriate for use as the weight of the distributed strain data.

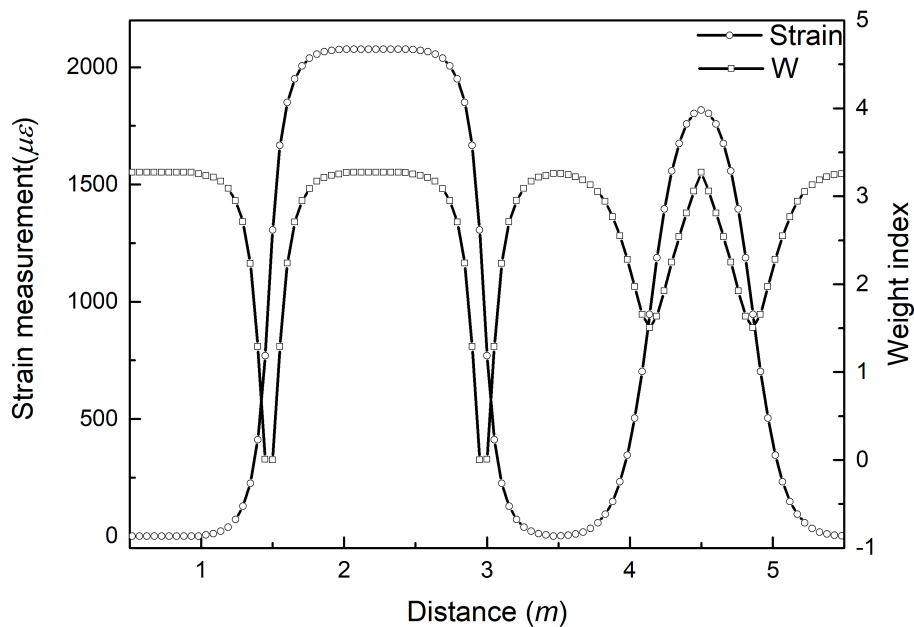


Fig. 6.7 Profile of a step strain followed by a polynomial strain change shape and the normalized data reliability index

The above strain shape is then simulated and back analyzed both with and without (making all weight values as 1) considering data reliability to demonstrate the effectiveness of introducing  $\mathbf{W}$ . The simulated input and the reconstructed strain is illustrated in Fig. 6.8. In this figure, the reconstructed strain considering data reliability shows better agreement with the input strain.

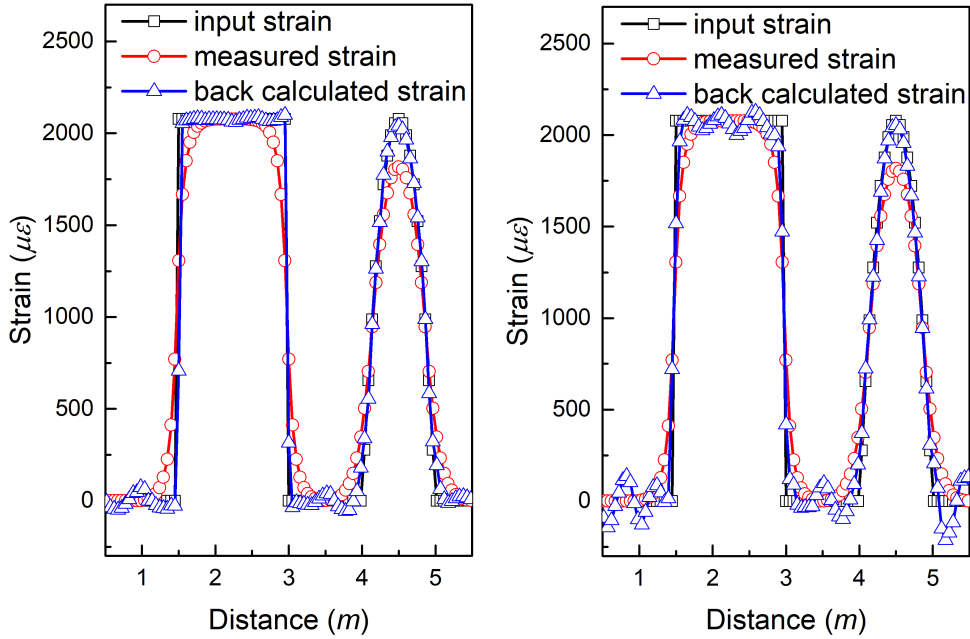


Fig. 6.8 Illustration of the simulated reconstructed strain using the data interpretation algorithm a) considering data reliability and b) without considering data reliability

The accuracy of the two data interpretation results is evaluated quantitatively by the standard deviation error  $R$ , which is defined as:

$$R = \sqrt{\frac{1}{N} \sum_{i=1}^N (\varepsilon_i^x - \varepsilon_i^y)^2} \quad (6.18)$$

where  $\varepsilon_i^x$  is the reconstructed strain and  $\varepsilon_i^y$  is the real strain level. The number of measurement points is  $N$ . The calculated  $R$  value of the reconstructed strain in Fig. 6.8 is  $42.5 \mu\epsilon$  for the algorithm considering data reliability, and  $122.9 \mu\epsilon$  for the algorithm without considering data reliability. It can be said that the strain is reconstructed with high accuracy and that the accuracy is improved more than 65.4% by introducing data reliability. This result confirms the appropriateness of the proposed data interpretation method of introducing data reliability factors using the measured strain gradient.

### 6.3.3 Algorithm characterization

To analyze the spectrum shape and extract the strain information with the 3D spectrum decomposing data interpretation algorithm, several issues need to be identified. First of

all, a spectrum peak may be buried in the noise of the measurement when the measured strain change is of short length. Second, the maximum accuracy this algorithm can achieve considering the noise of the sensing system has to be clarified.

White noise is therefore added to the 3D spectrum before the back analysis process as a representation of the analyzer noise. Simulations are then performed on different strain lengths and magnitudes in the step strain case. The accuracy of the simulation results is calculated as the sum of difference between the real strain and the back calculated strain. Its dependence on strain length and magnitude is shown in Fig. 6.9.

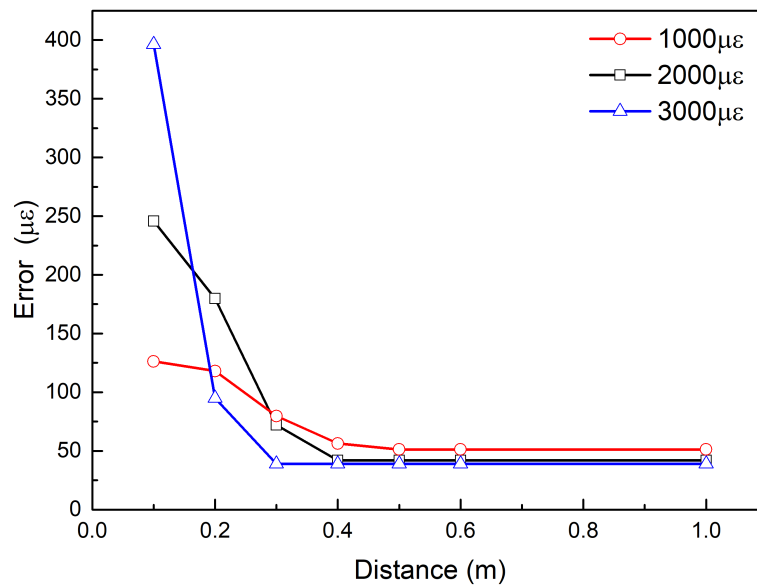


Fig. 6.9 The simulated accuracy of the data interpretation algorithm as a function of strained section length at three strain levels for step strain

The figure reveals that the maximum accuracy that this algorithm can achieve is close to  $50 \mu\epsilon$  for a step strain change shape. At strain levels lower than  $2000 \mu\epsilon$  and the strained length longer than  $0.4 m$ , the back calculated strain has a good agreement with the actual strain. However, when the strained length is less than  $0.4 m$ , the back calculated strain decreases in proportion with the strain length. At strain levels larger than  $2000 \mu\epsilon$ , the accuracy of the back calculated strain shows similar trends with distance except that the transition point changes to  $0.3 m$  which is probably due to that larger strain differences make it easier to separate Brillouin spectrum profiles.

In order to characterize the effectiveness of the algorithm, a normalized accuracy to strain profile curve is proposed (Fig. 6.10). This diagram relates the strained section length and

the amplitude of the strain to the reliability of the back analysis algorithm. The normalized accuracy is calculated as the percentage of error to strain magnitude. As shown in the figure, the border-line separates good data regions (where the algorithm reliability cannot be improved any more considering the sensing system noise) and bad data regions (where the algorithm is less reliable due to short strain length). At bad data regions, the algorithm reliability is proportional to the strain length, and a larger strain magnitude leads to a sharper curve between algorithm accuracy and strain length. At good data regions, the algorithm reliability is only dependent on the strain magnitude. A higher strain level leads to better reliability of the back analyzed strain. In total, a higher strain level tends to have better performance in this back analysing algorithm. At strain section lengths longer than 0.5 m, the accuracy of the back calculated strain is close to 5% of the real strain, verifying that this algorithm is appropriate for back calculating the strain during data interpretation process.

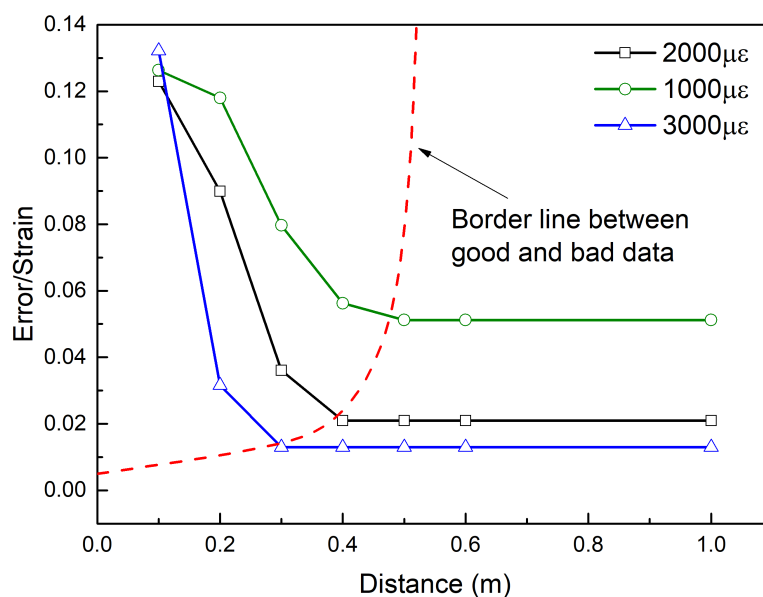


Fig. 6.10 Diagram showing the borderline between good results and bad results regions, and the curve representing the normalized algorithm error as a function of the strained section length

## 6.4 Test case

The effectiveness of the proposed strain reconstruction algorithm is verified by experiments in which the detection of two connected step strains were presented. The geometrical

configuration of the optical fibre is shown in Fig. 6.11. In the test, the Fujikura reinforced strain sensing cable is hung and clamped at three points. The first section had a length of  $1.05\text{ m}$  (longer than the analyzer's spatial resolution) and the second one is  $0.65\text{ m}$  (shorter than the analyzer's spatial resolution) for constructing complex strain distribution. Loads are applied to clamp 2 and clamp 3 to extend the cable in two sections. The strain change of the cable is therefore in a step shape in two sections.

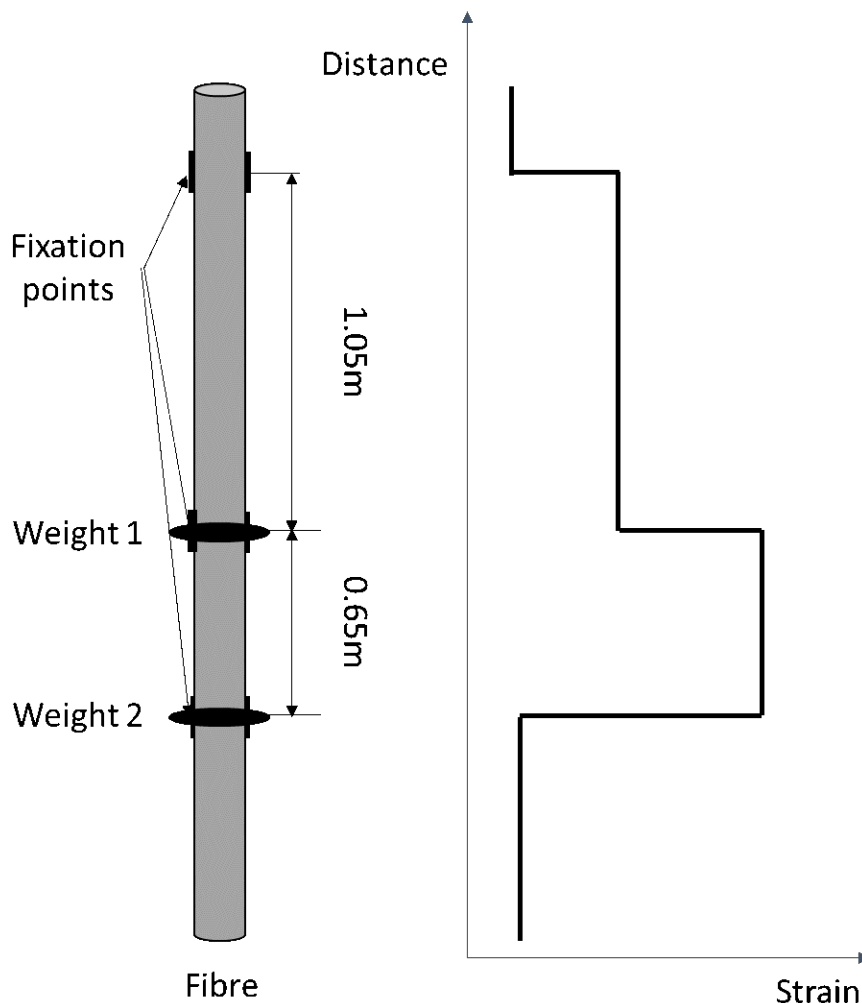


Fig. 6.11 Graphical illustration of the test set up and expected strain change of the cable

In section 1, the sensing cable is extended by both load 1 and load 2, while in section 2 the sensing cable is extended by only load 2. As a result, the input step strain for section 1 is always higher than section 2 as long as there is a load applied to clamp 3. The two input strains are connected, that is the stopping point of the first step strain being the starting point of the second step strain. Because of the limit of the analyzer's spatial resolution, the

BOTDR strain measurement should be smaller than the real strain input in section 2, and indicate the real strain in section 1.

The Young's modulus of the tested cable is  $70 \text{ GPa}$ . Load 1 and load 2 used to extend the cable, are  $8.5 \text{ kg}$  and  $12 \text{ kg}$  respectively. Therefore, the input strain should be  $1250 \mu\epsilon$  and  $1750 \mu\epsilon$  for the two strain sections. It is noted that both of the strained section lengths lay within algorithm good data regions.

### 6.4.1 Strain reconstruction

To increase the accuracy of the reconstruction result, the back analysis process is separated into three different sections based on the measured strain gradient information. At each section, the raw Brillouin spectrum is decomposed based on the proposed algorithm. The determined weights, which are derived from the measured strain gradient, are plotted in Fig. 6.12. Low weight index is determined especially at strain transit sections. The amount of weight is reduced to nearly zero at points in the middle of strain transit sections. At other sections where strain does not vary rapidly, the determined weight increases to a relatively higher value. Data with highest weights locates at sections where there is no strain change.

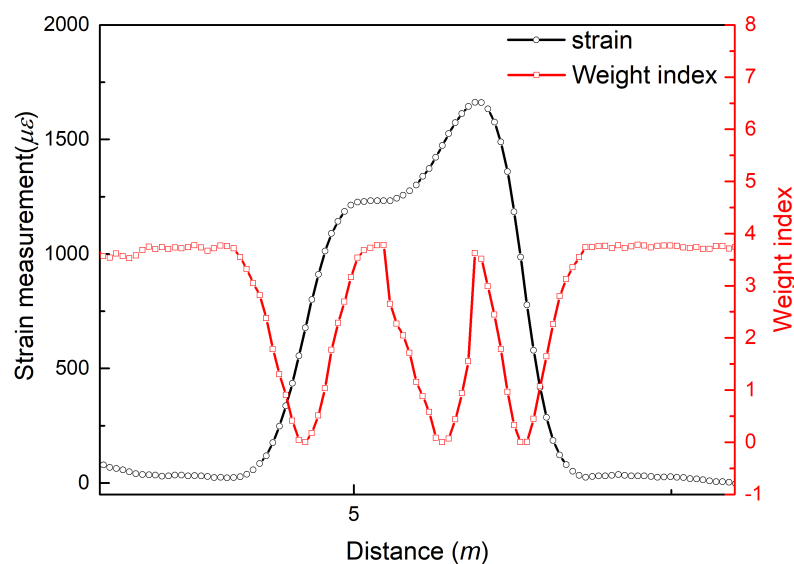


Fig. 6.12 Measured strain profile and its weight index profile

Figure 6.13 and 6.14 show the measured 3D Brillouin spectrum and the back calculated 3D Brillouin spectrum using the proposed data interpretation algorithm with the weight index as shown in Fig. 6.12. It can be clearly seen that the peak centre frequency which changed

gradually due to the limit of the analyzer's spatial resolution is successfully reconstructed back to the sharp peak centre frequency change, especially at  $z = 4.6\text{ m}$ ,  $5.7\text{ m}$  and  $6.4\text{ m}$ . As a result, the fitted strain profile should be reconstructed from the gradual strain change to the real strain condition, that is step strain change.

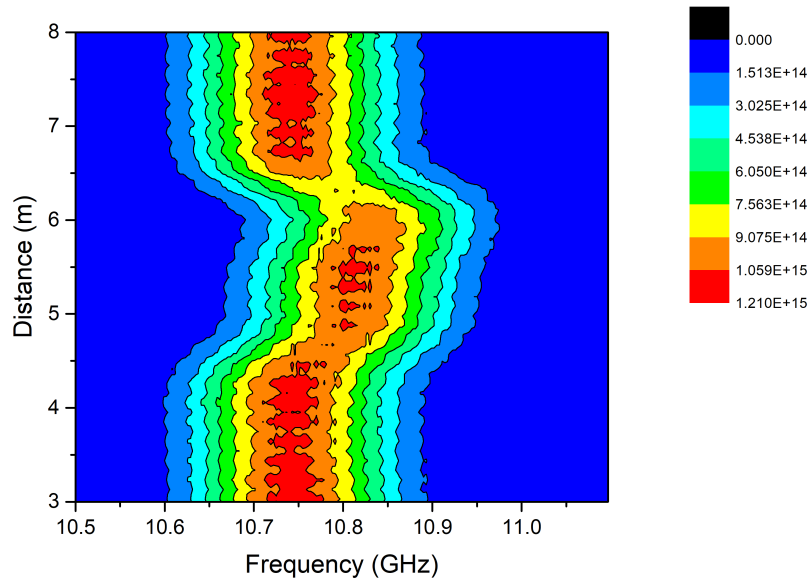


Fig. 6.13 Analyser measured Brillouin power in the lab test

To see the spectrum decomposition process in more detail, Fig. 6.15 presents the analyzer measured spectrum at a strain transition point along with its decomposed spectrum using the proposed algorithm. The measured spectrum has a larger bandwidth and higher peak power level due to pulse convolution, but the back calculated spectrum is successfully separated into two Brillouin spectrum profiles from the composed spectrum, representing measurements at both strained and unstrained sections. Therefore, the two decomposed spectra contain two different centre frequency peaks with a smaller bandwidth for each peak.

After fitting the decomposed spectrum and detecting the peak centre frequency, the estimated strain is illustrated in Fig. 6.16, where the red points are the analyzer measured distributed strain data, the black points are the real strain, and the blue points are the back analyzed strain results. In estimating these strain functions, the characterized weight function and the normalized data reliability index  $W$  for each data point are used.

The accuracy of the strain derived by the back analysis algorithm is  $104\mu\epsilon$ , and that directly measured from the analyzer is  $401\mu\epsilon$ . The reconstructed strain accuracy is improved largely by using the proposed algorithm. The result of this verification demonstrates that highly accurate shape reconstruction is possible by decomposing the measured Brillouin

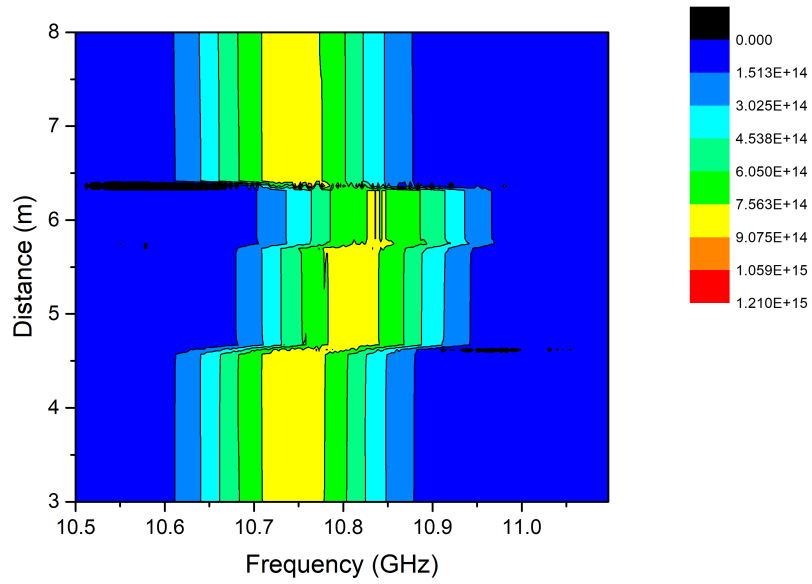


Fig. 6.14 Back calculated Brillouin power in the lab test

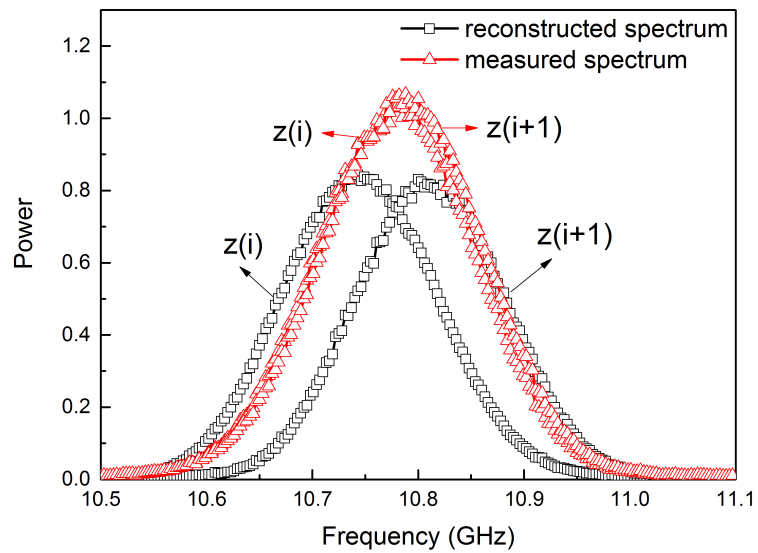


Fig. 6.15 The analyzer measured Brillouin spectrum and back calculated decomposed spectrum

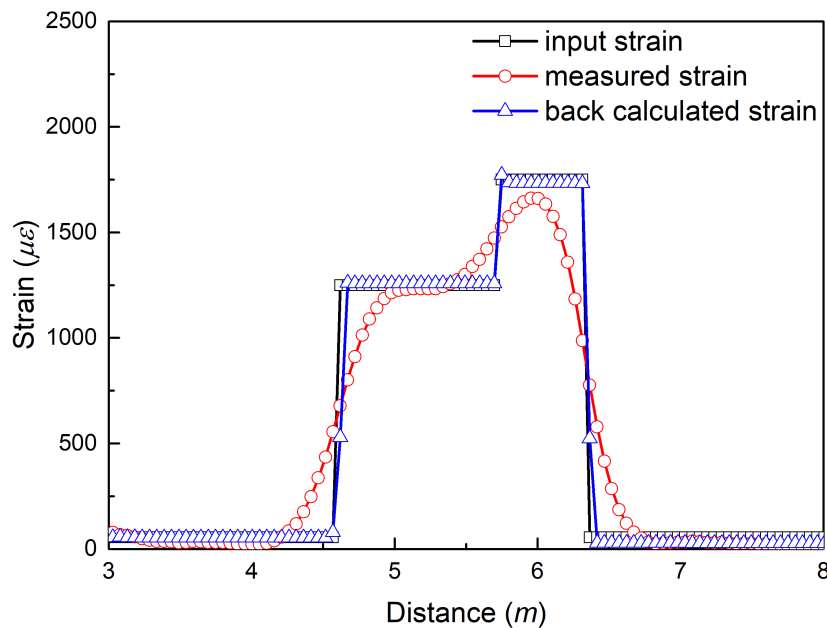


Fig. 6.16 Reconstructed strain using the back calculation method with a connected step shape input strain

power at each frequency as well as taking advantage of the measured strain gradient data from the analyzer. This procedure, which introduces spectrum decomposing using a weight function with a data reliability factor, is expected to be a general way of reconstructing strain information for a distributed fibre optics sensor.

### 6.4.2 Strain increment calculation

However this strain reconstruction algorithm using 3D Brillouin spectrum information is only suitable for absolute strain calculation and short length of monitoring applications considering time consuming of the algorithm. For some site applications, relative strain change is used to monitor structure conditions. It is unrealistic to obtain the 3D power spectrum information of relative strain change and therefore inapplicable to use this algorithm. A simplified error characterization process is therefore conducted to compensate systematic error of strain increment measurements.

Given the strain reconstruction algorithm, the systematic error is investigated with regard to the strain increment calculation and how the calculated increment is affected by the non-uniformity of the original strain profile. The experimental set up used was similar to the

previous tension test to construct an original non-uniform pre-strain (two connected step strains) profile. The pre-strained cable was then loaded onto clamp 3, leading to a uniform strain increment added to the cable all along the two strained sections.

Figure 6.17 illustrates the strain measurement results of the tested cable at different loading levels. The blue line is the pre-strain of the cable which contains two step strain changes at  $z = 4.5\text{ m} \sim 6.5\text{ m}$ . The blue line is approximately horizontally lifted up at around  $z = 5\text{ m} \sim 6\text{ m}$  for the rest measurements, representing the uniformly distributed loading applied afterwards.

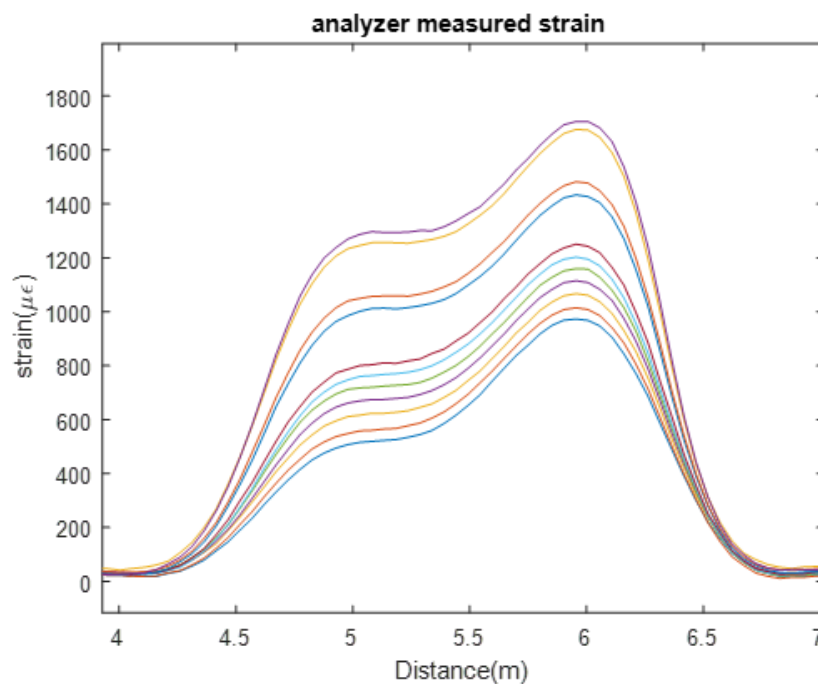


Fig. 6.17 BOTDR measurements of the tested cable with a non-uniform pre-strain distribution

The measured strain increments (as shown in Fig. 6.18) were therefore calculated by subtracting the baseline reading from the measurements. However, the calculated strain increment was not distributed as uniform as the input loading. A variation in strain increment measurement along cable length was found, especially at  $z = 5.5\text{ m} \sim 5.8\text{ m}$ . In addition, the variation of the strain increment tended to increase with the input loading (e.g. reading at  $z=5.6\text{ m}$  where the strain change rate was relatively larger). For example, at the lowest loading level, the increment of strain along the strained cable sections is close to constant along distance. However at the highest loading level, a maximum of  $150\text{ μϵ}$  difference can be found between the larger strain change rate point (at  $z=5.6\text{ m}$ ) and the smaller strain change rate point (at  $z=5.1\text{ m}$ ). These results indicate that the strain increment variation is

dependent on the strain gradient of the original strain profile. A larger strain gradient leads to a higher systematic error of strain increment.

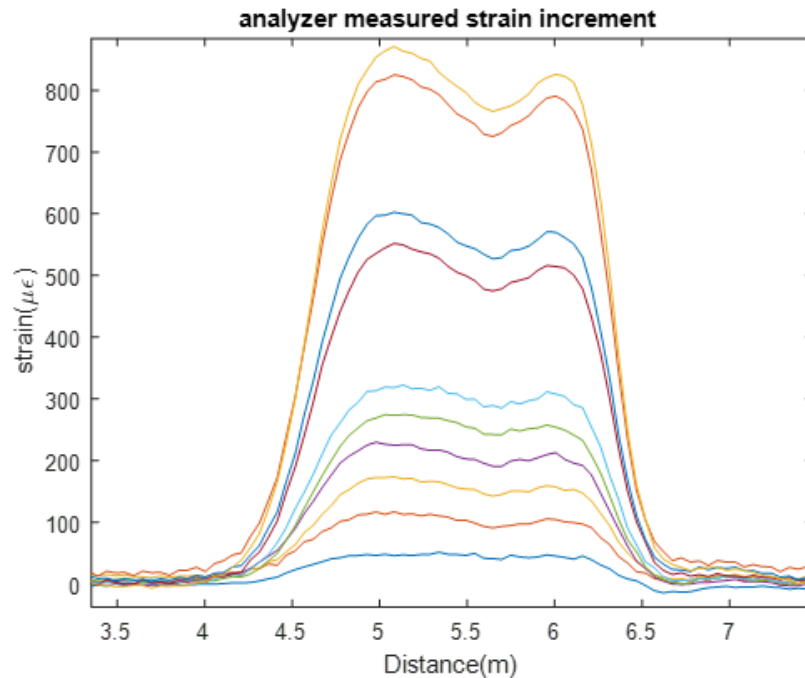


Fig. 6.18 Strain increment calculation along the tested cable

### 6.4.3 Systematic error compensation

The characteristics of the strain increment variation were investigated. Taking the largest measurement as an example, the reconstructed strain using Brillouin 3D spectrum information is shown in Fig. 6.19. The back calculated result indicated that the first section of step strain change was 1.1 *m* and the second section was 0.6 *m*, different from the input original strain profile which were 1.05 *m* and 0.65 *m* respectively. In that case, the first step strain profile length increased by 0.05 *m* after 3 *kg* of loading was applied to the system. The increase of strain length could be either analyzer systematic error or real strain change. To remove the effect of slippage or strain hysteresis, the unloading process was conducted and it was found that the measurement was able to get back to its original condition. This indicated that the shift of the border between the two step strains does not represent real strain. As a result the variation of the strain increment is measurement error which is probably due to the mechanical limit of the analyzer which is related to double peak-induced distance error in STFT-BOTDR event detection and the recovery method [Yu et al.]. Because the strain

increment variation follows a similar pattern with different measurements and thus can not be minimized by averaging, it is regarded as measurement systematic error.

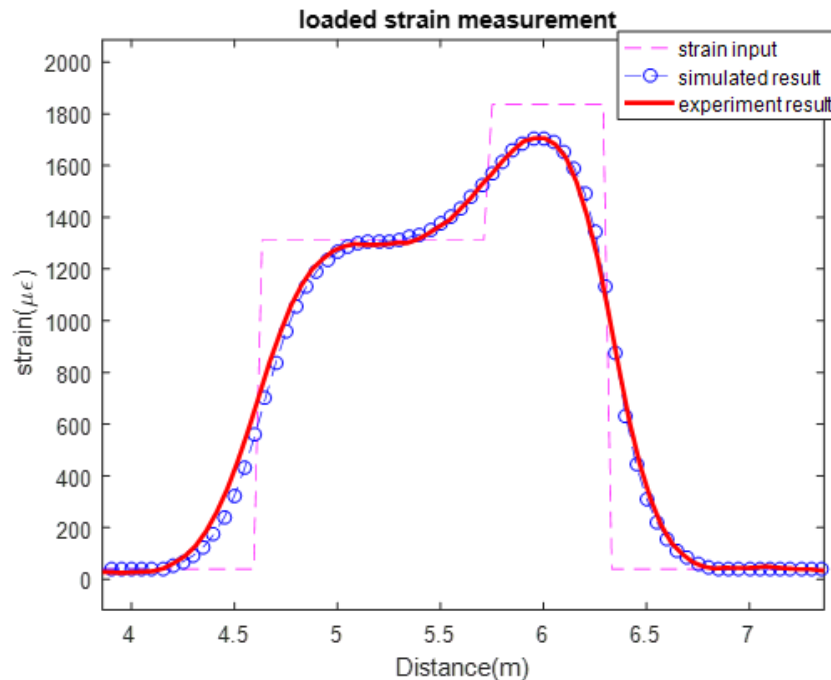


Fig. 6.19 Back calculated strain measurements using the reconstruction algorithm

Therefore, when strain is initially non-uniformly distributed, the calculated strain increment will have systematic error, the quantity of which is dependent on the change rate of the original strain profile. One possible solution for systematic error reduction is to compensate for the length change of strain sections induced by the analyzer mechanical limitations. During this process, measurements are adjusted to overlap each other at one certain strain level. By realign the measurements with regard to strain length, systematic error can be minimized.

In the main flow of this strain increment systematic error compensation method, the strain readings especially at faster strain change rate sections are adjusted with regard to strain change locations. During this process, the strain measurement gradient is used to separate data in different sections for later systematic error compensation. The strain measurement is realigned to compensate for the strain section length error due to the mechanical limitation of the analyzer. The strain increment result is finally obtained by calculating the difference between two realigned strains. Figure 6.20 shows the final result of the strain increment calculation.

As Fig. 6.20 shows, a less variable strain increment result is obtained comparing to raw data calculation results. The variations of strain increment from raw data calculations

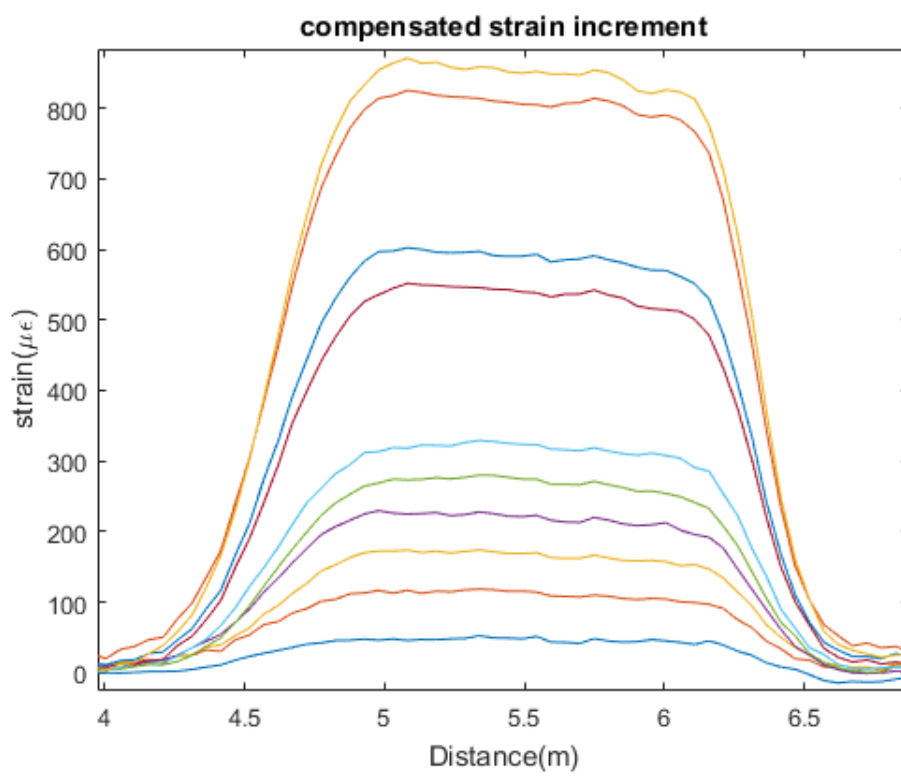


Fig. 6.20 Compensated strain increment along the tested cable

(Fig. 6.18 are minimized in large quantity. The maximum strain increment difference along the cable strained section reduces from  $150 \mu\epsilon$  to less than  $20 \mu\epsilon$  using this strain increment systematic error compensation method.

## 6.5 Summary

In most previous studies of structural monitoring using BOTDR, the structural conditions were directly evaluated from acquired strain distributions without considering the measurement systematic error. This chapter develops a novel data interpretation algorithm after charactering the systematic error of the analyser measured results. It is found that:

1. A Brillouin spectrum reconstruction algorithm using the regularization decomposing method was constructed, taking advantage of characteristics of the distributed strain data, which was acquired from a Brillouin optical time domain system. The remarkable point is that, using not only the raw strain data but also the Brillouin spectrum information (e.g. width and power level), this algorithm eliminates lower qualified Brillouin spectrum data through the strain gradient calculation and obtains the peak frequency of the Brillouin spectrum by statistically decomposing the rest of Brillouin spectrum data.
2. The simulation result indicated that this algorithm can be applied to various strain shapes and levels without limitation of parameter characterization, and that the accuracy of the back calculated strain result can be greatly improved compared to the raw strain data. The reliability of the algorithm was finally verified by experimental tests where two continuous step strains were measured and analyzed. The result indicated that this algorithm can largely the accuracy of the interpreted strain.
3. Strain increment fluctuation error along the cable largely comes from the combined effect of analyzer systematic error and the original strain condition of the cable. A faster strain gradient will enlarge the systematic error. Experiments indicated that this error can achieve  $150\mu\epsilon$ .
4. When the strain increment is calculated by subtracting one measurement from another, the amount of measurement error will be enlarged. This is why unexpected fluctuations of strain increment were mostly observed in the site strain monitoring cases. To minimise this error, strain section length compensation method in different cable sections are developed.

# Chapter 7

## Case studies

Using the established precision and systematic error compensation methods, a novel data interpretation algorithm for measurements based on Brillouin scattering is achieved. During this process, the analyzer measurement is firstly separated into different distance sections based on data quality. The quality of the data is calculated from strain gradient as there is a verified linear relationship between data reliability and strain gradient. In different sections, the systematic error is compensated for by horizontally shifting the strain to the baseline reading as previously verified that the systematic error of the strain increment is equivalent to distance error. The strain increment is then obtained by subtracting the baseline reading from the strain measurement. Finally, the filtering process is conducted to minimise precision error by fitting the shifted strain with the smoothing spline function using the data reliability index as fitting weight.

With the novel data interpretation algorithm, this chapter presents DFOS data interpretation examples in two field sites where (i)Woo pile site and (ii) Newfoundland pile site, both in London were installed with optical fibres. The precision error prediction method by evaluating frequency resolution as well as distance resolution is conducted with two pile measurements. The precision and systematic error of the measurements are then compensated for using the novel data interpretation methodology. The accuracy of the interpreted results are discussed in the final part of this chapter.

### 7.1 Data interpretation flow chart

The reconstruction of strain profiles for the distributed fibre optics sensing system based on Brillouin scattering normally uses strain readings directly obtained from the analyzer without considering precision error or systematic error. In this novel developed data interpretation methodology, the accuracy of the reconstructed strain is improved by utilizing the previously

revealed relationship between the shape of the measured strain profile and the measurement errors. For example, the measured strain is approximately linearly related to the precision error, and the systematic error of the measured strain fluctuation can be regarded as distance error of the sensing system. Based on that, an interface including several computing models to handle data interpretation procedures is constructed as in the following flow chart:

The parameters of the fibre optics sensing system are initially imported into the data analysis interface. The fibre parameters include the experimentally characterized Brillouin conversional strain/temperature coefficients of the sensing cable, the cable optic attenuation, and the refractive index of the cable. The systematic error of the measurement is related to the setting up of the sensing analyzer such as sampling resolution and spatial resolution. These parameters are induced to the data analysis model as well. The backscattered Brillouin spectrum information of the baseline reading is stored for later precision error prediction. The construction site type is specified at this stage for later data analysis outputs determinations.

The next step of this data analysis methodology is to import the Brillouin frequency shift measurements. The raw data measurements are transferred from different formats (such as .bsb from Neubrex BOTDR analyzer) to the particular code suitable format. The datasets are separated into baseline readings and others. The positions of each measuring points need to be realigned. For example, The Brillouin frequency shift readings need to be flipped upside down when the laser injected directions are not consistent and extra measurements are cut off when there is fibre re-splicings.

The obtained Brillouin frequency shift readings are then used to reconstruct strain increment profiles considering systematic error and precision error minimisation. The centre frequency profiles under one loading condition are first averaged to minimise random noise. The measurements are then temperature compensated. The strain increment profile is obtained by subtracting the baseline reading from the temperature compensated measurements. The weight which represents the reliability of different measuring points is calculated from precision error which can be predicted from the Brillouin spectrum information. Using this weight profile, the strain increment is separated into different sections based on the data quality. The horizontal shift function is conducted to minimize the systematic error as previously revealed in the lab that the fluctuation error of strain increment can be regarded as the distance error. The filtering process which uses smoothing splines to fit the data is used to minimize the precision error.

The final part of this interface is to generate the output of this data analysis procedure. In this section, different engineering parameters are calculated based on the project type. For example, for a pile, strain results on the excavation side are lifted up and matched to

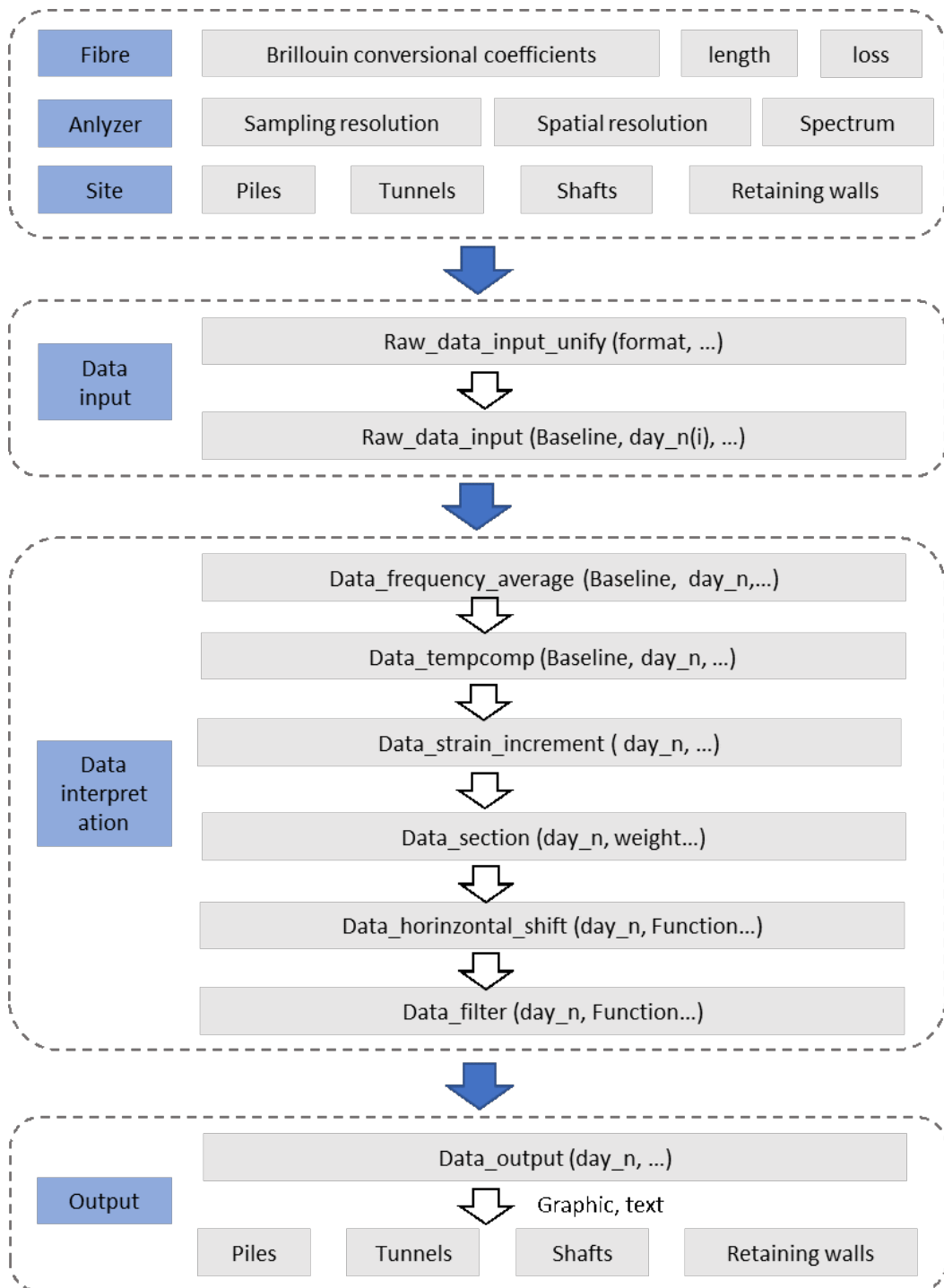


Fig. 7.1 The flow chart of the data interpretation methodology

the results on the soil side to calculate the curvature of the pile. An engineer can choose to calculate their parameters of interest and export them as graphs or text files.

Using this novel data interpretation algorithm, measurements from two pile sites () are processed. The results are shown in the following two sections.

## 7.2 WOO case study

The WOO construction site was located in the docklands area in London, close to the River Thames. The test pile at this site was 0.9m in diameter and 24.8m in depth. An Osterberg cell (O-Cell) system was installed at the bottom section of the pile to examine the pile shaft capacity and end capacity separately. A distributed fibre optics sensing system (the Fujikura reinforced strain cable adjacent with the Brugg V1 strain cable) was instrumented along the pile cage to measure the bi-axial strain profile of the pile.

The test pile was a rotary bored pile under bentonite support. Here are the construction dates:

Table 7.1 The construction process of the WOO site

Date	Duration (h)	Construction process
6.15	6	Pile bore excavated
6.15	1	Cage inserted in bore
6.15~6.16	4	Concreted
6.29	0.5	Base cracked
7.27~7.28	16	Base grouted
8.29~9.2	87	Load tested

After the cage was inserted into the borehole, concrete was cast in the borehole to create a pile on 15<sup>th</sup> June 2015. The hydration of the concrete continued for 7 days, so everything was settled down by 29<sup>th</sup> June 2015. The base was cracked on 15<sup>th</sup> June 2015, and the grouting of the base was conducted one month later, on 27<sup>th</sup> July 2015. The load test was performed on 29<sup>th</sup> August 2015. Before the test, 200 repeated FO data readings were collected continuously with a Neubrex BOTDR analyzer (NBX-5000) for later precision error analysis.

The implementation of the monitoring system has the following objectives:

1. Performing a detailed investigation about the actual response of the concrete during the different construction states, with particular attention to the stress losses in the pre-tensioned steel.
2. Assessing the overall structural response of the bridge during the different construction states, by controlling the deformations in the deck and in the piers.

3. Periodically assessing the structural performance and functionality during the service life.

### 7.2.1 Precision error prediction

The precision error is predicted by calculating frequency resolution and distance resolution induced error using one Brillouin spectrum reading obtained from the analyzer. Figure 7.2 shows the interpreted strain  $\varepsilon$ , analyzer measured Brillouin peak power, strain gradient  $\varepsilon'$ , and measurement precision error  $\Delta\varepsilon$  along the test pile, from the top nearside to the top outside of the pile. The strain is converted from the measured Brillouin frequency shift, using the calibrated conversional coefficient ( $0.46\text{MHz}/\mu\varepsilon$ ), and the precision error is calculated as the standard deviation of 200 measurement data sets. The strain profile is in a range of  $0 - 2000\mu\varepsilon$  along the test pile distance. The peak power of the received signal varies between  $153\text{dB}$  and  $155\text{dB}$ . The power loss reaches a maximum at distance  $z = 49\text{m}$  where the strain reduces sharply from  $2000\mu\varepsilon$  to zero. The measured Brillouin spectrum bandwidth does not fluctuate significantly except at distance  $z = 49\text{m}$  where the bandwidth achieves its maximum level of  $200\text{MHz}$ . The measurement precision error significantly increases from  $10\mu\varepsilon$  to  $75\mu\varepsilon$  at distance  $z = 49\text{m}$ . This finding is consistent with the previous lab observations, where a dependent relationship between the SNR, the bandwidth of the measured spectrum and the measurement precision error with the measured strain gradient was verified.

The frequency resolution is derived from the analyzer measured SNR and FWHM using Eq. 5.1. Figure 7.3 compares the predicted frequency resolution induced precision error as well as the analyzer measured precision error. The analyzer measured precision error displays a varying precision error along the cable length, with a baseline of about  $10\mu\varepsilon$  and a peak value as much as  $79\mu\varepsilon$ . The baseline value is close to the uniform precision error recorded in the lab, attributed to the analyzer random noise. The predicted frequency resolution induced error stays at around  $8\mu\varepsilon$ , while the analyzer measured error varies in a larger range and achieved to as much as  $75\mu\varepsilon$ . This again verifies that besides frequency resolution, there are other sources of precision error.

The distance resolution induced error is calculated using Eq. 5.10, with the previous lab calibrated timing error. Figure 7.4 compares the predicted distance resolution induced error and the analyzer measured precision error. It can be seen that, the predicted distance error was close to zero where there is little strain change, and it significantly increases where there is rapid strain change (at distance around  $z = 49\text{m}$ ). Similar trend can be found in analyzer measured precision error. In most parts of the cable, the predicted distance error varies in a range of  $0 - 8\mu\varepsilon$  and the analyzer measured error is  $8 - 15\mu\varepsilon$ . The maximum predicted distance induced error is  $59\mu\varepsilon$  and the measured error is again relatively larger, which is

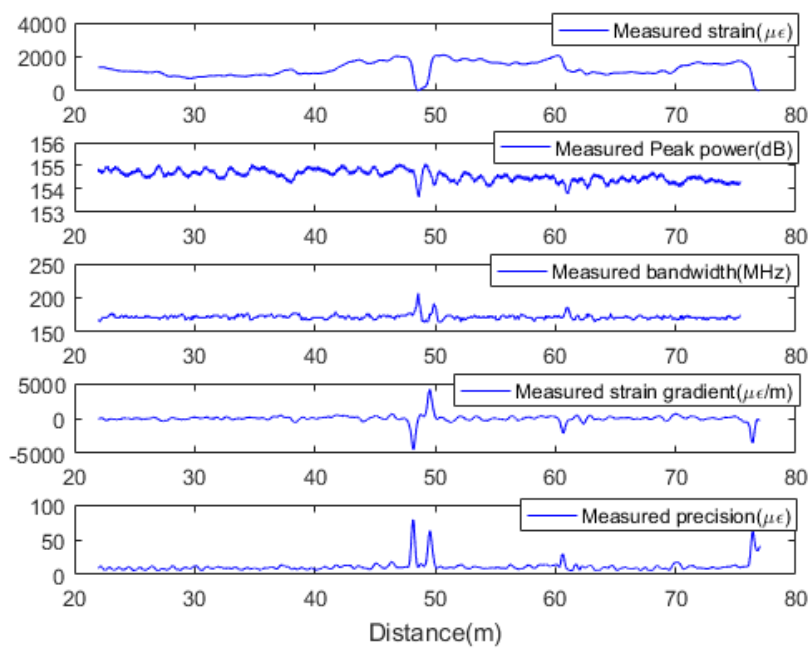


Fig. 7.2 The analyzer measured result including strain, peak power and bandwidth of the Brillouin spectrum, strain gradient and precision error

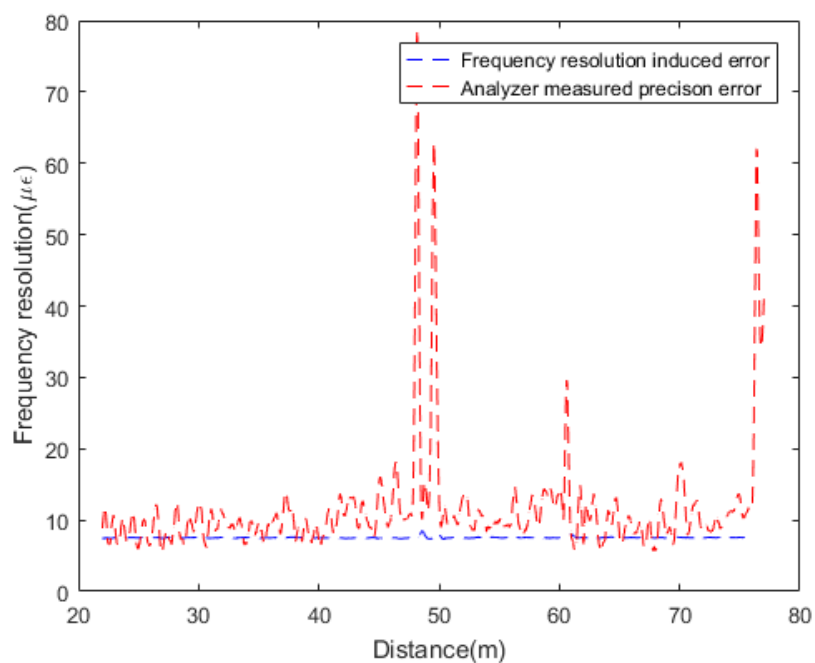


Fig. 7.3 The comparison of the analyzer measured precision error and the frequency resolution induced error calculated from the SNR and bandwidth of the Brillouin spectrum

$78 \mu\epsilon$ . Although the predicted distance induced error is generally smaller than the analyzer measured precision error, it can effectively represent the trend of the measured precision error change along the fibre. Compared to the predicted frequency resolution, the predicted distance error induced precision error is more effective in predicting the relationship between the precision and the non-uniformity of the strain profile.

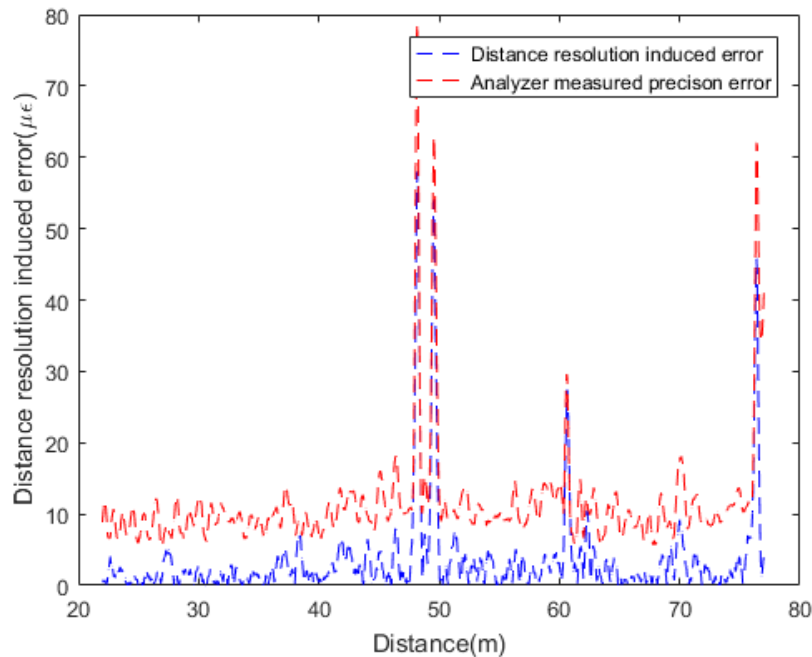


Fig. 7.4 The comparison of the analyzer measured precision error and the distance resolution induced error calculated from the calibrated timing error of the analyzer

The WOO site measurement precision error is finally calculated by combining the frequency resolution induced error and the distance resolution induced error together using Eq. 5.11. The final predicted precision error is then compared to the analyzer measured precision error, as shown in Fig. 7.5. A good agreement between the two errors can be clearly seen in the whole cable length.

Figure 7.6 indicates the agreement between the predicted and the analyzer measured precision error more clearly. The blue dots are the predicted precision error with regard to the analyzer measured error for all the measuring points along the test cable. The red line is a reference line with a uniform slope, representing the perfect situation where all the predicted errors are the same as the analyzer measured errors. It can be seen that the blue dots scatters closely around the red reference line (especially at small error range), verifying the good agreement between the predicted precision error and the analyzer measured errors.

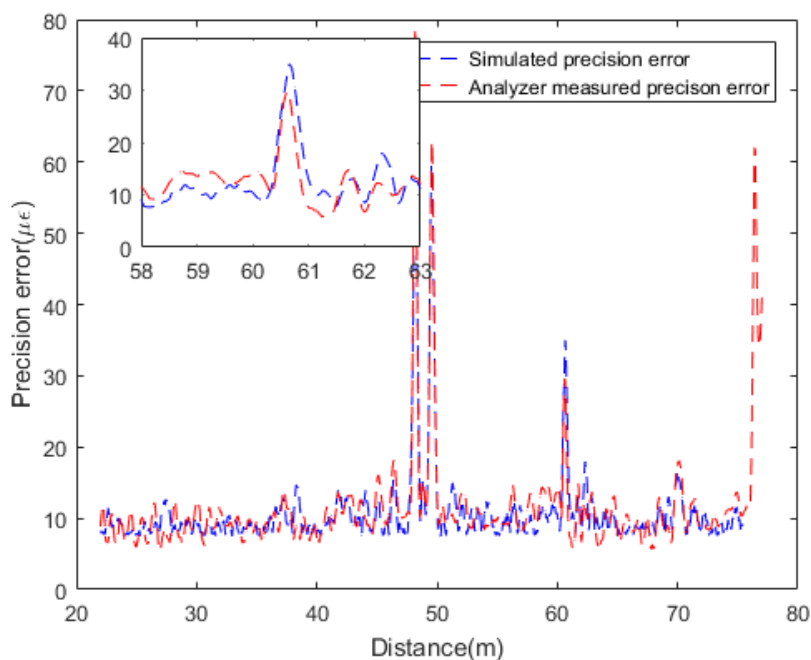


Fig. 7.5 The comparison of the analyzer measured precision error and the predicted precision error which is the combining effect of distance error and frequency resolution

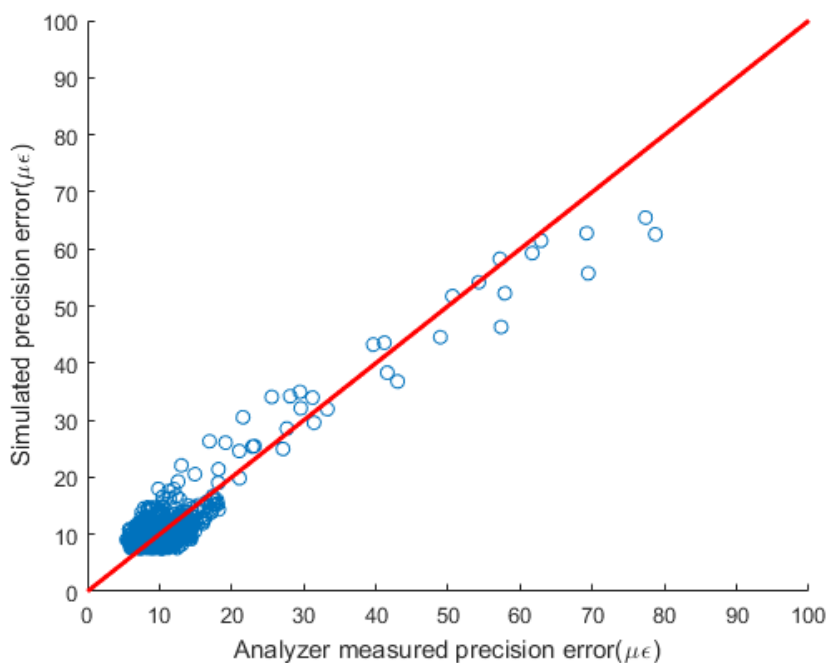


Fig. 7.6 The illustration of the agreement between the analyzer measured precision error and the simulated precision error

### 7.2.2 Data interpretation

The axial strain measurements of the pile load test are used to investigate the full behaviour of the tested WOO pile diaphragm wall. Fujikura reinforced strain sensing cable and the Brugg V1 strain sensing cable were installed adjacent to each other in the pile for pile behaviour monitoring. Five load levels were applied to the pile through the O-cell. At each load, six repeated measurements were taken for pile behaviour analysis. In this process, the mean value of the six Brillouin centre frequencies is used for monitoring the strain increment at each tested load. The calculated strain data is processed using the established horizontal shift methodology to minimize the systematic error. Filtering is conducted by contributing different weights to the measurements to minimize the precision error.

Figure 7.7 illustrates the analyzer measured Brillouin frequency shift of the Fujikura reinforced strain sensing cable as well as the Brugg strain sensing cable at different loading levels. Because of concrete hydration, measurement fluctuation over the distance can be observed for both cable test results, especially at  $z = 50m$  where there is a sharp strain drop. Under one loading level, the maximum Brillouin frequency shift difference is close to  $0.1 GHz$  ( $2000 \mu\varepsilon$ ) for the Fujikura cable and  $0.3 GHz$  ( $6000 \mu\varepsilon$ ) for the Brugg cable. This is most likely induced by the interactions between the cables and concrete aggregates. It is also possible that the concrete hydration during the curing process may have contributed to the uneven strain profile. Under different loading levels, the increments of the Brillouin frequency shift varies along the two fibres. With the O-Cell installed at the bottom of the pile, the applied loads decreases with the pile depth. As a result, the axial Brillouin frequency shift differences are larger at the top of the pile and smaller at the bottom of the pile. As in Fig. 7.7, the Brillouin frequency shift differences are at a maximum at the two ends and at a minimum in the middle of the measurements for both the Fujikura and Brugg cables.

### 7.2.3 Raw strain increment

The raw strain measurement is temperature compensated to remove any thermal strain. Because the temperature does not vary significantly with distance underground, the bottom loop temperature is assumed to be same as the tunnel loop temperature. Therefore, the strain measurement is vertically shifted based on the reference bottom loop reading as temperature compensation.

The temperature compensated strain measurements are used to obtain the strain increment along the pile during the loading test. The results are indicated in Fig. 7.8. It can be seen that the Brugg cable results displays a larger spatial variation than the Fujikura cable, even though the two sensing cables were placed adjacent to each other. Visible strain development trends

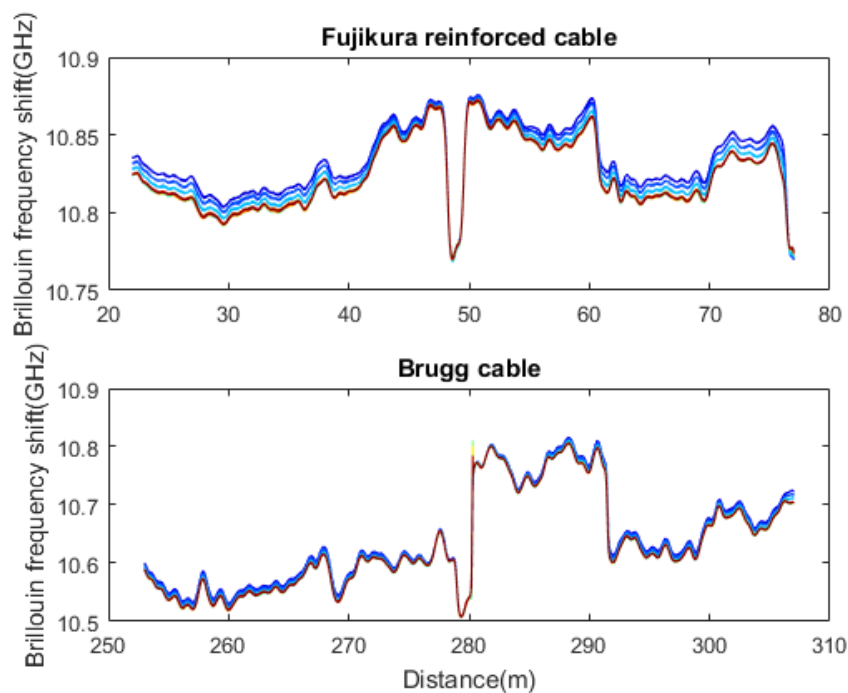


Fig. 7.7 Analyser measurement of the Fujikura strain sensing cable as well as the Brugg strain sensing cable for the WOO pile load test

can be found in the Fujikura cable results but not in the Brugg cable results, due to notable measurement fluctuations. However, for both sensing cables the general strain development trend and magnitude are in good agreement. The strain increment is close to zero at  $z = 50\text{m}$ , where the bottom of the pile and the O-cell are located. As the cable approaches the ground level of the pile, the strain increments at different load levels reaches a maximum, around  $400\mu\epsilon$  for both the cables under the highest loading level.

The spatial variations of the strain increments are compared under different loading levels for the two tested cables. Under the baseline condition, the strain increment variation over distance mainly comes from the analyzer frequency resolution. The calculated spatial variation of the strain increment is  $15.3\mu\epsilon$  for the Fujikura cable and  $18.1\mu\epsilon$  for the Brugg cable. The reason for the relatively larger spatial fluctuation in the Brugg cable measurements is that the measured Brillouin peak power of the Brugg cable is  $2.5\text{dB}$  lower than the Fujikura cable, leading to a lower SNR and thus larger analyzer frequency resolution. In addition, as previously tested in the lab, the Brugg V1 cable shows creeping effects at large strains. During the load test, the Brugg cable is likely to creep, inducing unexpected strain to the tested results. Therefore more fluctuations occur in the final strain increment results of the Brugg cable.

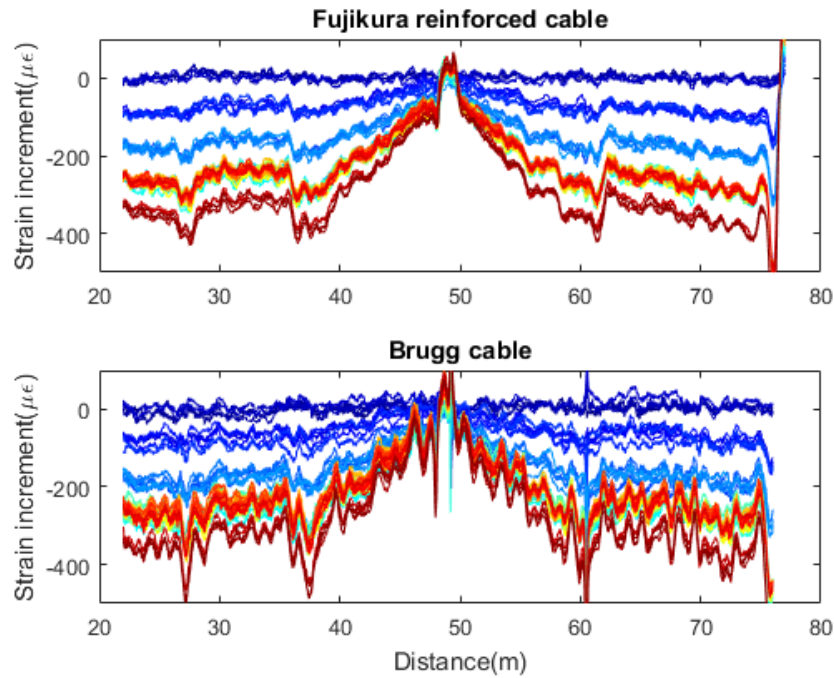


Fig. 7.8 The raw strain increment results of the adjacently installed Fujikura and Brugg cables during the WOO pile loading test

With increasingly higher loads applied, the spatial variation of the strain increments becomes larger for both the Fujikura cable and Brugg cable results. The strain increment fluctuation of the Brugg cable presents nearly twice that of the Fujikura cable results ( $22.7 \mu\epsilon$  for the Fujikura cable and  $47.7 \mu\epsilon$  for the Brugg cable under the maximum load condition). At this time, not only the analyzer frequency resolution, but also the non-uniformity of the measured strain profile starts to influence the spatial variation of the strain increment calculation. It can be seen that the strain increment results shows spikes at faster strain change sections, such as  $z = 38m$ ,  $50m$  and  $63m$ . The spikes grow bigger with loads, and generally bigger for the Brugg cable results. One source of these spikes could be measurement systematic error which can be minimized by horizontally moving the measurement in sections, as previously verified in Chapter 6 that the measurement systematic error of the strain increment can be equal to the distance error.

#### 7.2.4 Interpreted strain increment

During the data interpretation process, the systematic error is minimized by horizontally shifting the measured Brillouin centre frequency profile. As previously verified in the lab, systematic error is related to the location determination error, and a faster strain gradient

leads to a larger strain increment error. Therefore, the horizontal shift process is conducted in sections based on the potential systematic error of the strain increment calculation. Weights which represent data reliability are allocated to each measurement point using Eq. 6.17 with strain gradient information. Lower weight measurements is then shifted in sections for systematic error minimization.

Figure 7.9 presents the calculated weight (blue line) and the analyzer measured Brillouin centre frequency (red line). Based on the weight profile, the horizontal shift sections are determined, marked as dashed lines in the figure. The measurement of the Fujikura cable is separated into seven parts and the Brugg cable is separated into nine parts. In each section, the measurements with faster strain gradients (lower data weights) are horizontally moved against the baseline reading, to achieve the minimum distance error between the two measurements. In this way, the distance error induced systematic error of the strain increment calculation can be minimised.

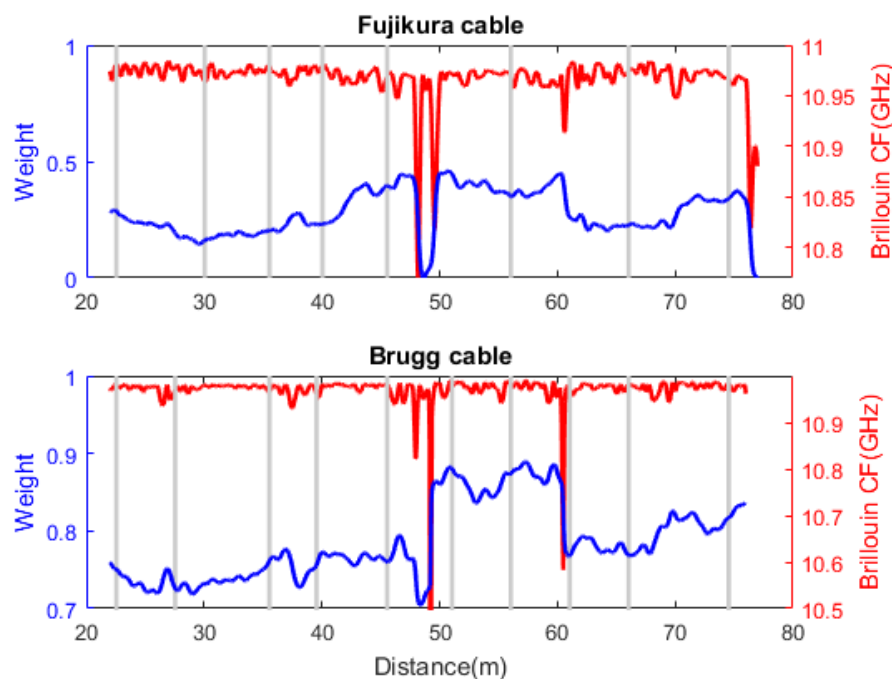


Fig. 7.9 The illustration of the data interpretation section (shown as grey lines) which is determined by the data weight profile for the Newfoundland pile load test

The results of the strain increment calculation, after horizontal shifting of the measured Brillouin centre frequency in sections, are shown in Fig. 7.10. Compared to the raw strain increments (Fig. 7.8), the horizontal shifted strain increments present less fluctuations and therefore clearer trends of strain development along the cable length, especially for the Brugg cable results.

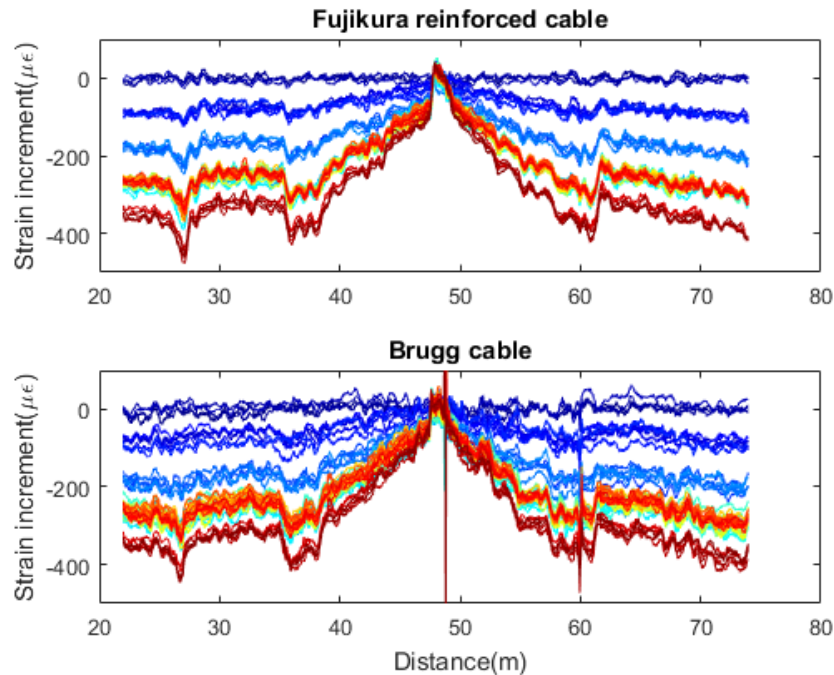


Fig. 7.10 The interpreted strain increment results after horizontal shift treatment for the adjacently installed Fujikura and Brugg cables during the WOO pile loading test

Table 7.2 lists the measurement spatial variations with and without the horizontal shift process for the Brugg cable and the Fujikura cable under different load conditions. At each load level, the variation is calculated as the standard deviation of all measuring points at  $z = 28.5\text{ m} - 33.5\text{ m}$  for six repeated measurements. It can be seen from the table that the raw measurement fluctuation increases with loading, for example  $7.4\ \mu\epsilon$  more variation are found under the 125% DVL load condition compared to that under the baseline condition for the Fujikura cable measurements, and  $29.6\ \mu\epsilon$  more variation are found for the Brugg cable measurements. After horizontal shifting, the measurement variation is reduced to  $18.0\ \mu\epsilon$  for the Fujikura cable and  $23.6\ \mu\epsilon$  for the Brugg cable.

It can be concluded that the horizontal shift data interpretation process can reduce the measurement fluctuation and thus improve the measurement accuracy. Under the baseline condition, the spatial variation reduces by  $0.6\ \mu\epsilon$  for the Fujikura cable and  $2.1\ \mu\epsilon$  for the Brugg cable with the horizontal shift data interpretation process. When the cable is under the load level of 125% DVL, the spatial variation reduces by  $4.7\ \mu\epsilon$  for the Fujikura cable and  $24.1\ \mu\epsilon$  for the Brugg cable with the horizontal shift data interpretation process. The relatively larger accuracy improvement for the Brugg cable measurement indicates that the effect of the horizontal shift method is more significant with the original fluctuated measurement under a higher loading condition.

Table 7.2 Comparison of strain increment fluctuations with or without using the horizontal shift interpretation method under different loading conditions for the Fujikura cable and the Brugg cable

Loading condition	Fujikura cable variation		Brugg cable variation	
	No shift	Shift	No shift	Shift
0% DVL	15.3 $\mu\epsilon$	14.7 $\mu\epsilon$	18.1 $\mu\epsilon$	16.0 $\mu\epsilon$
25% DVL	17.1 $\mu\epsilon$	16.8 $\mu\epsilon$	20.8 $\mu\epsilon$	16.0 $\mu\epsilon$
75% DVL	18.0 $\mu\epsilon$	15.2 $\mu\epsilon$	28.2 $\mu\epsilon$	23.5 $\mu\epsilon$
100% DVL	21.0 $\mu\epsilon$	16.4 $\mu\epsilon$	38.3 $\mu\epsilon$	23.3 $\mu\epsilon$
125% DVL	22.7 $\mu\epsilon$	18.0 $\mu\epsilon$	47.7 $\mu\epsilon$	23.6 $\mu\epsilon$

### 7.2.5 Data filtering

The final strain increment results are obtained by fitting the shifted strain increment ( $y_i$ ) with a smoothing spline to minimize the precision error. The smoothing spline minimizes the objective:

$$p \sum_i w_i (y_i - s(x_i))^2 + (1 - p) \int \left( \frac{d^2 s}{dx^2} \right) dx \quad (7.1)$$

in which  $s$  is the smoothing spline. It is constructed for the specified smoothing parameter  $p$  and the specified weight  $w_i$ .  $p$  is the parameter that defines how smooth the fitting line is.  $p = 0$  produces a least squares straight-line fit to the data, and  $p = 1$  produces a cubic spline interpolation. It is stated that the interesting range of  $p$  is typically near  $\frac{1}{1+h^3/6}$  and  $h$  is the average spacing of the data points [2].

The effect of the smoothing parameter is then studied. Table 7.3 illustrates the mean error of the filtered WOO site measurements using different smoothing parameters. The mean error is calculated as the mean difference between the filtered curves and the non-filtered curves at each loading conditions. It can be seen that the filtering process does not induce much change to the raw data as the maximum mean difference is 14.4  $\mu\epsilon$  when the smoothing parameter is used as 0.9. This amount of strain variation is even smaller than the random noise of the analyzer. Therefore it is assumed that the strain distribution shape will not be missed using a smoothing parameter larger than 0.9.

In the WOO pile load test, the measurement sampling resolution is 0.05 m, leading to a smoothing parameter of 0.99998 for the fitting process. The weight profile is calculated from the measured strain gradient using Eq. 6.17 to represent the data reliability as previously verified in the lab. The final fitting result of the strain increment during the load test is shown

Table 7.3 Comparison of the smoothing parameter effect on the filtered results

Data spacing ( $m$ )	Smoothing parameter	Mean error ( $\mu\epsilon$ )
0.05	0.99998	6.6
0.1	0.9998	8.7
0.23	0.998	10.6
0.5	0.98	12.5
0.68	0.95	13.4
0.87	0.9	14.4

in Fig. 7.11 where the small dots are the previously shifted strain increments and the coloured lines are the fitted results of the shifted strain.

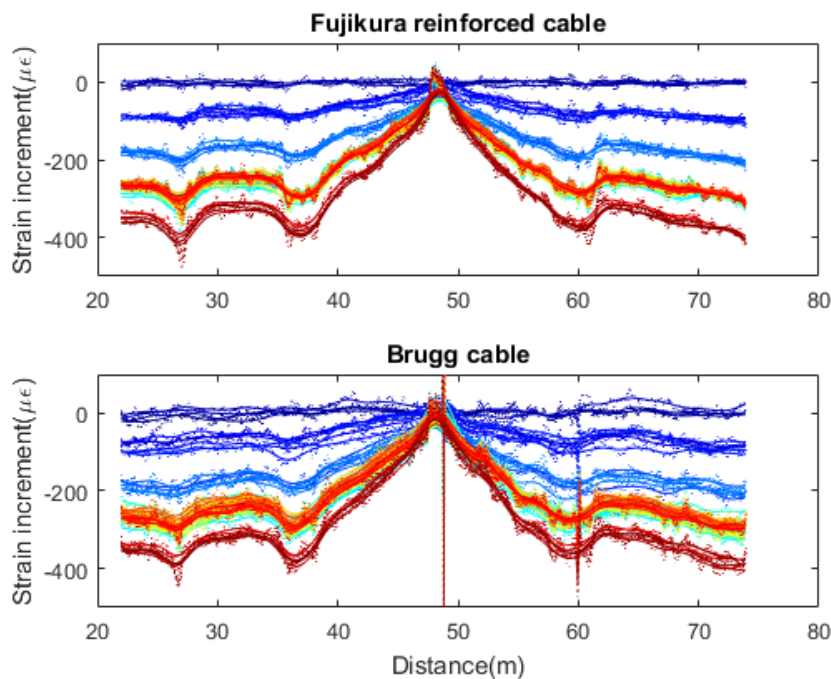


Fig. 7.11 The interpreted strain increment results after horizontal shift and filtering interpretation processes for the adjacently installed Fujikura and Brugg cables during the WOO pile loading test

The above figure presents that after horizontal shift and fitting, the variations of the strain increment are reduced significantly and therefore reveals clearer strain development trends during the pile load test. In addition, the strain increments including strain change magnitude as well as length, are in good agreement for the Fujiukura cable and the Brugg cable. Both the cable monitoring results show that under the loading condition, the strain is zero at  $z = 48.5m$ , at the bottom of the pile. From the bottom of the pile, the strain linearly

increases along the two axes of the pile for about 12 *m*. At  $z = 16.5\text{ m}$  and  $z = 60.5\text{ m}$ , a discontinuity of the linear strain increase is found. After that, the right side of the strain profile continues to increase but with a smaller changing coefficient for about 13 *m*. The left side of the strain keeps nearly constant for 10 *m* and then presents another strain change discontinuity at  $z = 26.5\text{ m}$ .

## 7.3 Newfoundland case study

The Newfoundland (NFL) construction site was located at No. 1 Park Place, Canary Wharf, London. In this project, the Fujikura reinforced strain cable was installed in a 1.5 *m* diameter pile, to monitor the development of strain and/or temperature during the concrete curing process. Detailed information of the construction site can be found in Chapter 5.

### 7.3.1 Precision error prediction

Field continuous sensing datasets is used to examine the prediction of the strain measurement precision error and its relation with strain gradient for BOTDR sensing system. Figure 7.12 shows the interpreted strain  $\epsilon$ , analyzer measured Brillouin peak power, strain gradient  $\epsilon'$ , and measurement precision error  $\Delta\epsilon$  along the pile. The strain is converted from the measured Brillouin frequency shift using a lab calibrated conversional coefficient ( $0.46\text{ MHz}/\mu\epsilon$ ), and the precision error is calculated as the standard deviation of 40 measurement data sets. It is clear from Fig. 7.12 that the strain profile along the fibre is rather non-uniform. This is most likely induced by the interactions between the cables and concrete aggregates. It is also possible that the concrete hydration during the curing process may have contributed to the uneven strain profile. It is very interesting to note that there is a close link between the precision error and strain gradient, as indicated in the figure. The larger the absolute value of the strain gradient, the higher the precision error appears.

The frequency resolution is predicted from the analyzer measured SNR and FWHM using Eq. 5.1. Figure 7.13 compares the predicted frequency resolution induced precision error as well as the analyzer measured precision error. Because the peak power and FWHM distribute comparatively uniformly, the frequency resolution, which is calculated from the peak power and the bandwidth, varies in a small range,  $24\mu\epsilon$  to  $27\mu\epsilon$  along the pile. However, the analyser measured precision error varies in a much larger range,  $23\mu\epsilon$  to  $45\mu\epsilon$ . It can be stated that the frequency resolution can properly predict the baseline noise of the analyzer measurement results but not able to predict the higher value of the analyzer measured precision error.

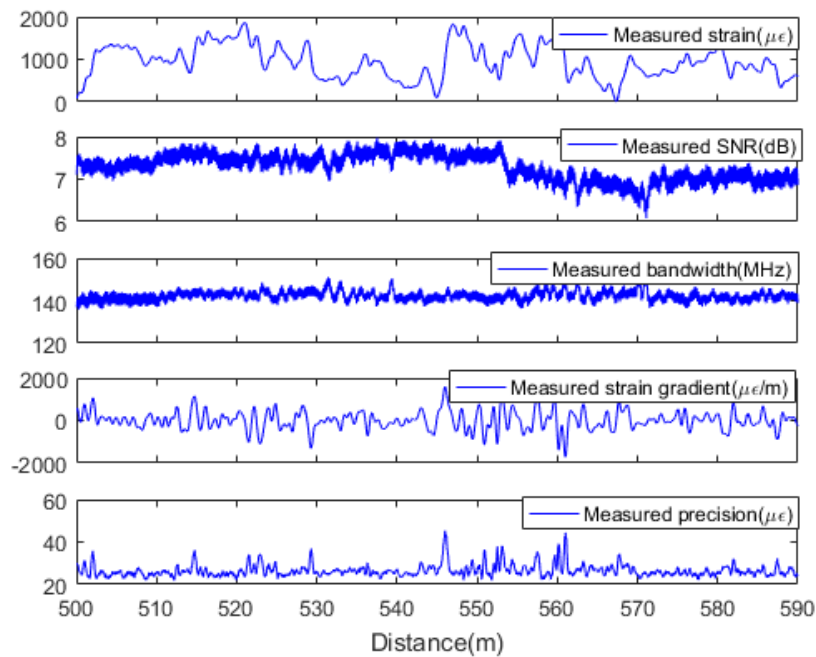


Fig. 7.12 Analyser measured strain, Brillouin peak power, strain gradient and measurement precision error profile along the pile

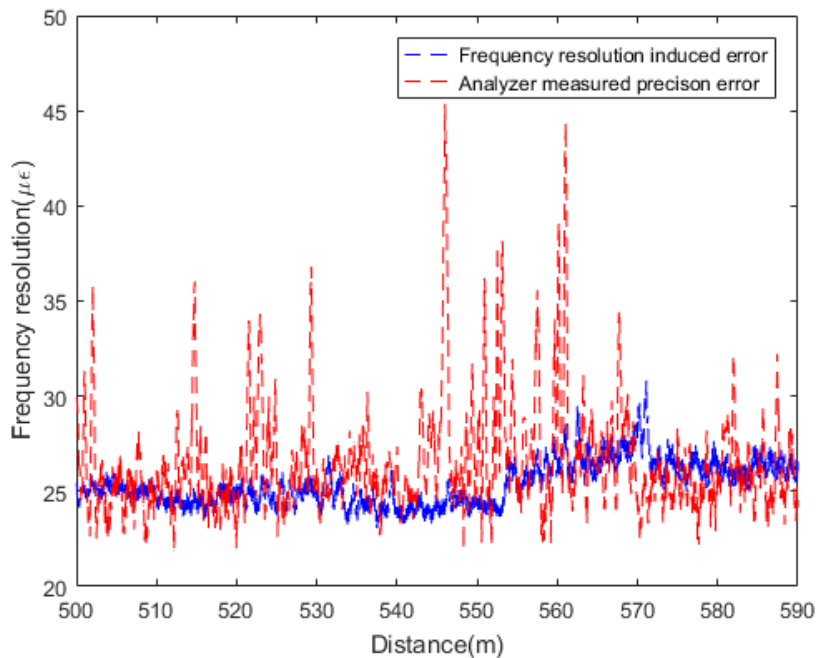


Fig. 7.13 Comparison of the predicted frequency resolution induced error obtained from analyzer measured Brillouin peak power information and the analyzer measured precision in Newfoundland pile site

The distance resolution induced error is calculated using Eq. 5.10, with the previous lab calibrated timing error ( $8.9\text{ ps}$ ). Figure 7.14 compares the predicted distance resolution induced error and the analyzer measured precision error. It can be seen from the figure that, on one hand, the distance error is close to zero where there is little strain change, but on the other hand the distance error significantly increases where there is rapid strain change. As a result, the predicted distance resolution induced error varies in a range of  $0 - 40\ \mu\epsilon$  along the cable although the previous predicted frequency resolution is much smaller ( $24\ \mu\epsilon$  to  $27\ \mu\epsilon$ ), indicating that distance resolution induced precision error is more significantly affected by the non-uniformity of the strain profile. Therefore the distance resolution induced error is more appropriate to predict the strain non-uniformity induced precision error rather than the the noise of the analyzer.

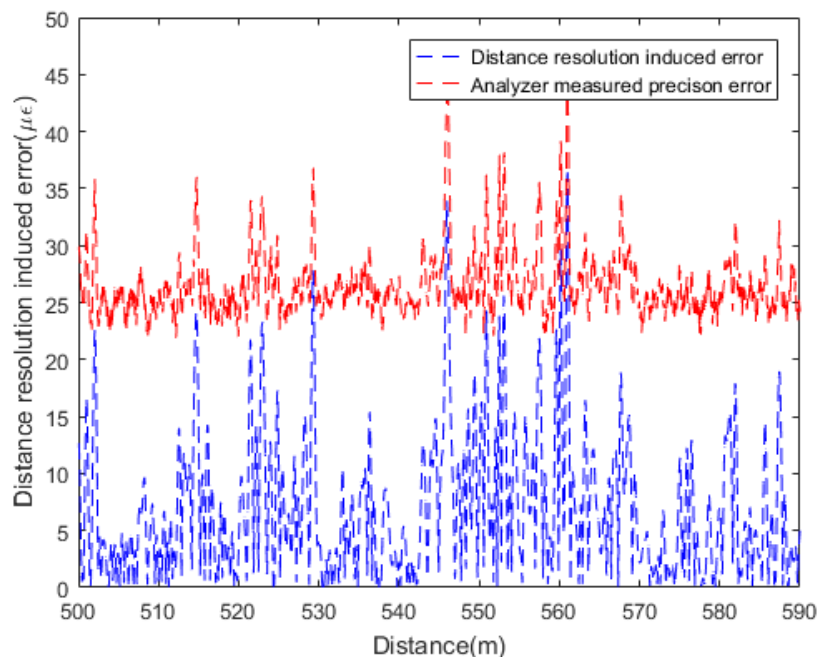


Fig. 7.14 Comparison of the predicted distance resolution induced error and the analyzer measured precision at the Newfoundland pile site

The NFL site measurement precision error is finally calculated by combining the frequency resolution induced error and the distance resolution induced error together using Eq. 5.11. The combined precision error is then compared to the analyzer measured precision error in Fig. 7.15. A good agreement can be clearly seen between the predicted precision error and the analyzer measured precision along the cable. The measurement precision error as shown in the figure displays a varying precision error along the cable length, with baseline of about  $25\ \mu\epsilon$  and peak values of around  $45\ \mu\epsilon$ . This is much larger than that of the free

cable, where a uniform precision error of  $15 \mu\epsilon$  was reported [85], attributed to the analyzer random noise.

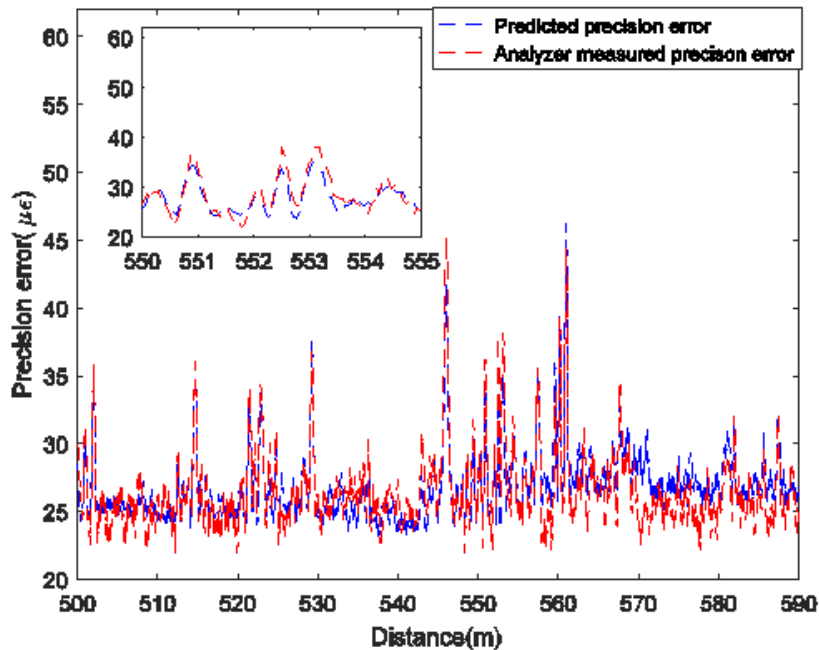


Fig. 7.15 Comparison of the analyzer measured precision error and the predicted precision error at the Newfoundland pile site

The analyser measured precision error versus the predicted precision error is shown in Fig. 7.16. A remarkable agreement between the measured precision error and the predicted precision error can be observed. In the figure all the blue points obtained by combining the frequency resolution induced error and the distance error induced strain imprecision are scattered along a straight line with a uniform slope, verifying the good agreement between the predicted precision error and the analyzer measured errors.

### 7.3.2 Data interpretation

The loading test was conducted by the O-cell which was installed in the bottom of the pile. During the load test, the pile load was gradually increased from 0 to  $22.43 MN$  in steps of  $1.78 MN$ . The Brillouin frequency profiles along the tested cable were recorded by the BOTDR analyzer at each load step. Figure 7.17 illustrates the Brillouin centre frequency profile under different loading conditions along the cable length from the pile ground level (cable distance at  $z = 490 m$ ) to the bottom (cable distance at  $z = 540 m$ ) and then to the ground level of the other side of the pile (cable distance at  $600 m$ ). Along each side of the

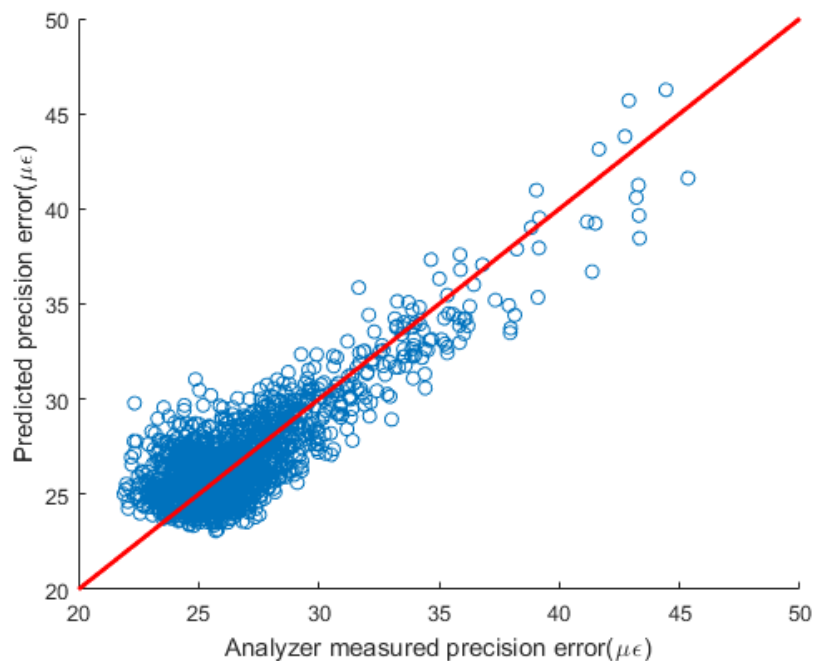


Fig. 7.16 The linearity between the analyzer measured precision error versus the predicted precision error.

pile, a 35 m length of the cable was loaded by the O-cell. There was a 10 m section of free cable loop that was not affected by the O-cell loads attached to the bottom of the pile.

### 7.3.3 Raw strain increment

The strain increment profile along the cable is shown in Fig. 7.18. Initially, the strain increment is close to zero all along the cable. As the load increases, an approximately linearly increased strain increment is found along the pile from the bottom to the ground level (distance at  $z = 490\text{m} - 530\text{m}$  and  $z = 560\text{m} - 600\text{m}$ ). During the loading test, the maximum strain increment is recorded as  $500\ \mu\epsilon$  near the bottom of the pile. As expected, the bottom loop data at a distance of around  $z = 540\text{m} - 550\text{m}$  stay close to zero when the pile is loaded, as this section of the cable is in the free condition.

The spatial fluctuation of the strain under the non-loading condition is about  $50\ \mu\epsilon - 60\ \mu\epsilon$  corresponding to the measurement precision error under the slow strain change condition. As the pile load increases, the strain increment profile becomes more spatially varied. Near the bottom loop of the cable, two spikes of strain increment can be clearly observed which is probably caused by the connection between the cable and the concrete.

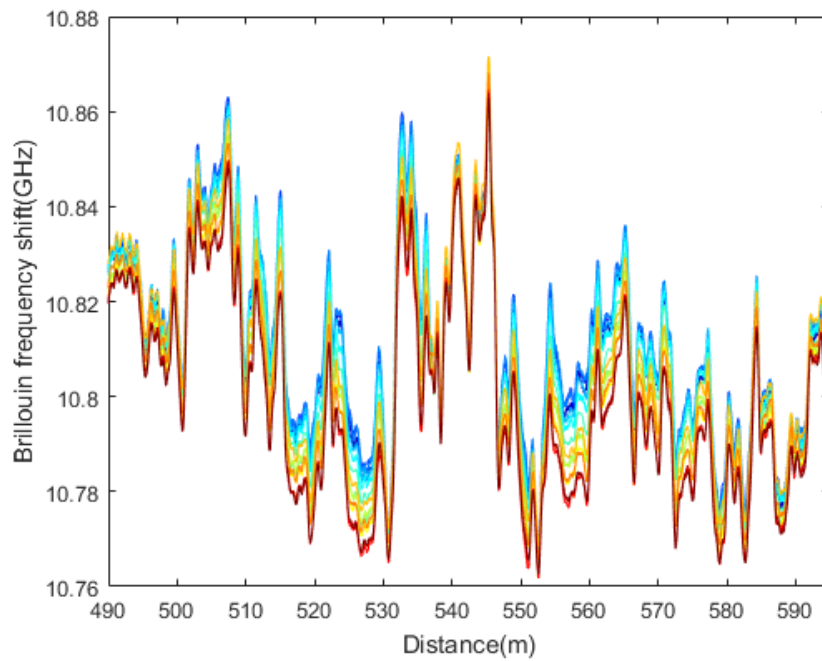


Fig. 7.17 The Brillouin frequency shift measurements along the tested cable during the Newfoundland pile load test

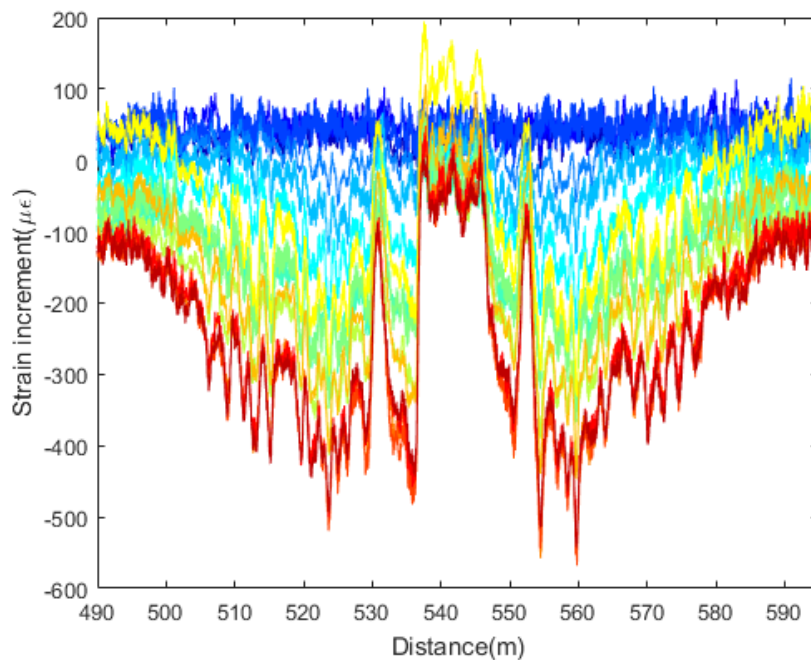


Fig. 7.18 The raw strain increment results along the cable during the Newfoundland pile load test

### 7.3.4 Interpreted strain increment

The strain interpretation process includes temperature compensation and horizontal shifting of the compensated strain. During this process the data reliability of the measurements which is calculated from the strain gradient of the measurements is used to attribute different weight to the data.

The weights of the measured data sets are calculated using Eq. 6.17 and are illustrated in Fig. 7.19. The sections of the data sets for horizontally shifting are shown as grey lines in the figure. Compared to the WOO pile site, the data weights are more non-uniformly distributed along the strain cable distance for the NFL case, indicating that the data of the NFL site is less reliable.

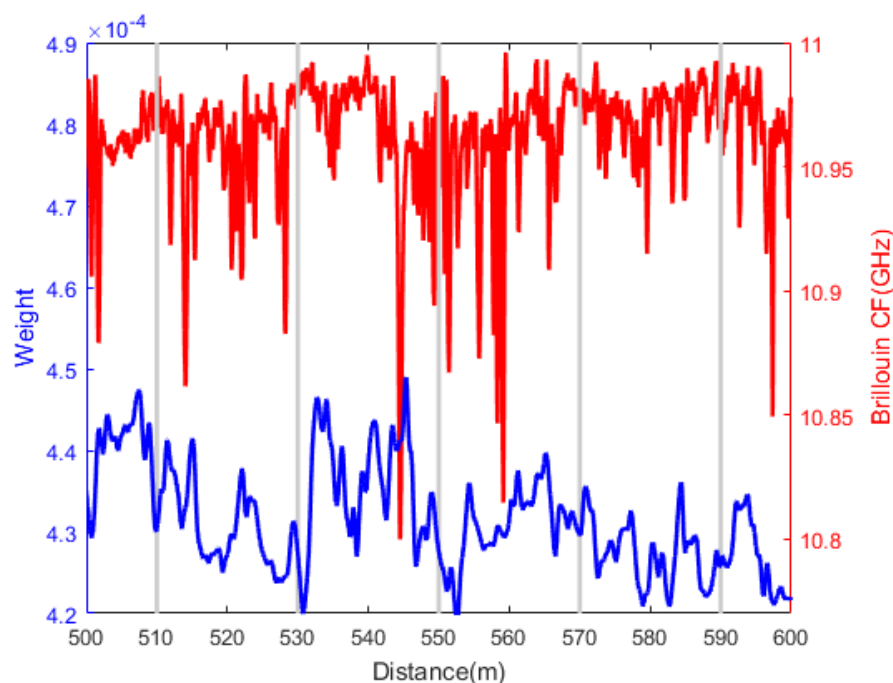


Fig. 7.19 The illustration of the data interpretation section (shown as grey lines) which was determined by the data weight profile for the Newfoundland pile load test

In each data sections, the measurements are horizontally shifted to minimize the distance error of the distributed fibre sensor. Figure 7.20 indicates the results of the strain increment after compensating for the distance error. However, no significant differences can be found after this process as Fig. 7.20 and Fig. 7.18 present approximately the same strain increment results. To further investigate the effect of this distance error compensation process, the spatial fluctuation of the measurements are summarized in Table 7.4.

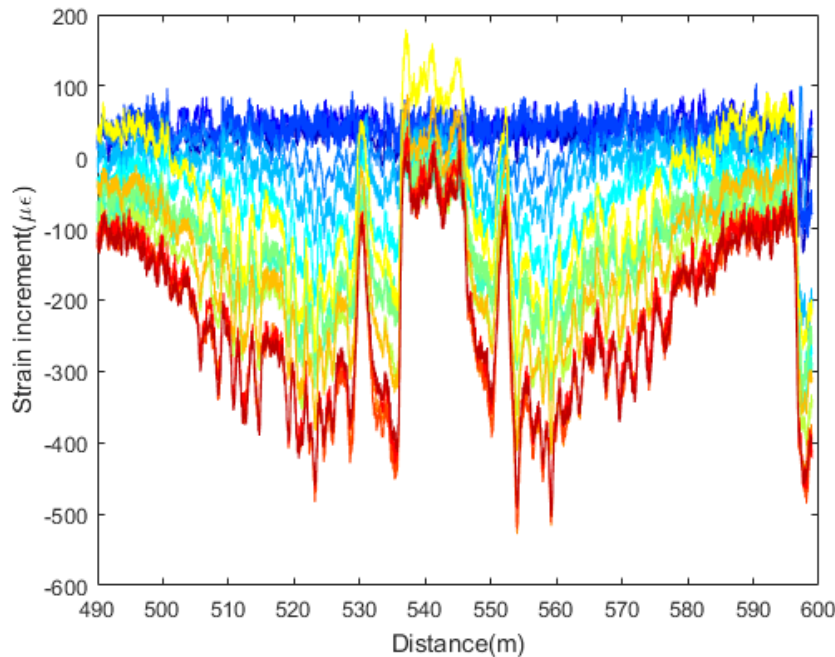


Fig. 7.20 The interpreted strain increment results along the cable after horizontal shift treatment during the Newfoundland pile load test

The strain fluctuation in Table 7.4 is calculated as the standard deviation of the data at a distance of 515 m to 518 m. The mean value of the strain fluctuation for all load steps is  $12.37 \mu\epsilon$  for the raw data and  $11.78 \mu\epsilon$  for the processed data. The raw data does not show clear dependency of the strain fluctuation on the load level for the NFL case, whereas the relationship can be clearly seen in the WOO site measurements. In the NFL case the strain fluctuation stays around  $12 \mu\epsilon$  during the whole load test, indicating that the non-uniformity of the strain profile does not induce a large amount of distance error. As a result, the horizontal shift process which can minimize the non-uniformity induced distance error does not have a significant effect on the data accuracy improvement. In general, the horizontal shift process can increase the strain accuracy but that is only a very small amount for this particular case.

### 7.3.5 Data filtering

The horizontally shifted data is filtered using smoothing splines functions. The smoothing parameter is used as 0.99998 for the fitting process similar to the WOO construction site as the sampling resolution of the tested analyzer is consistent for the two pile sites. The smoothing weight function is used as the previously calculated weight data. Figure 7.21

Table 7.4 Comparison of strain increment fluctuations with or without using the horizontal shift interpretation method under different loading conditions for the Fujikura cable at the Newfoundland pile site

Load steps (MN)	Strain fluctuation ( $\mu\epsilon$ )		Load steps (MN)	Strain fluctuation ( $\mu\epsilon$ )	
	No shift	Shift		No shift	Shift
0	11.27	9.93	12.21	15.15	11.75
1.78	11.86	11.42	13.72	11.76	11.40
3.64	16.46	14.77	15.51	14.40	13.51
5.92	10.61	9.71	17.29	7.19	10.67
6.93	12.85	11.99	18.94	12.64	12.90
8.58	11.96	11.54	20.51	12.20	11.55
10.53	12.98	12.22	22.43	11.73	11.54

presents the final results of the processed strain increments for the NFL pile loading test. An more visible trend of the strain increment development, which is in agreement with the real site conditions can be clearly seen.

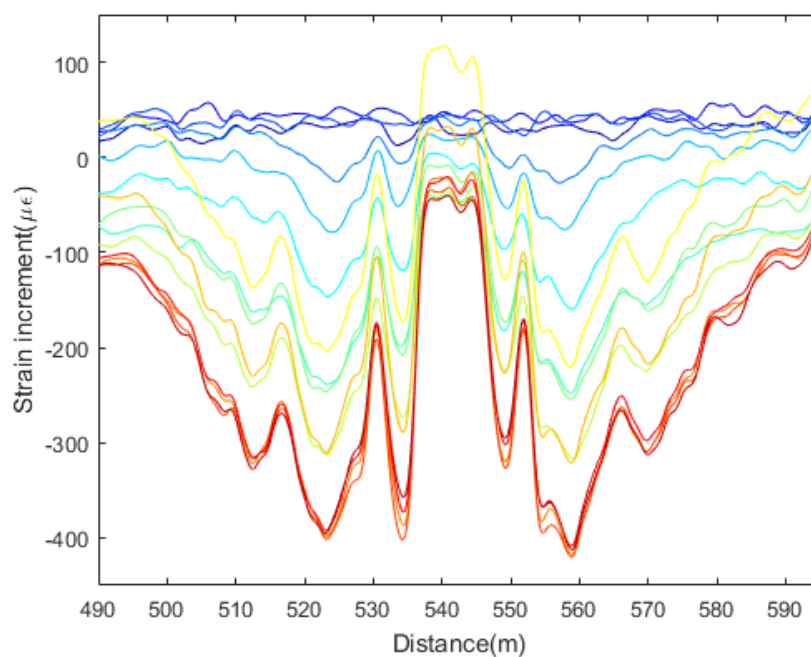


Fig. 7.21 The interpreted strain increment results along the cable after filtering treatment during the Newfoundland pile load test

## 7.4 Summary

1. A novel BOTDR data interpretation methodology was developed. The process mainly includes horizontal shifting of the data in sections to compensate for the non-uniform strain profile induced spatial error, and filtering of the data with data reliability as an input function to compensate for precision error.
2. The reliability of the data can be quantified as a function of the strain gradient. Data interpretation is separated in sections based on the measured strain gradient.
3. BOTDR measurement spatial error is compensated for by a sectional horizontally shift process. The data error can be decreased by  $24.1 \mu\epsilon$  as verified by one field site measurements. The method can significantly improve the data accuracy when the measured data shows dependency of the spatial variation on the load level.
4. BOTDR measurement repeatability error is compensated for by the filtering process. The objective of this process is minimizing the difference between the raw data and the filtered data using least squares equations with data reliability as an input of the weight function during the difference minimizing process.



# Chapter 8

## Conclusions

Over the last decade, infrastructure monitoring has proven to be a demanding application of distributed fibre optic sensors (DFOS) in terms of strain and temperature measurements. The technology is continuously developing. For instance, advances in the systems have reduced the minimum spatial resolution of an advanced system to the centimetre scale. However, interpretation of the distributed strain/temperature data obtained in the field is sometimes not easy because of unavoidable measurement errors.

In this work, BOTDR measurement systematic and precision error has been thoroughly evaluated. It was revealed that Brillouin sensing error is related to spatial variations in temperature/strain. The relationships between the strain change rate with both measurement precision error and systematic error were investigated experimentally and theoretically, and it was determined that the faster the strain change rate, the larger the measurement precision error and systematic error. Obtaining the above characteristics of BOTDR measurement error with regard to strain non-uniformity parameters such as strain gradient, measurement error can be predicted and reliably compensated for.

### 8.1 Summary of thesis and important findings

The summary of the work is divided into the following five sections.

#### 8.1.1 Sensor calibration

Experimental results indicated that the accuracy of the BOTDR measurement is influenced by the fibre core and cladding diameters, the fibre polarization state, and the tight buffering jacket.

- A bigger core and smaller cladding of the tested fibre leads to a larger measurement error.
- A polarization maintaining fibre will increase the measurement accuracy by  $3 \mu\epsilon$ .
- The measurement error of a tight buffered cable is  $1.7 \mu\epsilon$  larger than that of the standardized single mode fibre.

A novel strain and temperature calibration platform was developed for the distributed fibre optic sensor. This test platform includes a water bath for accurate temperature calibration, and an aluminium linear-stage rig for accurate strain calibration.

Loading and unloading experiments were done to determine the repeatability, precision and accuracy of strain measurement. Four types of tight buffered strain sensing cable were calibrated in the laboratory. The steel wire reinforced strain sensing cable was proposed as the best suited sensing cable, considering its relatively higher measurement accuracy and little slippage occurring during the loading and unloading tests. Some of the strain sensing cable showed worse ability in strain measurements due to low linearity between the strain change and the measured Brillouin centre frequency.

The temperature cable was found out to have larger sensing hysteresis compared to strain cable which is probably due to the unstable property of the cable gel. After one cycle of heating/cooling the cable gel property tended to stabilize, and temperature hysteresis was observed to be significantly minimized. Bare optical fibre was tested in the same way and did not show any temperature hysteresis during the experiment.

### 8.1.2 Spontaneous Brillouin optical model

A novel spontaneous Brillouin scattering model was developed including:

- The simulation of the backscattered Brillouin scattering by the convolution of the injected pulse light and the intrinsic Lorentz shape distribution, the characteristic of which is influenced by the strain/temperature of the cable.
- The simulation of the Brillouin spectrum after signal processing by the weighted average process. The characteristic of the weight is dependent on the analyzer.
- The simulation of the noise by introducing power fluctuation to the simulated Brillouin spectrum. The amount of the fluctuation is dependent on the power level as revealed by experimental results.

The developed Brillouin optical model was used to investigate the relationship between the measurement error and different input parameters including SNR, bandwidth, and scanning steps. The model was also used for later error characterization.

### 8.1.3 Error characterization

It was observed in the experiment that when the cable is non-uniformly distributed, the measurement precision error is largely increased. Through modelling and experimental measurements, it was found out that:

- BOTDR measurement precision error is influenced by both the frequency resolution and the distance resolution. The repeatability error was approximately linearly related to the strain gradient.
- The frequency resolution induced and the distance resolution induced error can be compensated for by horizontal shifting in sections.
- The systematic error compensation method is based on minimizing a weighted sum of regularization objective function, to solve the inverse problem of the measured Brillouin spectrum data. It uses a weight function suited for different strain levels, minimizes the effect of low quality power data, and obtains the peak frequency of the Brillouin spectrum by statistically analyzing the weighted power data using the least squares method.
- Experimental results revealed that the systematic error of the strain increment fluctuation can be equivalent to location determination error induced measurement fluctuation. It can be compensated for by horizontal shifting in sections.

A repeatability error prediction method was constructed considering the distance resolution and frequency resolution induced measurement precision error. This predicted error can be used to quantify the data reliability during data interpretation.

Experimental results showed that step strain change induces systematic error in BOTDR. This was verified by the developed optics model which simulates the error using a step strain distribution with various strain inputs. Non-uniformly distributed strain was simulated using the model, and the results showed that a sharp strain change is more likely to induce systematic error, which is related to the limit of the analyzer's spatial resolution.

### 8.1.4 Data interpretation methodology

A strain data interpretation algorithm was developed to reconstruct strain with precision error and systematic error minimization. The reliabilities of the data points were calculated from the precision error which can be predicted using the measured Brillouin spectrum as well as the strain gradient profile. The systematic error was minimized by horizontal shifting function and the precision error was minimized by using a smoothing spline fitting function with weight profile inputs.

The remarkable advantage of this algorithm is that the deformed strain can be largely corrected back to the real strain in most cases. The verification results clearly demonstrated that the reliability of a narrower strain change measurement was able to be improved by 75% using this algorithm.

### 8.1.5 Field monitoring

Strain measurements obtained from the WOO pile site, and the Newfouldland pile site were processed and analyzed using the newly developed data interpretation methodology. It was found out that:

- The precision error prediction method can properly predict the BOTDR precision error as verified by the two pile site case studies.
- The horizontal shift in sections based on the data reliability can improve measurement accuracy by 24.1  $\mu\epsilon$  for the WOO site Brugg cable measurements.
- The improvement of the measurement accuracy is larger using the novel data interpretation methodology for original unreliable data.

## 8.2 Future work

The work presented in this study has demonstrated the precision and systematic error characterization as well as compensation method during data interpretation process for fibre optic distributed strain sensing to monitor the performance of structures. It is envisaged that the amount of BOTDR fibre optic sensor error is dependent on the non-uniformity of the measured strain. Generally a faster strain change rate leads to a larger measurement error.

In the context of future work of this error analysis study, there are cable and analyzer characterizations requiring follow up, and more work on strain reconstruction using Brillouin spectrum information need investigation. This is discussed below.

### **8.2.1 Analyzer characterization**

This study only focus on one type of BOTDR analyzer, in the future, the measurement error of different analyzers can be compared to construct an error minimization algorithm that specifically minimizes error for different types of analyzers.

### **8.2.2 Cable development**

In the future, new types of strain/temperature sensing cables can be developed based on the characterization results of their sensing performance. Temperature cable that is free from temperature hysteresis shall be designed and used for future temperature compensation process.

### **8.2.3 Strain reconstruction algorithm**

The model developed in this study to reconstruct strain from Brillouin 3D spectrum measurement results is time consuming and not applicable for strain increment calculations. Model simplifications can be done in the future to broaden its usage. Data obtained from sites can be interpreted using this model to verify its applicability.



# References

- [1] Adachi, S. (2008). Distributed optical fiber sensors and their applications. *SICE Annual Conference 2008*, pages 329–333.
- [2] Andersen, Z. J., Hermansen, M., Scheikel, T., Hertel, O., Stage, M., and Bisgaard, H. (2005). Time Series Study of Air Pollution Health Effects in COPSAC Children. Technical Report 1005, Danish ministry of the environment.
- [3] Ansari, F. (2007). Practical implementation of optical fiber sensors in civil structural health monitoring. *Journal of Intelligent Material Systems and Structures*, 18(8):879–889.
- [4] Bao, X. and Chen, L. (2011). Recent progress in Brillouin scattering based fiber sensors. *Sensors*, 11(4):4152–4187.
- [5] Bao, X., DeMerchant, M., Brown, A., and Bremner, T. (2001). Tensile and compressive strain measurement in the lab and field with the distributed Brillouin scattering sensor. *Journal of Lightwave Technology*, 19(11):1698–1704.
- [6] Bao, Y. and Chen, G. (2016). Temperature-dependent strain and temperature sensitivities of fused silica single mode fiber sensors with pulse pre-pump Brillouin optical time domain analysis. *Measurement Science and Technology*, 27(6):065101.
- [7] Bernini, R., Fraldi, M., Minardo, A., Minutolo, V., Carannante, F., Nunziante, L., and Zeni, L. (2006). Identification of defects and strain error estimation for bending steel beams using time domain Brillouin distributed optical fiber sensors. *Smart Materials and Structures*, 15(2):612–622.
- [8] Bohidar, H., Jossang, T., Feder, J., and Dil, J. G. (1989). Brillouin scattering study of pressure dependence of hypersonic sound velocity in binary liquids. *Journal of Physics D: Applied Physics*, 22:1252–1256.
- [9] Bouyahi, M., Zrelli, A., Rezig, H., and Ezzedine, T. (2016). Modeling the Brillouin spectrum by measurement of the distributed strain and temperature. *Optical and Quantum Electronics*, 48(2):1–10.
- [10] Boyd, R. W. (2013). *Nonlinear Optics*, volume 53. Third edit edition.
- [11] Brown, A. W., Demerchant, D., Bao, X., and Bremner, T. W. (1999). Analysis of the precision of a Brillouin scattering based distributed strain sensor. In *SPIE Conference on Sensory Phenomena and Measurement Instrumentation for Smart Structures and Materials*, volume 3670, pages 359–365.

- [12] Buchoud, E., Vrabie, V., Mars, J. I., D'Urso, G., Girard, A., Blairon, S., and Hénault, J. M. (2016). Quantification of submillimeter displacements by distributed optical fiber sensors. *IEEE Transactions on Instrumentation and Measurement*, 65(2):413–422.
- [13] Chen, G., Ph, D., and Asce, F. (2012). Pilot Study on Rugged Fiber Optic Brillouin Sensors for Large-Strain Measurements to Ensure the Safety of Transportation Structures. Technical report, Mid-America Transportation Center.
- [14] Cheung, L. L. K., Soga, K., Bennett, P. J., Kobayashi, Y., Amatya, B., and Wright, P. (2010). Optical fibre strain measurement for tunnel lining monitoring. *Proceedings of the Institution of Civil Engineers - Geotechnical Engineering*, 163(3):119–130.
- [15] Chunge, M. P. M. (2014). *Monitoring the Integrity of Bored Concrete Piles using Distributed Fibre Optic Sensors*. Master of philosophy, University of Cambridge.
- [16] Derosa, D. (2012). *Thermal effects on monitoring and performance of reinforced concrete structures*. PhD thesis, Queen's University.
- [17] Dhliwayo, J., Webb, D., and Pannell, C. (1996). Statistical analysis of temperature measurement errors in a Brillouin scattering based distributed temperature sensor. *SPIE*, 2838:276–286.
- [18] Di Sante, R. (2015). Fibre Optic Sensors for Structural Health Monitoring of Aircraft Composite Structures: Recent Advances and Applications. *Sensors*, 15(8):18666–18713.
- [19] Fajkus, M., Nedoma, J., Kepak, S., Jaros, J., Cubik, J., Zboril, O., Novak, M., and Vasinek, V. (2016). Effect of the geometric deformations on the Brillouin scattering in the standard single-mode optical fiber. In *Optical Modelling and Design*, page 98892E.
- [20] Fellay, A. (2003). *Extreme Temperature Sensing Using Brillouin Scattering in Optical Fibers*. PhD thesis.
- [21] Ferdinand, P. (2014). the Evolution of Optical Fiber Sensors Technologies During the 35 Last Years and Their Applications in Structural Health Monitoring. *Structural Health Monitoring*, 16:914–929.
- [22] Garis, D., Krebber, K., Schlip, F., and Gogolla, T. (1996). Distributed sensing technique based on Brillouin optical-fibre frequency-domain analysis. *Opt. Lett.*, (21):1042.
- [23] Garus, D., Gogolla, T., Krebber, K., and Schliep, F. (1997). Brillouin optical-fiber frequency-domain analysis for distributed temperature and strain measurements. *Journal of Lightwave Technology*, 15(4):654–662.
- [24] Goldfeld, Y. and Klar, a. (2011). Identification of the Stiffness Distribution Using BOTDR. *Proceedings of the 8th International Workshop on Structural Health Monitoring 2011: Conditioned-based Maintenance and Intelligent Structures*, (July):1376–1383.
- [25] Hao, Z. and Zhishen, W. (2008). Performance evaluation of BOTDR-based distributed fiber optic sensors for crack monitoring. *Structural Health Monitoring*, 7(2):143–156.
- [26] He, J., Chen, G., and Ou, J. (2009). Measurement Accuracy Improvement of Brillouin Signal Using Wavelet Denoising Method. In *Proceedings of SPIE*, volume 7293, pages 1–7.

- [27] Hoepffner, R. (2008). *Distributed fiber optic strain sensing in hydraulic concrete and earth structures : measuring theory and field investigations on dams and landslides*. PhD thesis, Technische Universität München.
- [28] Horiguchi, T., Kurashima, T., and Tateda, M. (1989). Tensile strain dependence of Brillouin frequency shift in silica optical fibers. *Photonics Technology Letters*, I(8928256):107–108.
- [29] Horiguchi, T., Shimizu, K., Kurashima, T., Tateda, M., and Koyamada, Y. (1995). Development of a Distributed Sensing Technique Using Brillouin Scattering. *Journal of Lightwave Technology*, 13(7):1296–1302.
- [30] Hotate, K. (2014). Recent achievements in BOCDA/BOCDR. *IEEE SENSORS 2014 Proceedings*, pages 142–145.
- [31] Hotate, K. and Tanaka, M. (2002). Distributed fiber Brillouin strain sensing with 1-cm spatial resolution by correlation-based continuous-wave technique. *IEEE Photonics Technology Letters*, 14(2):179–181.
- [32] Imai, M., Nakano, R., Kono, T., Ichinomiya, T., Miura, S., and Mure, M. (2010). Crack Detection Application for Fiber Reinforced Concrete Using BOCDA-Based Optical Fiber Strain Sensor. *Journal of Structural Engineering*, 136(8):1001–1008.
- [33] Iten, M. (2011). *Novel Applications of Distributed Fiber- Optic Sensing in Geotechnical Engineering*. PhD thesis, ETH ZURICH.
- [34] Jacobs, S., Refi, J., and Fangmann, R. (1997). Statistical estimation of PMD coefficients for system design. *Electronics Letters*, 33(7):619.
- [35] Jin, W. (1997). Simultaneous measurement of strain and temperature: error analysis. *Optical Engineering*, 36(2):598.
- [36] Kaur, M. and Kaur, N. (2014). A Novel Approach for Simple Distributed Brillouin Scattering Modeling for Temperature and Strain Sensing Scattering mechanisms :. *International journal om recent and innovation trends in computing and communication*, 2(12):4070–4074.
- [37] Kechavarzi, C., Soga, K., de Battista, N., Pelecanos, L., Elshafie, M., and Mair, R. (2016). *Distributed fibre optic strain sensing for monitoring civil infrastructure*. ICE, Cambridge, 1st edition.
- [38] Klar, A., Bennett, P., Soga, K., Mair, R. J., Tester, P., Fernie, R., St John, H. D., and Torp-Peterson, G. (2006). Distributed strain measurement for pile foundations. In *Proceedings of the ICE - Geotechnical Engineering*, volume 159, pages 135–144.
- [39] Klar, A. and Linker, R. (2010). Feasibility study of automated detection of tunnel excavation by Brillouin optical time domain reflectometry. *Tunnelling and Underground Space Technology*, 25(5):575–586.
- [40] Klug, F., Lackner, S., and Lienhart, W. (2017). Monitoring of Railway Deformations Distributed Fiber Optic Sensors. pages 1–8.

- [41] Lees, G. P., Wait, P. C., Cole, M. J., and Newson, T. P. (1998). Advances in optical fiber distributed temperature sensing using the Landau-Placzek ratio. *IEEE Photonics Technology Letters*, 10(1):126–128.
- [42] Li, W., Chen, L., and Bao, X. (2013). Compensation of temperature and strain coefficients due to local birefringence using optical frequency domain reflectometry. *Optics Communications*, 311:26–32.
- [43] Liehr, S., Lenke, P., and Wendt, M. (2009). Polymer optical fiber sensors for distributed strain measurement and application in structural health monitoring. *IEEE Sensors Journal*, 9(11):1330–1338.
- [44] Liu, X. (2011). *Characterization of Brillouin Scattering Spectrum in LEAF Fiber*. PhD thesis, University of Ottawa.
- [45] Mafang, S. F. (2011). *Brillouin Echoes for Advanced Distributed Sensing in Optical Fibres*. PhD thesis.
- [46] Mair, R. (2011). *TUNNELLING IN URBAN AREAS AND EFFECTS ON INFRASTRUCTURE Advances in research and practice*. Number July.
- [47] Mao, Y., Guo, N., Yu, K. L., Tam, H. Y., and Lu, C. (2012). 1-Cm-Spatial-Resolution Brillouin Optical Time-Domain Analysis Based on Bright Pulse Brillouin Gain and Complementary Code. *IEEE Photonics Journal*, 4(6):2243–2248.
- [48] Mei, Y., Xu, X., Yan, J., and Soga, K. (2016). Characterization on the distributed fibre optic sensors using a newly developed calibration system. In *Transforming the Future of Infrastructure through Smarter Information: Proceedings of the International Conference on Smart Infrastructure and Construction*, pages 105–110.
- [49] Minardo, A. (2003). *Fiber-optic distributed strain/temperature sensors based on stimulated Brillouin scattering*. PhD thesis, Seconda Università degli Studi di Napoli.
- [50] Minardo, A., Bernini, R., and Zeni, L. (2007). Stimulated Brillouin scattering modeling for high-resolution, time-domain distributed sensing. *Optics express*, 15(16):10397–10407.
- [51] Mohamad, H. (2008). *Distributed Optical Fibre Strain Sensing of Geotechnical Structures*. PhD thesis, University of Cambridge.
- [52] Mohamad, H. (2012). Temperature and strain sensing techniques using Brillouin optical time domain reflectometry. In *SPIE*, volume 8346, page 83461M.
- [53] MOHAMAD, H., BENNETT, P., SOGA, K., MAIR, R., and BOWERS, K. (2010). Behaviour of an old masonry tunnel due to tunnelling-induced ground settlement. *Géotechnique*, 60(12):927–938.
- [54] Mohamad, H., Soga, K., Pellew, a., and Bennett, P. (2011). Performance monitoring of a secant-piled wall using distributed fiber optic strain sensing. *Journal of Geotechnical and Geoenvironmental Engineering*, 137(12):1236–1243.

- [55] Motil, A., Bergman, A., and Tur, M. (2016). [INVITED] State of the art of Brillouin fiber-optic distributed sensing. *Optics and Laser Technology*, 78:81–103.
- [56] Motra, H., Hildebrand, J., and Dimmig-Osburg, A. (2014). Assessment of strain measurement techniques to characterise mechanical properties of structural steel. *Engineering Science and Technology, an International Journal*, 17(4):260–269.
- [57] Murayama, H., Kageyama, K., Naruse, H., Shimada, A., and Uzawa, K. (2003). Application of fiber-optic distributed sensors to health monitoring for full-scale composite structures. *Journal of Intelligent Material Systems and Structures*, 14(1):3–13.
- [58] Naruse, H. and Tateda, M. (1999). Trade-off between the spatial and the frequency resolutions in measuring the power spectrum of the Brillouin backscattered light in an optical fiber. *Applied optics*, 38(31):6516–6521.
- [59] Naruse, H. and Tateda, M. (2000). Launched pulse-shape dependence of the power spectrum of the spontaneous Brillouin backscattered light in an optical fiber. *Applied optics*, 39(34):6376–6384.
- [60] Naruse, H., Tateda, M., Ohno, H., and Shimada, A. (2002). Linear strain distribution dependence of the Brillouin gain spectrum. *2002 15th Optical Fiber Sensors Conference Technical Digest, OFS 2002*, 41(34):309–312.
- [61] nee Zhong, W. E., Stiller, B., Elser, D., Heim, B., Marquardt, C., and Leuchs, G. (2015). Depolarized guided acoustic wave Brillouin scattering in photonic crystal fibers. *arXiv*, 17(2007):1508.01309v1.
- [62] Neubrex (2018). Neural Optical Fiber Scope The Brillouin Backscattering Analyzer with patented Pulse-Pre-Pump technology with long distance measuring capability for Strain and/or Temperature measurement. Technical report, Neubrex Co.Ltd, Kobe.
- [63] Niklès, M. (2007). Fibre optic distributed scattering sensing system: perspectives and challenges for high performance applications. Technical report, Micron Optics.
- [64] Nishiguchi, K., Li, C. H., Guzik, A., and Kishida, K. (2014). Synthetic spectrum approach for Brillouin optical time-domain reflectometry. *Sensors (Switzerland)*, 14(3):4731–4754.
- [65] Nishio, M., Mizutani, T., and Takeda, N. (2010). Structural shape reconstruction with consideration of the reliability of distributed strain data from a Brillouin-scattering-based optical fiber sensor. *Smart Materials and Structures*, 19(3):035011.
- [66] Noergaard, T. (2010). An Introduction to the Fundamentals of Database Systems. Technical Report WP5051, Corning Incorporated, New York.
- [67] Omnisens SA (2005). Fiber optic distributed temperature & strain sensing technique. Technical report.
- [68] Pannell, C. N., Dhliwayo, J., and Webb, D. J. (1998). The accuracy of parameter estimation from noisy data, with application to resonance peak estimation in distributed Brillouin sensing. *Measurement Science and Technology*, 9(1):50–57.

- [69] Rajan, G. (2010). *Optical Fiber Sensors Advanced Techniques and Applications*.
- [70] Ravet, F., Bao, X., Li, Y., Yu, Q., Yale, A., Kalosha, V. P., and Chen, L. (2007). Signal processing technique for distributed Brillouin sensing at centimeter spatial resolution. *Journal of Lightwave Technology*, 25(11):3610–3618.
- [71] Ravet, F., Briffod, F., Glisic, B., Nikles, M., and Inaudi, D. (2009). Submillimeter crack detection with Brillouin-based fiber-optic sensors. *IEEE Sensors Journal*, 9(11):1391–1396.
- [72] Reichel, L. and Ye, Q. (2008). Simple square smoothing regularization operators. *Electronic Transactions on Numerical Analysis*, 33:63–83.
- [73] Rochat, E. and Niklès, M. (2014). Enhanced Brillouin distributed strain and temperature sensing for structural health monitoring in industrial applications. In *7th European Workshop on Structural Health Monitoring*, pages 938–945, Nantes. European Workshop on Structural Health Monitoring.
- [74] Rogers, A. J. (1988). Distributed optical-fibre sensors for the measurement of pressure, strain and temperature. *Physics Reports*, 169(2):99–143.
- [75] Schenato, L. (2017). *A Review of Distributed Fibre Optic Sensors for Geo-Hydrological Applications*, volume 7.
- [76] Smith, J., Brown, A., DeMerchant, M., and Bao, X. (1999). Simultaneous distributed strain and temperature measurement. *Applied Optics*, 38(25):5372.
- [77] Soga, K., Chaiyasarn, K., Viola, F., Yan, J., Seshia, A., and Cipolla, R. (2010). Innovation in Monitoring Technologies for Underground Structures. In *Information Technology in Geo-Engineering*, pages 3–18, Shanghai, China.
- [78] Soto, M. A. and Thévenaz, L. (2013). Modeling and evaluating the performance of Brillouin distributed optical fiber sensors. *Optics Express*, 21(25):31347.
- [79] Teis, P. H.-F. I. K. (1998). Keynote papers. In *Journal of Constructional Steel Research*, volume 46, pages A1–A2.
- [80] Thévenaz, L. (2010). Brillouin distributed time-domain sensing in optical fibers: State of the art and perspectives. *Frontiers of Optoelectronics in China*, 3(1):13–21.
- [81] Wang, F., Zhan, W., Zhang, X., and Lu, Y. (2013). Improvement of spatial resolution for BOTDR by iterative subdivision method. *Journal of Lightwave Technology*, 31(23):3663–3667.
- [82] Wilcock, M. J., Seo, H., and Soga, K. (2015). Monitoring TBM Thrust Load Propagation along Segmental Concrete Tunnel Lining Using Distributed Optical Fibre Strain Sensing. In *ITA WTC 2015 Congress and 41st General Assembly May 22-28, 2015 Lacroma Valamar Congress Centre, Dubrovnik, Croatia*, number February 2011, Dubrovnik, Croatia.
- [83] Wu, Z. S., Xu, B., Takahashi, T., and Harada, T. (2008). Performance of a BOTDR optical fibre sensing technique for crack detection in concrete structures. *Structure and Infrastructure Engineering*, 4(4):311–323.

- [84] Xie, S., Pang, M., Bao, X., and Chen, L. (2012). Polarization dependence of Brillouin linewidth and peak frequency due to fiber inhomogeneity in single mode fiber and its impact on distributed fiber Brillouin sensing. *Optics Express*, 20(6):6385.
- [85] Yamauchi, Y., Co, N., Neubrex, K., and Neubrex, G. (2007). A study of the stability, reliability, and accuracy of neubrex-based pipe thinning detection system. In *SHMII-3 2007. The 3rd International Conference on Structural Health Monitoring of Intelligent Infrastructure*, number March, Vancouver, British Columbia, Canada. Neubrex Co., Ltd.
- [Yu et al.] Yu, Y., Luo, L., Li, B., Guo, L., Yan, J., and Soga, K. Double Peak-Induced Distance Error in STFT-BOTDR Event Detection and the Recovery Method.
- [87] Yu, Y., Luo, L., Li, B., Soga, K., and Yan, J. (2016). Frequency Resolution Quantification of Brillouin-Distributed Optical Fiber Sensors. *IEEE Photonics Technology Letters*, 28(21):2367–2370.
- [88] Zeni, L., Picarelli, L., Avolio, B., Coscetta, A., Papa, R., Zeni, G., Di Maio, C., Vassallo, R., and Minardo, A. (2015). Brillouin optical time-domain analysis for geotechnical monitoring. *Journal of Rock Mechanics and Geotechnical Engineering*, 7(4):458–462.
- [89] Zhang, D., Cui, H., and Shi, B. (2013). Spatial resolution of DOFS and its calibration methods. *Optics and Lasers in Engineering*, 51(4):335–340.
- [90] Zhang, D., Shi, B., Gui, H. L., and Xu, H. Z. (2004). Improvement of spatial resolution of Brillouin optical time domain reflectometer using spectral decomposition. *Optica Applicata*, 34(2):291–301.
- [91] Zhang, D., Xu, H., Shi, B., Sui, H., and Wei, G. (2009). Brillouin power spectrum analysis for partially uniformly strained optical fiber. *Optics and Lasers in Engineering*, 47(9):976–981.
- [92] Zhang, W., Gao, J., Shi, B., Cui, H., and Zhu, H. (2006). Health monitoring of rehabilitated concrete bridges using distributed optical fiber sensing. *Computer-Aided Civil and Infrastructure Engineering*, 21(6):411–424.
- [93] Zhou, Z., He, J., Yan, K., and Ou, J. (2008). Fiber-reinforced polymer-packaged optical fiber sensors based on Brillouin optical time-domain analysis. *Optical Engineering*, 47(1):014401.
- [94] Zou, W., He, Z., and Hotate, K. (2009). Complete discrimination of strain and temperature using Brillouin frequency shift and birefringence in a polarization-maintaining fiber. *Optics Express*, 17(3):1248.

